



**Max-Planck-Institut für Metallforschung**  
Stuttgart

---

# **Interface Stability in Solid Oxide Fuel Cells for Intermediate Temperature Applications**

Nuri Solak

Dissertation  
an der  
**Universität Stuttgart**

---

Bericht Nr. 197  
Juni 2007

# **Interface Stability in Solid Oxide Fuel Cells for Intermediate Temperature Applications**

Dissertation

Von der Fakultät Chemie der Universität Stuttgart  
zur Erlangung der Würde eines  
Doktors der Naturwissenschaften (Dr. rer. nat)  
genehmigte Abhandlung

vorgelegt von

**Nuri Solak**

aus Gürün, Türkei

Hauptberichter: Prof. Dr. rer. nat. F. Aldinger

Mitberichter: Prof. Dr. rer. nat. Dr. h. c. mult. G. Petzow

Vorsitz : Prof. Dr. Ir. E. J. Mittemeijer

Tag der mündlichen Prüfung: 01.06.2007

Institut für Nichtmetallische Anorganische Materialien der Universität Stuttgart  
Max-Planck-Institut für Metallforschung  
Pulvermetallurgisches Laboratorium

2007

# Acknowledgements

I would like to express my sincerest thanks to the many people who made this thesis possible. In particular:

Foremost, I am deeply indebted to Prof. F. Aldinger for supervising my PhD work and for providing me the opportunity to work in the PML, especially in the field of computational thermodynamics, where the group at PML has played a pivotal role as a world pioneer.

I would like to thank Prof. Petzow and Prof. Mittemeijer, for accepting to be the co-examiners of my thesis exam committee.

Special thanks to my group leader, Dr. M. Zinkevich, whose expertise, understanding, and patience, added considerably to my work.

I would like to express my gratitude to Prof. S. Aydın, Prof. M. Ürgen and Prof. F. Üstel (Fatih Abi), for without their encouragement and support, I would never have imagined pursuing graduate study abroad. Thank you first for opening my vision, providing the scientific support but most importantly for believing in me.

This thesis would not have been possible without the friendly environment of the Max-Planck-Institut für Metallforschung (MPI-MF) and Pulvermetallurgisches Laboratorium (PML), and without the support of the International Max-Planck Research School for Advanced Materials (IMPRS-AM). I would like to thank Mr. Kaiser, Mr. Labitzke, Ms. Thomas, Mr. Mager, Ms. Heinrichs, Mr. Hammoud, and all the other technicians not only for their technical help but also for being the perfect host during my stay in the PML.

Special thanks to Seher Abla, “Frau Baydar” and her family and “Fadime Abla” and the Guendogan family. Also thanks to, Dr. Libuda and Ms. Paulsen, for always having time for me, listening to me patiently and trying to solve the bureaucratic difficulties.

I would like to thank my colleagues, Dr. Fabrichnaya, Dr. Golczewski, Wang, Manga, Marija, Sandra, Dejan, YouPing, my officemates Nana & Vladimir, Gautam, Datta, Ravi, Fares, Mohammed, and the other friends whose company made my days at PML memorable.

Thanks also go out to the members of “Turkish Mafia”, “MPI\_TURK”, for organizing tea breaks, barbecue parties, chatting. I want to thank Nalan & Murat, and also Gülin, for the last summer in Stuttgart.

Last but not least, I would like to thank Cleva, and to say once again “müteşekkirim”.

I cannot end without thanking my parents, Şefika and Turan, and brothers, Kıvanç and Orçun, for their constant encouragement and conviction. It is to them that I dedicate this work.

# Table of Contents

Acknowledgements .....	2
Table of Contents .....	3
Abstract.....	5
Zusammenfassung .....	7
<i>Chapter 1</i> Introduction .....	9
1.1. Intermediate Temperature Solid Oxide Fuel Cells (IT-SOFC) .....	9
1.2. Scope of This Dissertation.....	11
<i>Chapter 2</i> Experimental Techniques and Thermodynamic Modeling .....	13
2.1. Sample Preparation and Characterization.....	13
2.1.1. The Calphad Method .....	16
2.1.2. Models for the Gibbs Energy .....	17
2.1.2.1. Pure Elements and the Gas Phase.....	17
2.1.2.2. The Liquid Phase .....	18
2.1.2.3. The Stoichiometric Phases .....	18
2.1.2.4. The $A_2BO_4$ ( $K_2NiF_4$ -type) Phases .....	19
2.1.2.5. The $ABO_3$ (perovskite-type) phases .....	23
2.1.2.6. The $A_{n+1}B_nO_{3n+1}$ (Ruddlesden-Popper-type) phases .....	23
2.1.2.7. The MO (halite-type) phase.....	24
2.1.2.8. The $M_2O_3$ (rare earth oxides-type) phases.....	24
<i>Chapter 3</i> Experimental and Computational Phase Studies of Selected Systems of Relevance to the IT-SOFC Technology .....	26
3.1. Binary Subsystems .....	26
3.2. LSGM- and CGO-type Electrolyte Materials.....	27
3.2.1. The La-Sr-O Subsystem .....	28
3.2.2. The La-Ga-O Subsystem .....	29
3.2.3. The La-Mg-O Subsystem .....	30
3.2.4. The Sr-Ga-O Subsystem.....	30
3.2.5. The Sr-Mg-O Subsystem.....	31
3.2.6. The Ga-Mg-O Subsystem.....	31
3.2.7. The La-Sr-Ga-O Subsystem .....	33
3.2.8. The La-Sr-Mg-O Subsystem .....	33
3.2.9. The La-Ga-Mg-O Subsystem .....	34
3.2.10. The Sr-Ga-Mg-O subsystem.....	35
3.2.11. The La-Sr-Ga-Mg-O System (the LSGM electrolyte) .....	35

3.2.12.	The Ce-Gd-O System (CGO Electrolyte).....	37
3.3.	Reactivity of LSGM-based Electrolytes with Relevant Electrode Materials .....	38
3.3.1.	The La-Ni-O Subsystem.....	38
3.3.2.	The Sr-Ni-O Subsystem .....	49
3.3.3.	The Ga-Ni-O Subsystem .....	50
3.3.4.	The Mg-Ni-O Subsystem .....	50
3.3.5.	The La-Sr-Ni-O Subsystem.....	52
3.3.6.	The La-Ga-Ni-O subsystem.....	59
3.3.7.	The La-Mg-Ni-O Subsystem.....	69
3.3.8.	The Sr-Ga-Ni-O Subsystem .....	77
3.3.9.	The Sr-Mg-Ni-O Subsystem.....	77
3.3.10.	The Ga-Mg-Ni-O Subsystem .....	78
3.3.11.	The La-Sr-Ga-Ni-O subsystem.....	79
3.3.12.	The La-Ga-Mg-Ni-O Subsystem.....	81
3.3.13.	The La-Sr-Ga-Mg-Ni-O System.....	85
3.4.	The Reactivity in IT-SOFC with CGO electrolyte.....	87
3.4.1.	The Ce-Ni-O Subsystem.....	87
3.4.2.	The Ce-Sr-O Subsystem .....	91
3.4.3.	The Gd-Ni-O Subsystem .....	98
3.4.4.	The Gd-Sr-O Subsystem.....	102
3.4.5.	The Ce-Gd-Ni-O Subsystem .....	107
3.4.6.	The Ce-Gd-Sr-O Subsystem.....	109
3.4.7.	The Ce-Sr-Ni-O subsystem .....	117
3.4.8.	The Gd-Sr-Ni-O Subsystem .....	122
3.4.9.	The Ce-Gd-Sr-Ni-O system.....	129
3.4.10.	The Ce-Gd-La-Ni-O system .....	131
<i>Chapter 4</i>	Summary and Outlook.....	134
Appendix	.....	137
	The thermodynamic parameters obtained in the present work.....	137
References	.....	143
Curriculum Vitae (Lebenslauf)	.....	152

# Abstract

Strontium- and magnesium-doped lanthanum gallate (LSGM) perovskite-type compounds and doped ceria-based materials have recently been considered the most promising solid electrolytes for intermediate temperature solid oxide fuel cell (IT-SOFC) applications. While nickel metal is commonly used for the fabrication of cermet-type anodes, the rare earth nickelates, such as Sr-doped  $\text{La}_2\text{NiO}_4$  (LSN), are recently developed high-performance cathode materials. For successful implementation in IT-SOFC, it is therefore essential to know the phase equilibria and thermodynamic properties for systems representing the solid electrolyte and electrode materials across their various combinations.

This thesis aims to determine the phase equilibria and the thermodynamics of the relevant phases in the systems La-Sr-Ga-Mg-Ni-O, Ce-Gd-Sr-Ni-O, and Ce-Gd-La-Ni-O. Subsystems of these multi-component systems were thermodynamically modeled, based on the available literature and experimental data obtained from this work. The experimental studies were designed based on the calculated phase diagrams. A minimum number of compositions was chosen strategically to obtain a preliminary prediction of the phases in equilibrium in each constituent subsystem. Finally, the experimental and computational results were used to predict the compatibility/reactivity of IT-SOFC components under fabrication and/or operation conditions.

Various experimental techniques were employed for determination of the phase equilibria such as Scanning Electron Microscopy (SEM) and Energy Dispersive X-ray analysis (EDX), X-ray Diffraction (XRD), Differential Scanning and Adiabatic Calorimetry, and Mass Spectrometry (MS). The CALPHAD-method (CALculation of PHase Diagrams) and THERMOCALC software were used to obtain self-consistent sets of Gibbs energy functions.

The following systems were investigated experimentally:

La-Ni-O, La-Ga-Ni-O, La-Sr-Ni-O, La-Mg-Ni-O, La-Ga-Mg-Ni-O, La-Sr-Ga-Ni-O, La-Sr-Ga-Mg-Ni-O, Ce-Ni-O, Ce-Sr-O, Gd-Ni-O, Gd-Sr-O, Ce-Gd-Ni-O, Ce-Gd-Sr-O, Ce-Sr-Ni-O, Gd-Sr-Ni-O, Ce-Gd-Sr-Ni-O and Ce-Gd-La-Ni-O.

Using results from this experimental work and data from the literature, the following systems were thermodynamically modeled:

La-Ni-O, La-Ga-Ni-O, La-Sr-Ni-O, La-Mg-Ni-O, Ce-Ni-O, Ce-Sr-O, Gd-Ni-O and Gd-Sr-O.

The systems, La-Ga-Mg-Ni-O, La-Sr-Ga-Ni-O, and Ce-Gd-Ni-O were extrapolated using parameters optimized from the constituent lower-order systems.

In the *La-Ni-O* system, the enthalpy of formation, entropy and heat capacity of  $\text{La}_3\text{Ni}_2\text{O}_7$ ,  $\text{La}_4\text{Ni}_3\text{O}_{10}$ , and  $\text{LaNiO}_3$ , were determined experimentally for the first time using equilibration with the gas phase, adiabatic calorimetry and differential scanning calorimetry. In the *La-Ga-Ni-O*, *La-Sr-Ni-O* and *La-Mg-Ni-O* systems, extended solid solutions of  $\text{La}(\text{Ga},\text{Ni})\text{O}_3$ ,  $\text{La}_2(\text{Ni},\text{Ga})\text{O}_4$ ,  $\text{La}_4(\text{Ni},\text{Ga})_3\text{O}_{10}$ ,  $(\text{La},\text{Sr})_2\text{NiO}_4$ , and  $\text{La}_2(\text{Ni},\text{Mg})\text{O}_4$  were found, and the limits of their homogeneity ranges have been established for the first time. In addition, the compound  $\text{LaNiGa}_{11}\text{O}_{19}$ , with a magnetoplumbite-type structure was identified, which has not been reported in the literature to date. In the *La-Ga-Mg-Ni-O* system, the temperature dependence of the quasi-ternary homogeneity range of  $\text{La}(\text{Ga},\text{Mg},\text{Ni})\text{O}_3$  was determined. In the *La-Sr-Ga-Ni-O* system, a reaction was observed between  $\text{LaGaO}_3$  and  $\text{LaSrNiO}_4$  that formed a melilite-type  $\text{La}_{1-x}\text{Sr}_{1+x}\text{Ga}_3\text{O}_{7+\delta}$ ,  $\text{LaGaSrO}_4$  and  $\text{NiO}$  phase. Similar reaction mechanisms were observed in the *La-Sr-Ga-Mg-Ni-O* system.

Experiments in the *Ce-Ni-O* system were conducted in air as well as in a reducing atmosphere. It has been found that  $\text{NiO}$  does not react with  $\text{CeO}_2$ . In the *Ce-Sr-O* system, the entropy and heat capacity of  $\text{Sr}_2\text{CeO}_4$  were experimentally determined for the first time. In the *Gd-Ni-O* system a eutectic reaction was observed ( $\text{liquid} \rightleftharpoons \text{B-Gd}_2\text{O}_3 + \text{NiO}$ ). The *Gd-Sr-O* system was modeled thermodynamically based on data from the literature and the experimentally determined homogeneity range on the  $\text{Gd}_2\text{O}_3$ -rich site. In the *Ce-Sr-Ni-O* system the solid solution of  $(\text{Ce},\text{Sr})_2\text{NiO}_{4-\delta}$  was determined. No reaction between  $\text{NiO}$  and  $\text{SrCeO}_3 / \text{Sr}_2\text{CeO}_4$  was found. Similarly, in the *Ce-Gd-Ni-O* system, no reaction was observed between  $(\text{Ce},\text{Gd})\text{O}_{2-\delta}$  and  $\text{NiO}$ . In contrast, solid solutions of  $\text{Sr}(\text{Ce},\text{Gd})\text{O}_3$ ,  $\text{Sr}_2(\text{Ce},\text{Gd})\text{O}_4$  and  $(\text{Gd},\text{Sr})_2(\text{Sr},\text{Ce})\text{O}_4$  were determined in the *Ce-Gd-Sr-O* system. Also, an extended solid solution of  $(\text{Gd},\text{Sr})_2\text{NiO}_4$  was found in the *Gd-Sr-Ni-O* system that does not exist in the quasi-binary sections, but is stable in higher-order systems only because a solid solution is formed. It has been also found that there is no  $\text{NiO}$  solubility in the  $\text{Gd}_2\text{SrO}_4$  phase.

It could be concluded that doped ceria-based materials are chemically compatible with  $\text{NiO}$  during conditions typical for both the fabrication and the operation of IT-SOFC's, whereas LSGM-type electrolytes react with  $\text{NiO}$  under the fuel cell fabrication conditions. Moreover, although  $\text{La}_2\text{NiO}_4$  is a high-performance cathode, it cannot be used in combination with LSGM- or CGO-type electrolytes, due to its reactivity with both of these materials under fabrication conditions.

# Zusammenfassung

Strontium- und Magnesium- dotierte Lanthangallat Verbindungen des Perowskit-Typs und dotierte Ceroxid-basierte Materialien (DC) wurden kürzlich als hoffnungsvolle Festelektrolyte für die Festoxidbrennstoffzelle bei intermediärer Temperatur (IT-SOFC) betrachtet. Normalerweise wird metallisches Nickel zur Herstellung der Komposit-Anode verwendet, wobei neuerdings die Nickelate von Seltenerdmetallen, wie z.B. Sr-dotierte  $\text{La}_2\text{NiO}_4$  (LSN), zur Hochleistungskathode entwickelt werden. Um IT-SOFC erfolgreich herzustellen und auszunutzen sind die Kenntnisse der Phasengleichgewichten und Thermodynamik für Systeme notwendig, welche die Kathoden, Festelektrolyt, Anoden und ihre mögliche Kombinationen repräsentieren.

Ziel der Arbeit ist die Phasengleichgewichten und Thermodynamik von La-Sr-Ga-Mg-Ni-O, Ce-Gd-Sr-Ni-O und Ce-Gd-La-Ni-O Systeme zu bestimmen. Die Subsysteme wurden thermodynamisch berechnet auf der Basis von Literaturdaten, während die experimentelle Untersuchungen durch berechnete Phasendiagramm entworfen wurden, wodurch weniger Aufwand benötigt wurde. Schließlich wurden die experimentellen und rechnerischen Ergebnisse verwendet, um die Kompatibilität und Reaktivität von IT-SOFC Komponenten unter Herstellungs- und Arbeitsbedingungen vorauszusagen.

Für die experimentelle Bestimmung der Phasengleichgewichte der Systeme wurden verschiedene Untersuchungsmethoden verwendet, wie z.B. Rasterelektronmikroskopie (REM), Energiedispersive Röntgenspektroskopie (EDX), Dynamische Differenzkalorimetrie und Thermogravimetrie. Die CALPHAD-Methode (Calculation of PHase Diagrams) mit THERMOCALC Software wurde auch verwendet, um eine selbstkonsequente Reihe von freien Enthalpie Funktionen zu bekommen.

Die folgenden Systeme wurden experimentell untersucht:

La-Ni-O, La-Ga-Ni-O, La-Sr-Ni-O, La-Mg-Ni-O, La-Ga-Mg-Ni-O, La-Sr-Ga-Ni-O, La-Sr-Ga-Mg-Ni-O, Ce-Ni-O, Ce-Sr-O, Gd-Ni-O, Gd-Sr-O, Ce-Gd-Ni-O, Ce-Gd-Sr-O, Ce-Sr-Ni-O, Gd-Sr-Ni-O, Ce-Gd-Sr-Ni-O, Ce-Gd-La-Ni-O.

Durch erhaltenen Ergebnisse und Literaturdaten wurden thermodynamische Modelle für die folgenden Systemen gestellt:

La-Ni-O, La-Ga-Ni-O, La-Sr-Ni-O, La-Mg-Ni-O, Ce-Ni-O, Ce-Sr-O, Gd-Ni-O, Gd-Sr-O.



Mit optimierte Parameter von Systemen niedrigerer Ordnung wurden die Systeme La-Ga-Mg-Ni-O, La-Sr-Ga-Ni-O, und Ce-Gd-Ni-O extrapoliert.

Im La-Ni-O System wurden die Bildungsenthalpie, Entropie und Wärmekapazität von  $\text{La}_3\text{Ni}_2\text{O}_7$ ,  $\text{La}_4\text{Ni}_3\text{O}_{10}$  und  $\text{LaNiO}_3$  durch Gleichgewicht mit Gasphase, adiabatische Kalorimetrie und Dynamische Differenzkalorimetrie experimentell bestimmt. In den La-Ga-Ni-O, La-Sr-Ni-O, La-Mg-Ni-O Systeme wurden erweiterten Mischkristalle  $\text{La}(\text{Ga},\text{Ni})\text{O}_3$ ,  $\text{La}_2(\text{Ni},\text{Ga})\text{O}_4$ ,  $\text{La}_4(\text{Ni},\text{Ga})_3\text{O}_{10}$ ,  $(\text{La},\text{Sr})_2\text{NiO}_4$  und  $\text{La}_2(\text{Ni},\text{Mg})\text{O}_4$  gefunden und ihre Homogenitätsbereiche bestimmt. Zusätzlich wurden die Magnetoplumbite-Typ Verbindung  $\text{LaNiGa}_{11}\text{O}_{19}$  gefunden, die bislang noch nicht in der Literaturen bekannt war. Im La-Ga-Mg-Ni-O System wurde die Temperaturabhängigkeit von  $\text{La}(\text{Ga},\text{Mg},\text{Ni})\text{O}_3$  Homogenitätsbereich untersucht. Im La-Sr-Ga-Ni-O System wurde eine Reaktion zwischen  $\text{LaGaO}_3$  und  $\text{LaSrNiO}_4$  untersucht, die Melilite-Typ  $\text{La}_{1-x}\text{Sr}_{1+x}\text{Ga}_3\text{O}_{7+\delta}$ ,  $\text{LaGaSrO}_4$  und  $\text{NiO}$  bildet. Der gleiche Reaktionsmechanismus wurde auch im La-Sr-Ga-Mg-Ni-O System beobachtet.

Die Experimente für Ce-Ni-O System wurden sowohl an Luft als auch im Reduktions-Atmosphäre durchgeführt. Es wurde gefunden, dass  $\text{NiO}$  nicht mit  $\text{CeO}_2$  reagiert. Für Ce-Sr-O System wurden zuerst die Entropie und Wärmekapazität von  $\text{Sr}_2\text{CeO}_4$  experimentell bestimmt. Für Gd-Ni-O System wurde eine eutektische Reaktion ( $\text{Schmelze} \leftrightarrow \text{B-Gd}_2\text{O}_3 + \text{NiO}$ ) untersucht. Für das Gd-Sr-O System wurde ein thermodynamisches Modell aus Literaturdaten aufgestellt und auf  $\text{Gd}_2\text{O}_3$ -reichen Seite die Homogenitätsbereiche experimentell untersucht. Im Ce-Sr-Ni-O System wurde auf SrO-reichen Seite das Mischkristall  $(\text{Ce},\text{Sr})_2\text{NiO}_{4-\delta}$  untersucht. Es wurde festgestellt, dass keine Reaktion zwischen  $\text{NiO}$  und  $\text{SrCeO}_3$  /  $\text{Sr}_2\text{CeO}_4$  stattgefunden hat. Im Ce-Gd-Ni-O System wurde keine Reaktion zwischen  $(\text{Ce},\text{Gd})\text{O}_{2-\delta}$  und  $\text{NiO}$  gefunden. Im Ce-Gd-Sr-O System wurden Mischkristalle  $\text{Sr}(\text{Ce},\text{Gd})\text{O}_3$ ,  $\text{Sr}_2(\text{Ce},\text{Gd})\text{O}_4$  und  $(\text{Gd},\text{Sr})_2(\text{Sr},\text{Ce})\text{O}_4$  untersucht. Im Gd-Sr-Ni-O System wurde ein Mischkristall  $(\text{Gd},\text{Sr})_2\text{NiO}_4$  untersucht, der in quasi-binären Schnitten nicht existiert, aber im System höherer Ordnung stabilisiert wird. Es wurde auch gefunden, dass in die  $\text{Gd}_2\text{SrO}_4$  Phase keine  $\text{NiO}$  gelöst wird.

Daraus kann man schliessen, dass dotierte Ceroxide (DC) basierte Materialien mit  $\text{NiO}$  während der Herstellung und Betrieb von IT-SOFC chemisch kompatibel sind, wobei LSGM Elektrolyte unter Herstellungsbedingungen in der Zelle mit  $\text{NiO}$  reagieren. Obwohl  $\text{La}_2\text{NiO}_4$  eine Hochleistungskathode ist, lässt es sich nicht in Kombination mit LSGM oder DC benutzen, weil es mit den beiden Materialien unter Herstellungsbedingungen in der Zelle miteinander reagiert.

# Chapter 1

## Introduction

### 1.1. Intermediate Temperature Solid Oxide Fuel Cells (IT-SOFC)

A fuel cell is an electrochemical device for the direct conversion of chemical energy into electrical energy. The cell is constructed with having two porous electrodes separated by an electrolyte. During operation, oxygen (air) and a hydrogen-containing fuel flow along the cathode and anode, respectively. When an oxygen molecule contacts the cathode/electrolyte interface, it acquires electrons from the cathode to form ions, which then diffuse into the electrolyte material. The ions migrate to the anode side and encounter the fuel at the anode/electrolyte interface and react with hydrogen, giving off water, carbon dioxide (depending on fuel used), heat and electrons. Electron transport through the external circuit provides the electrical energy. A schematic diagram of a typical solid oxide fuel cell is shown in Fig. 1.1. Single cells contain an electrical interconnect, which links individual cells together in series or in parallel, to form a “stack”. The interconnect serves as the electrical conduit to the external circuit.

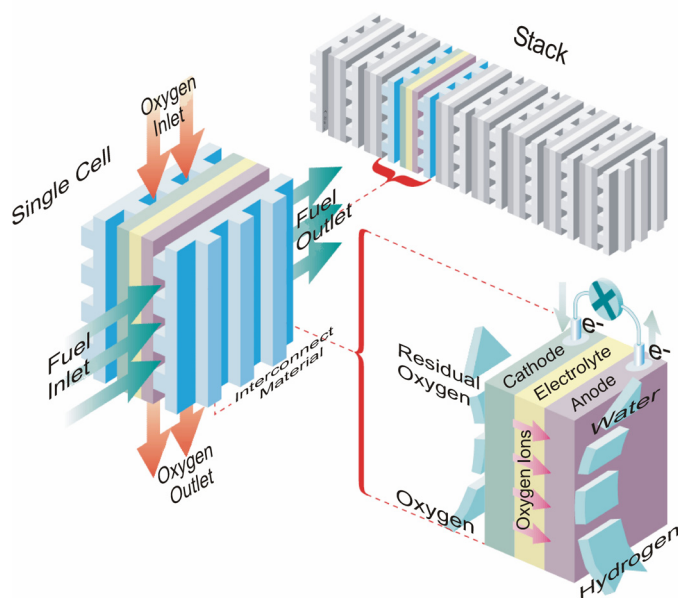


Fig. 1.1 Schematic diagram of a typical solid oxide fuel cell (SOFC).

As indicated by their name, solid oxide fuel cells (SOFCs) use solid oxide ceramics as the electrolyte. In terms of efficiency, state of the art SOFC systems are normally operated around 1000 °C, and the electrolyte material is doped zirconia ( $Zr_{1-x}Y_xO_{2-x/2}$  and  $Zr_{1-x}Sc_xO_{2-x/2}$ , where

$x = 0.08-0.11$  and  $0.09-0.11$ , respectively) [99Ara, 00Sin, 04DoE, 04Kha]. The operating temperature of a SOFC is restricted by many different thermally activated processes, such as the ionic conductivity of the solid electrolyte and the different chemical and electrochemical reaction steps in the electrodes or at the electrode/electrolyte interfaces [01Ste, 04Kha].

Activities in the field of SOFC systems have recently been focused on lowering the operation temperature for reducing raw material and operation costs, in addition to the chemical and mechanical stability of the cell components [00Sin, 01Hui, 01Ste, 03Bra]. Decreasing the electrolyte thickness is one of the first methods successfully applied in order to reduce the ohmic loss of the electrolyte at lower operating temperatures. In Fig. 1.2, the electrical conductivity data can also be seen to depend on the electrolyte thickness; in order to achieve the same conductivity at a lower temperature, the film thickness could simply be decreased [01Ste, 04DoE]. For example, to operate the SOFC at  $800\text{ }^{\circ}\text{C}$  instead of  $1000\text{ }^{\circ}\text{C}$ , the electrolyte thickness would have to be reduced by roughly an order of magnitude to maintain a similar ohmic loss in the electrolyte [01Ste, 04DoE]. In fact, the thickness has been decreased from  $150-200\text{ }\mu\text{m}$  to  $10-20\text{ }\mu\text{m}$  for the dense, impermeable, technologically favored solid electrolyte, yttria-stabilized zirconia (YSZ), by using supported electrolytes [03Bra]. However, this material is not without problem and even more reducing temperature is desired. Finally, another solution for obtaining the same performance at a lower temperature is to replace the electrolyte with other materials having a higher conductivity at lower temperatures.

In pursuit of alternative electrolyte materials, much attention has been devoted to gadolinium-doped ceria (CGO) and Sr- and Mg-doped lanthanum gallate (LSGM:  $(\text{La,Sr})(\text{Ga,Mg})\text{O}_3$ ) [98Hua, 98Hui, 00Wan, 01Ste, 01Ive, 01Hui, 03Bra, 04DoE]. As shown in Fig. 1.2, these materials have a very high conductivity at low temperatures, and even at  $700\text{ }^{\circ}\text{C}$ , the conductivity of LSGM is as high as that of YSZ at  $1000\text{ }^{\circ}\text{C}$ .

An important problem with CGO is the reduction of  $\text{Ce}^{4+}$  to  $\text{Ce}^{3+}$  under the fuel-rich conditions on the anode side of the electrolyte [03Bra, 04Kha]. Under these conditions, the electronic conductivity would fluctuate. Any valence state changes in the membrane would introduce electronic charge carriers in the membrane, which would cause internal short circuits in the cell. Moreover, lattice expansion would occur, and in such a thin membrane, the associate mechanical stresses induced would be severe. On the other hand, LSGM shows comparable ionic conductivity with CGO at temperatures as low as  $500\text{ }^{\circ}\text{C}$ , without the problems of CGO associated with the reducing conditions. Furthermore, although LSGM is

an excellent oxygen conductor at low temperatures, the chemical and mechanical stability of the cell components are still not clearly established and are still under intense scrutiny [99Hua, 01Ive, 04Kha].

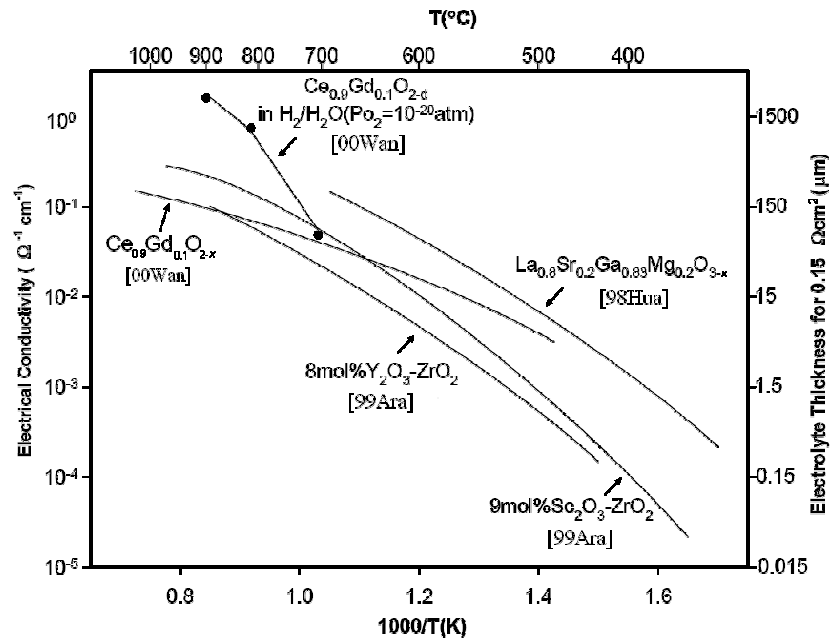


Fig. 1.2. Electrolyte conductivity as a function of temperature [04DoE].

As for developments in electrode materials, nickel metal is commonly used for the fabrication of cermet anodes [00Sin, 01Ste, 03Bra]. Meanwhile, the rare earth nickelates, such as Sr-doped  $\text{La}_2\text{NiO}_4$  (LSN) [99Vas, 99Kha, 00Vas, 00Ski, 05Mun, 06Amo1, 06Amo2, 06Agu1] or  $\text{La}_{0.9}\text{Sr}_{0.1}\text{Ga}_{0.5}\text{Ni}_{0.5}\text{O}_3$  (LSGN) [99Lon, 00Lec] have recently been developed for high-performance cathodes.

Aside from the enormous volume of electrochemical studies on the systems described above, thermodynamic data are still scarce. Clearly, it is imperative to establish the knowledge of phase equilibria and thermodynamics for the systems, which represent cathode, solid electrolyte and anode as well as their possible combinations for successful fabrication and exploitation of IT-SOFCs.

## 1.2. Scope of This Dissertation

Experimental and computational phase studies of the selected systems were systematically carried out from oxygen containing binaries to higher-order oxide systems with particular emphasis placed on their relevance for IT-SOFC technology. Data from the literature on the electrolyte subsystems were reviewed in order to maintain consistency between the literature data and experimental-computational results obtained in the present work. Phase diagrams of the subsystems were either calculated using the literature data or extrapolated from the

subsystems. Since the literature data on Ni-containing system are very limited, almost all the experimental work had to be conducted in the present work. Based on available information in the literature and preliminary extrapolation from subsystems, compositions were strategically selected. That is, by coordinating experimental work and calculations, an optimized number of subsystems were investigated, and the system equilibria established with streamlined effort. Briefly, the thesis works consists of the following sections:

- Using equilibration with the gas phase, adiabatic calorimetry and differential scanning calorimetry, thermodynamics of the ternary compounds in the La-Ni-O system were determined experimentally for the first time. The compounds are considered as promising cathode materials for IT-SOFC system. The derived thermodynamic functions were used to construct the phase stability diagram of the La-Ni-O system in terms of temperature and oxygen pressure.
- Experimental phase diagrams were constructed for the La-Sr-Ni-O, La-Ga-Ni-O and La-Mg-Ni-O on the quasi-ternary sections. The systems were thermodynamically modeled and chemical potential diagrams were calculated.
- Using the data obtained from the subsystems, phase equilibria in the La-Ga-Mg-Ni-O, La-Sr-Ga-Ni-O and La-Sr-Ga-Mg-Ni-O system were discussed. The temperature-dependent homogeneity range of the  $\text{La}(\text{Ga},\text{Mg},\text{Ni})\text{O}_3$  was determined, and the reaction mechanism was experimentally determined for the Sr-doped  $\text{La}_2\text{NiO}_4$  (LSN) cathode and undoped  $\text{LaGaO}_3$  and LSGM electrolytes.
- The Ce-Ni-O system was thermodynamically modeled and experimentally investigated at highly reducing conditions, to simulate the operation conditions of IT-SOFC cermet anodes. The other ternary subsystems, Ce-Sr-O, Gd-Sr-O and Gd-Ni-O systems, were experimentally studied and thermodynamically modeled, using the obtained data.
- The Ce-Gd-Ni-O, Ce-Gd-Sr-O, Ce-Sr-Ni-O and Gd-Sr-Ni-O systems were experimentally investigated for the first time in this work.
- Using the phase equilibria obtained from the subsystems, the behavior of components was predicted for higher order systems. Reaction mechanisms were experimentally determined for the  $\text{K}_2\text{NiF}_4$ -type cathodes and  $\text{Ce}_{0.9}\text{Gd}_{0.1}\text{O}_{2-\delta}$  (CGO10) electrolyte interface.

# *Chapter 2*

## **Experimental Techniques and Thermodynamic Modeling**

### **2.1. Sample Preparation and Characterization**

The samples from the Ce-Ni-O system were prepared via the conventional mixed oxide (CMO) route. Powders of CeO<sub>2</sub> (Ventron, 99.9 %) and NiO (Merck, extra pure) were mixed in molar ratios of 1:1 and 2:1 and ground in ethyl alcohol by ball milling, using zirconia balls. Mixed powders were compacted into cylindrical pellets by first isostatic pressing (800 MPa), then sintering in air at 1200 °C for a total of 120 h, with intermediate regrinding and recompaction. An additional 1:1-ratio sample was also heat-treated in air at 1600 °C for 10 h and quenched. The La-Ga-Ni-O system was similarly investigated using high purity oxides of La<sub>2</sub>O<sub>3</sub> (Alfa GmbH, 99.99 %), Ga<sub>2</sub>O<sub>3</sub> (Sigma Aldrich, >99.99 %) and NiO (Merck, extra pure) for producing samples of 15 different compositions. The samples were heat-treated three times at 1300 °C in air for a total of 144 h with intermediate regrinding, at each processing step, the samples were examined by X-ray diffraction (XRD).

Preparation of samples by the CMO route required a significantly long annealing time with several intermittent re-grinding steps, in order to reach thermodynamic equilibrium. However, according to the literature, it is not possible to obtain some compounds as a single phase using the conventional powder processing techniques, such as La<sub>3</sub>Ni<sub>2</sub>O<sub>7</sub> [94Zha, 97Car, 01Vor], La<sub>4</sub>Ni<sub>3</sub>O<sub>10</sub> [97Car, 01Vor], Sr<sub>2</sub>CeO<sub>4</sub> [04Bas]. Therefore, a Pechini-type [Pech] soft chemical (PSC) process was used, which provided a mixing of the elements at an atomic scale and accelerated the phase formation reaction. The starting materials used were lanthanum acetate hydrate La(CH<sub>3</sub>COO)<sub>3</sub>·1.5H<sub>2</sub>O (Fluka, >99.9%), nickel nitrate hexahydrate Ni(NO<sub>3</sub>)<sub>2</sub>·6H<sub>2</sub>O (Merck, extra pure), magnesium acetate tetrahydrate Mg(CH<sub>3</sub>COO)<sub>2</sub>·4H<sub>2</sub>O (Merck, analytical grade), strontium nitrate SrNO<sub>3</sub> (Merck, water free, analytical grade), cerium nitrate hexahydrate Ce(NO<sub>3</sub>)<sub>3</sub>·6H<sub>2</sub>O (Alfa GmbH, 99.99 %) and gadolinium nitrate hexahydrate Gd(NO<sub>3</sub>)<sub>3</sub>·6H<sub>2</sub>O (Strem, 99.9%). In order to determine the water content in the salts precisely, known amounts of samples were decomposed at 1000 °C in air and weighed for comparison with their respective oxides. Stoichiometric amounts of cation salts were dissolved in deionized water by heating and continuous stirring on a hot plate. For a chelating agent,

slightly more than 1 mole of citric acid per mole of cations was added to the mixture. Upon further heating, the solution evolved to a gel and was then dried by heating until auto-ignition/combustion of the product occurred.

The products were calcined at 700 °C for 12 h. The calcined powders were ground, cold isostatic pressed into pellets at 800 MPa (for 1 min), and sintered at various temperatures and atmospheres for a total of 96 h, with an intermediate regrinding. When the sintering conditions for the ternary compounds in the La-Ni-O system were selected, consideration was given to the thermodynamic stability of the compounds. In the La-Ni-O system, the LaNiO<sub>3</sub> sample was sintered at 800 °C in pure O<sub>2</sub>; the La<sub>4</sub>Ni<sub>3</sub>O<sub>10</sub> and the La<sub>3</sub>Ni<sub>2</sub>O<sub>7</sub> samples were sintered in air, at 1000 and 1100 °C, respectively. Sintering in air at 1300°C was performed for the SrCeO<sub>3</sub> and Sr<sub>2</sub>CeO<sub>4</sub> compounds in the Ce-Sr-O system, and for the Gd<sub>2</sub>SrO<sub>4</sub> compound in the Gd-Sr-O system. Most of the samples were furnace-cooled, although quenching was used in some cases, where indicated in the text. When the results were compared, it has been found that because of the slow kinetics, the cooling rate did not have a significant effect. Therefore, furnace cooling was preferred, but in some special cases, *e.g.* with the determination of the SrO solubility in CeO<sub>2</sub> in the form of (Ce,Sr)O<sub>2-x</sub>, only quenching was applied.

The cation ratios were determined in the precursor solutions and in the samples after the final sintering step by inductively coupled plasma optical emission spectroscopy (ICP; Model CIRO, Spectro Inc). Using the carrier-gas hot extraction method, the oxygen (Model TC-436DR, Leco) and carbon (Model CWA 5003, Fisher-Rosemount) content were measured in the samples. The oxygen stoichiometry was also calculated from the total weight loss for the ternary compounds in the La-Ni-O system, by decomposing samples to La<sub>2</sub>NiO<sub>4</sub> and NiO, since both are known to be stoichiometric [90Tay, 95Kow, 03Ski] compounds at high temperatures.

The microstructural characterization of samples was performed by using scanning electron microscopy (SEM; Model DSM 982 Gemini, Karl Zeiss, Germany) and energy dispersive X-ray spectroscopy (EDX; Oxford-Instrument ISIS 300). The X-ray diffraction (XRD) spectra of the powder specimens were recorded using a Siemens D5000 diffractometer (CuK $\alpha$  radiation,  $\lambda = 0.15406$  nm,  $2\theta$  range 10 - 80°,  $2\theta$  step of 0.016°, time per step 0.2 s). Silicon and quartz were used as internal standards to correct for systematic errors.

The low-temperature specific heat capacity of the samples between 4 and 305 K was measured by means of a home-made high-precision calorimeter applying Nernst's quasi-adiabatic step heating method [87Gme, 92Ota]. The sample holder was 0.1 mm thick sapphire disc supporting the heater (evaporated stainless steel,  $\sim 2 \text{ k}\Omega$ ) and a commercially calibrated resistance thermometer (depending on the temperature range, either a CERNOX or a Pt100). The 300-600 mg samples were cemented to the sample holder, using a known mass of Apiezon-N grease. The contributions of the grease and the sapphire disc to the specific heat were subtracted to obtain the net sample values. The heat capacity above room temperature (up to 673 K) was measured by DSC (Model Pyris 1, Perkin-Elmer Instruments) using Al-crucibles and sapphire as a standard reference material.

The equilibrium temperatures and oxygen pressures were determined for the decomposition reactions of the ternary compounds in the La-Ni-O system using a thermogravimetric and differential scanning calorimetry system (TG/DSC, Model STA 449C, Netzsch Gerätebau GmbH) coupled with a mass spectrometer (MS, Model GAM 200, IPI) using platinum crucibles and alumina as reference material. For the carrier gas, Ar/O<sub>2</sub> mixtures were used, where the oxygen content ranged between 1 and 100 vol% O<sub>2</sub> or was held constant using a needle valve controlled by the MS. The gas flow rate was maintained at a level of 60 ml/min. Two types of experiments were carried out. In the *dynamic* experiments, samples were heated at a rate of 1 to 20 K·min<sup>-1</sup> under a constant oxygen pressure. *Isothermal* experiments were also designed, according to the determined decomposition temperatures. The samples were heated rapidly to the selected temperature at higher oxygen partial pressure than that required for decomposition, and after 30 min of equilibration, the oxygen content in the gas flow was gradually decreased. A temperature of 1400 °C was the upper limit for dynamic and isothermal experiments. After the TG/DSC experiments, the samples were characterized by XRD.

The reducing-atmosphere annealing experiments of the Ce-Ni-O samples were performed in a horizontal tube furnace, which is shown in Fig. 2.1. The temperature was controlled by an additional thermocouple placed close to the sample. Hydrogen, saturated with water vapor was used as a furnace atmosphere to control the oxygen partial pressure in the system. This was achieved by bubbling hydrogen gas through water, which was kept at a constant temperature between 5–85 °C using a thermostat. Since the water vapor was in equilibrium with liquid water, the partial pressure of gaseous H<sub>2</sub>O ( $P_{\text{H}_2\text{O}}$ ) was a function of the thermostat temperature only and was taken from the literature [01CRC].



Inside the furnace, hydrogen saturated with water vapor reached a new equilibrium, for which the oxygen partial pressure could be calculated according to

$$\frac{1}{2} \log P_{\text{O}_2} = \log K + \log \left( \frac{P_{\text{H}_2\text{O}}}{P_{\text{H}_2}} \right) \quad (2.1)$$

using the equilibrium constant,  $K$ , for the reaction  $\text{H}_2\text{O}_{(\text{g})} \Leftrightarrow \text{H}_2 + \frac{1}{2} \text{O}_2$  at the furnace temperature. The  $P_{\text{H}_2\text{O}}/P_{\text{H}_2}$  ratio controls  $P_{\text{O}_2}$  in the furnace, where  $P_{\text{H}_2}$  was taken as 1 bar.

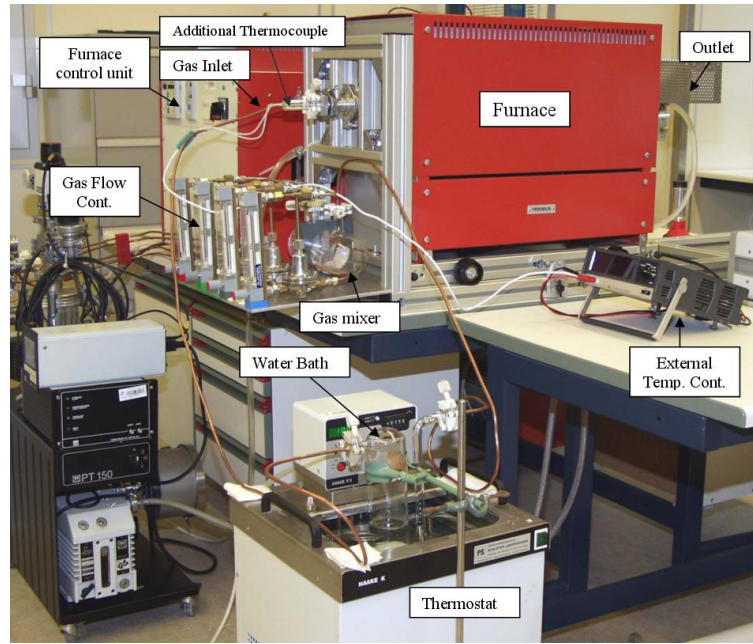


Fig. 2.1. The furnace and gas control units of the experimental setup.

The general notation used to define samples was based on overall composition. In the quasi-binary systems, such as  $\text{CeO}_2\text{-SrO}$ , *for example*, a sample consisting of 40 mol%  $\text{CeO}_2$  and 60 mol%  $\text{SrO}$  was designated as CS60. In the quasi-ternary systems, such as  $\text{LaO}_{1.5}\text{-GaO}_{1.5}\text{-NiO}$ , a sample consisting of 50 mol %  $\text{LaO}_{1.5}$ , 30 mol %  $\text{GaO}_{1.5}$  and 20 mol %  $\text{NiO}$  was designated as LGN50-30.

### 2.1.1. The Calphad Method

The essence of the CALPHAD-method [70Kau, 98Sau] is the analytical representation of the Gibbs energy of individual phases in a system in terms of state variables, such as temperature, pressure, and composition (*i.e.*, a thermodynamic description). Such expressions contain adjustable parameters. For unknown parameters, the optimal values, providing the best match between the calculated quantities and their experimental counterparts, could be obtained by the weighted non-linear least squares minimization procedure. In Fig. 2.2, a schematic flowchart is presented for the Calphad method. The thermodynamic optimizations and calculations in the present work were carried out by the ‘‘Thermo-Calc’’ software [02And],

using mainly experimental data obtained in the present work as input, supplemented by that from the literature.

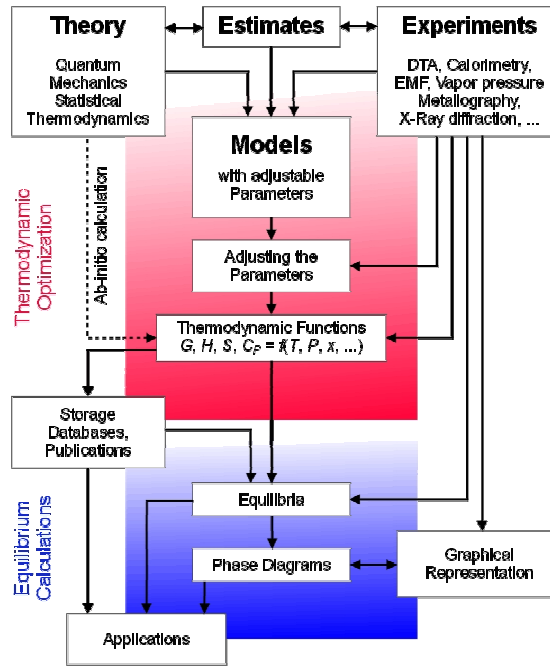


Fig. 2.2. Schematic flowchart of the Calphad-method.

## 2.1.2. Models for the Gibbs Energy

The molar Gibbs energy of each component is given by the equation:

$${}^{\circ}G(T) = a + bT + cT \ln(T) + \sum_n d_n T^n \quad (2.2)$$

The coefficient  $a$  is related to the enthalpy, the coefficient  $b$  to the entropy, while the coefficients  $c$  and  $d_n$  describe the temperature dependence of the heat capacity. Since the enthalpies cannot be defined absolutely, the Gibbs energy is referred to the constant enthalpy values of the so-called Stable Element References,  $H^{\text{SER}}$ , at 298.15 K and 1 bar [91Din]. By differentiating equation (2.2), the other thermodynamic functions could be derived, *i.e.*,

$${}^{\circ}H(T) - H^{\text{SER}} = a - cT - \sum_n (n-1)d_n T^n \quad (2.3)$$

$${}^{\circ}S(T) = -b - c - c \ln(T) - \sum_n n d_n T^{n-1} \quad (2.4)$$

$$C_p(T) = -c - \sum_n n(n-1)d_n T^{n-1} \quad (2.5)$$

### 2.1.2.1. Pure Elements and the Gas Phase

The Gibbs energy of the pure elements was taken from the SGTE (Scientific Group Thermodata Europe) unary database [SGTE].

The gas phase was treated as ideal mixture of species in the respective system, *e.g.* in the Ce-Ni-O system, O, O<sub>2</sub>, O<sub>3</sub>, Ce, CeO, Ni, NiO, according to the SGTE substance database [SGTE]. The Gibbs energy function could be formulated by:

$$G_m = \sum_i x_i {}^\circ G_i + RT(x_i \ln x_i) + RT \ln\left(\frac{P}{P_0}\right) \quad (2.6)$$

in which  $x_i$  is the mole fraction of constituent  $i$ , and  ${}^\circ G_i$  is Gibbs energy of the pure substance  $i$  in the gas state.  $P_0$  is the standard pressure of 1 bar.

### 2.1.2.2. The Liquid Phase

Although the present work was intended to investigate subsolidus phase equilibria, the liquid phase was optimized for the quasi-binary CeO<sub>2</sub>-SrO, Gd<sub>2</sub>O<sub>3</sub>-NiO and Gd<sub>2</sub>O<sub>3</sub>-SrO phase diagrams, by using the two-sublattice model for ionic liquids [2001Hil]. No vacancies were introduced in the second sublattice. For the Gd<sub>2</sub>O<sub>3</sub>-NiO and CeO<sub>2</sub>-SrO systems, only a regular solution interaction parameter was used, whereas for the Gd<sub>2</sub>O<sub>3</sub>-SrO system, both regular and subregular interaction parameters were necessary.

### 2.1.2.3. The Stoichiometric Phases

The Gibbs energy of such compounds can be simply described by applying the form of Eqn. 2.2. For example, this was applied for ternary compounds in the La-Ni-O systems, where the thermodynamic data on heat capacity and entropy are available. However, for a case in which the thermodynamic data are not known, (*e.g.* the Gd<sub>2</sub>SrO<sub>4</sub> compound), the Gibbs energy function could be expressed simply by the Neumann-Kopp rule [98Hil], which states that the heat capacity is estimated as an average of the values of the components:

$$G_m = \sum_i x_i {}^\circ G_i + A + BT \quad (2.7)$$

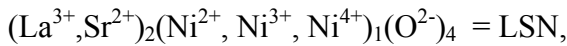
where the  $x_i$  and  ${}^\circ G_i$  are the mole fraction and Gibbs energy of component  $i$ , respectively.  $A$  and  $B$  are the parameters to be determined, and they are generally considered as the enthalpy and entropy of formation of the compound from the components, respectively. For a situation where there is insufficient thermodynamic data,  $A$  and  $B$  can be optimized from phase equilibria data [98Hil].

#### 2.1.2.4. The A<sub>2</sub>BO<sub>4</sub> (K<sub>2</sub>NiF<sub>4</sub>-type) Phases

The K<sub>2</sub>NiF<sub>4</sub>-type solid solutions were found in the systems La-Sr-Ni-O, La-Ga-Ni-O, and La-Mg-Ni-O in the forms of (La,Sr)<sub>2</sub>NiO<sub>4</sub>, La<sub>2</sub>(Ni,Ga)O<sub>4</sub> and La<sub>2</sub>(Ni,Mg)O<sub>4</sub>, respectively. Although they were of the same structural type, the same model could not be used for all the systems, since substitution takes place on different sublattices, and valence states of the substituting atoms would also be different. The models used are described separately below:

##### *The (La,Sr)<sub>2</sub>NiO<sub>4</sub> phase*

It was confirmed in the literature that La<sub>2-x</sub>Sr<sub>x</sub>NiO<sub>4</sub> is an extended solid solution, where  $x \leq 1.5$  [90Tak]. It was also reported that the average formal valence state of Ni can reach 3.5+, which would be possible only in the presence of Ni<sup>4+</sup> ions [90Tak, 91Cav, 95Rei]. This phenomenon was first reported by Takeda and coworkers [90Tak], and later, it was confirmed in a number of studies [91Cav, 94Sre]. In the whole composition range, the oxygen sublattice would be filled completely [77Gop, 88Nit, 90Tak, 90Sre, 91Kat, 93Dic, 93Say, 98Hea, 99Man, 99Mil] and the charge would be compensated by changing the valence state of Ni ions. In the undoped La<sub>2</sub>NiO<sub>4</sub>, the valence state of Ni is 2+, but with increasing SrO content, Ni changes its valence state from 2+ to 3+, and both can coexist in order to ensure charge neutrality. The LaSrNiO<sub>4</sub> composition contains only Ni<sup>3+</sup> ions. However, as mentioned previously, further SrO dissolution would be possible, and Ni ions could change their valence state from 3+ to 4+; both could coexist simultaneously, but there was no data on existence of Ni<sup>2+</sup> ion in such a highly doped composition. This phenomenon could be modeled by



and the molar Gibbs energy of the solid solution could be written as

$$\begin{aligned} G_m^{LSN} = & y_{\text{La}^{3+}} y_{\text{Ni}^{2+}} y_{\text{O}^{2-}} \circ G_{\text{La}^{3+}; \text{Ni}^{2+}; \text{O}^{2-}}^{LSN} + y_{\text{La}^{3+}} y_{\text{Ni}^{3+}} y_{\text{O}^{2-}} \circ G_{\text{La}^{3+}; \text{Ni}^{3+}; \text{O}^{2-}}^{LSN} + y_{\text{La}^{3+}} y_{\text{Ni}^{4+}} y_{\text{O}^{2-}} \circ G_{\text{La}^{3+}; \text{Ni}^{4+}; \text{O}^{2-}}^{LSN} \\ & + y_{\text{Sr}^{2+}} y_{\text{Ni}^{2+}} y_{\text{O}^{2-}} \circ G_{\text{Sr}^{2+}; \text{Ni}^{2+}; \text{O}^{2-}}^{LSN} + y_{\text{Sr}^{2+}} y_{\text{Ni}^{3+}} y_{\text{O}^{2-}} \circ G_{\text{Sr}^{2+}; \text{Ni}^{3+}; \text{O}^{2-}}^{LSN} + y_{\text{Sr}^{2+}} y_{\text{Ni}^{4+}} y_{\text{O}^{2-}} \circ G_{\text{Sr}^{2+}; \text{Ni}^{4+}; \text{O}^{2-}}^{LSN} \\ & + 2RT(y_{\text{La}^{3+}} + \ln y_{\text{La}^{3+}} + y_{\text{Sr}^{2+}} + \ln y_{\text{Sr}^{2+}}) \\ & + RT(y_{\text{Ni}^{2+}} + \ln y_{\text{Ni}^{2+}} + y_{\text{Ni}^{3+}} + \ln y_{\text{Ni}^{3+}} + y_{\text{Ni}^{4+}} + \ln y_{\text{Ni}^{4+}}) + {}^E G_m^{LSN} \end{aligned} \quad (2.8)$$

where  $y_j$  represents the site fraction of species  $j$ . The excess Gibbs energy  ${}^E G_m^{LSN}$  is set to zero. The model could be visualized by the composition half-cube (Fig. 2.3). Each corner of the cube would represent a  ${}^0 G$  parameter.

According to the modeling, only La<sub>2</sub>NiO<sub>4</sub> and Sr<sub>2</sub>NiO<sub>4</sub> “corner-phases” would be neutral, whereas and the others would be charged. The numbered surfaces could be separately used to

get relations between each corners. The surface number “1” is given in Fig. 2.4 and similarly, the relations between the others are found.

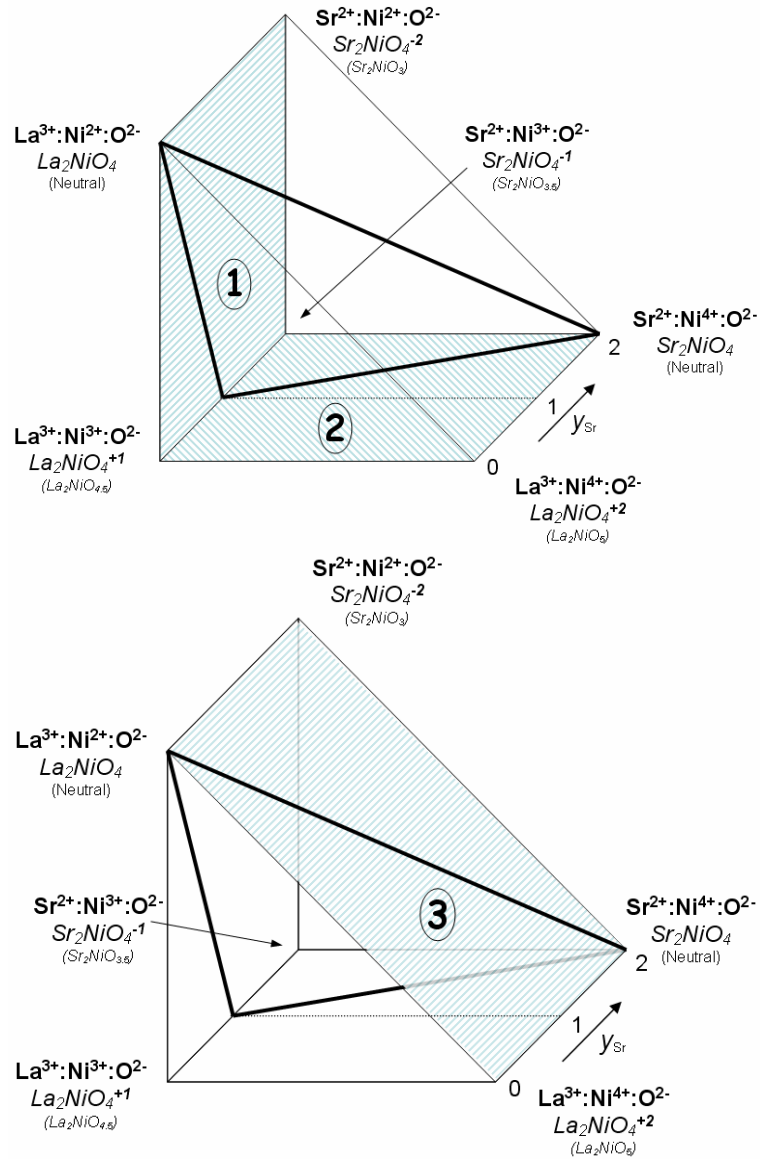


Fig. 2.3. Model illustrating the  $\text{La}_{2-x}\text{Sr}_x\text{NiO}_4$  solid solution.

The Gibbs energies of the end points on the neutral line between  $\text{La}_2\text{NiO}_4$  and  $\text{LaSrNiO}_4$  (LS3) would be given respectively by

$${}^\circ G_{\text{La}^{3+}:\text{Ni}^{2+}:\text{O}^{2-}}^{\text{LSN}} = {}^\circ G_{\text{La}_2\text{NiO}_4} \quad (2.9)$$

$$\frac{1}{2} {}^\circ G_{\text{LS3}}^{\text{LSN}} + \frac{1}{2} {}^\circ G_{\text{S3}}^{\text{LSN}} + 2RT \left[ \frac{1}{2} \ln\left(\frac{1}{2}\right) + \frac{1}{2} \ln\left(\frac{1}{2}\right) \right] = G_{\text{LS3}}^{\text{LSN}} + A + B \cdot T \quad (2.10)$$

The  ${}^\circ G_{\text{Sr}^{2+}:\text{Ni}^{3+}:\text{O}^{2-}}^{\text{LSN}}$  was selected as the reference, and the value would be given

$${}^{\circ}G_{Sr^{2+};Ni^{3+};O^{2-}}^{LSN} = 2 \cdot {}^{\circ}G_{SrO}^{SrO} + {}^{\circ}G_{NiO}^{NiO} + \frac{1}{2} {}^{\circ}G_{O_2}^{Gas} \quad (2.11)$$

The fourth equation would be given by the reciprocal relation:

$$\Delta G_r^{LSN} = {}^{\circ}G_{La^{3+};Ni^{2+};O^{2-}}^{LSN} + {}^{\circ}G_{Sr^{2+};Ni^{3+};O^{2-}}^{LSN} - ({}^{\circ}G_{La^{3+};Ni^{3+};O^{2-}}^{LSN} + {}^{\circ}G_{Sr^{2+};Ni^{2+};O^{2-}}^{LSN}) \quad (2.12)$$

$\Delta G_r^{LSN}$  would be set to zero. Similar relations were used for the surfaces “2” and “3”. In fact, the surface “3” was used to cross-check the relations. The optimization was performed according to the phase equilibria determined in the present work, and the parameters obtained are given in the Appendix.

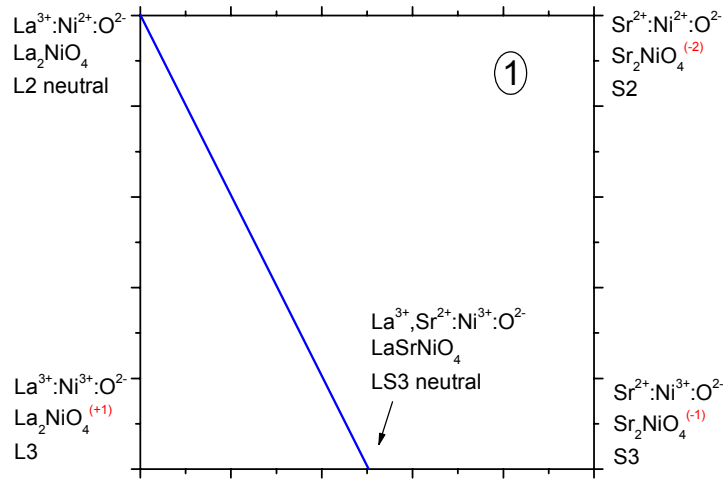


Fig. 2.4. Surface “1” of the model representation of the solid solution given in Fig. 2.3.

#### The $La_2(Ni,Ga)O_4$ phase

No work has been published on the defect structure of Ga-doped  $La_2NiO_4$  phase to date. While the oxygen interstitials indeed exist in  $La_2NiO_{4+\delta}$  at low temperatures, this compound was perfectly stoichiometric in the range of temperatures and oxygen pressure considered in the present work [03Ski]. Therefore, the charge surplus was compensated by introducing vacancies in the second sub-lattice represented by the following formula:



and the molar Gibbs energy of the solid solution could be written by

$$G_m^{LGN} = y_{La^{3+}} y_{Ni^{2+}} y_{O^{2-}} {}^{\circ}G_{La^{3+};Ni^{2+};O^{2-}}^{LGN} + y_{La^{3+}} y_{Ga^{3+}} y_{O^{2-}} {}^{\circ}G_{La^{3+};Ga^{3+};O^{2-}}^{LGN} + y_{La^{3+}} y_{Va} y_{O^{2-}} {}^{\circ}G_{La^{3+};Va;O^{2-}}^{LGN} + RT(y_{Ni^{2+}} + \ln y_{Ni^{2+}} + y_{Ga^{3+}} + \ln y_{Ga^{3+}} + y_{Va} + \ln y_{Va}) + {}^E G_m^{LGN} \quad (2.13)$$

The excess Gibbs energy  ${}^E G_m^{LGN}$  would be given by

$$\begin{aligned}
{}^E G_m^{LGN} &= y_{La^{3+}} y_{Ni^{2+}} y_{Ga^{3+}} y_{O^{2-}} {}^0 L_{La^{3+}:Ni^{2+},Ga^{3+}:O^{2-}}^{LGN} + y_{La^{3+}} y_{Ni^{2+}} y_{Va} y_{O^{2-}} {}^0 L_{La^{3+}:Ni^{2+},Va:O^{2-}}^{LGN} \\
&+ y_{La^{3+}} y_{Ga^{3+}} y_{Va} y_{O^{2-}} {}^0 L_{La^{3+}:Ga^{3+},Va:O^{2-}}^{LGN} + y_{La^{3+}} y_{Ni^{2+}} y_{Ga^{3+}} y_{Va} y_{O^{2-}} {}^0 L_{La^{3+}:Ni^{2+},Ga^{3+},Va:O^{2-}}^{LGN}
\end{aligned} \tag{2.14}$$

The solid solution could be visualized by the composition triangle shown in Fig. 2.5. The  $La_2NiO_4$  corner was the only neutral composition, while the others were positively or negatively charged. The neutral line was constructed on the diagram and neutral composition determined was  $(La^{3+})_2(Ga^{3+}_{2/3} Va_{1/3})_1(O^{2-})_4$ . The  ${}^\circ G$  parameters of the neutral components could be given by

$${}^\circ G_{La^{3+}:Ni^{2+}:O^{2-}}^{LSN} = {}^\circ G_{La_2NiO_4} \tag{2.15}$$

and for the end point of the neutral line,

$$\frac{2}{3} \cdot {}^\circ G_{La^{3+}:Ga^{3+}:O^{2-}}^{LGN} + \frac{1}{3} {}^\circ G_{La^{3+}:Va:O^{2-}}^{LGN} + RT \left( \frac{2}{3} \ln \frac{2}{3} - \frac{1}{3} \ln \frac{1}{3} \right) = G_{La^{3+}:Ga^{3+}:O^{2-}}^{LGN} \tag{2.16}$$

The  ${}^\circ G_{La^{3+}:Va:O^{2-}}^{LGN}$  was selected as

$${}^\circ G_{La^{3+}:Va:O^{2-}}^{LGN} = {}^\circ G_{A-La_2O_3}^{La_2O_3} + \frac{1}{2} {}^\circ G_{O_2}^{Gas} + A + B \cdot T \tag{2.17}$$

And the other parameters, as well as the interaction parameter,  $L_{La^{3+}:Ni^{2+},Ga^{3+}:O^{2-}}^{LGN}$ , were optimized based on the experimental results.

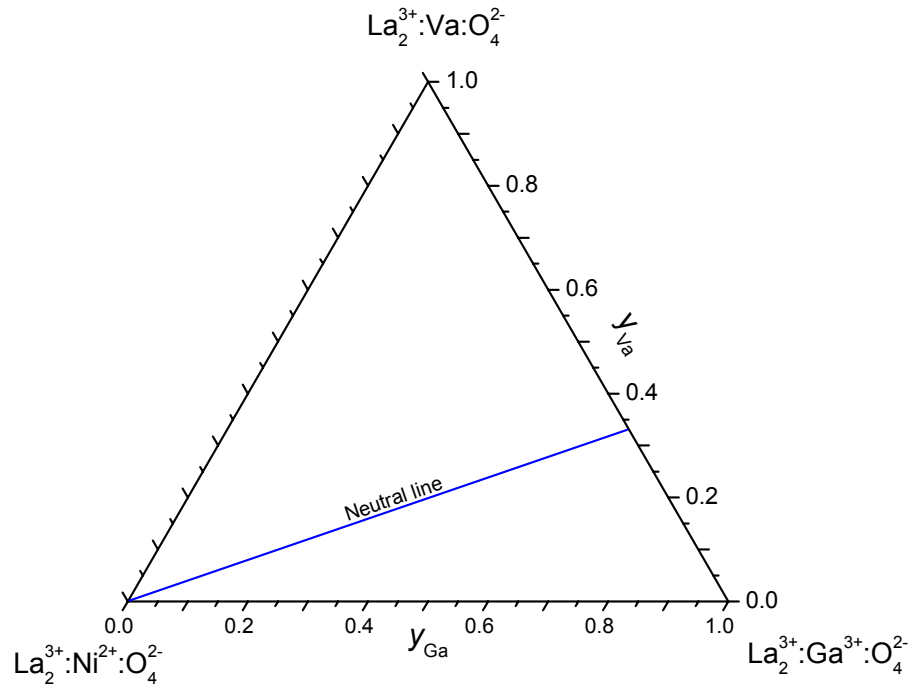
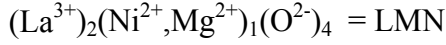


Fig. 2.5. Model representation of the  $La_2(Ni,Ga)O_4$  solid solution.

### The $La_2(Ni,Mg)O_4$ phase

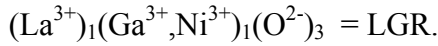
Modeling of the  $La_2(Ni,Mg)O_4$  phase was relatively simple in comparison with the previous systems, because  $Ni^{2+}$  can be substituted by  $Mg^{2+}$  without affecting the total charge of the system. The formula for the solid solution could be given by



A similar expression as given in Eqn.2.13 could be written.. Since the quasi-binary MgO-NiO system showed complete miscibility in both the liquid and the solid state [32War] and is characterized by ideal mixing behavior [05Zin1], it was assumed that  $Ni^{2+}$  and  $Mg^{2+}$  also mix ideally in the  $La_2(Ni,Mg)O_4$  solid solution. Thus, the  $L_{La^{3+}:Ni^{2+},Mg^{2+}:O^{2-}}^{LMN}$  interaction parameter was set to zero. The unstable neutral  ${}^{\circ}G_{La^{3+}:Mg^{2+}:O^{2-}}^{LMN}$  ( $La_2MgO_4$ ) phase was modeled by assuming a mechanical mixture of the constituent oxides, and the added parameters were optimized according to the experimental results.

#### 2.1.2.5. The $ABO_3$ (perovskite-type) phases

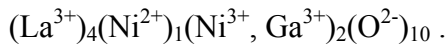
According to the experimental results in the extended  $La(Ga,Ni)O_3$  solid solution, Ni was in the 3+ valence state. The end-member of the solid solution  $LaNiO_3$  was also a neutral compound. Therefore, this solid solution would be represented by the following formula



A regular interaction parameter,  $L_{La^{3+}:Ga^{3+},Ni^{3+}:O^{2-}}^{LGR}$ , was used and optimized according to the experimental results.

#### 2.1.2.6. The $A_{n+1}B_nO_{3n+1}$ (Ruddlesden-Popper-type) phases

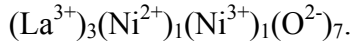
The  $La_4Ni_3O_{10}$  is a stable neutral compound existing in the La-Ni-O system and according to the experimental results, the  $Ga^{3+}$  ions substituted only for the  $Ni^{3+}$  ions. The model used for the undoped  $La_4Ni_3O_{10}$  was taken and adopted for the  $Ga^{3+}$  substituted one as



The end member  $(La^{3+})_4(Ni^{2+})_1(Ga^{3+})_2(O^{2-})_{10}$  composition was neutral but it was not a stable compound. For the modeling, it was treated as a stoichiometric compound, and the Gibbs energy was described according to the Neumann-Kopp rule [98Hil]. In addition, using the phase equilibria data obtained, regular interaction parameters,  $L_{La^{3+}:Ni^{2+}:Ni^{3+},Ga^{3+}:O^{2-}}^{LGN4310}$ , was defined.

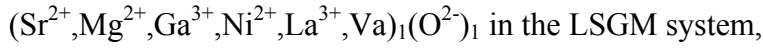


The  $\text{La}_3\text{Ni}_2\text{O}_7$  phase was found in all the investigated systems as phase-pure, without dissolution of the other components, and the three sublattice models was used as

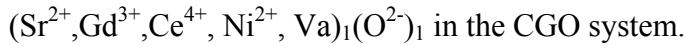


### 2.1.2.7. The MO (halite-type) phase

The halite-type MO phases were modeled as follows:



and



The Gibbs energy for the  $(\text{Va})\text{O}^{2-}$  was set to zero.

### 2.1.2.8. The $\text{M}_2\text{O}_3$ (rare earth oxides-type) phases

A generalized formula was used for the B-, C-, H-, A- and X- modifications of the rare earth oxide type solid solutions, according to:



The molar Gibbs energy for the C- $\text{Gd}_2\text{O}_3$  could be written as

$$\begin{aligned} G_m^{M_2O_3} = & y_{M^{3+}} y_{O^{2-}} \circ G_{M^{3+}, O^{2-}}^{M_2O_3} + y_{Sr^{2+}} y_{O^{2-}} \circ G_{Sr^{2+}, O^{2-}}^{M_2O_3} + y_{M^{3+}} y_{Va} \circ G_{M^{3+}, Va}^{M_2O_3} + y_{Sr^{2+}} y_{Va} \circ G_{Sr^{2+}, Va}^{M_2O_3} \\ & + RT \left[ 2 \cdot (y_{M^{3+}} + \ln y_{M^{3+}} + y_{Sr^{2+}} + \ln y_{Sr^{2+}}) + 3 \cdot (y_{O^{2-}} + \ln y_{O^{2-}} + y_{Va} + \ln y_{Va}) \right] + {}^E G_m^{M_2O_3} \end{aligned} \quad (2.18)$$

The model could be visualized by the composition square given in Fig. 2.6. The Gibbs energy of the end points of the neutral line were given respectively by

$$\circ G_{M^{3+}, O^{2-}}^{M_2O_3} = \circ G_{M_2O_3}^{M_2O_3} \quad (2.19)$$

and

$$\frac{2}{3} \circ G_{SrO}^{M_2O_3} + \frac{1}{3} \circ G_{SrVa}^{M_2O_3} + 3RT \left( \frac{2}{3} \ln \left( \frac{2}{3} \right) + \frac{1}{3} \ln \left( \frac{1}{3} \right) \right) = 2 \cdot \circ G_{SrO}^{SrO} + A + B \cdot T \quad (2.20)$$

The  $\circ G_{M^{3+}, Va}^{M_2O_3}$  was chosen as the reference, and its value was give according to

$$\circ G_{M^{3+}, Va}^{M_2O_3} = \circ G_{M_2O_3}^{M_2O_3} - \frac{3}{2} \circ G_{O_2}^{Gas} \quad (2.21)$$

Using the reciprocal relation, the fourth equation could be written as

$$\Delta G_r^{M_2O_3} = {}^\circ G_{M^{3+}:O^{2-}}^{M_2O_3} + {}^\circ G_{Sr^{2+}:Va}^{M_2O_3} - ({}^\circ G_{M^{3+}:Va}^{M_2O_3} + {}^\circ G_{Sr^{2+}:O^{2-}}^{M_2O_3}) \quad (2.22)$$

from these equations, the parameters could be determined, the other modifications of  $Gd_2O_3$  were also modeled in the same way.

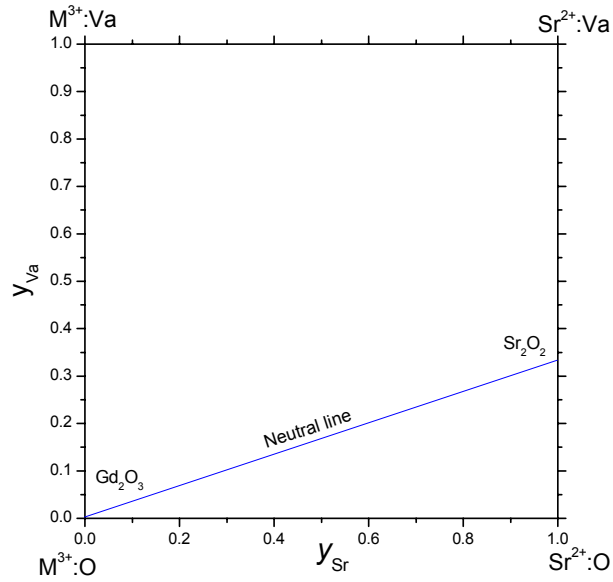


Fig. 2.6. Model representation of the  $(Gd,Sr)_2O_3$  solid solution.

## Chapter 3

# Experimental and Computational Phase Studies of Selected Systems of Relevance to the IT-SOFC Technology

### 3.1. Binary Subsystems

Thermodynamic optimization of the *La-O* system [01Gru] had revealed a system characterized by complete liquid phase miscibility and by 3 polymorphs of the  $\text{La}_2\text{O}_3$  compound, denoted A, H, and X. At high temperatures, the hexagonal A- $\text{La}_2\text{O}_3$  had transformed into partially ordered hexagonal H- $\text{La}_2\text{O}_3$ , and then into cubic X- $\text{La}_2\text{O}_3$ . The solubility limit was high for oxygen in solid lanthanum, and  $\text{La}_2\text{O}_3$  was sub-stoichiometric in equilibrium with La-metal. Recently, thermodynamics of rare earth sesquioxides were reviewed critically [06Zin1], and data for the stoichiometric  $\text{La}_2\text{O}_3$  compounds were modified slightly, to obtain better agreement with heat capacity measurements.

For the *Sr-O* system, experimental information is limited to the properties of the pure component, Sr, SrO and  $\text{SrO}_2$ . The system was modeled thermodynamically by Risold, *et al* [96Ris].

Thermodynamic optimization of the *Ga-O* system had reported [04Zin1] one, which was characterized by a wide liquid phase miscibility gap and by the presence of a stoichiometric, congruently melting compound,  $\beta\text{-Ga}_2\text{O}_3$ . Lattice stabilities were also assessed for the metastable  $\alpha$ -,  $\delta\text{-Ga}_2\text{O}_3$  [04Zin1] and  $\gamma\text{-Ga}_2\text{O}_3$  [04Zin2]. At high temperatures, the Ga-rich liquid reacted with  $\beta\text{-Ga}_2\text{O}_3$  to form  $\text{Ga}_2\text{O}$  gas.

In the *Mg-O* system, only stoichiometric MgO (periclase) forms and oxygen solubility is low in solid and liquid Mg. Thermodynamic data for the Mg-O system have been reviewed [93Hal].

In the *Ni-O* system, only the stoichiometric NiO solid oxide, bunsenite forms and behaves as a metal-deficient p-type conductor, with major lattice defects of  $\text{Ni}^{3+}$  cations and cation site vacancies. The thermodynamics the binary system had first been described by Taylor and Dinsdale [90Tay], using the ionic two-sublattice model for the description of the liquid phase

and neglecting oxygen solubility in solid nickel. Kowalski and Spencer [95Kow] had re-evaluated the description of the Ni-O liquid phase, using the associate model, and had modeled the oxygen solubility in solid nickel. Both assessments provided excellent reproduction of the experimental data below 2100 K, but generated different high temperature phase equilibria, so the calculated phase diagram either showed both a restricted liquid phase miscibility gap and a congruent melting of NiO [90Tay] or showed complete liquid miscibility and gas-peritectic formation of NiO [95Kow]. This thermodynamic description was later updated to include the solubility of oxygen in fcc nickel [04Zin3].

In the *Ce-O* system under ambient conditions, there are two oxides:  $\text{Ce}_2\text{O}_3$  and  $\text{CeO}_2$ . Cerium dioxide (ceria) has a fluorite-type structure of space group  $Fm\bar{3}m$ . The stoichiometry may deviate widely without changing the crystal structure, and the oxide may be classified also as a metal-excess *n*-type semiconductor [75Pan]. With increasing temperature and under reducing conditions,  $\text{CeO}_{2-x}$  reduces to nonstoichiometric compositions with  $x < 0.5$ . At relatively low temperatures (*i.e.*,  $T < 727$  K), ceria, like  $\text{PrO}_{2-x}$  and  $\text{TbO}_{2-x}$ , forms a series of discrete stoichiometric compounds  $\text{Ce}_n\text{O}_{2n-2}$ , where *n* is an integer  $\geq 4$  [64Bev, 75Ray, 84Ric]. A miscibility gap exists between  $\text{Ce}_{11}\text{O}_{20}$  and ceria [60Bra1, 60Bra2, 64Bev, 84Ric]. The system was first assessed by Lindemer [86Lin], using a sub-regular solution model, then subsequently by Hillert [86Hil], using a two-sublattice model. Recently, the Ce-O phase diagram was assessed over the entire range of compositions at elevated temperatures, simultaneously considering the thermochemical properties and the defect chemistry [06Zin2].

The *Gd-O* system contains only one oxide:  $\text{Gd}_2\text{O}_3$ , although the sesquioxide could exist in five structural modifications [66Foe, 71Tre, 71Bou, 06Zin1]. The cubic room temperature modification (C- $\text{Gd}_2\text{O}_3$ ) is stable up to  $\sim 1425 \pm 20$  K [06Zin1]. The transformation of C- $\text{Gd}_2\text{O}_3$  to monoclinic B- $\text{Gd}_2\text{O}_3$  is kinetically hindered [71Bou], but could occur in the presence of water atmosphere [59Sha,] or when doped with other oxides [65Foe, 70Rud, 80Dub]. The monoclinic structure exists over a broad temperature range up to 2443K [70Rud, 06Zin1]. At higher temperatures, it transforms into A- $\text{Gd}_2\text{O}_3$ , then into H- $\text{Gd}_2\text{O}_3$  and finally into the cubic X- $\text{Gd}_2\text{O}_3$  phase. Recently, thermodynamic data was assessed for all the five modifications, as well as the liquid phase [06Zin1].

### 3.2. LSGM- and CGO-type Electrolyte Materials

Information from the literature is being summarized here for gadolinia-doped ceria (CGO) and, Sr- and Mg-doped lanthanum gallate (LSGM:  $(\text{La,Sr})(\text{Ga,Mg})\text{O}_3$ ) from ternaries to

higher-order system, in order to maintain consistency between the literature data and results obtained in the present work.

### 3.2.1. The La-Sr-O Subsystem

The *La-Sr-O* system contains two compounds, the  $\beta$ -phase, which is centered around the stoichiometric  $\text{La}_4\text{SrO}_7$  with a homogeneity range, and an almost stoichiometric phase with the composition  $\text{La}_4\text{Sr}_3\text{O}_9$ . All three structural modifications of  $\text{La}_2\text{O}_3$  could dissolve a considerable amount of  $\text{SrO}$ , while  $\text{SrO}$  has a low solubility limit in  $\text{La}_2\text{O}_3$ . The quasi-binary system was first investigated experimentally by Lopato [69Lop] and Queyroux [69Que]. Later, a detailed diagram was published by Lopato [76Lop]. Recently, experimental work and a Calphad assessment have been published by Grundy and coworkers [02Gru]. Generally reasonable agreement was obtained between the literature data and the assessment. The main difference between the results of Grundy, *et al.* and Lopato, *et al.* was the limit of  $\text{SrO}$  solubility in A- $\text{La}_2\text{O}_3$ , above the formation temperature of the  $\beta$ -phase. Lopato [76Lop] reported a linear increase of the solubility up to the three-phase equilibrium,  $\text{L} \Leftrightarrow \text{A-La}_2\text{O}_3 + \beta$  and lower  $\text{SrO}$  solubility in the H- and X- $\text{La}_2\text{O}_3$ , whereas Grundy and coworkers [02Gru] found a sharp decrease in the  $\text{SrO}$  solubility above the transformation to  $\beta$  and an increasing  $\text{SrO}$  solubility in the other modifications of  $\text{La}_2\text{O}_3$ . The diagram given in Fig. 3.1 is based on the assessment of Grundy, *et al.*, with slight a modification using the new description of  $\text{La}_2\text{O}_3$  [06Zin1].

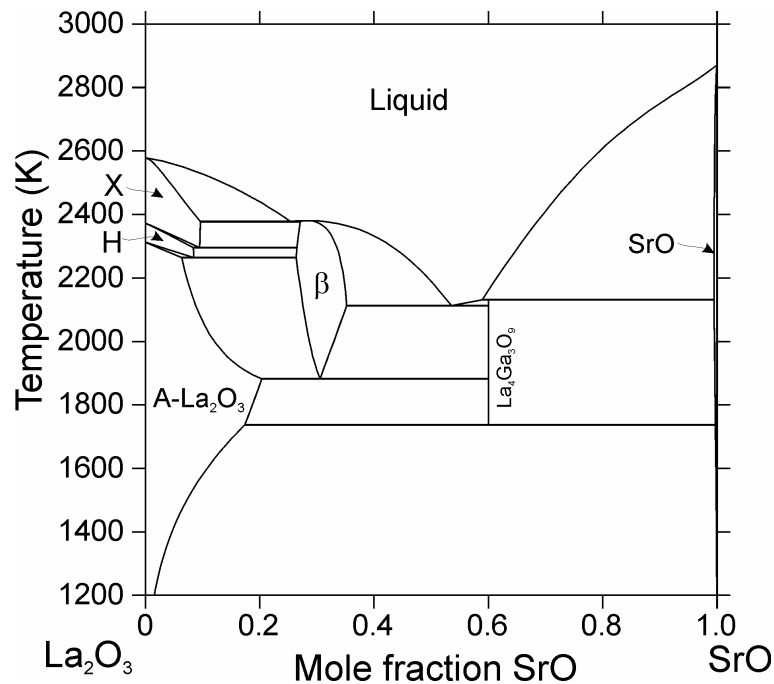


Fig. 3.1. The calculated  $\text{La}_2\text{O}_3$ - $\text{SrO}$  phase diagram.

### 3.2.2. The La-Ga-O Subsystem

The  $\text{La}_2\text{O}_3$ - $\text{Ga}_2\text{O}_3$  quasi-binary section of the *La-Ga-O* system, has been studied in detail by several techniques over broad composition and temperature ranges. The system contains two ternary congruently melting compounds,  $\text{LaGaO}_3$  and  $\text{La}_4\text{Ga}_2\text{O}_9$ . At room temperature and ambient pressure,  $\text{LaGaO}_3$  has a distorted perovskite structure with tilting of the  $\text{GaO}_6$  octahedra, resulting in an orthorhombic unit cell (LGO), which transforms to a rhombohedral structure (LGR) at  $\sim 420$  K. This transition could also be induced by the application of pressure [01Ken].

The quasi-binary system was first schematically reported below 1773 K, showing the compounds and phase transition of  $\text{LaGaO}_3$  [61Sch]. Later Mizuno, *et al.* [85Miz] proposed a diagram above 1473 K, including the liquidus across the entire temperature range, but excluding the phase transitions of the compounds. A detailed phase diagram and thermodynamic study of the quasi-binary diagram was subsequently reported by Zinkevich, *et al.*, measuring low temperature heat capacity, solubility of the components and phase transitions on both compounds by dilatometry [04Zin4]. Recently, the diagram and thermodynamics of the compounds were revised, adding new experimental results and first-principles quantum-mechanical calculations [06Zin3]. In Fig. 3.2 the calculated  $\text{La}_2\text{O}_3$ - $\text{Ga}_2\text{O}_3$  phase diagram is given.

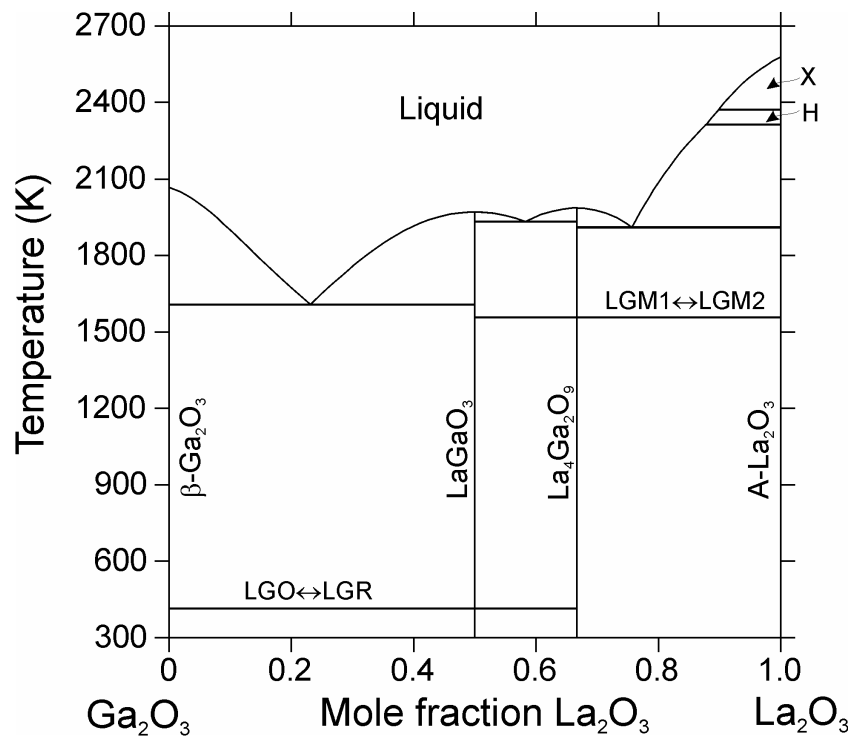


Fig. 3.2. The calculated  $\text{La}_2\text{O}_3$ - $\text{Ga}_2\text{O}_3$  phase diagram.

### 3.2.3. The La-Mg-O Subsystem

There is no ternary phase in the *La-Mg-O* system. The liquidus curve of the  $\text{La}_2\text{O}_3$ -MgO system was first determined by Wartenburg and Prophet [37War] and later the data confirmed by Tresvyatskii and Lopato [64Tre]. A simple eutectic reaction was reported for 48 mol% MgO at  $2000 \pm 30$  °C [64Tre]. According to Lopato [76Lop], the eutectic was formed at 50 mol% MgO at 1955 °C, as observed by differential thermal analysis (DTA) measurements. The system, as shown in Fig. 3.3, was obtained from the literature data modeled thermodynamically by Geupel, *et. al* [04Geu] and revised by Zinkevich [Per].

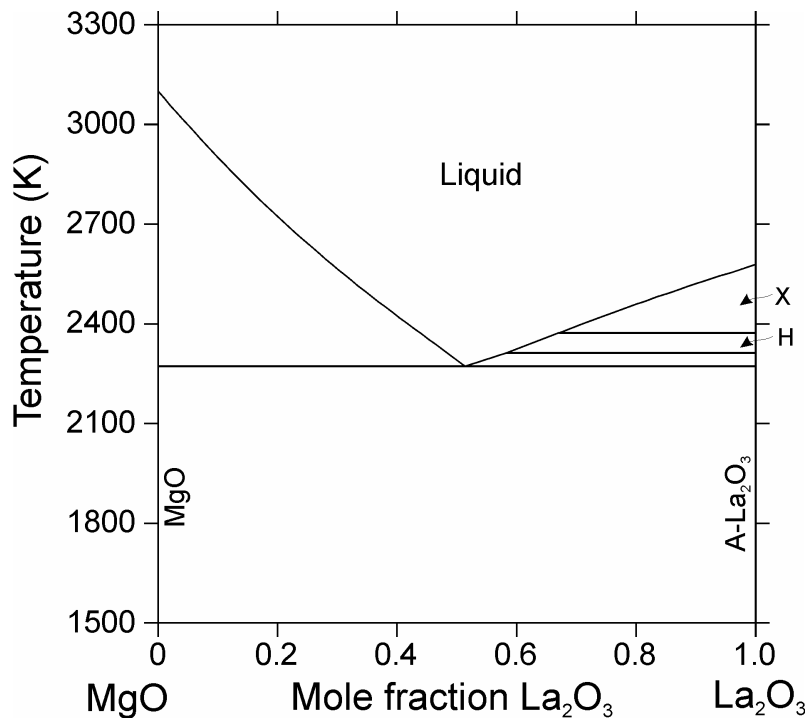


Fig. 3.3. The calculated  $\text{La}_2\text{O}_3$ -MgO phase diagram.

### 3.2.4. The Sr-Ga-O Subsystem

The existence of seven compounds in the system is well-established:  $\text{Sr}_4\text{Ga}_2\text{O}_7$ ,  $\text{Sr}_{10}\text{Ga}_6\text{O}_{19}$ ,  $\text{Sr}_3\text{Ga}_2\text{O}_6$ ,  $\text{Sr}_3\text{Ga}_4\text{O}_9$ ,  $\text{SrGa}_2\text{O}_4$ ,  $\text{SrGa}_4\text{O}_7$  and  $\text{SrGa}_{12}\text{O}_{19}$ . Complete phase diagrams of the SrO- $\text{Ga}_2\text{O}_3$  system were published by Batti and Slocari [69Bat] and Kobzareva et al. [76Kob], which are in reasonable agreement. Recently, calorimetric and thermodynamic assessments were performed for the system [Per]. No homogeneity range was assumed for any intermediate compound, due to the lack of available data. Only  $\text{SrGa}_2\text{O}_4$  showed a congruent melting point, while other compounds were formed by peritectic, or as in the case of  $\text{Sr}_3\text{Ga}_2\text{O}_6$ , by peritectoid reactions. The enthalpy of formation for  $\text{Sr}_4\text{Ga}_2\text{O}_7$ ,  $\text{SrGa}_2\text{O}_4$  and  $\text{SrGa}_{12}\text{O}_{19}$  and the enthalpy of mixing of the liquid were measured by Zinkevich, using high-

temperature oxide melt drop solution calorimetry [Per]. The calculated SrO-Ga<sub>2</sub>O<sub>3</sub> phase diagram is given in Fig. 3.4.

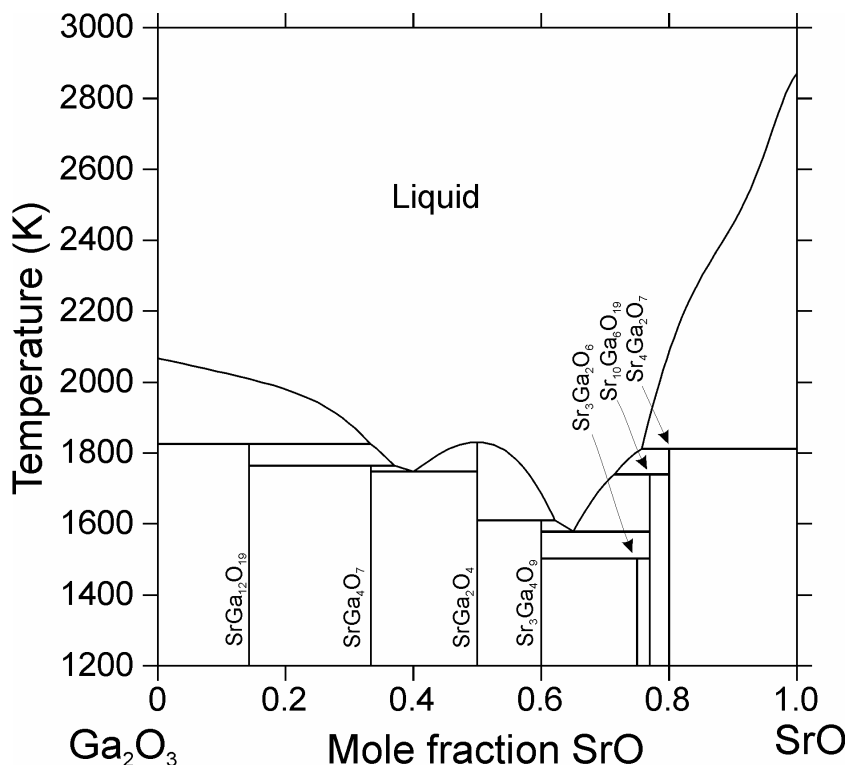


Fig. 3.4. The calculated Ga<sub>2</sub>O<sub>3</sub>-SrO phase diagram.

### 3.2.5. The Sr-Mg-O Subsystem

The only experimental investigation in the quasi-binary section MgO-SrO was for the determination of the liquidus [32War]. The same work also reported the lack of mutual solubility between solid MgO and SrO, and the non-existence of a ternary phase. In the study of van der Kemp and coworkers [94Kem], thermodynamic properties of alkaline earth oxide mixtures were estimated by analogy with well known alkali halide mixtures. Recently the system was re-assessed [Per], generating the quasi-binary MgO-SrO phase diagram shown in Fig. 3.5.

### 3.2.6. The Ga-Mg-O Subsystem

The *Ga-Mg-O* system contains one ternary compound. The spinel-type phase melts congruently at  $2223 \pm 75$  K [72Sco], and dissolves a considerable amount of Ga but a very limited amount of Mg (the limits of the homogeneity range are 47.4 and 50.7 mol% MgO at 1673 K) [05Zin]. The Ga solid solubility in MgO was reported to increase from 4.7 mol% at 1673 K to 12.7 mol% Ga<sub>2</sub>O<sub>3</sub> at 1873 K [01Maj1, 01Maj2, 69Kat], whereas Mg was not soluble in  $\beta$ -Ga<sub>2</sub>O<sub>3</sub> [05Zin]. The system was investigated experimentally and



thermodynamically in detail, and a self-consistent thermodynamic description for the system has been reported by Zinkevich, *et al* [05Zin]. Fig. 3.6 shows the generated quasi-binary  $\text{Ga}_2\text{O}_3$ - $\text{MgO}$  phase diagram.

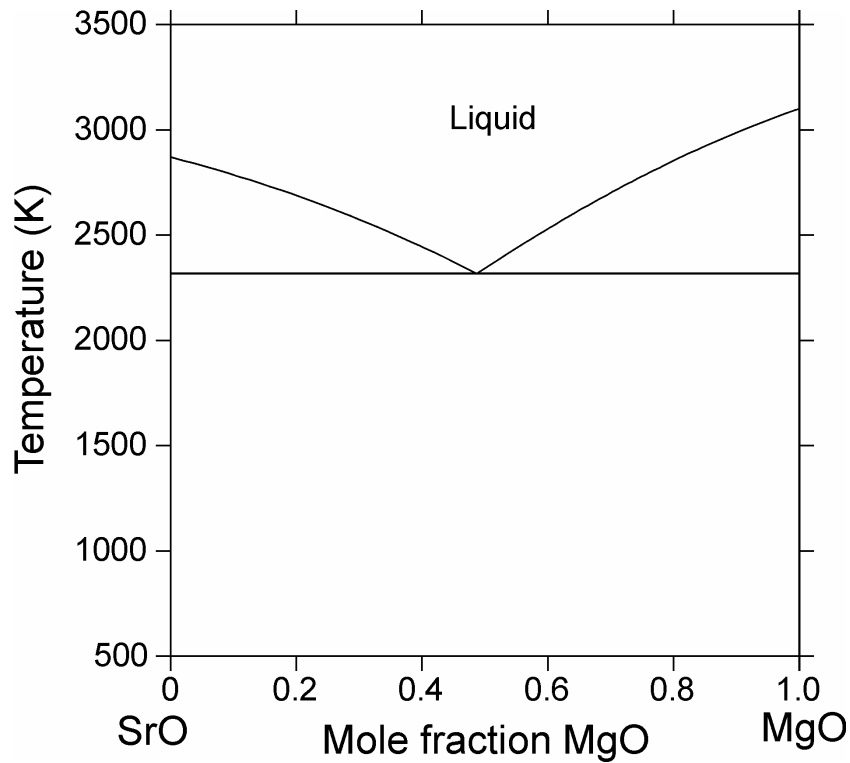


Fig. 3.5. The calculated SrO-MgO phase diagram.

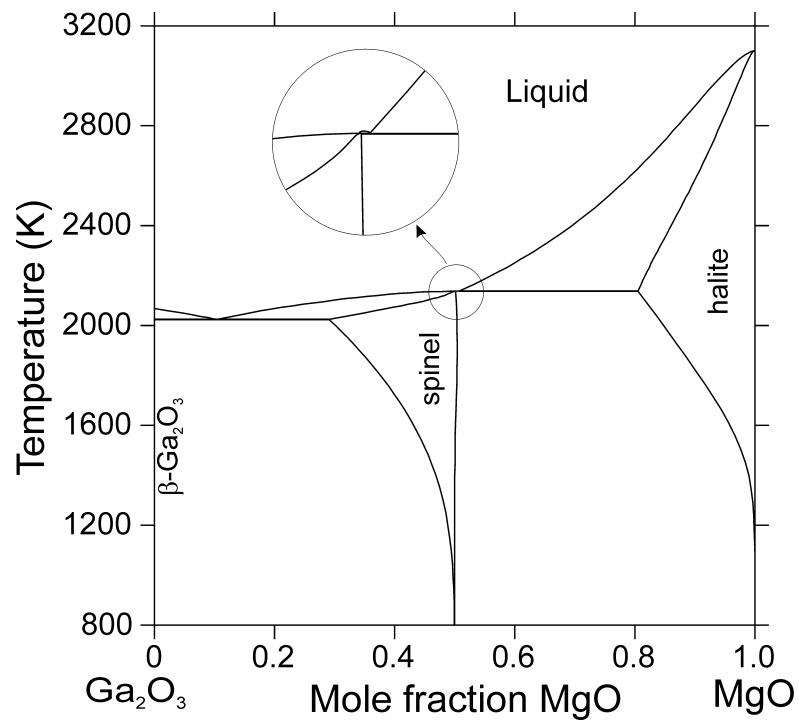


Fig. 3.6. The calculated  $\text{Ga}_2\text{O}_3$ - $\text{MgO}$  phase diagram.

### 3.2.7. The La-Sr-Ga-O Subsystem

The quasi-ternary  $\text{La}_2\text{O}_3$ - $\text{Ga}_2\text{O}_3$ - $\text{SrO}$  system was first investigated by Majewski, *et al.* [01Maj1]. Later Matraszek, *et al.* [04Mat] published an isothermal section at  $1400^\circ\text{C}$ . The existence of four ternary phases was confirmed in the literature [01Maj1, 04Mat]. The solubility of Sr in the  $\text{La}_{1-x}\text{Sr}_x\text{GaO}_{3-x/2}$  solid solution was found by Matraszek, *et al.* [04Mat], where  $x = 0.02$ , which is lower than the value determined earlier ( $x = 0.08$ ) [01Maj1]. The homogeneity of the melilite-type  $\text{La}_{1+x}\text{Sr}_{1-x}\text{Ga}_3\text{O}_{7-6}$  is in agreement in both studies, whereas in the work of Matraszek, *et al.* [04Mat], the liquid phase was found to be in equilibrium with the melilite phase at  $1400^\circ\text{C}$ . The system has been thermodynamically modeled by Zinkevich [Per], using the lower order system and the reported phase equilibria. The calculated phase diagram is given in Fig. 3.7, which is in reasonable agreement with the literature data. According to the calculated diagram, the aforementioned liquid phase exists at  $1400^\circ\text{C}$ , which is also known from the  $\text{La}_2\text{O}_3$ - $\text{Ga}_2\text{O}_3$  quasi binary section.

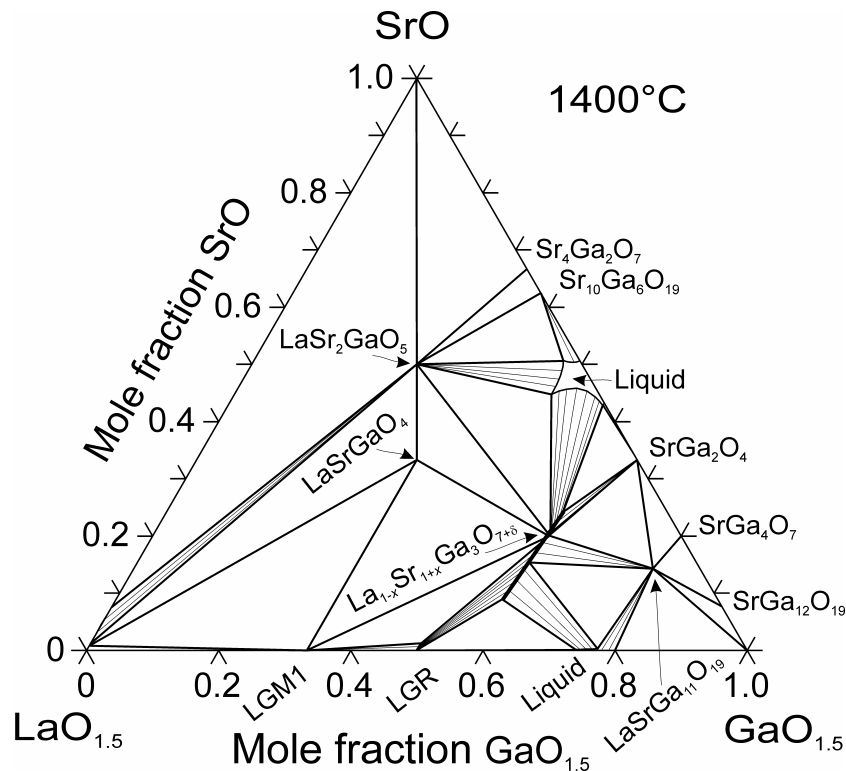


Fig. 3.7. The calculated  $\text{La}_2\text{O}_3$ - $\text{SrO}$ - $\text{Ga}_2\text{O}_3$  phase diagram.

### 3.2.8. The La-Sr-Mg-O Subsystem

There are no experimental phase studies reported in the literature on the system  $\text{La-Sr-Mg-O}$ . In addition, no data have been found on the existence of any quaternary compound. Therefore, the  $\text{La}_2\text{O}_3$ - $\text{SrO}$ - $\text{MgO}$  quasi-ternary system has been extrapolated from the lower order systems

in the present work. The calculated 1727 °C isothermal section is given in Fig. 3.8, which contains all solid phases in the La<sub>2</sub>O<sub>3</sub>-SrO quasi-binary system.

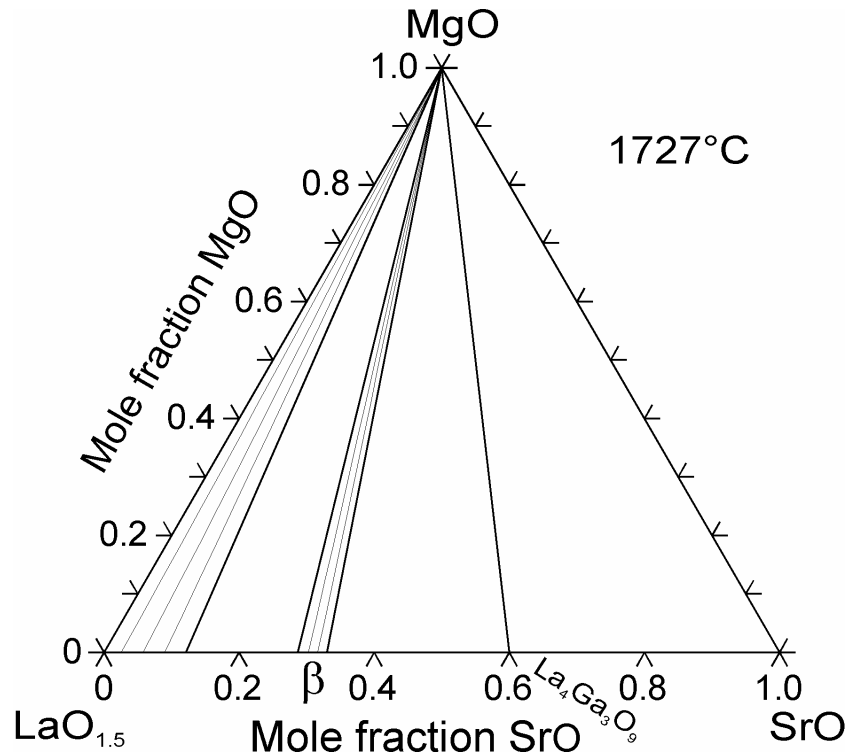


Fig. 3.8. The calculated La<sub>2</sub>O<sub>3</sub>-SrO-MgO phase diagram.

### 3.2.9. The La-Ga-Mg-O Subsystem

Phase relations in the *La-Ga-Mg-O* system of the La<sub>2</sub>O<sub>3</sub>-Ga<sub>2</sub>O<sub>3</sub>-MgO quasi-quaternary section at 1400 °C in air have been studied using various techniques [01Maj1, 01Maj2, 04Mat]. LaGaO<sub>3</sub> has been found to exist in equilibrium with La<sub>4</sub>Ga<sub>2</sub>O<sub>9</sub>, MgGa<sub>2</sub>O<sub>4</sub> (spinel), MgO and Ga<sub>2</sub>O<sub>3</sub>, with no detectable liquid phase. However, the diagrams generated differed substantially from each other. The diagram proposed by Majewski, *et al.* did not contain the two quasi-ternary phases La<sub>3</sub>MgGaO<sub>7</sub> and LaMgGa<sub>11</sub>O<sub>19</sub> of magnetoplumbite-type structure. Moreover, the MgO solubility in LaGaO<sub>3</sub> detected by Matraszek, *et al.* (14 mol%) was considerably higher than that determined by Majewski, *et al.* (4-5 mol%). The MgO solubility in the La<sub>4</sub>Ga<sub>2</sub>O<sub>9</sub> (LGM) phase was reported in both studies to be almost the same (1-3 mol %). Taking into account the solubility data and the quasi-binary subsystems, thermodynamic modeling of the La<sub>2</sub>O<sub>3</sub>-Ga<sub>2</sub>O<sub>3</sub>-MgO system was performed by Geupel, *et al.* [04Geu]. Recently, the system was re-investigated experimentally and computationally [Per]. The results revealed that the La<sub>3</sub>MgGaO<sub>7</sub> compound is actually a solid solution of La<sub>4</sub>(Mg,Ga)<sub>3</sub>O<sub>10</sub> with the same structure as the La<sub>4</sub>(Ni,Ga)<sub>3</sub>O<sub>10</sub> solid solution found in the La-

Ga-Ni-O system [06Sol]. In light of these new phase equilibria, the system was thermodynamically re-modeled [Per], and the resulting diagram is given in Fig. 3.9.

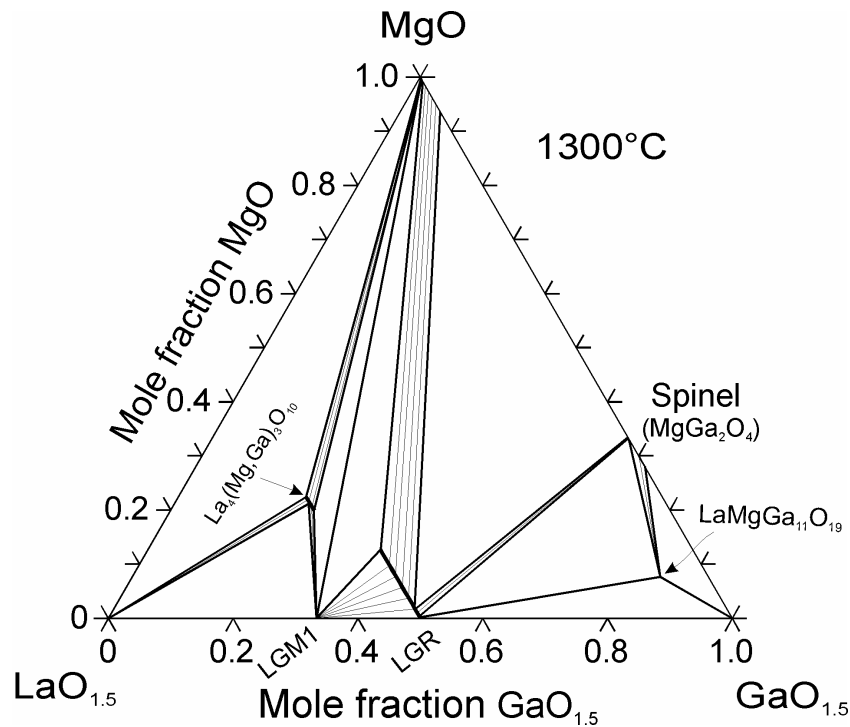


Fig. 3.9. The calculated  $\text{La}_2\text{O}_3$ - $\text{Ga}_2\text{O}_3$ - $\text{MgO}$  phase diagram.

### 3.2.10. The Sr-Ga-Mg-O subsystem

The quasi-ternary  $\text{SrO}$ - $\text{Ga}_2\text{O}_3$ - $\text{MgO}$  system was experimentally investigated by Majewski, *et al.* [01Maj1]. The 1400 °C isothermal section was dominated by the liquid phase and did not contain any quaternary phase. There are no additional experimental data available in the literature. In the present study, the quasi-ternary system has been extrapolated from the lower order systems. The calculated 1200 °C isothermal section is given in Fig. 3.10. The phase relations and tie-lines are in agreement with the experimental results of Majewski, *et al.* [01Maj1].

### 3.2.11. The La-Sr-Ga-Mg-O System (the LSGM electrolyte)

Using all the subsystems and experimental data on the phase equilibria, the phase diagram of the LSGM system has been calculated by Zinkevich [Per]. The calculations were mainly based on experimental work of Huang, *et al.* [98Hua], Matraszek, *et al.* [04Mat], and Majewski, *et al.* [01Maj1, 01Maj2], as well as experimental values measured by the author [Per]. The calculated phase equilibria was very consistent with the literature data. A low  $\text{SrO}$  solubility in the first sublattice and a moderate  $\text{MgO}$  solubility in the second sublattice have

been revealed as a result of the calculations. Substitution in both the sublattices enhanced the formation of solid solution. Thus, the total solubility of the cations was much higher than in the case where substitution was restricted to the respective single sublattices. The calculated 1400 °C isothermal section is given in Fig. 3.11, together with the experimental results [Per].

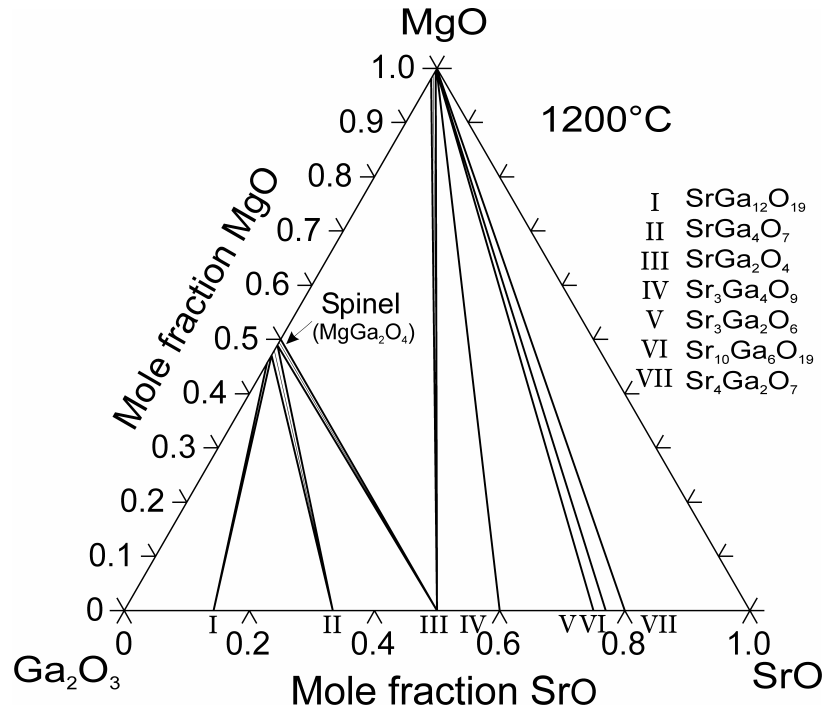


Fig. 3.10. The calculated SrO-Ga<sub>2</sub>O<sub>3</sub>-MgO phase diagram.

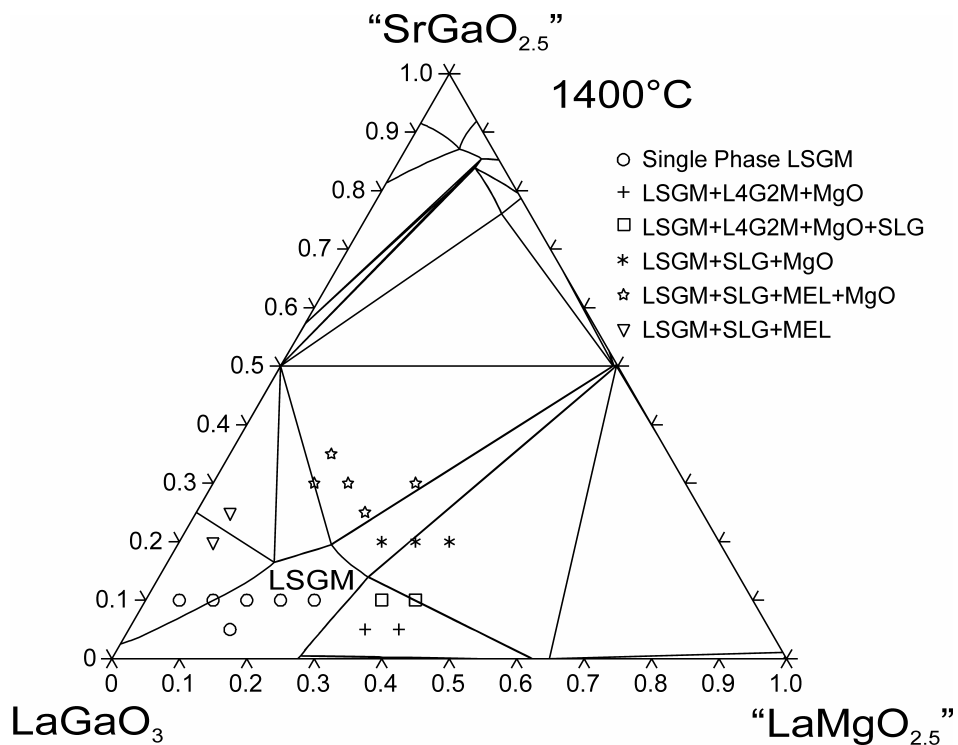


Fig. 3.11. The calculated La<sub>2</sub>O<sub>3</sub>-SrO-Ga<sub>2</sub>O<sub>3</sub>-MgO phase diagram. The abbreviations are, L4G2M: La<sub>4</sub>(Mg,Ga)<sub>3</sub>O<sub>10</sub>, SLG: SrLaGaO<sub>4</sub>, MEL: melilite-type La<sub>1+x</sub>Sr<sub>1-x</sub>Ga<sub>3</sub>O<sub>7-δ</sub> solid solution.

### 3.2.12. The Ce-Gd-O System (CGO Electrolyte)

The electrical conductivity and defect association properties have been investigated intensively for the *Ce-Gd-O* system. However, despite the technological importance of this system, the measured thermodynamics and phase equilibria data are very limited, with the exception of the recent work by Zinkevich, *et al.* on the thermodynamics of ceria doped with Sm, Gd, and Y [06Zin2]. In the quasi-binary  $\text{CeO}_2\text{-GdO}_{1.5}$  system, the fluorite-type phase (F) was reported to extend from pure ceria up to 45-54 mol %  $\text{GdO}_{1.5}$ , while single C-type phase was detected between 69-74 and 92 mol %  $\text{GdO}_{1.5}$ , with the precise composition depending on temperature [64Bev]. It was also reported that the C-type phase could coexist with the monoclinic phase (B), which is the high temperature polymorphic modification of gadolinia [64Bev]. The enthalpy of formation was measured by high-temperature drop solution calorimetry for  $\text{CeO}_2\text{-GdO}_{1.5}$ , covering the full composition range. Based on these results and phase equilibria data from the literature, the system was thermodynamically modeled [06Zin2]. The calculated  $\text{CeO}_2\text{-Gd}_2\text{O}_3$  phase diagram is given in Fig. 3.12. In another recent work [06Che], the formation enthalpy from the oxide members in the fluorite phase field was measured using the same technique, but the endothermic heat of formation of the fluorite solid solution reported, was not consistent with the existence of the defect complexes between the dopant cations and oxygen vacancies experimentally demonstrated in structural studies.

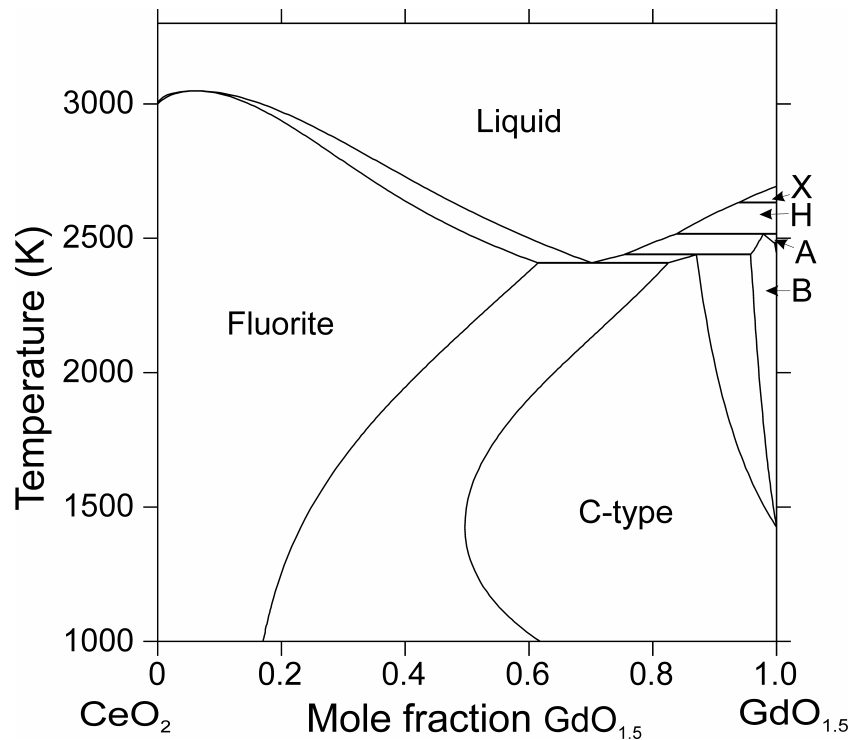


Fig. 3.12. The calculated  $\text{CeO}_2\text{-Gd}_2\text{O}_3$  phase diagram.

### 3.3. Reactivity of LSGM-based Electrolytes with Relevant Electrode Materials

#### 3.3.1. The La-Ni-O Subsystem

The *La-Ni-O* system contains the ternary compounds,  $\text{La}_2\text{NiO}_4$ ,  $\text{La}_3\text{Ni}_2\text{O}_7$ ,  $\text{La}_4\text{Ni}_3\text{O}_{10}$ , and  $\text{LaNiO}_3$ , which belong to the Ruddlesden-Popper (RP) homologous series with the general formula,  $\text{La}_{n+1}\text{Ni}_n\text{O}_{3n+1}$ , where  $n = 1, 2, 3$ , and  $\infty$ , respectively. The crystal structure of these oxides consists of  $n$  layers of perovskite-type  $\text{LaNiO}_3$ , separated by single rocksalt-type  $\text{LaO}$  layers. Attempts to obtain single-phase compounds with  $n \geq 4$  have not been successful, although these compounds may form on the nanometer scale as intergrowths in the structure of  $\text{La}_3\text{Ni}_2\text{O}_7$  and  $\text{La}_4\text{Ni}_3\text{O}_{10}$  [86Ram]. Kitayama had reported the synthesis of a compound with the stoichiometry  $\text{La}_6\text{Ni}_5\text{O}_{15}$  [90Kit], but had proposed that it might be a solid solution of  $\text{La}_4\text{Ni}_3\text{O}_{10}$ , due to the similarity between x-ray diffraction patterns. It could therefore be concluded that the  $n \geq 4$  members of the  $\text{La}_{n+1}\text{Ni}_n\text{O}_{3n+1}$  series do not belong to the thermodynamically stable phases in the *La-Ni-O* system. Among them,  $\text{La}_2\text{NiO}_4$  is the only compound, for which the thermodynamic properties are well known. Until recently, the thermodynamics data pertaining to other members of the RP series have been limited to a few measurements of temperatures and oxygen pressures for the following decomposition reactions:



This information has been used to obtain a reasonable thermodynamic description of the system, and the first Calphad assessment has been published [04Zin3]. However, a lack of experimental data prevented the precise determination of the enthalpy of formation and the entropy of formation of  $\text{La}_3\text{Ni}_2\text{O}_7$ ,  $\text{La}_4\text{Ni}_3\text{O}_{10}$ , and  $\text{LaNiO}_3$ . Furthermore, heat capacities of these compounds were approximated by the Neumann-Kopp rule, *i.e.*, as a sum of heat capacities of the constituent elements. Since then, a number of papers have been published, reporting the enthalpy of formation of  $\text{LaNiO}_3$  [05Che, 06Ban1],  $\text{La}_4\text{Ni}_3\text{O}_{10}$  [06Ban1],  $\text{La}_3\text{Ni}_2\text{O}_7$  [06Ban1], the decomposition temperature of  $\text{LaNiO}_3$  in air [06Ban2], the boundary of stability for  $\text{La}_4\text{Ni}_3\text{O}_{10}$  [06Ban2], the oxygen content and the phase transition data for  $\text{La}_3\text{Ni}_2\text{O}_7$  and  $\text{La}_4\text{Ni}_3\text{O}_{10}$  [06Amo2]. However, the complete thermodynamic descriptions of the ternary phases are still missing. Therefore, in order to measure the thermodynamic

properties, phase-pure compounds were prepared using the Pechini-type soft chemical method (PSC).

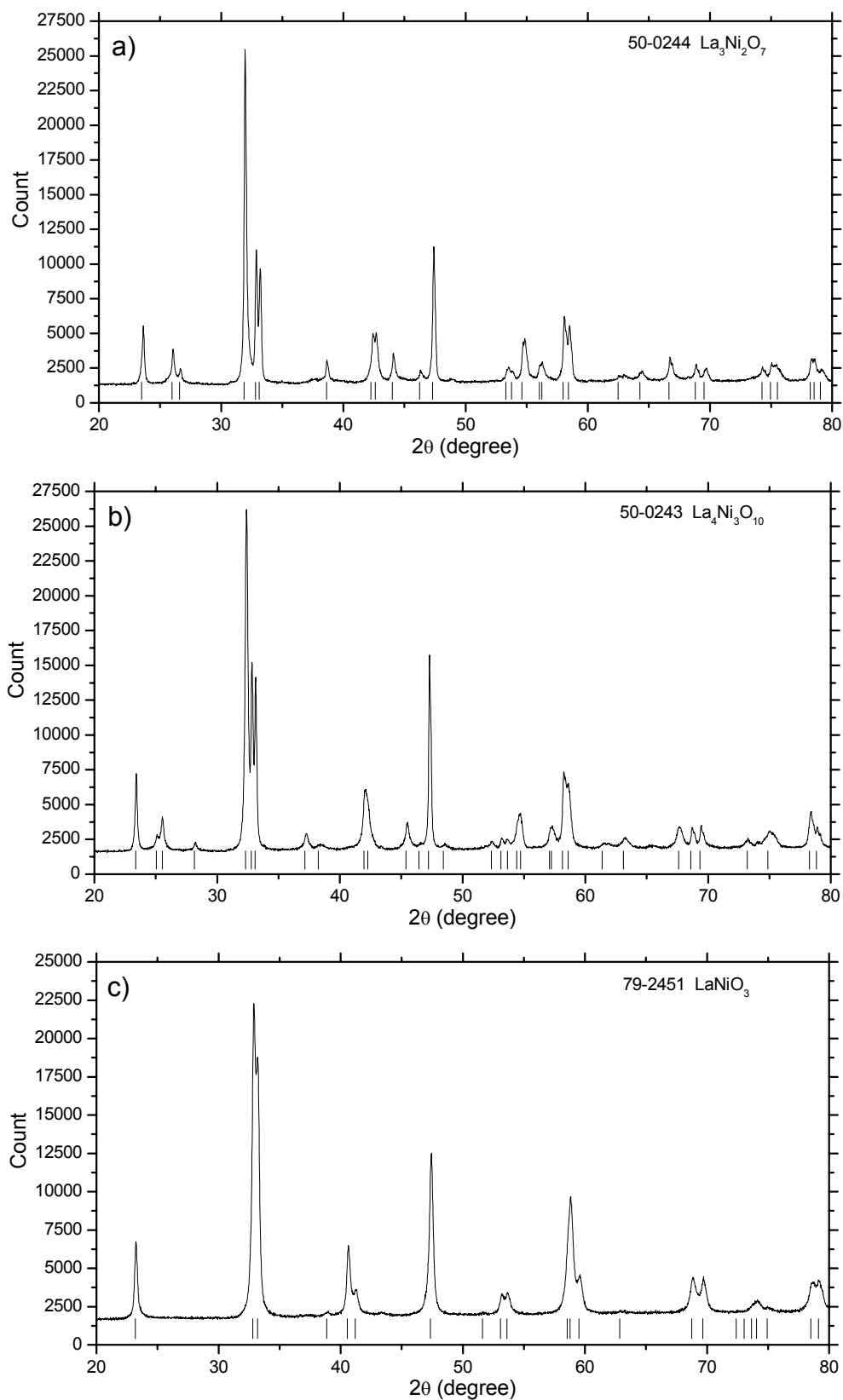


Fig. 3.13. XRD powder patterns of the as-prepared samples  $\text{La}_3\text{Ni}_2\text{O}_7$  (a),  $\text{La}_4\text{Ni}_3\text{O}_{10}$  (b), and  $\text{LaNiO}_3$  (c).



Fig. 3.13 shows the XRD powder patterns of  $\text{La}_3\text{Ni}_2\text{O}_7$ ,  $\text{La}_4\text{Ni}_3\text{O}_{10}$ , and  $\text{LaNiO}_3$  after the final sintering step. A comparison with ICDD database [ICDD] (PDF #50-0244, #50-0243, and #79-2451, respectively) reveals that all three compounds were obtained as single phases. The La/Ni ratio, as well as the oxygen and carbon content in the as-prepared samples, are given in Table 3.1. It can be seen that all RP-phases show negligible deviations from the stoichiometric compositions, and thus, in terms of crystal chemistry, they can be represented as  $(\text{La}^{3+})_3(\text{Ni}^{2+})_1(\text{Ni}^{3+})_1(\text{O}^{2-})_7$ ,  $(\text{La}^{3+})_4(\text{Ni}^{2+})_1(\text{Ni}^{3+})_2(\text{O}^{2-})_{10}$ , and  $(\text{La}^{3+})_1(\text{Ni}^{3+})_1(\text{O}^{2-})_3$ , respectively.

Table 3.1. The molar La/Ni ratios, oxygen and carbon content of the as-prepared  $\text{La}_3\text{Ni}_2\text{O}_7$ ,  $\text{La}_4\text{Ni}_3\text{O}_{10}$ , and  $\text{LaNiO}_3$  samples.

Compound	La/Ni ratio	O (wt.%)	Weight loss (%) <sup>a</sup>	<x>	C (wt.%)
$\text{La}_3\text{Ni}_2\text{O}_x$	$1.49 \pm 0.05$	$17.6 \pm 0.1$	$1.1 \pm 0.1$	$7.04 \pm 0.05$	0.0022
$\text{La}_4\text{Ni}_3\text{O}_x$	$1.32 \pm 0.05$	$17.8 \pm 0.1$	$1.7 \pm 0.1$	$9.95 \pm 0.05$	0.0059
$\text{LaNiO}_x$	$1.02 \pm 0.03$	$19.4 \pm 0.1$	$2.8 \pm 0.2$	$2.96 \pm 0.05$	0.0256

<sup>a</sup> After decomposition to  $\text{La}_2\text{NiO}_4$  and NiO

Examples of thermal analysis curves recorded on heating the  $\text{La}_{n+1}\text{Ni}_n\text{O}_{3n+1}$  compounds under a constant oxygen pressure (*i.e.*, dynamic experiments) are shown in Fig. 3.14. The thermal decomposition of the RP-phases was an endothermic reaction manifested by an abrupt weight loss. The corresponding onset temperatures were determined by a combined treatment of TG and DSC curves, extrapolating from the construction of tangent lines. The decomposition of  $\text{La}_3\text{Ni}_2\text{O}_7$ ,  $\text{La}_4\text{Ni}_3\text{O}_{10}$ , and  $\text{LaNiO}_3$  produced  $\text{La}_2\text{NiO}_4$ , NiO and  $\text{O}_2$  in one, two, and three steps, respectively (Fig. 3.14a-c), in accordance with the reactions in Eqn. 3-1, 3-2 and 3-3. It should be noted that, because of a finite heating rate, the ratios of weight loss at each individual steps differ from the theoretical one. Similar thermogravimetric curves were reported for the decomposition of  $\text{LaNiO}_3$  in air and oxygen atmosphere [93Hof]. The decreasing thermodynamic stability of  $\text{La}_{n+1}\text{Ni}_n\text{O}_{3n+1}$  compounds upon lowering the oxygen pressure resulted in the corresponding shifts of the onset temperatures. At the lowest oxygen pressure of 0.01 bar, decomposition occurred very rapidly, and the individual steps could not be distinguished clearly (Fig. 3.14b-c). Some minor weight loss preceding the decomposition (0.1 - 0.2 % depending on the oxygen pressure and the heating rate) could be associated with the oxygen release due to non-stoichiometry. Similar weight loss upon heating up to 1173 K in air has been found in a recent thermogravimetric study [06Ban2].

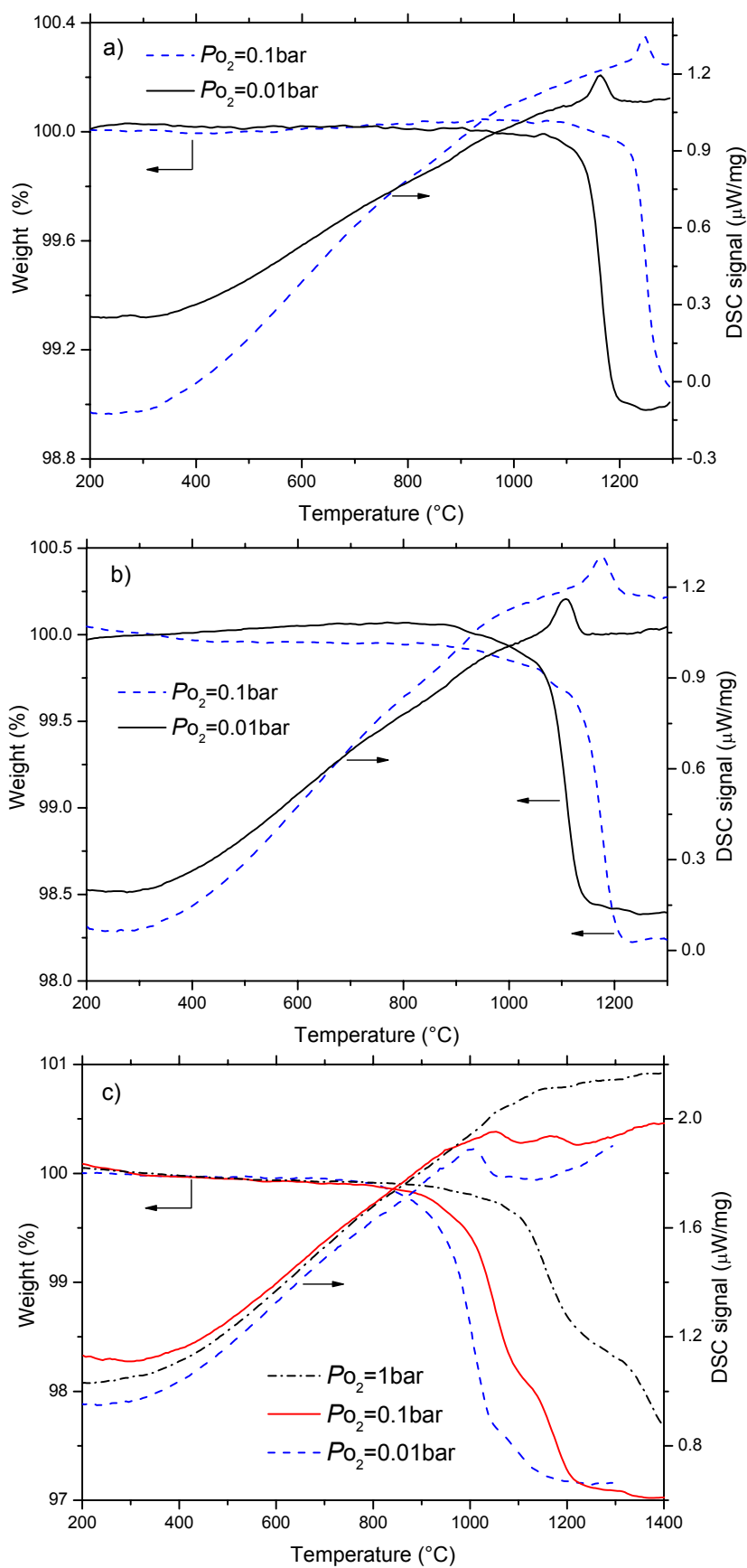


Fig. 3.14. TG and DTA curves recorded on heating the  $\text{La}_3\text{Ni}_2\text{O}_7$  (a),  $\text{La}_4\text{Ni}_3\text{O}_{10}$  (b), and  $\text{LaNiO}_3$  (c) compounds with a rate of  $10 \text{ K}\cdot\text{min}^{-1}$  at several different oxygen pressures.

The maximum oxygen deficiency in the investigated range of temperatures and oxygen pressures corresponds to the compositions of  $\text{La}_3\text{Ni}_2\text{O}_{6.92}$ ,  $\text{La}_4\text{Ni}_3\text{O}_{9.90}$ , and  $\text{LaNiO}_{2.97}$ , in good agreement with data in the literature. Indeed, the stoichiometry of RP-phases in the La-Ni-O system in air has been reported as  $\text{LaNiO}_{2.97}$  at 1000 °C [93Hof] and  $\text{La}_3\text{Ni}_2\text{O}_{6.92}$  at 700 °C [94Zha]. Nonetheless, these deviations from oxygen stoichiometry are small enough to be neglected. No evidence was found for the substantial oxygen deficiency in  $\text{LaNiO}_3$  reported in some publications [75Gai, 75Oba, 90Tak2].

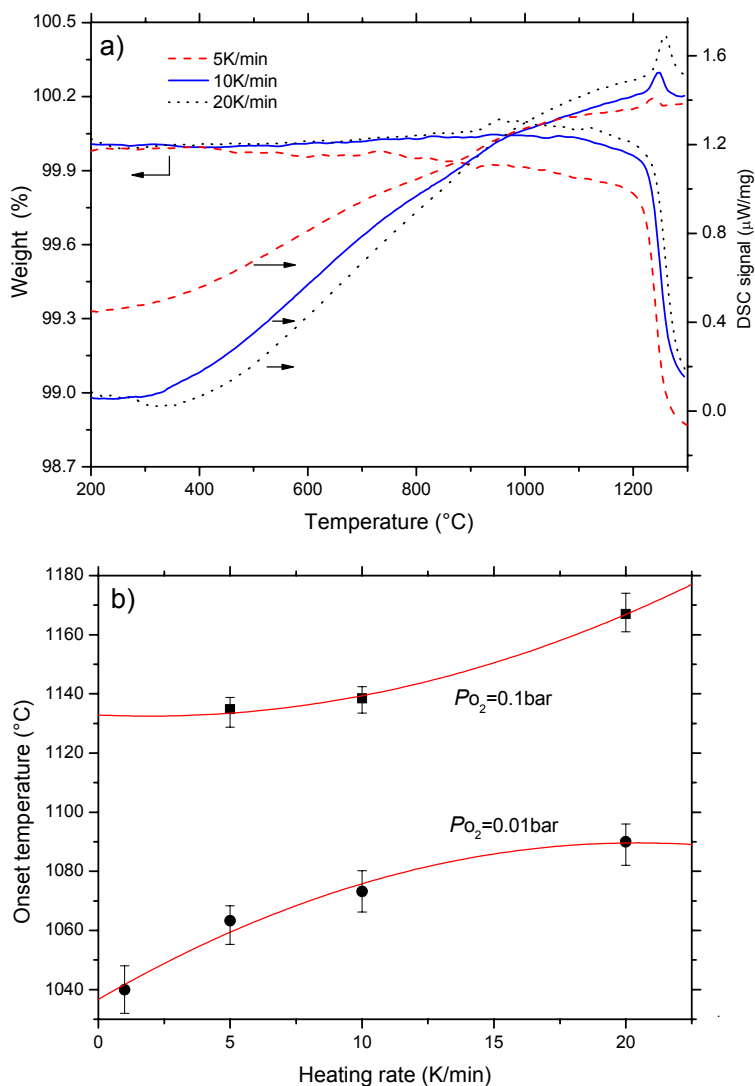


Fig. 3.15. Influence of the heating rate on the thermal decomposition behavior of  $\text{La}_3\text{Ni}_2\text{O}_7$  at  $P_{\text{O}_2} = 0.1$  bar (a) and of  $\text{La}_4\text{Ni}_3\text{O}_{10}$  at different oxygen pressures (b).

Attention was paid in particular to the effect of the heating rate. Fig. 3.15a shows the TG/DSC curves for the  $\text{La}_3\text{Ni}_2\text{O}_7$  sample at an oxygen pressure of 0.1 bar recorded with rates of 5, 10, and 20  $\text{K}\cdot\text{min}^{-1}$ . It is evident that increasing the heating rate yielded a systematic shift of the curves to higher temperatures. At the same time, the DSC peak became sharper. In order to estimate the equilibrium temperature of decomposition (Eqn. 3-1, 3-2 and 3-3), the onset

temperatures were extrapolated to a heating rate of zero, as shown in Fig. 3.15. At high oxygen pressures, an asymptotic behavior was observed and at 0.1 bar of  $O_2$ , the onset temperature fell within the limits of error, when estimated using Eqn. 3-2 determined at heating rates of 10 and 5  $K \cdot \text{min}^{-1}$ . At low oxygen pressures, the dependence of the onset temperature on heating rate could at best be fitted by a parabolic function, although it is also possible to use a linear fit. However, regardless of the method used, the extrapolated onset temperature differed insignificantly from the value obtained with a rate of 1  $K \cdot \text{min}^{-1}$ .

As an example of isothermal experiments, Fig. 3.16 shows the isothermal TG curve of the  $\text{La}_4\text{Ni}_3\text{O}_{10}$  sample, that was recorded over a range of gradually decreasing oxygen pressures. The weight remained constant until an oxygen pressure of 0.200 bar was reached. The oscillations around 99.95 % were due to the relatively large changes in gas composition. A further decrease in the oxygen pressure to 0.198 bar induced the onset of perceptible weight loss, indicating corresponding to the decomposition reaction in Eqn. 3-2. Equilibrium oxygen pressures, associated with the decomposition of RP-phases at given temperatures, were obtained from the intersection points of tangents lines, as illustrated in Fig. 3.16.

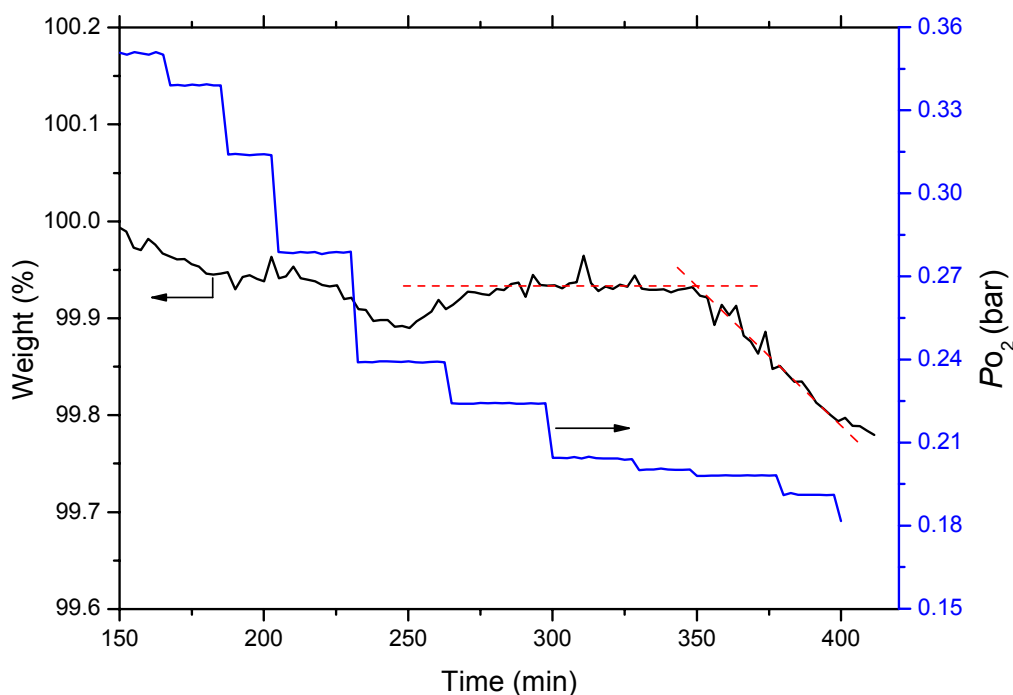


Fig. 3.16. Isothermal decomposition of  $\text{La}_4\text{Ni}_3\text{O}_{10}$  at  $1150^\circ\text{C}$ , as a consequence of decreasing oxygen pressure.

Fig. 3.17 shows the heat capacity data of  $\text{La}_3\text{Ni}_2\text{O}_7$ ,  $\text{La}_4\text{Ni}_3\text{O}_{10}$ , and  $\text{LaNiO}_3$ . In every case, the room temperature data, when combined with the DSC measurements, agreed well at the overlap region. The low-temperature adiabatic calorimetry data for  $\text{La}_3\text{Ni}_2\text{O}_7$  (Fig. 3.17a) exhibited a large scatter due to the unusually low thermal conductivity of this compound

[07Sol]. The heat capacity of  $\text{LaNiO}_3$  revealed a regular behavior (Fig. 3.17c), while the other two compounds showed anomalies on the heat capacity curves in the high- and low-temperature ranges, respectively (Fig. 3.17a,b). In the case of  $\text{La}_3\text{Ni}_2\text{O}_7$ , the peak at 560 K (onset of transformation at 490 K) was associated with the symmetry change from orthorhombic to tetragonal [06Amo2, 07Sol], which is accompanied by dramatic changes in electrical resistivity and magnetic susceptibility [96Kob, 97Sas]. This conversion cannot be seen in the DSC curve (Fig. 3.14a). Indeed, the integration of the heat capacity peak yields a mild enthalpy effect of only  $1.8 \text{ kJ}\cdot\text{mol}^{-1}$ . However, Kobayashi and co-workers [96Kob] were able to detect subtle endothermic and exothermic effects during heating and cooling, respectively, using differential thermal analysis. Since the high-temperature XRD studies [97Sas] indicated a discontinuous change in the unit cell parameter  $c$  at  $\sim 550 \text{ K}$ , the orthorhombic to tetragonal transformation of  $\text{La}_3\text{Ni}_2\text{O}_7$  should be classified as a first-order phase transition. No remarkable changes were apparent in the temperature dependence of the heat capacity both before and after the transition (Fig. 3.17a). The heat capacity anomaly of  $\text{La}_4\text{Ni}_3\text{O}_{10}$  around 135 K could be associated with a second-order electronic phase transition [01Wu]. In fact, no structural changes and no long-range magnetic ordering of  $\text{La}_4\text{Ni}_3\text{O}_{10}$  and  $\text{La}_3\text{Ni}_2\text{O}_7$  below 300 K were detected [00Lin], whereas a discontinuity in the electrical resistivity at 140 - 160 K has been confirmed in several works [91Tka, 97Gre, 00Lin, 01Wu].

The description of the  $\text{La}_2\text{NiO}_4$  phase obtained strongly resembled that of previous work [04Zin3] based on the same datasets, *i.e.*, in terms of the heat capacity of  $\text{LaNiO}_3$  [97Kyo] and the EMF of the cell,  $\text{La}_2\text{NiO}_4, \text{Ni}, \text{La}_2\text{O}_3, \text{O}_2(\text{Pt}) | \text{O}^{2-} | (\text{Pt})\text{O}_2$ , where the corresponding reaction was  $\text{La}_2\text{O}_3 + \text{Ni} + 0.5\text{O}_2 = \text{La}_2\text{NiO}_4$  [88Pet]. However, a slight modification was necessary, because of a recent update for the thermodynamic functions of  $\text{La}_2\text{O}_3$  [06Zin1]. The description of  $\text{La}_3\text{Ni}_2\text{O}_7$ ,  $\text{La}_4\text{Ni}_3\text{O}_{10}$ , and  $\text{LaNiO}_3$  were obtained by simultaneously fitting the  $T - \log(P_{\text{O}_2})$  data pertaining to the decomposition (Eqn. 3-1, 3-2 and 3-3), the heat capacity data above 298 K, and the standard entropy values. These values were calculated by numerical integration of the curve  $C_p/T$  vs.  $T$ , within the limits of 0 - 298 K, in accordance with the third law of thermodynamics. Heat capacities below 4 K were calculated using the  $T^3$ -approximation. The calculated enthalpy and entropy of the phase transition of  $\text{La}_3\text{Ni}_2\text{O}_7$  were taken into account, while the same expression was used for the heat capacity of both the orthorhombic and tetragonal modifications.

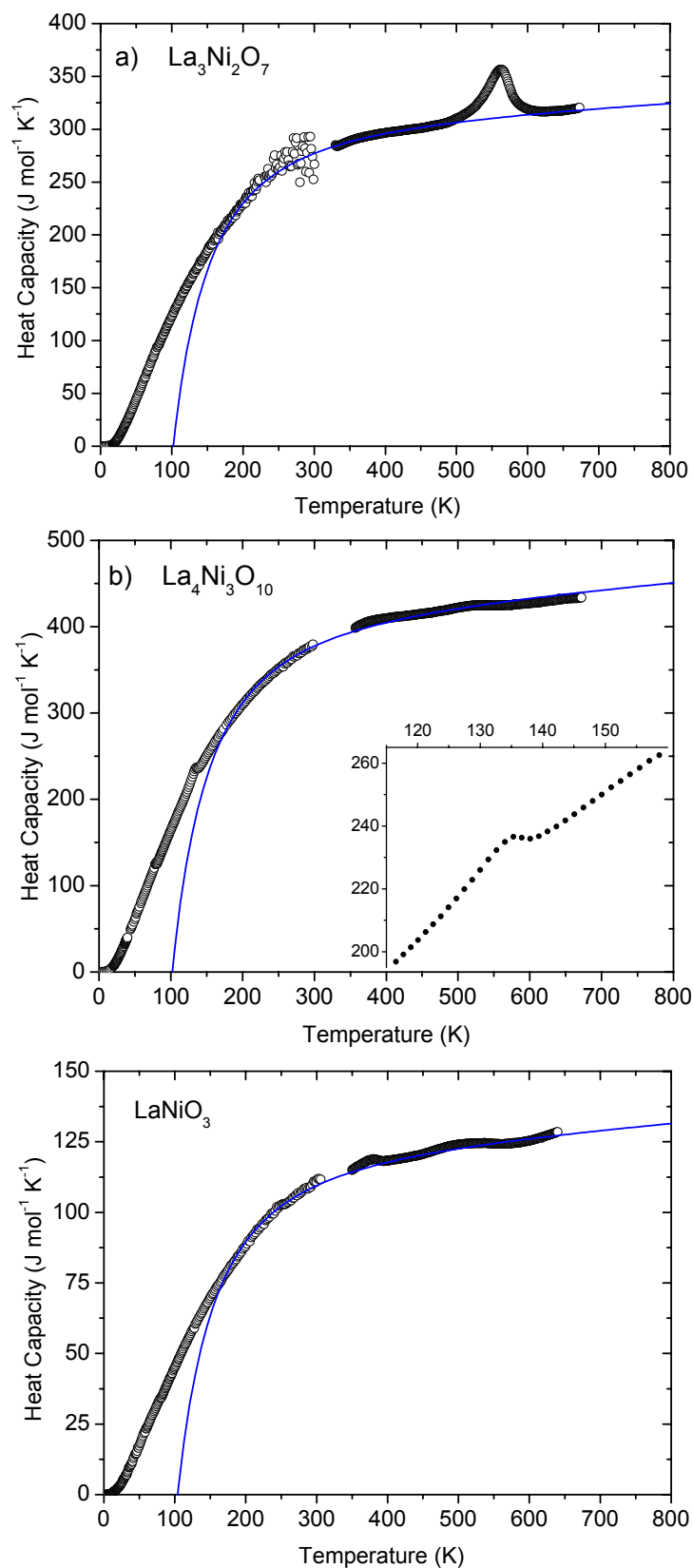


Fig. 3.17. The molar heat capacity of  $\text{La}_3\text{Ni}_2\text{O}_7$  (a),  $\text{La}_4\text{Ni}_3\text{O}_{10}$  (b), and  $\text{LaNiO}_3$  (c). The circles correspond to measured data, while the lines represent the results of polynomial-fitting to Eqn 2-5. The inset in Fig. 3.17b shows the temperature-dependent variation in the heat capacity of  $\text{La}_4\text{Ni}_3\text{O}_{10}$  between 115 and 160 K.

A second-order phase transition from the orthorhombic to tetragonal phase has been reported to occur in  $\text{La}_4\text{Ni}_3\text{O}_{10}$  at 985 K [91Lav], while Amow, *et al.* [06Amo2] had already observed it at temperatures as low as 758 K. Also,  $\text{LaNiO}_3$  is known to undergo a phase transformation into the cubic structure at 1213-1273 K, presumably also second order in nature [75Oba, 93Hof]. However, since no corresponding thermal effects were observed in the DSC curves (Fig. 3.14), these phase transitions have very little influence on thermodynamic properties and therefore, they were neglected in the present work.

The standard enthalpy of formation,  $\Delta_f H_{298}^\circ$ , the standard entropy,  $^\circ S_{298}$ , and the coefficient of heat capacity equations for all four RP-phases are listed in Table 3.2. The assessed enthalpy of formation of the compounds, as well as the entropy of  $\text{La}_2\text{NiO}_4$ , is very close to their experimental counterparts, whereas a systematic shift is evident for the results of Bannikov and coworkers [06Ban1]. The heat capacity of  $\text{La}_3\text{Ni}_2\text{O}_7$ ,  $\text{La}_4\text{Ni}_3\text{O}_{10}$ , and  $\text{LaNiO}_3$  calculated according to Eqn. 2.5 is shown as the solid lines in Fig. 3.17. The derived thermodynamic functions are clearly consistent with the experimental data.

Table 3.2. Assessed thermodynamic functions of the Ruddlesden-Popper phases in the La-Ni-O system, as compared with the literature information.

Compound	$\Delta_f H_{298}^\circ$ (kJ·mol <sup>-1</sup> )	$^\circ S_{298}$ (J·mol <sup>-1</sup> ·K <sup>-1</sup> )	$C_p$ (J·mol <sup>-1</sup> ·K <sup>-1</sup> )
$\text{La}_2\text{NiO}_4$	-2033.65 -2103.7 [06Ban1]	174.477 174.4 [97Kyo]	$178.04 + 0.014178 T - 2\,428\,380 T^{-2}$
$\text{La}_3\text{Ni}_2\text{O}_7^a$	-3256.86 -3333.6 [06Ban1]	267.729	$301.86 + 0.03424 T - 3\,160\,000 T^{-2}$
$\text{La}_4\text{Ni}_3\text{O}_{10}$	-4461.42 -4478.6 [91Yok] <sup>b</sup> -4552.4 [06Ban1]	389.428 390.0 [91Yok] <sup>b</sup>	$405.25 + 0.0652 T - 4\,260\,000 T^{-2}$
$\text{LaNiO}_3$	-1208.55 -1192.41 [05Che] -1236.0 [06Ban1]	107.949	$118.12 + 0.0192 T - 1\,296\,000 T^{-2}$

<sup>a</sup> Phase transition at 490 K,  $\Delta_{tr}H = 1800 \text{ J}\cdot\text{mol}^{-1}$ ,  $\Delta_{tr}S = 3.674 \text{ J}\cdot\text{mol}^{-1}\cdot\text{K}^{-1}$

<sup>b</sup> Predicted value.

Fig. 3.18 shows plots of the enthalpy of formation and entropy of  $\text{La}_{n+1}\text{Ni}_n\text{O}_{3n+1}$  compounds at 298.15 K, normalized to a basis of per mole of cations, *versus* the relative amount of perovskite structural units. It is interesting that the enthalpy of formation displayed a linear dependence (Fig. 3.18a), thus emphasizing the structural relationship of RP-phases. A similar

linear behavior, with a slightly different slope as well as the aforementioned shift, could be observed in the results of Bannikov and coworkers (Fig. 3.18a) [06Ban1]. The entropy decreased from  $\text{La}_2\text{NiO}_4$  to  $\text{LaNiO}_3$ , but showed a local minimum for  $\text{La}_3\text{Ni}_2\text{O}_7$  (Fig. 3.18b). The lower entropy of this compound may be associated with an unusually low thermal conductivity [07Sol] and the difficulties in preparing a phase-pure state [94Zha]. In general, the energetic trends displayed in Fig. 3.17 are consistent with decreasing thermal stability of  $\text{La}_{n+1}\text{Ni}_n\text{O}_{3n+1}$  compounds with increasing  $n$ .

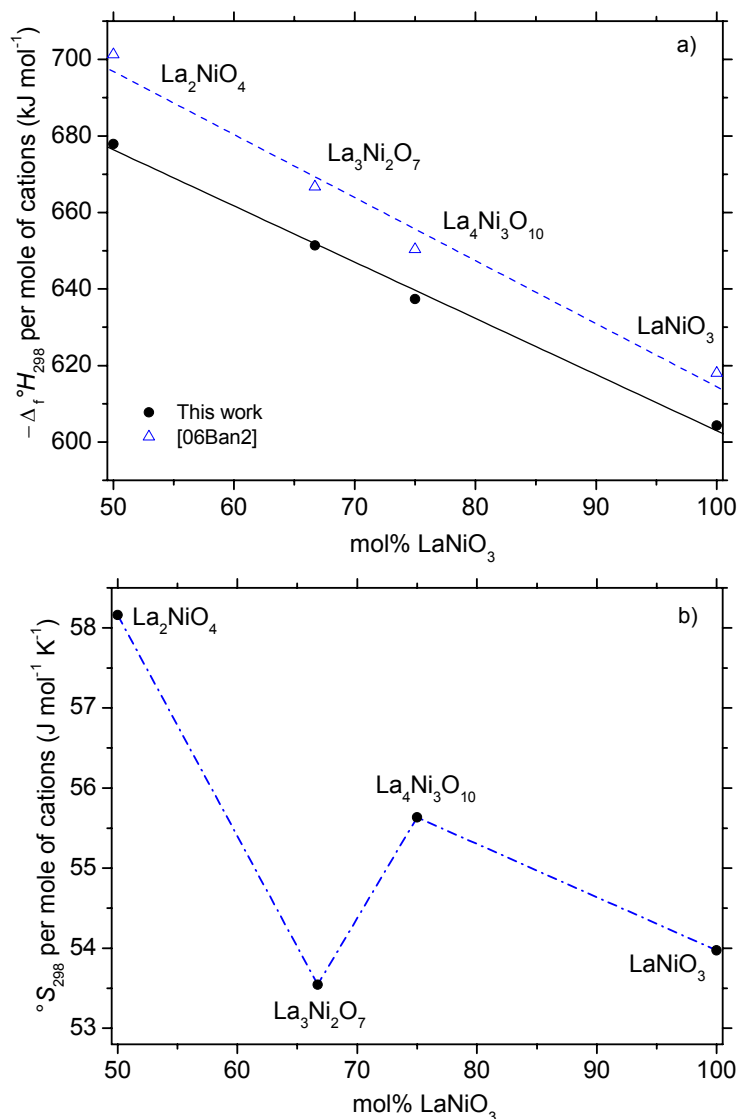
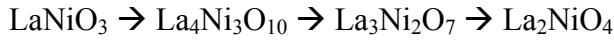


Fig. 3.18. The normalized enthalpy of formation (a) and entropy (b) of  $\text{La}_{n+1}\text{Ni}_n\text{O}_{3n+1}$  at 298.15 K versus fraction of perovskite building blocks in the structure. The solid and dashed lines in a are for the line-fit, while the dash-dotted line in b serves only as a visual guide.

Fig. 3.19 presents the calculated La-Ni-O phase stability diagram. The oxygen pressure in the gas phase is given on the vertical axis. Different symbols indicate which of the points were taken from dynamic experiments, which were obtained from isothermal ones in this study,



and which were culled from data in the literature. The results of the dynamic and isothermal experiments are in excellent agreement, which should be expected for a system in thermodynamic equilibrium. Each line corresponds to a four-phase equilibrium. It is also worth noting that the lines are slightly curved (due to the differences in the normalized heat capacities of RP-phases) and do not intersect, suggesting the following sequence of events during decomposition, with increasing temperature or decreasing oxygen pressure



as confirmed experimentally in the present work and in the literature. In general, a good agreement can be observed between the calculations and experimental data obtained in this work and those taken from the literature. Also, the calculated line for the four-phase equilibrium  $\text{La}_4\text{Ni}_3\text{O}_{10}$ ,  $\text{La}_3\text{Ni}_2\text{O}_7$ ,  $\text{NiO}$  and  $\text{O}_2$  is consistent with the stability boundary of  $\text{La}_4\text{Ni}_3\text{O}_{10}$ , as was determined in a recent EMF study [06Ban2], despite the authors' claim of a different decomposition mechanism, *i.e.*,  $\text{La}_4\text{Ni}_3\text{O}_{10} = 2\text{La}_2\text{NiO}_4 + \text{NiO} + 0.5\text{O}_2$  (Fig. 3.20).

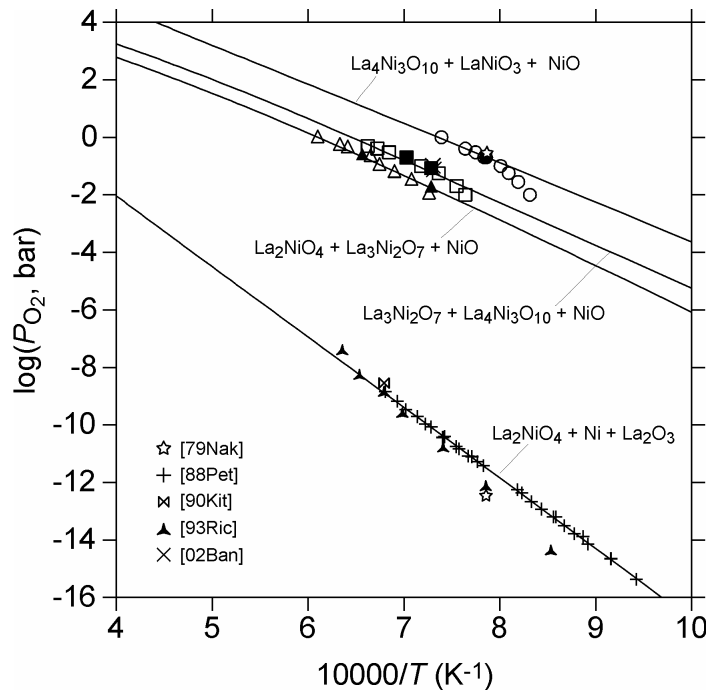


Fig. 3.19. The calculated La-Ni-O phase stability diagram in terms of temperature and gas phase oxygen pressure (which is always present in the system) compared with experimental data. Circles, squares, and triangles are results of this work (open symbols: dynamic experiments, filled symbols: isothermal experiments).

However, it should be noted that fitting all of the experimental points in Fig. 3.20 yielded the Gibbs energy equations, which could not be reconciled with experimental values for the entropy and enthalpy of formation. At low temperatures, the experimental points shift to lower oxygen pressures, relative to the lines. This may be due to the slower decomposition

kinetics or increasing uncertainty in mass spectrometric determination of oxygen content in the gas flow with decreasing oxygen partial pressure. Similar problems seemed to occur in the thermogravimetric studies of the reaction,  $\text{La}_2\text{NiO}_4 \rightarrow \text{La}_2\text{O}_3 + \text{Ni} + 0.5\text{O}_2$  [79Nak, 93Ric], since the corresponding points showed progressive deviations from the EMF data with decreasing temperature. In contrast, the results of a recent determination of the  $\text{La}_2\text{NiO}_4$  stability region, by the annealing and quenching method [06Dra], essentially confirmed the EMF data [88Pet].

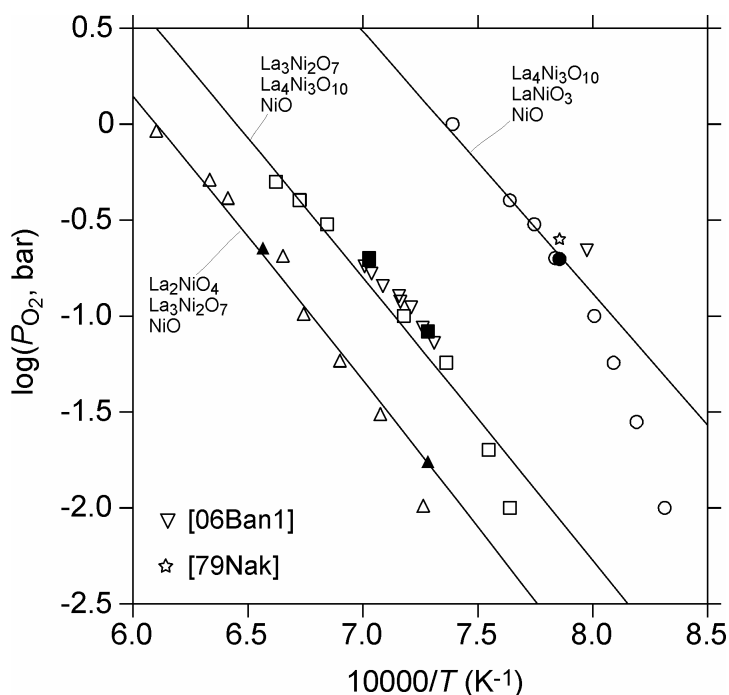


Fig. 3.20. An enlargement of the high oxygen pressure region of Fig. 3.19.

### 3.3.2. The Sr-Ni-O Subsystem

The *Sr-Ni-O* system has been experimentally studied first by Zinkevich [05Zin2], using high-temperature XRD, scanning electron microscopy and TG-DTA. In the SrO-NiO quasi-binary section, a eutectic reaction,  $\text{liquid} \rightleftharpoons \text{SrO} + \text{NiO}$ , was reported to occur at  $1396 \pm 5$  °C with negligible homogeneity range of both oxides. Three intermediate compounds,  $\text{SrNiO}_{2.5}$ ,  $\text{Sr}_5\text{Ni}_4\text{O}_{11}$  and  $\text{Sr}_9\text{Ni}_7\text{O}_{21}$ , were also reported. The latter was the only stable compound in air, decomposing at  $1030 \pm 6$  °C. During heating in air, the other compounds transformed to a mixture of  $\text{Sr}_9\text{Ni}_7\text{O}_{21}$  and NiO. The isobaric and isothermal sections of the SrO-NiO-O system were constructed [05Zin2]. In Fig. 3.21, the quasi-binary SrO-NiO section is shown. The liquidus part of it was calculated and combined with the experimental data on the decomposition of  $\text{Sr}_9\text{Ni}_7\text{O}_{21}$ .

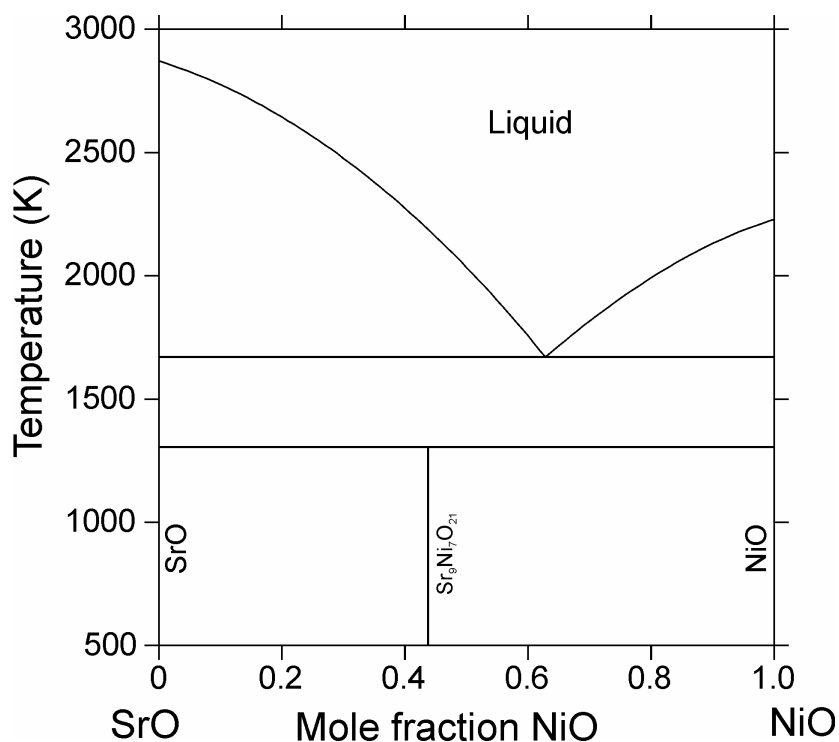


Fig. 3.21. The calculated SrO-NiO phase diagram.

### 3.3.3. The Ga-Ni-O Subsystem

The *Ga-Ni-O* system is very similar to the *Ga-Mg-O* system. Both the spinel and halite phases formed in these systems possess wide homogeneity ranges at high temperatures. The homogeneity range of the spinel phase extends largely beyond the stoichiometric composition,  $\text{NiGa}_2\text{O}_4$ , on both of the  $\text{Ga}_2\text{O}_3$ - and NiO-rich sides (27.1 and 58.4 mol% NiO at 1983 K). The Ga solubility in NiO is high (12.4 mol%  $\text{Ga}_2\text{O}_3$  at 1983 K), while no measurable solubility of Ni in  $\beta\text{-Ga}_2\text{O}_3$  has been observed. Thermodynamically and experimentally, the system has been investigated by Zinkevich as subsection of the work concerning the *Ga-Mg-Ni-O* system [05Zin1]. The calculated diagram is given in Fig. 3.22.

### 3.3.4. The Mg-Ni-O Subsystem

There is no ternary oxide in the *Mg-Ni-O* system, and the quasi-binary MgO-NiO system shows complete miscibility in both the liquid and the solid state [32War], which is characterized by ideal mixing behavior [05Zin]. Lattice parameter measurements of the solid solution showed a linear composition dependency (Vegard's law). The system was modeled thermodynamically [05Zin1], and a good agreement was found with the experimental data [32War]. The calculated MgO-NiO phase diagram is given in Fig. 3.23.

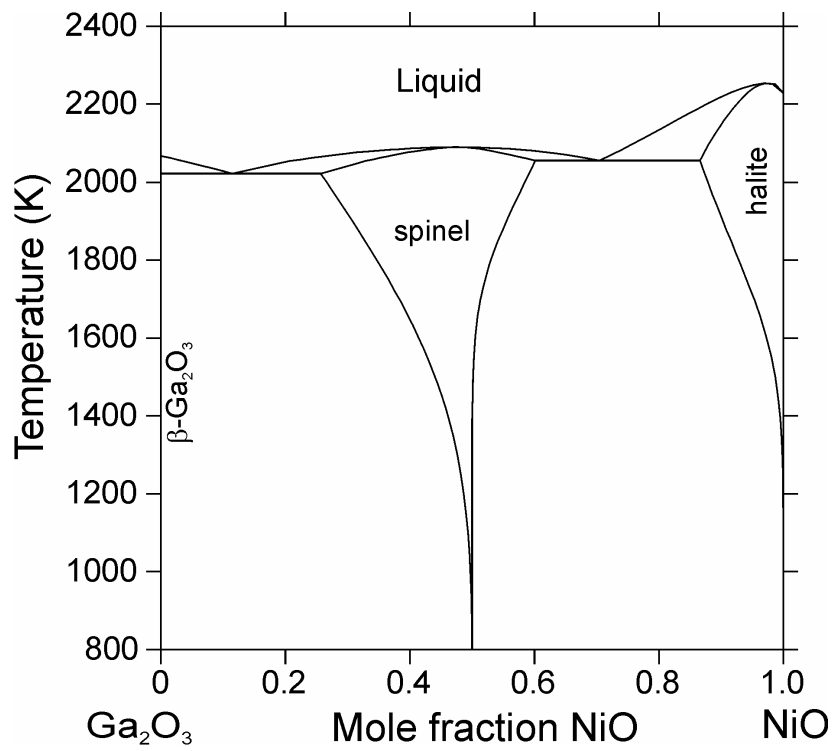


Fig. 3.22. The calculated Ga<sub>2</sub>O<sub>3</sub>-NiO phase diagram.

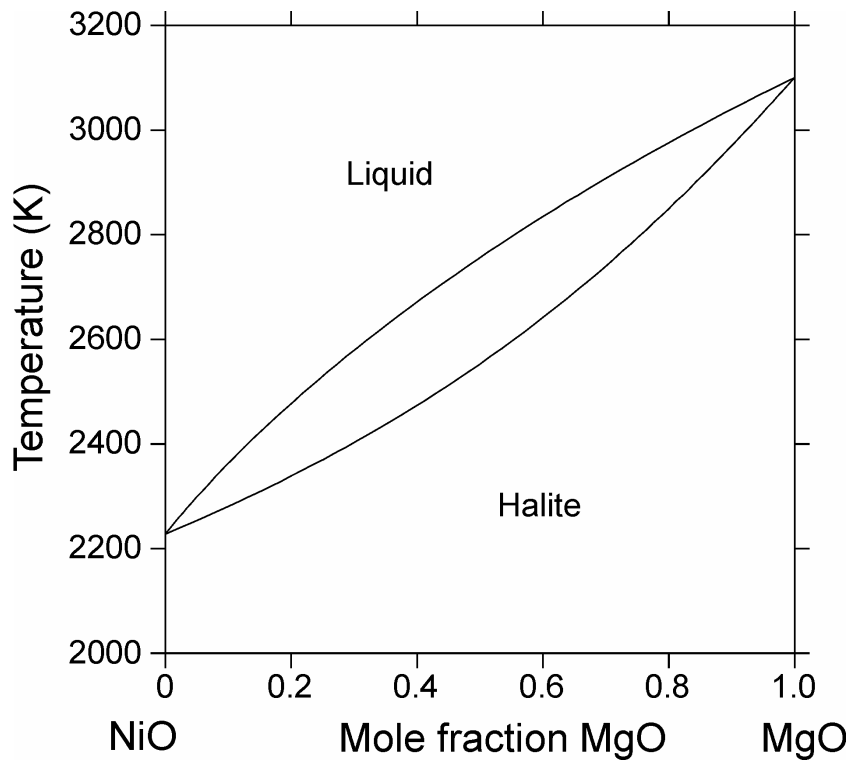


Fig. 3.23. The calculated MgO-NiO phase diagram.

### 3.3.5. The La-Sr-Ni-O Subsystem

Since the  $\text{La}_{2-x}\text{Sr}_x\text{NiO}_{4\pm\delta}$  (LSN) solid solution is structurally analogous to the superconducting phase  $(\text{La,Sr})_2\text{CuO}_4$ , it has been the focus of much intensive study, from the crystal chemistry [90Tak, 00Tan] and to the magnetic [90Tak, 91Cav, 92Fur] and the electrical properties [90Tak, 91Cav, 92Fur, 93Gra, 98Vas, 00Tan, 06Agu1, Agu2]. However, no superconductivity was found down to temperatures as low as 30 mK [90Tak, 91Cav]. Moreover, discontinuities in a number of thermochemical [93Dic, 98Hea] and physical properties [77Gop, 90Tak, 91Cav, 93Gra] have been reported to be correlated to compositional changes in the LSN solid solution.

The 1100 °C isothermal section of the phase diagram for the  $\text{LaO}_{1.5}\text{-SrO-NiO}$  system has recently been published by Bobina, *et al.* [04Bob]. There was a significant difference in the reported SrO solubility in the  $\text{La}_{2-x}\text{Sr}_x\text{NiO}_{4\pm\delta}$  solid solution,  $x = 0.8$ , which is the lowest value reported in the literature. In the comprehensive work of Takeda and co-workers [90Tak], the crystal chemistry of this solid solution was formulated, showing compelling experimental evidence that the solubility limit of SrO should be at  $x = 1.6$ , *i.e.*  $\text{La}_{0.4}\text{Sr}_{1.6}\text{NiO}_{4-\delta}$ . It has also been widely reported [88Nit, 91Cav, 99Man, 00Tan, 03Rez] that Sr substitution in the A-sublattice could reach up to 75%, *i.e.*,  $x = 1.5$ . These discrepancies may be due to the fact that for LSN compositions in which  $x > 1.0$ , sintering of the solid solution would become extremely difficult [90Tak, 91Cav]. In the work of Bobina and co-workers, the low SrO-containing samples, around the RP-phase, were prepared using the Pechini method [Pech]. For the synthesis of other compositions, the mixed oxide route was used. Although several intermittent grindings were applied, the calcination temperature was too low to allow thermodynamic equilibrium to be reached by using the mixed oxide route as reported in the literature [90Tak, 91Cav]. Therefore, it is thus quite likely that the unusually low solubility of  $x = 0.8$  [04Bob] was obtained due to processing challenges.

In the present study, the experimental work was intended to determine the homogeneity range of the  $\text{La}_{2-x}\text{Sr}_x\text{NiO}_4$  solid solution, using the Pechini-type soft chemistry (PSC) method. A sample, LSN13-53, having an overall composition of 13.33 mol %  $\text{LaO}_{1.5}$ , 53.33 mol % SrO and 33.33 mol % NiO that equals to  $x = 1.6$ , had been prepared. Heat-treatments were performed at 1100 and 1300 °C. XRD patterns of these samples are given in Fig. 3.24, showing that both samples consist of the three phases  $\text{La}_{2-x}\text{Sr}_x\text{NiO}_4$  solid solution, NiO and SrO. The peak positions are almost identical for the samples heat treated at 1100 and 1300 °C. It should be noted that during the XRD sample preparation, SrO reacted directly with ethanol

to form Sr hydroxides (with 2 and/or 8 mol crystal water), because of its hygroscopic character. In fact, samples that were prepared under dry conditions also reacted with the ambient humidity, forming hydroxides and more carbonates. The XRD pattern obtained in this study matched the card file generated by ICDD [ICDD], based on the data of Takeda and co-workers [90Tak], but with the additional presence of SrO (in the form of hydroxides) and NiO peaks.

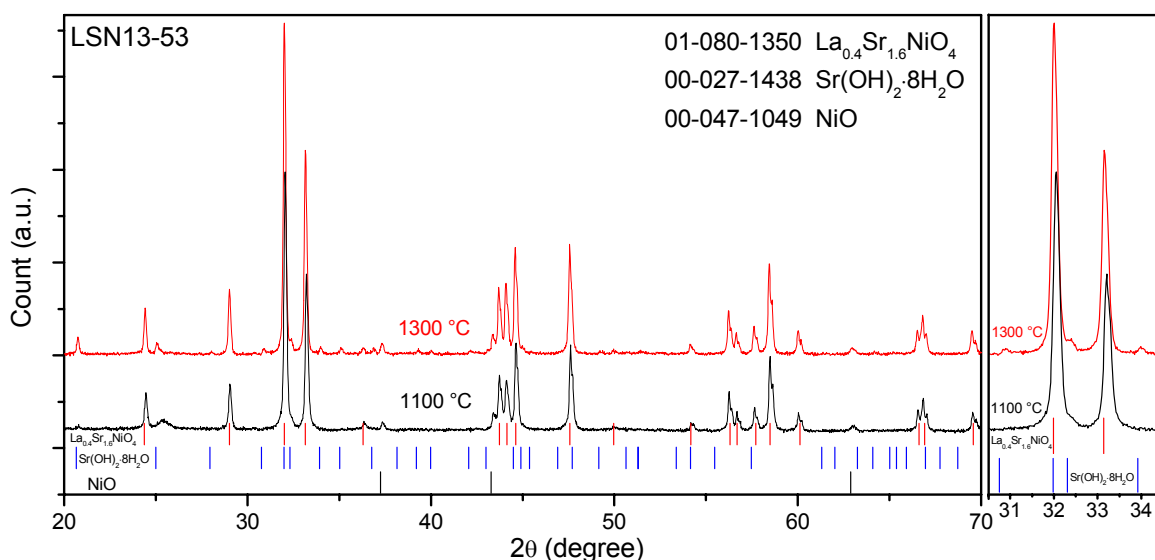


Fig. 3.24. XRD patterns of the LSN13-53 sample heat-treated at 1100 °C and 1300 °C. Vertical lines show the original positions of the peaks according to the ICDD database. Si was used as the internal standard to correct for systematic errors.

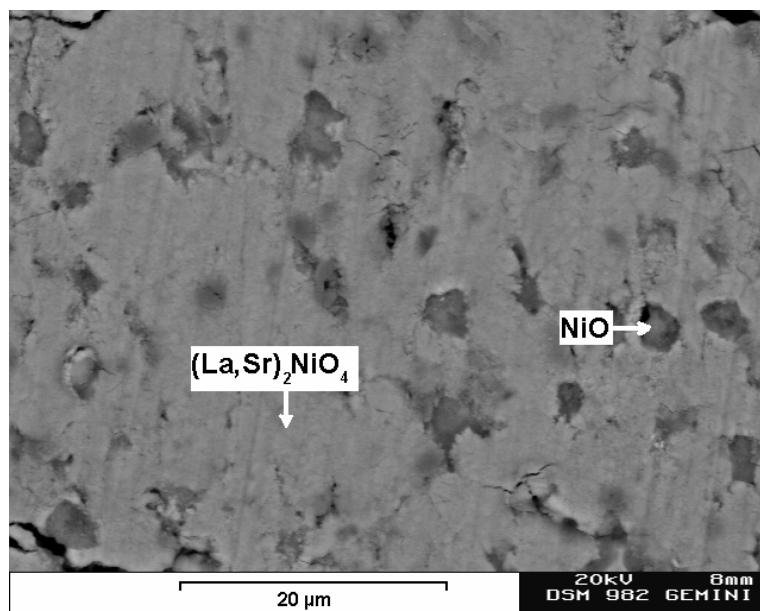


Fig. 3.25. SEM micrograph of the LSN13-53 sample heat-treated at 1300 °C.

The sample preparation for SEM-EDX analysis was challenging, due to the hygroscopic nature of SrO. To circumvent the problem, samples were quickly prepared immediately

following heat treatment and dry polished. In Fig. 3.25, an SEM micrograph is shown for the sample heat-treated at 1300 °C. Although the image quality is not high, the results were reproducible. The  $x$  values determined for  $\text{La}_{2-x}\text{Sr}_x\text{NiO}_4$  were around  $1.46 \pm 0.07$  and  $1.48 \pm 0.05$  for the samples heat-treated at 1100 °C and 1300 °C, respectively. The values are very close to 1.5, consistent with most of the literature data [88Nit, 91Cav, 99Man, 00Tan, 03Rez]. In fact, the work of Takeda, *et al* reported that the oxygen stoichiometry did not deviate from four in the solid solution up to  $x = 1.5$  (Fig. 3.26), a fact that is broadly supported in the literature [77Gop, 88Nit, 90Tak, 90Sre, 91Kat, 93Dic, 93Say, 98Hea, 99Man, 99Mil]. At that same composition, their work also showed that the average valence state of Ni reached a maximum value of +3.5. At values of  $x > 1.5$ , either the sub-stoichiometry of oxygen would be more pronounced or secondary phases would begin to appear. Moreover, the lattice parameters would reach constant values, indicating the existence of a multi-phase field.

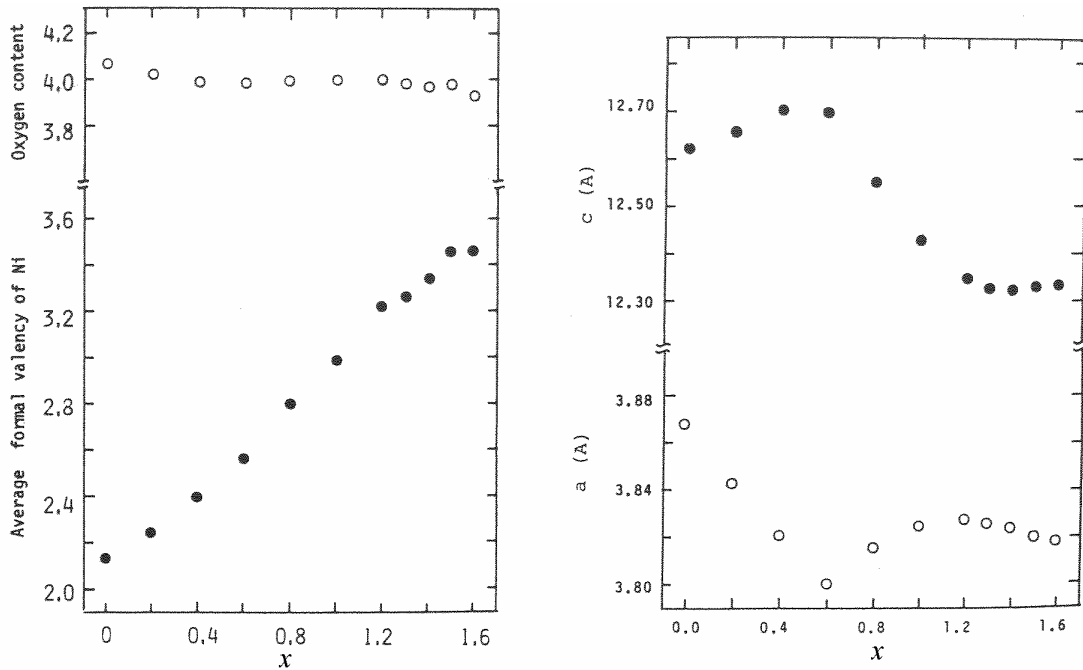


Fig. 3.26. Variation in oxygen content, average formal valence state of Ni, and lattice parameters changes in composition for the  $\text{La}_{2-x}\text{Sr}_x\text{NiO}_{4\pm\delta}$  solid solution as reported by Takeda *et. al* [90Tak].

Therefore, the solubility limit is established to lie at the  $\text{La}_{0.5}\text{Sr}_{1.5}\text{NiO}_4$  composition. Accordingly, the diagram was re-drawn in Fig. 3.27, maintaining the other parts as proposed by Bobina, *et al* [04Bob]. The homogeneity range of the  $\text{La}_{2-x}\text{Sr}_x\text{NiO}_4$  solid solution and respective tie-lines according to the later work are shown on the diagram by a circle and dashed lines, respectively.

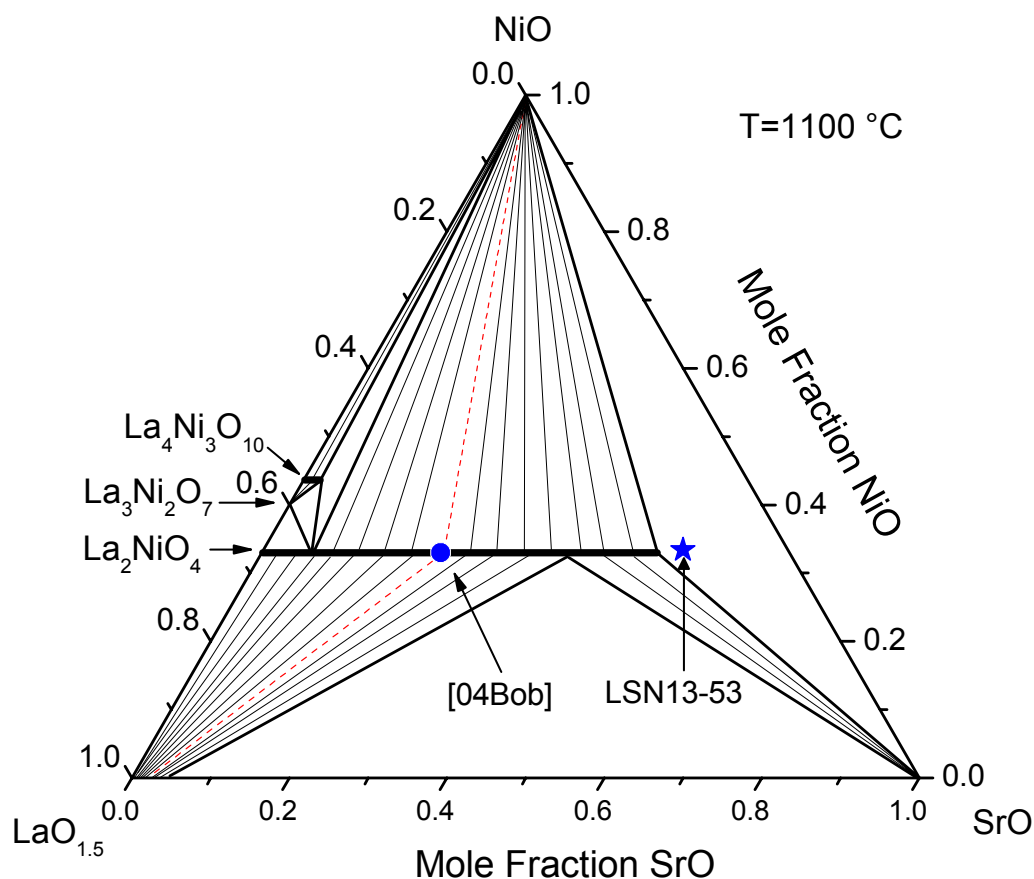


Fig. 3.27. The modified 1100 °C isothermal section of the phase diagram is presented for the  $\text{LaO}_{1.5}$ - $\text{SrO}$ - $\text{NiO}$  system in air. The star shows the sample prepared in the present study. The circle shows the solubility limit of the  $\text{La}_{2-x}\text{Sr}_x\text{NiO}_4$ , and the dashed lines show the phase boundary, both features as proposed by Bobina, *et al* [04Bob].

The effect of annealing temperature on the composition dependent phase separation of solid solution  $\text{La}_{2-x}\text{Sr}_x\text{NiO}_4$  reported in the literature [98Hea] was investigated by Millburn *et al.* [99Mil] and it was reported that the “multi-phasic” nature of the compound would be reduced for samples annealed above 1450 °C, suggesting that the cation inhomogeneity could be removed at high temperatures. Evidently, the sample preparation method and the sintering temperature have a strong influence of on the reported phase equilibria data. As explained above, meticulous care in synthesis in region of large  $x$  values would be necessary to obtain phase-pure samples. Obviously, phase separation takes place in high Sr-content samples at low temperatures, although, there is no reliable/reproducible data in the literature. Therefore, in the present work on the  $\text{La}_{2-x}\text{Sr}_x\text{NiO}_{4\pm\delta}$  solid solution, the no-phase-separation condition was not taken into account, and the calorimetric data reported by Dicarolo, *et al.* [93Dic] were not used.

The available thermodynamic data on the system is limited. Also, omitted from the optimization were the literature data on the low temperature heat capacity of  $\text{La}_{2-x}\text{Sr}_x\text{NiO}_4$  for



$0 \leq x \leq 0.65$  between 1.8 and 20 K [91Kat] and on the 200-290K heat capacity for the  $\text{La}_{1.67}\text{Sr}_{0.33}\text{NiO}_4$  composition [96Ram]. For the thermodynamic modeling, data on the subsystems and the phase equilibria were used, as well as the homogeneity range of  $\text{La}_{2-x}\text{Sr}_x\text{NiO}_4$  as determined in the present work. In addition, the measured enthalpy of formation was accepted for  $\text{LaSrNiO}_4$  as determined by Matskevich, *et al* [98Mat] by solution calorimetry (in concentrated nitric acid), on a sample prepared using soft chemical methods. All the other RP-phases were taken as pure stoichiometric compounds. This was justifiable on the basis that the SrO solubility is very low in  $\text{La}_{1-x}\text{Sr}_x\text{NiO}_3$  ( $x < 0.03$  [75Oba]),  $\text{La}_{4-x}\text{Sr}_x\text{Ni}_3\text{O}_{10}$  ( $x < 0.05$  [04Bob]) and  $\text{La}_{3-x}\text{Sr}_x\text{Ni}_2\text{O}_7$  ( $x \leq 0.075$  [94Zha] or  $x = 0$  [04Bob]). The parameters obtained in this work are presented in the Appendix, and the calculated 1100 and 1300 °C isothermal sections are shown in Fig. 3.28.

The 1100 °C isothermal section is in reasonable agreement with the experimentally determined diagram. The calculated two- and three-phase fields around the  $\text{La}_3\text{Ni}_2\text{O}_7$  and  $\text{La}_4\text{Ni}_3\text{O}_{10}$  compounds are slightly different, compared to those proposed by Bobina, *et al* [04Bob], since  $\text{La}_4\text{Ni}_3\text{O}_{10}$  was accepted as a stoichiometric ternary oxide. The homogeneity range of the  $(\text{La,Sr})_2\text{NiO}_4$  solid solution was reproduced with high consistency. The composition of the  $(\text{La,Sr})_2\text{NiO}_4$  solid solution in equilibrium with SrO and  $\text{LaO}_{1.5}$ , was calculated to be around  $\text{La}_{1.33}\text{Sr}_{0.67}\text{NiO}_4$  and to be almost temperature independent. Also, the  $\text{La}_4\text{Ni}_3\text{O}_{10}$  and  $\text{La}_3\text{Ni}_2\text{O}_7$  compounds are not stable in air at high temperatures, as known from the  $\text{La}_2\text{O}_3$ -NiO quasi-binary section. Instead, they decompose gradually and until a new equilibrium is established between  $\text{La}_2\text{NiO}_4$ , NiO and  $\text{O}_2$ . Therefore, the 1300 °C isothermal section contains only the  $(\text{La,Sr})_2\text{NiO}_4$  solid solution and equilibria with the respective constituent oxides  $\text{LaO}_{1.5}$ , SrO and NiO. At this temperature the SrO solubility in the  $(\text{La,Sr})_2\text{NiO}_4$  solid solution is slightly higher than that of 1100 °C isotherm.

In Fig. 3.29, the calculated SrO-dependent enthalpy of formation values are plotted together with the literature data. The obtained curve is almost linear and in fair agreement with the literature data. The experimentally determined value for the formation energy of  $\text{LaSrNiO}_4$  is -1738.4 kJ/mol [98Mat], and the calculated one -1737.81 kJ/mol. Theoretical estimations of the formation energy also revealed a linear trend in concentration dependence, whereas the absolute values were more negative than both the literature data and the theoretical value of the undoped  $\text{La}_2\text{NiO}_4$  as determined in the present work (chapter 3.3.1).

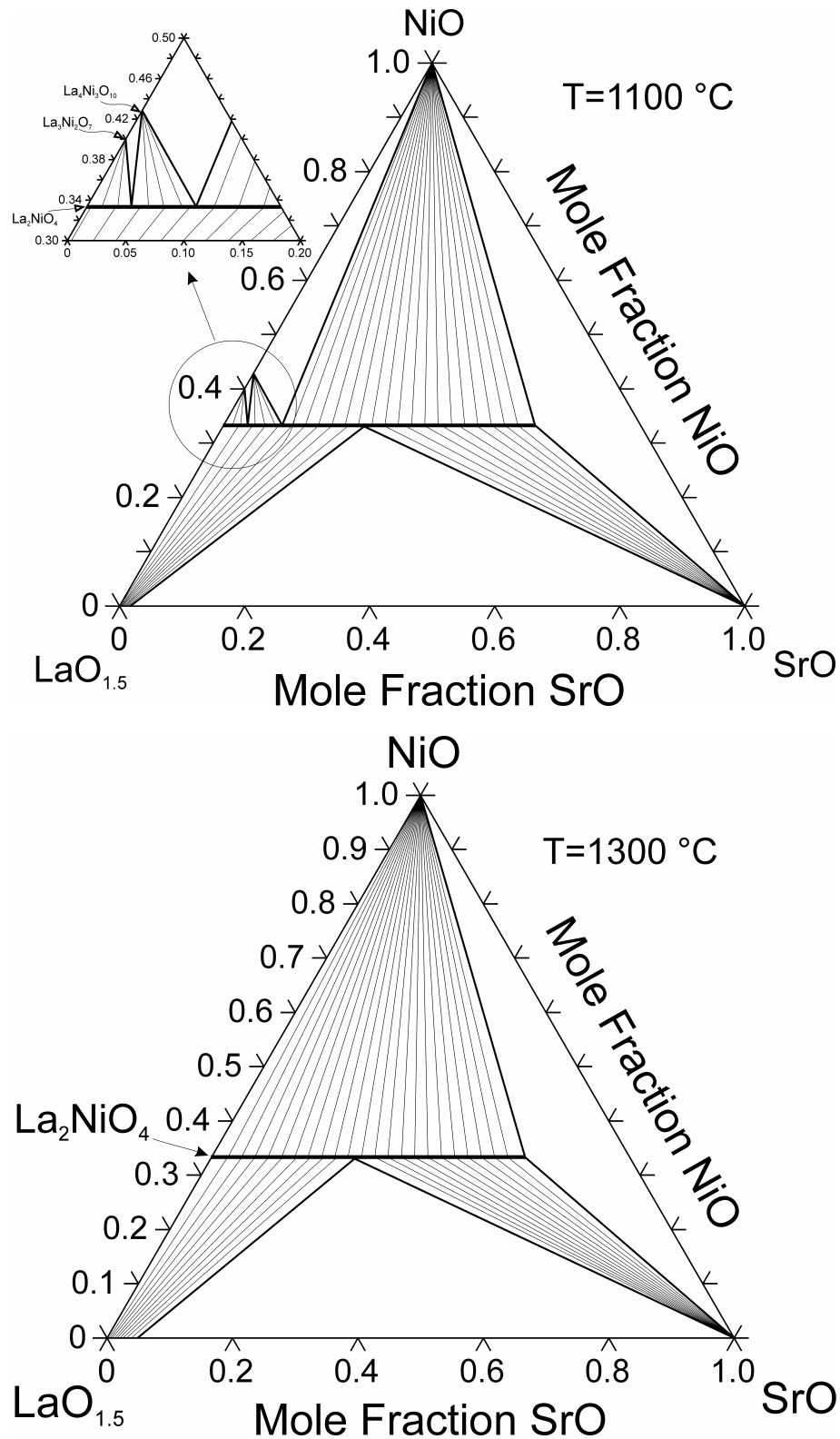


Fig. 3.28. Calculated 1100 °C and 1300 °C isothermal sections of the  $\text{LaO}_{1.5}$ - $\text{SrO}$ - $\text{NiO}$  phase diagram.

Fig. 3.30 shows the calculated chemical potential diagram of the  $\text{La}$ - $\text{Sr}$ - $\text{Ni}$ - $\text{O}$  system at 700 °C and  $P_{\text{O}_2} = 10^{-21}$  bar. From the diagram, it can be directly seen that at such a low oxygen partial pressure, the  $(\text{La},\text{Sr})_2\text{NiO}_4$  phase is still stable. According to the phase stability diagram of the

La-Ni-O system (Fig. 3.19) and information in the literature [06Sol], undoped  $\text{La}_2\text{NiO}_4$  is not stable in such a highly reducing environment, and the equilibrium phases are  $\text{La}_2\text{O}_3$ , Ni and  $\text{O}_2$ . However, the incorporation of SrO increased the stability of the  $(\text{La,Sr})_2\text{NiO}_4$  phase, and it became stable even at very low oxygen partial pressures. It should be pointed out here that, although  $(\text{La,Sr})_2\text{NiO}_4$  has only been considered thus far as a potential cathode material, because the solid solution is redox-stable and a good electrical conductor, it can be used as both cathode and anode material for SOFC applications.

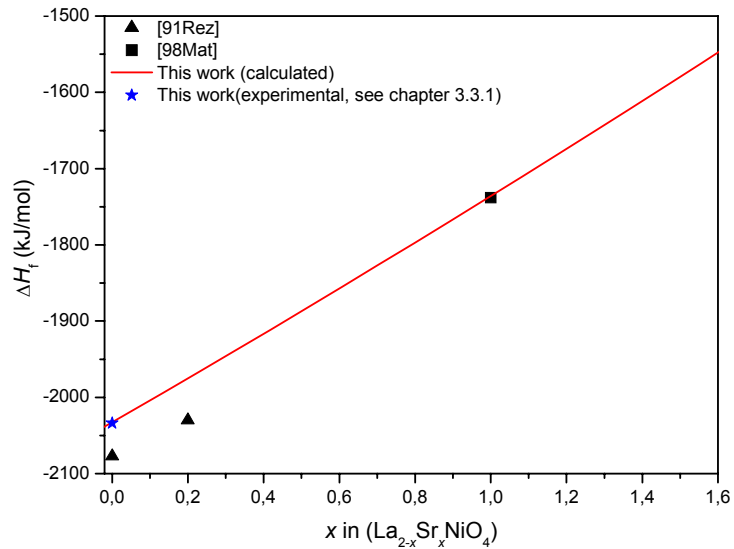


Fig. 3.29. Enthalpy of formation of  $(\text{La,Sr})_2\text{NiO}_4$  solid solution depending on SrO content.

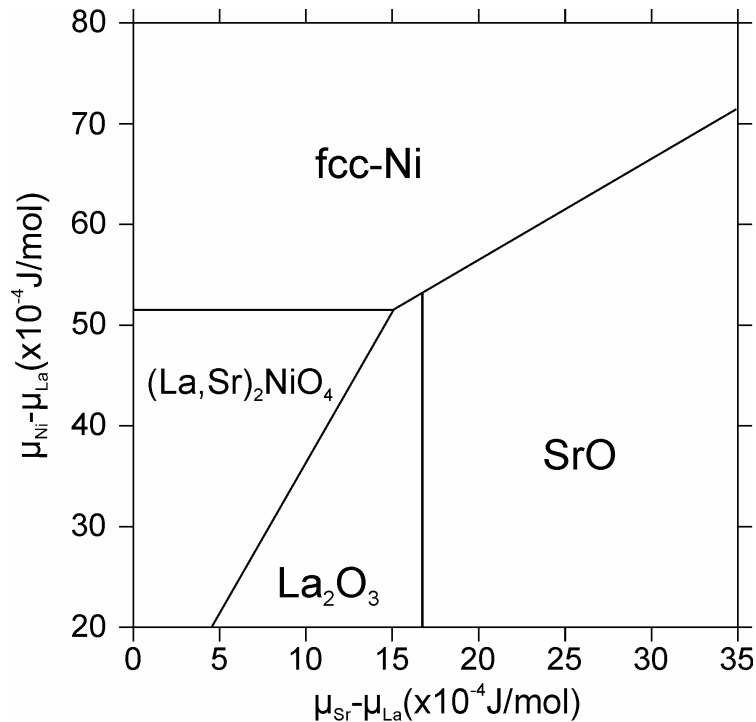


Fig. 3.30. Calculated chemical potential diagram of the La-Sr-Ni-O system at  $700^\circ\text{C}$  and  $P_{\text{O}_2}=10^{-21}$  bar.

### 3.3.6. The La-Ga-Ni-O subsystem

Subsolidus phase equilibria in the quaternary *La-Ga-Ni-O* system on the  $\text{La}_2\text{O}_3\text{-Ga}_2\text{O}_3\text{-NiO}$  quasi-ternary section were first investigated by Hrovat, *et al.* [99Hro].  $\text{La}_2\text{NiO}_4$  and  $\text{LaGaO}_3$  were reported to be in equilibrium, and the solid solubility between these compounds could be described by the formula  $\text{La}_2\text{Ga}_{2-x}\text{Ni}_{x/2}\text{O}_{6-x}$  ( $0 < x < 0.5$  on the  $\text{LaGaO}_3$  side and  $1.33 < x < 2$  on the  $\text{La}_2\text{NiO}_4$  side). Later, the system was modeled thermodynamically by Zinkevich, *et al.* [04Zin5], based on the assumption that no solid solubility existed between  $\text{LaGaO}_3$  and  $\text{La}_2\text{NiO}_4$  or the other compounds and that quaternary compounds did not form. As a result of the calculations, a tie-line between  $\text{NiO}$  and  $\text{La}_4\text{Ga}_2\text{O}_9$  was obtained, although Hrovat, *et al.* [99Hro] found that  $\text{La}_2\text{NiO}_4$  and  $\text{LaGaO}_3$  were in equilibrium. The corresponding data compiled from the literature and from selected experimental compositions (represented by stars) are shown on the diagram in Fig. 3.31. The inconsistency between the experimentally determined equilibrium [99Hro] and the calculations [04Zin5] is evident in the figure. The tie-line between  $\text{La}_2\text{NiO}_4$  and  $\text{LaGaO}_3$ , which was proposed by Hrovat, *et al.* [99Hro], is shown in dashed line, and the rest of the diagram is based on the calculations of Zinkevich, *et al.* [04Zin5]. Sample compositions along the proposed tie lines were selected in order to resolve this inconsistency.

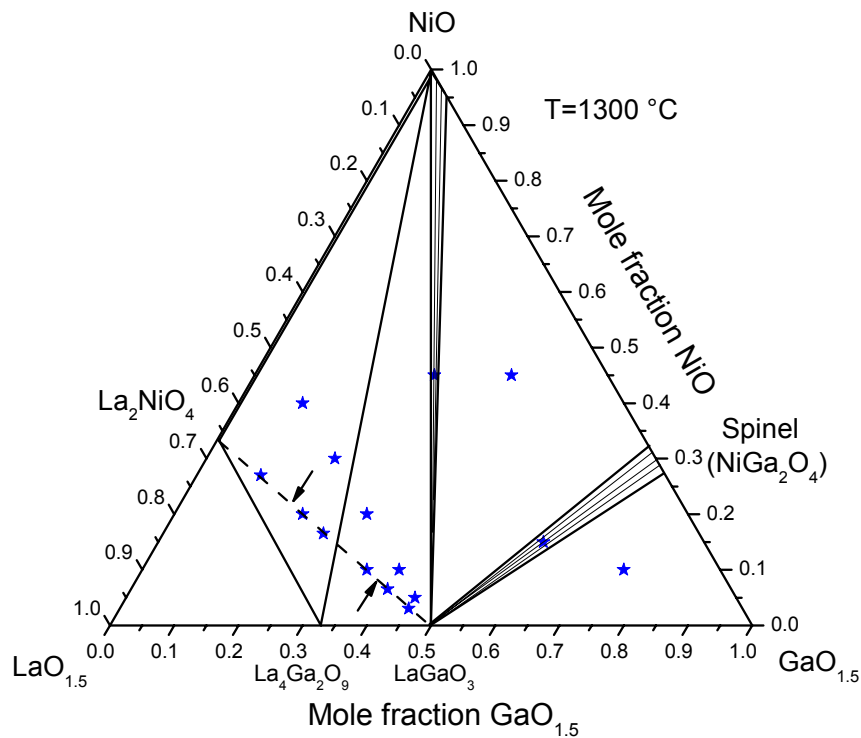


Fig. 3.31. Phase diagram of the system calculated (solid lines) by Zinkevich *et al.* [04Zin5]. The dashed line shows the experimentally determined equilibrium and arrows on it show homogeneity ranges determined by Hrovat, *et al.* [99Hro]. The stars represent experimental compositions selected for the present study.

Table 3.3 summarizes the XRD results obtained in this work. The  $\text{LaO}_{1.5}\text{-GaO}_{1.5}\text{-NiO}$  phase diagram, shown in Fig. 3.32, was determined experimentally from the XRD data and SEM-EDX results. The single phase regions, which correspond to extended solid solutions, are plotted in the graph as thick lines. The main differences in both the experimental data of Hrovat and the calculated phase diagram are wide solubility ranges of phases and stabilization of phases, which are unstable in lower-order systems at the experimental conditions, such as  $\text{La}_4\text{Ni}_3\text{O}_{10}$ , due to the formation of solid solutions. Both the calculated and experimental results are not in agreement with the experimental study of Hrovat and coworkers [99Hro]. As a result of the present study, it was observed that even after the second sintering, *i.e.*, after a total of 96 hours at 1300 °C, some reactions were still incomplete, particularly at the gallium-rich side of the system. XRD patterns after the first sintering showed mainly nickel gallium spinel ( $\text{NiGa}_2\text{O}_4$ ),  $\text{LaGaO}_3$ ,  $\text{Ga}_2\text{O}_3$  and an unidentified phase. After the second and third sintering, the  $\text{Ga}_2\text{O}_3$  peaks disappeared completely, and the unidentified peaks intensified. In the study of Hrovat and coworkers [99Hro], the samples were sintered for 20 h. Samples of similar compositions were considered to contain  $\text{Ga}_2\text{O}_3$ , in addition to spinel and  $\text{LaGaO}_3$ . The reason for the differences in the results could be attributed to such incomplete reactions.

Table 3.3. XRD results of the prepared samples, heat-treated at 1300 °C.

Sample	Equilibrium Phases
LGN27-28	NiO and LGO
LGN15-40	NiO, LGO and Spinel
LGN25-60	LGO and Spinel
LGN15-75	LGO, Spinel and $\text{LaNiGa}_{11}\text{O}_{19}$
LGN50-10	L4N3 and NiO
LGN50-20	LGR, L4N3 and NiO
LGN50-30	LGR
LGN50-40	LGR and LGO
LGN50-45	LGO
LGN63-10	L2N and L4N3
LGN60-20	L2N, L4N3 and $\text{La}_4\text{Ga}_2\text{O}_9$
LGN58.5-25	LGR, L4N3 and $\text{La}_4\text{Ga}_2\text{O}_9$
LGN55-35	LGO, L4N3 and $\text{La}_4\text{Ga}_2\text{O}_9$
LGN53.5-40	LGO and $\text{La}_4\text{Ga}_2\text{O}_9$
LGN52-45	LGO and $\text{La}_4\text{Ga}_2\text{O}_9$

L4N3:  $\text{La}_4(\text{Ni,Ga})_3\text{O}_{10}$ , L2N:  $\text{La}_2(\text{Ni,Ga})\text{O}_4$ , Spinel :  $\text{NiGa}_2\text{O}_4$   
LGR: Rhombohedral  $\text{La}(\text{Ga,Ni})\text{O}_3$ , LGO: Orthorhombic  $\text{La}(\text{Ga,Ni})\text{O}_3$ .

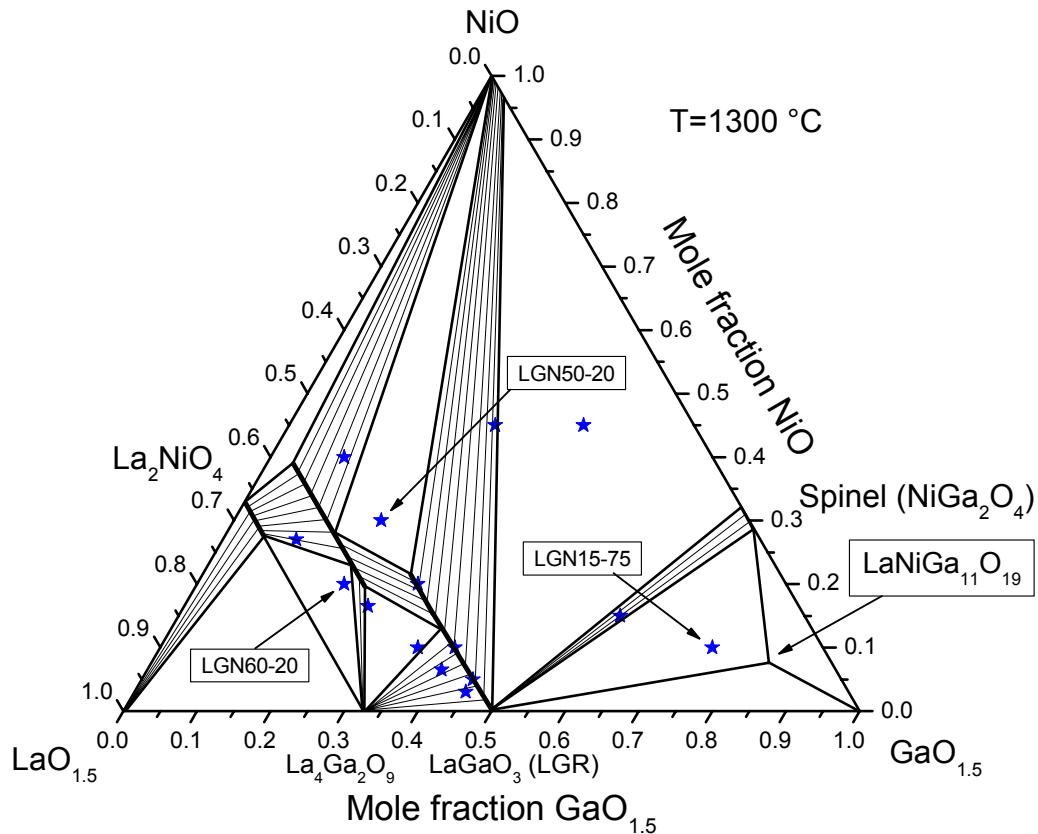


Fig. 3.32. The experimentally determined 1300 °C isothermal section is given for the  $\text{LaO}_{1.5}$ - $\text{GaO}_{1.5}$ -NiO phase diagram, in air. The stars represent the prepared samples.

As a result of the XRD analysis, the  $\text{LaGaO}_3$  phase was determined to be orthorhombic or rhombohedral, depending on the nickel content. In the literature, the polymorphic transition of the orthorhombic  $\text{LaGaO}_3$  to the rhombohedral form, which are abbreviated as LGO and LGR, respectively, had been reported to occur at  $\sim 148$  °C [04Zin4]. In the present study it was found that the transition temperature decreased with increasing nickel content. At room temperature the LGN50-45 sample had only the LGO structure, and the LGN50-30 sample had only the LGR structure, whereas the LGN50-40 sample showed reflections of both phases (see Fig. 3.33a). The peak shifts with respect to their original positions (vertical lines in the Fig. 3.33a) to higher angles have been determined, which is an indication of a NiO solubility in  $\text{LaGaO}_3$  in both LGR and LGO modifications. The effect of the NiO content on the LGO-LGR phase transition was investigated by DSC and curves obtained for the LGN50-45 and LGN50-40 samples are given in Fig. 3.33b. The LGN50-30 sample, which is the single phase LGR, in the entire composition range has the same DSC slope, and no transition peak was observed. However, an abrupt slope change on the DSC curve of LGN50-45 sample could be seen at  $\sim 100$  °C, and another slope change at  $\sim 140$  °C again, but this is more likely to be a transition peak. Almost at the same temperature, a transition peak on the DSC curve of the

LGN50-40 sample had been determined, which was the only peak determined in the whole composition range of the analysis. The DSC signals and the obtained phase information are combined in Fig. 3.33c, and a tentative phase diagram has been proposed. The slope changes here are interpreted as due to a transition from a single-phase field to a two-phase field and from a two-phase field to a single-phase field. In the latter case, the observed change had the shape of a broad peak, whereas in the former case, it was only a slope change, since the energy change was too small to be detectable with the technique used. A more detailed investigation is necessary to understand the mechanism. In the present study, only the LGR phase, which is the high temperature modification of  $\text{LaGaO}_3$ , has been used for the modeling and construction of the 1300 °C isothermal section.

On one hand, the Ni solubility of the  $\text{LaGaO}_3$  has been determined to be around 40 mol %  $\text{LaNiO}_3$ , using SEM-EDX analysis. On the other hand, it was found that the  $\text{La}_4\text{Ni}_3\text{O}_{10}$  phase could be stabilized by  $\text{Ga}^{3+}$ . In both cases, nickel was trivalent. In terms of electroneutrality  $\text{LaNiO}_3$  and  $\text{La}_4\text{Ni}_3\text{O}_{10}$  were represented by the formulas  $(\text{La}^{3+})_1(\text{Ni}^{3+})_1(\text{O}^{2-})_3$  and  $(\text{La}^{3+})_4(\text{Ni}^{2+})_1(\text{Ni}^{3+})_2(\text{O}^{2-})_{10}$ , respectively. The effective ionic radii of  $\text{Ni}^{3+}$  (Low Spin = 0.56 Å, High Spin = 0.60 Å) [69Sha] and  $\text{Ga}^{3+}$  (0.62 Å) [69Sha] are close enough, in order to form a substitutional solid solution. This also explains the observed peak-shift to higher  $2\theta$ -angles in Fig. 3.33a, owing to the smaller ionic radius of the  $\text{Ni}^{3+}$  ion.

The SEM image (a) and XRD pattern (b) of the LGN50-20 sample are given in Fig. 3.34. The original positions of the peaks are given at the bottom of the XRD pattern. Apparently the  $\text{LaGaO}_3$  peaks shifted to higher  $2\theta$  angles, while the  $\text{La}_4\text{Ni}_3\text{O}_{10}$  peaks shifted to lower  $2\theta$  angles, which would be expected from the difference in ionic radii. In contrast, no peak shift was observed with respect to the original position of the NiO peaks, and according to SEM-EDX analysis, pure NiO had been found.

Fig. 3.35 shows the SEM image (a) and XRD pattern (b) of LGN60-20 sample. Both SEM-EDX and XRD analysis showed that there is no solubility of NiO in the  $\text{La}_4\text{Ga}_2\text{O}_9$  phase, whereas both  $\text{La}_2\text{NiO}_4$  and  $\text{La}_4\text{Ni}_3\text{O}_{10}$  peaks shifted to lower  $2\theta$  angles with increasing content of  $\text{Ga}^{3+}$ , which has a larger ionic radius than  $\text{Ni}^{3+}$ . It can be seen clearly that, the  $\text{La}_2\text{NiO}_4$  phase is not stable when it is in contact with the LGR phase, since these two phases do not coexist in equilibrium. The  $\text{La}_2\text{NiO}_4$  phase is stable when it is in contact with  $\text{La}_4\text{Ga}_2\text{O}_9$  phase, whereas it reacts with LGR phase, producing an equilibrium phase mixture of  $\text{La}_4\text{Ni}_3\text{O}_{10}$  and  $\text{La}_4\text{Ga}_2\text{O}_9$  at the interface.

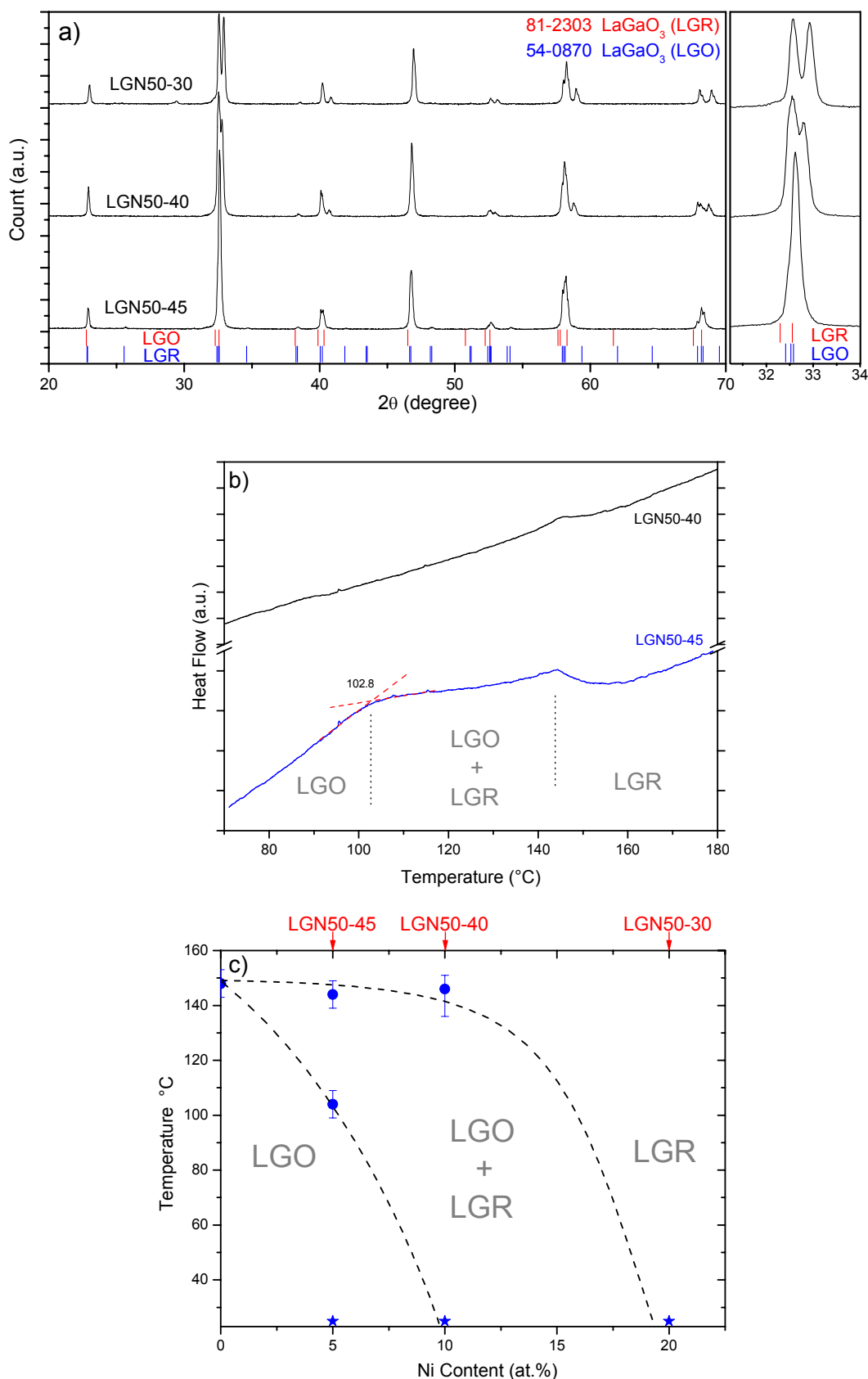


Fig. 3.33. XRD pattern of the samples from the single-phase  $\text{LaGaO}_3$  region; vertical lines represent original peak positions according to the ICDD database (a), results of the DSC measurements showing the LGO-LGR phase transition (b), a tentative phase diagram along the  $\text{LaGaO}_3$ - $\text{LaNiO}_3$  join (c), the stars show XRD data, while the circles show DSC results.



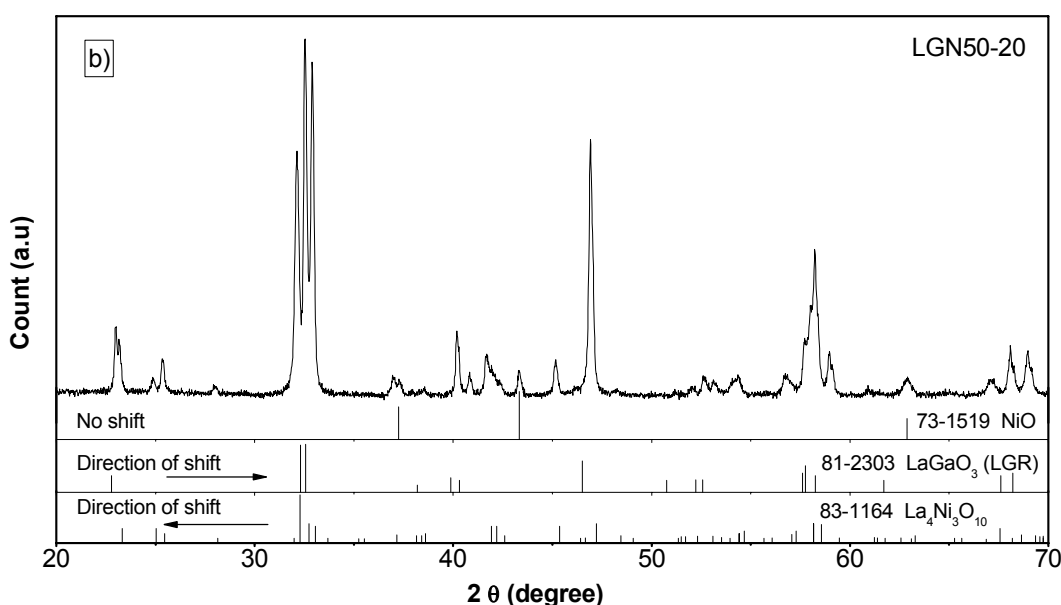
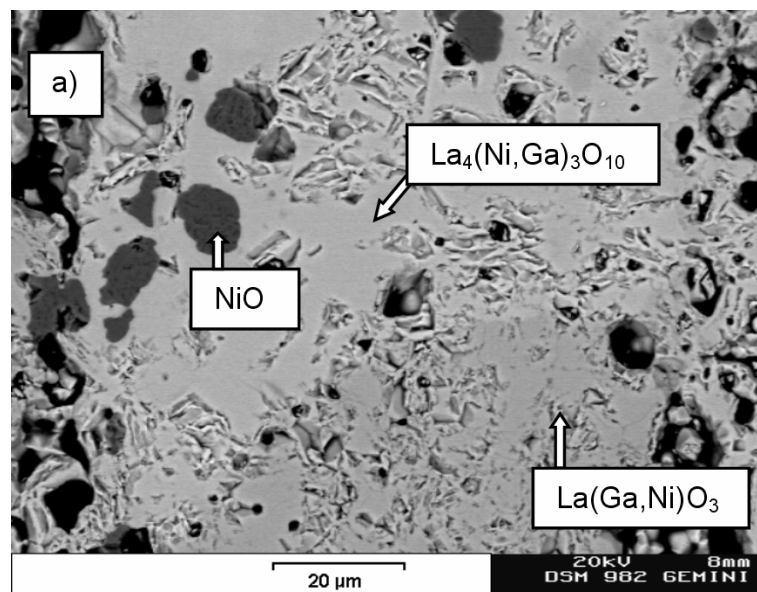


Fig. 3.34. SEM micrograph (a) and XRD pattern (b) of the LGN50-20 sample. Vertical lines show the original positions of the peaks according to the ICDD database [ICDD] and arrows show the direction of shift with respect to the original positions.

In the gallium-rich part of the diagram (LGN15-75), a new phase was found, according to SEM-EDX analysis of the microstructure, as shown in Fig. 3.36a. This new phase has a chemical composition, which is very close to that of  $\text{LaNiGa}_{11}\text{O}_{19}$ . The corresponding XRD patterns (Fig. 3.36-b) were evaluated by taking structural data for magnetoplumbite ( $\text{PbFe}_{12}\text{O}_{19}$  [89Moo]) into consideration and by assuming a peak shift due to the difference in lattice parameters. No information about the  $\text{LaNiGa}_{11}\text{O}_{19}$  phase is available in the literature. In this work it is found that this phase belongs to the space group  $P6_3/mmc$ , and the lattice parameters are  $a = 5.79 \text{ \AA}$ ,  $c = 22.61 \text{ \AA}$ .

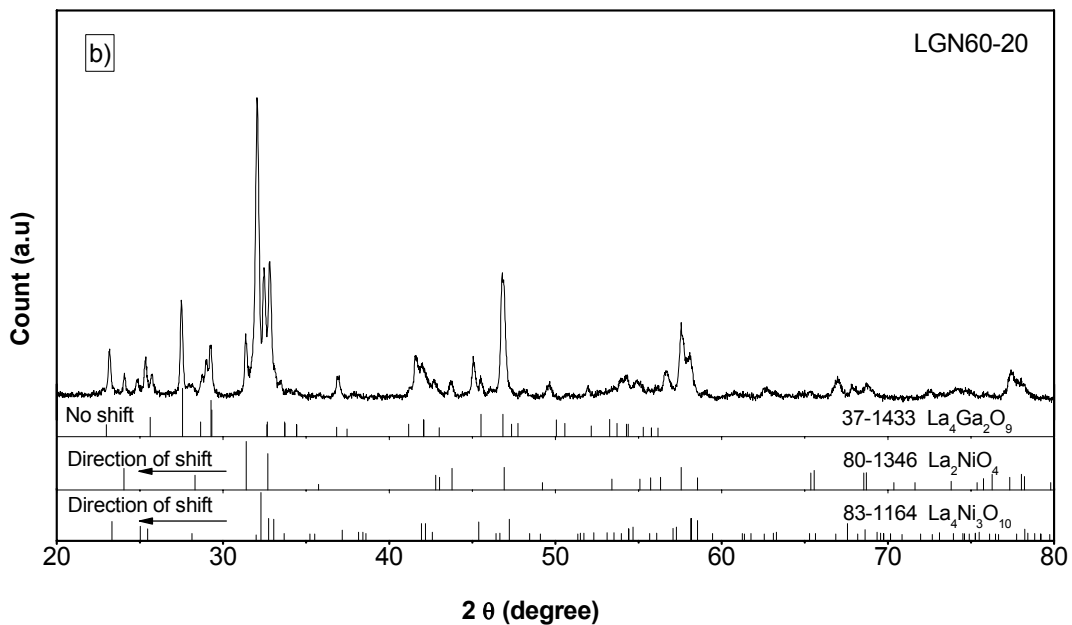
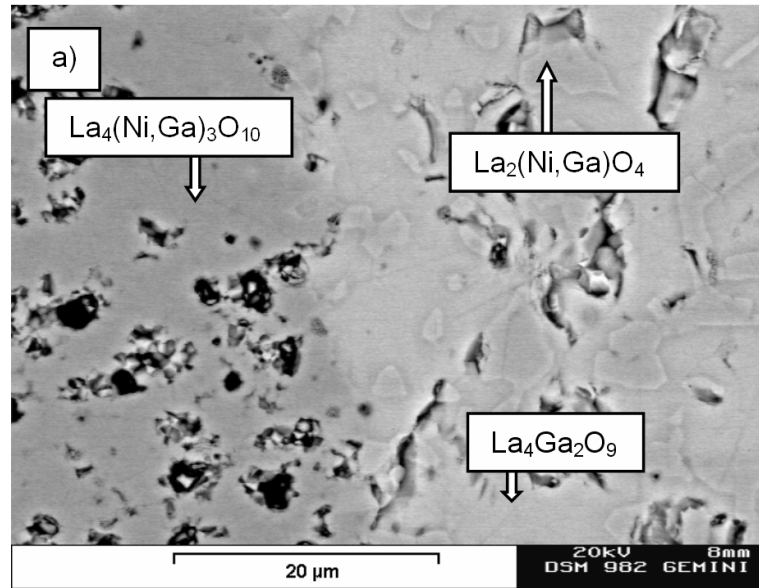


Fig. 3.35. SEM micrograph (a) and XRD pattern (b) of the LGN60-20 sample. Vertical lines show the original positions of the peaks according to the ICDD database [ICDD] and arrows show the direction of shift with respect to the original positions.

The system was modeled thermodynamically, based on only the phase equilibria data determined in this work, since there were no measured thermodynamics and reliable phase equilibria data in the literature. For the modeling, only the rhombohedral modification of  $\text{LaGaO}_3$  (LGR) has been taken into account. Since no Ni solubility in the  $\text{La}_4\text{Ga}_2\text{O}_9$  phase has been experimentally determined in this work, both modifications (LGM1 and LGM2) were taken as stoichiometric pure oxides. Similarly, there is no Ga solubility in  $\text{La}_3\text{Ni}_2\text{O}_7$  compound, and the description obtained in this work was used (section 3.3.1).

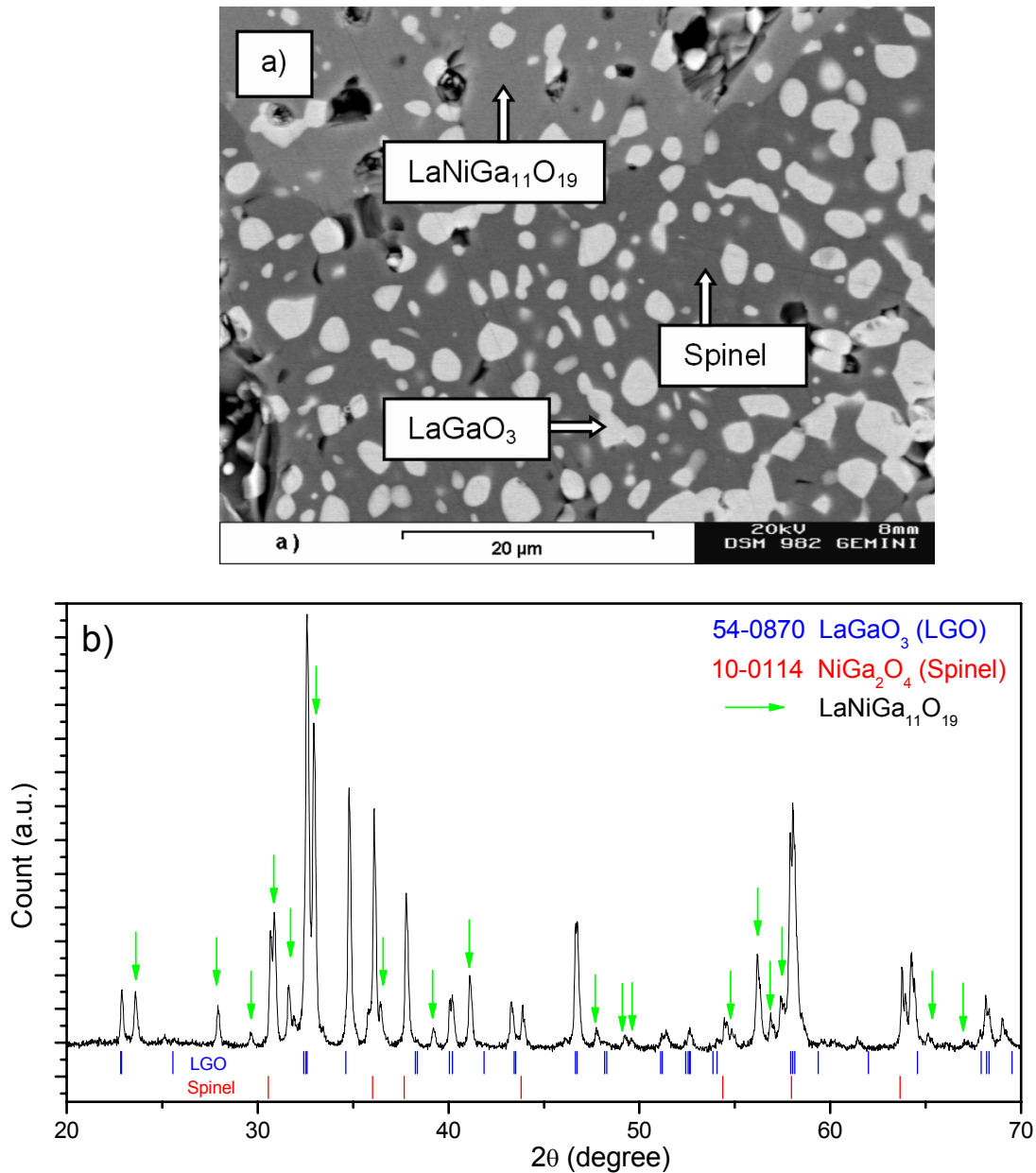


Fig. 3.36. SEM micrograph (a) and XRD pattern (b) of the LGN60-20 sample.

The compound  $\text{LaNiGa}_{11}\text{O}_{19}$ , which has a magnetoplumbite-type structure, has been modeled as a stoichiometric phase. The Gibbs energy of a mechanical mixture of the oxides was taken as a reference, and the optimization parameters were obtained using Gibbs energy functions for the other compounds in the three-phase fields. The parameters of  $\text{LaNiGa}_{11}\text{O}_{19}$  have the largest uncertainty compared to that of other phases, since available experimental thermodynamic data is scarce.

The obtained parameters are presented in the Appendix. Temperature dependent terms were not introduced, since the experiments were conducted at a temperature selected to correspond to the fabrication conditions of the SOFCs. The calculated isothermal section is shown for the  $\text{LaO}_{1.5}\text{-GaO}_{1.5}\text{-NiO}$  phase diagram at 1300 °C in Fig. 3.37. The diagram is in excellent

agreement with the experimentally determined one. All boundaries were reproduced well within the limits of error. As expected from the  $\text{La}_2\text{O}_3$ -NiO quasi-binary,  $\text{LaNiO}_3$ ,  $\text{La}_4\text{Ni}_3\text{O}_{10}$ , and  $\text{La}_3\text{Ni}_2\text{O}_7$  compounds are not stable at high temperatures. However,  $\text{La}_4\text{Ni}_3\text{O}_{10}$  could be stabilized by Ga, thus forming the  $\text{La}_4(\text{Ni,Ga})_3\text{O}_{10}$  solid solution (L4N3). Fig. 3.37 also presents the calculated 900 °C isothermal section of the system. A complete miscibility had been predicted between the two rhombohedral phases,  $\text{LaGaO}_3$  (LGR) and  $\text{LaNiO}_3$ , at temperatures low enough for  $\text{LaNiO}_3$  to be stable. The calculations show that the Ga-rich limit is almost the same at 900 and 1300 °C, for the homogeneity range of the  $\text{La}_4(\text{Ni,Ga})_3\text{O}_{10}$  solid solution (L4N3), which can be represented by the formula,  $\text{La}_4\text{Ni}_{1.6}\text{Ga}_{1.4}\text{O}_{10}$ . A temperature dependency could be expected for the homogeneity range, but it should also be taken into account that the  $\text{La}_4\text{Ni}_3\text{O}_{10}$  compound is not stable at high temperatures, and the stabilization of this phase is due to the  $\text{Ga}^{3+}$  ions. Thus, these two effects may compensate for each other, and such an expected temperature dependency is not seen in the calculation results.

Chemical potential diagrams were calculated for the La-Ga-Ni-O system at different temperatures and oxygen partial pressures and are shown in Fig. 3.38. The temperature and pressure parameters were chosen to simulated SOFC fabrication conditions, which are at 1300°C in ambient atmosphere. All stable phases in Fig. 3.37 can be seen on the chemical potential diagram, such as the L4N3 and L2N phases in the La-Ni-O system. The LGR phase is stable when in direct contact with  $\text{Ga}_2\text{O}_3$ ,  $\text{LaNiGa}_{11}\text{O}_{19}$ , spinel, and NiO. However, there is no direct contact between the  $\text{La}_2\text{O}_3/\text{La}_2\text{NiO}_4$  phase field and that of the LGR phase, which means that they cannot coexist in a stable equilibrium with each other, but instead would react to form  $\text{La}_4\text{Ga}_2\text{O}_9$  and/or L4N3.

Phase equilibria were also simulated for the operation conditions of the cathode side, *i.e.*, at 700°C and 1 bar of oxygen pressure, and are presented in Fig. 3.38b. It can be seen on the calculated diagram that the LGR phase exists continuously from  $\text{LaGaO}_3$  to  $\text{LaNiO}_3$  (see also Fig. 3.37), which means that there is a complete solubility in between these two compounds. At the given conditions, equilibrium between L4N3 and L2N was observed in the calculations, but it is not readily apparent on the diagram, since the L2N phase spans a very small area. No equilibrium was determined between the LGR and the L2N phases. Further reducing conditions were investigated in Fig. 3.38c and d, both at 700°C and an oxygen partial pressure of  $10^{-10}$  or  $10^{-21}$  bar, respectively. In Fig. 3.38c, the solid solution between  $\text{LaGaO}_3$  and  $\text{LaNiO}_3$  no longer exists, because the  $\text{LaNiO}_3$  compound is not stable under such a reducing environment. Again, under these conditions there is no direct contact between LGR and  $\text{La}_2\text{NiO}_4$ . Fig. 3.38d gives the results from simulating the anodic operation

conditions of the SOFC. It can be seen that, neither NiO and spinel, nor the ternary La-Ni-O phases, are stable. However, the LGR phase is stable in contact with Ni.

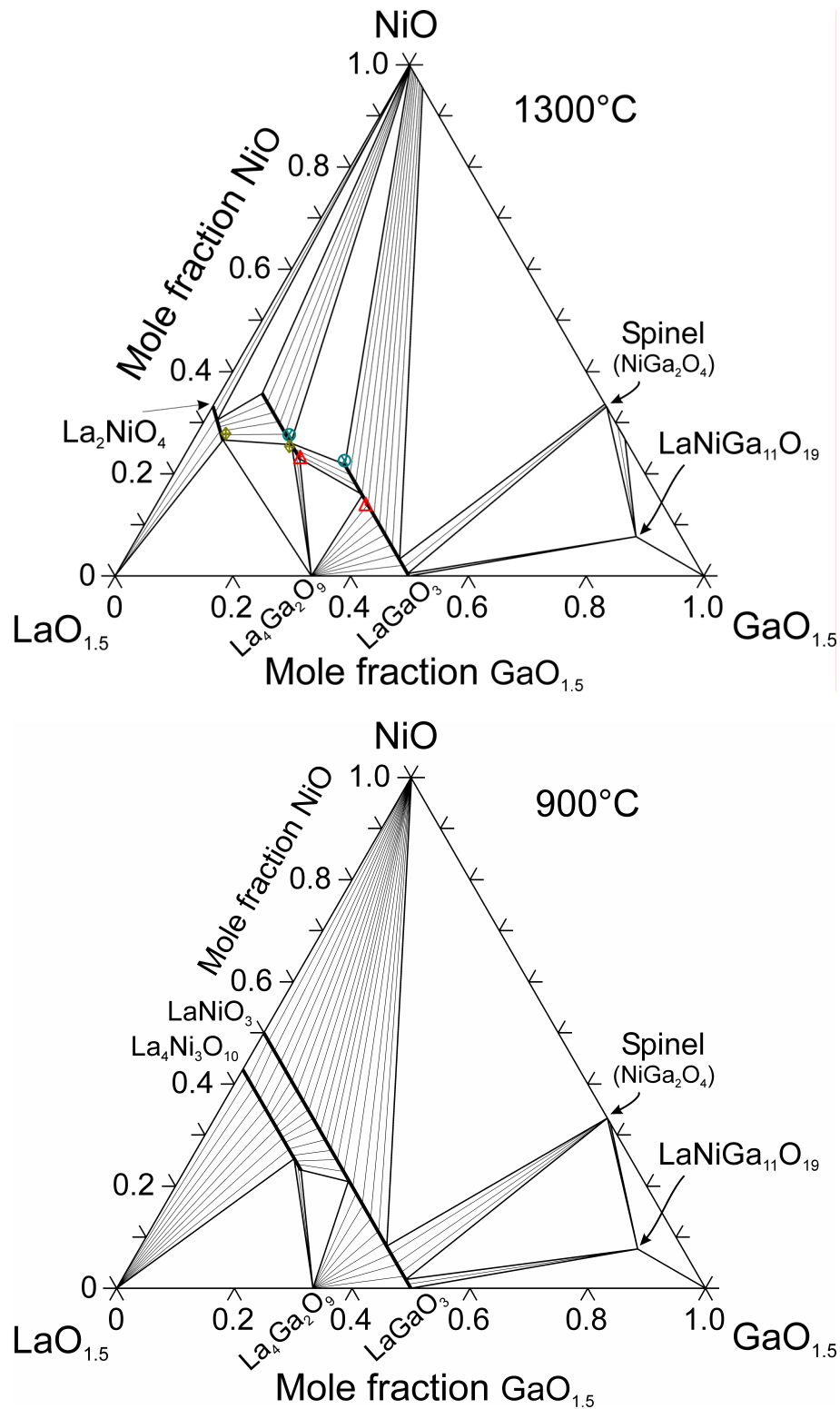


Fig. 3.37. The calculated 1300 and 900 °C isothermal phase diagram sections are shown for the  $\text{LaO}_{1.5}$ - $\text{GaO}_{1.5}$ - $\text{NiO}$  system in air. The symbol pairs show the experimentally determined boundaries of the three-phase fields.

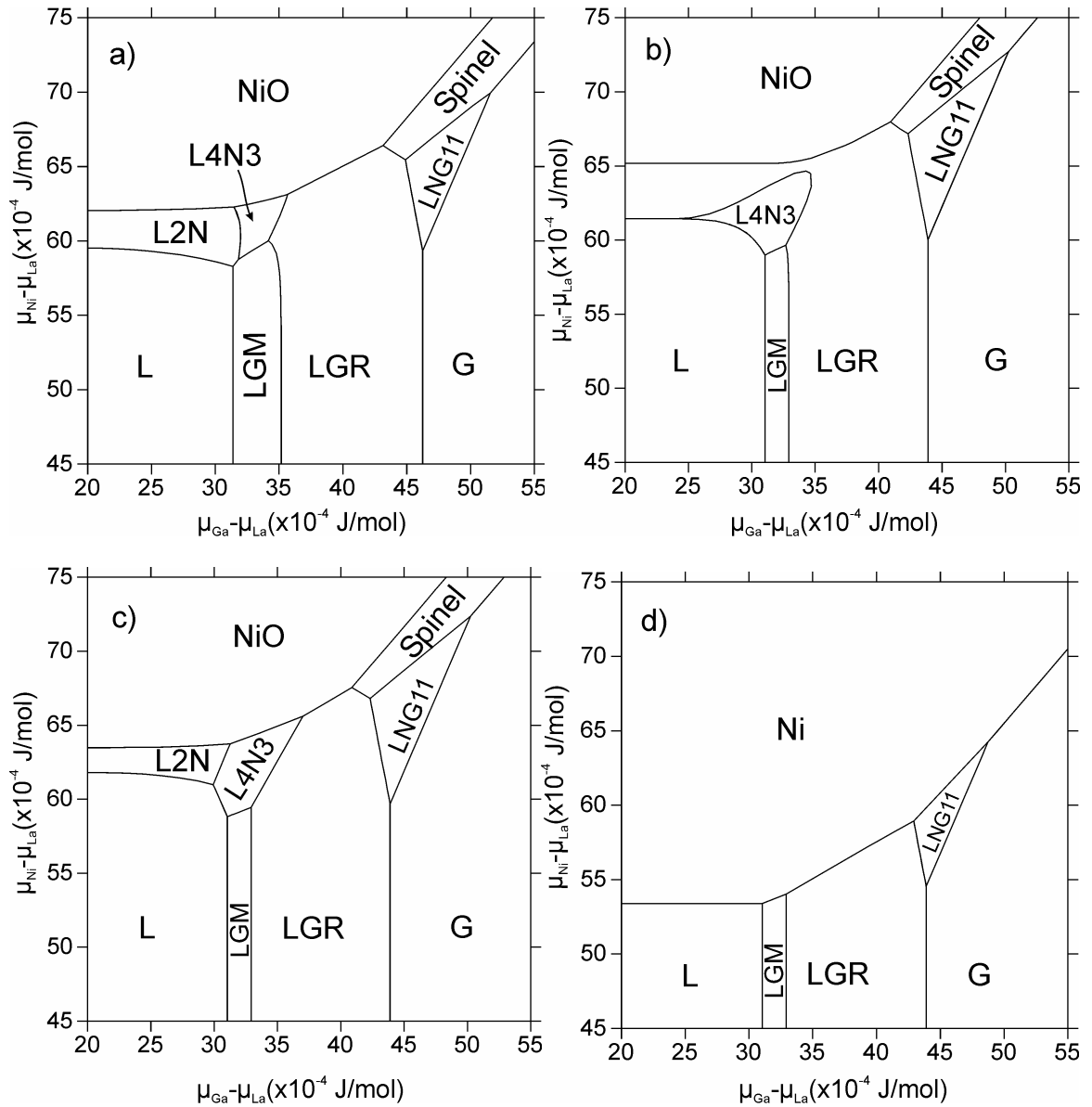


Fig. 3.38. Calculated chemical potential diagrams of the La-Ga-Ni-O system (a) SOFC fabrication conditions (1300 °C,  $P_{O_2} = 0.209$  bar), (b) cathodic operation conditions (700°C,  $P_{O_2} = 1$  bar), (c) reducing environments (700°C,  $P_{O_2} = 10^{-10}$  bar) and (d) highly reducing environments (anodic conditions) (700°C,  $P_{O_2} = 10^{-21}$  bar). The abbreviations used are the following: L:  $La_2O_3$ , G:  $Ga_2O_3$ , LGM:  $La_4Ga_2O_9$ , LGR:  $La(Ga,Ni)O_3$ , L4N3:  $La_4(Ni,Ga)_3O_{10}$ , L2N:  $La_2(Ni,Ga)O_4$ , LNG11:  $LaNiGa_{11}O_{19}$ .

### 3.3.7. The La-Mg-Ni-O Subsystem

Information in the literature is scarce for the *La-Mg-Ni-O* system. The synthesis, thermal stability and electrical properties were studied extensively by Vashuk *et al.* for the Mg-containing  $La_4Ni_3O_{10}$  compound [94Vas, 96Vas]. A solid solution was reported, surprisingly, in the form of  $La_{4-x}Mg_xNi_3O_y$ , where it was suggested that the  $Mg^{2+}$  ions substitute for the  $La^{3+}$  ions. From the crystallographic point of view, it could be expected that the  $Mg^{2+}$  ions preferentially substitute for the  $Ni^{2+}$  ion, instead of  $La^{3+}$  ions. The effective ionic radii of  $Ni^{2+}$

(0.70 Å) [69 Sha] and  $\text{Mg}^{2+}$  (0.72 Å) [69 Sha] are sufficiently close to form a substitutional solid solution, whereas  $\text{La}^{3+}$  ions are much larger (1.061 Å) [69 Sha]. In their earlier study [94Vas], the synthesis and electrical properties were investigated for the  $\text{La}_{4-x}\text{Mg}_x\text{Ni}_3\text{O}_y$  solid solution, and the solubility limit was reported to be  $x \leq 0.3$ . Above this value, a three-phase field exists for  $\text{La}_{3.7}\text{Mg}_{0.3}\text{Ni}_3\text{O}_y$ ,  $(\text{Mg},\text{Ni})\text{O}$  and  $\text{La}_2\text{NiO}_4$ . In the same work, it has also been reported that the  $\text{La}_{4-x}\text{Mg}_x\text{Ni}_3\text{O}_y$  solid solution has a metallic character, and its resistivity increased with increasing Mg content. In a later work [96Vas] the effect of divalent alkaline-earth cations was investigated for its impact on the thermal stability of  $\text{La}_4\text{Ni}_3\text{O}_{10}$ , and no improvement was found in the case of Mg. In both studies no MgO solubility in the  $\text{La}_2\text{NiO}_4$  phase was reported [94Vas, 96Vas], and no information was found, neither in these works nor in the literature, on MgO solubility in the  $\text{LaNiO}_3$  and  $\text{La}_3\text{Ni}_2\text{O}_7$  compounds. Based on these studies, and assuming the absence of quaternary compounds, a preliminary  $\text{LaO}_{1.5}\text{-NiO-MgO}$  phase diagram has been constructed and is given in Fig. 3.39. Although both  $\text{LaNiO}_3$  and  $\text{La}_3\text{Ni}_2\text{O}_7$  compounds are stable at the given temperature, they have not been included in the diagram, since the XRD patterns obtained by Vashuk, *et al.* [94Vas] do not contain these two phases. In the diagram, the stars indicate the experimental compositions selected in this work, which were specifically chosen around the ternary La-Ni-O compounds, close to the  $\text{LaO}_{1.5}\text{-NiO}$  quasi-binary section, in order to determine their homogeneity ranges and the orientation of the tie-lines. The expected direction of MgO solubility is shown on the figure by arrows.

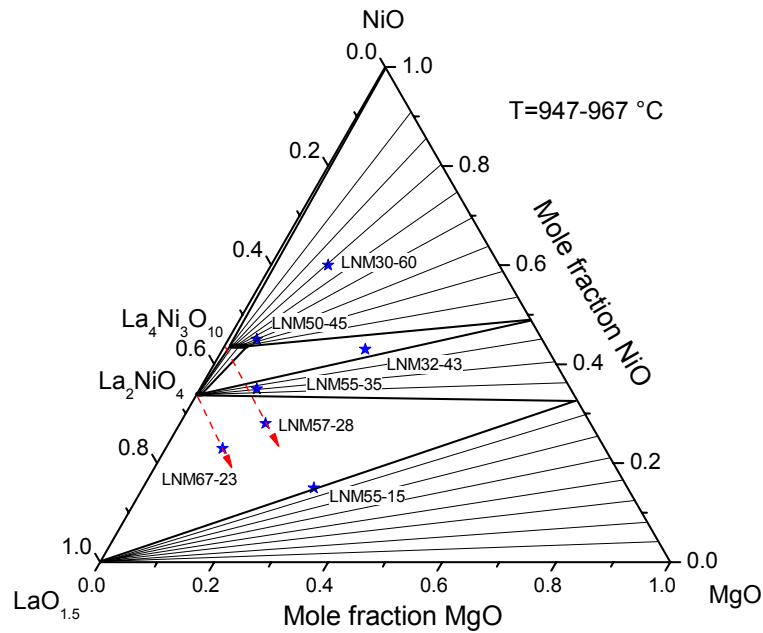


Fig. 3.39. A preliminary  $\text{LaO}_{1.5}\text{-NiO-MgO}$  phase diagram constructed according to the reported phase equilibria by Vashuk *et al.* [94Vas, 96Vas] and assuming the absence of any quaternary compound. The stars represent the selected experimental compositions evaluated in the present work. The arrows show the expected direction of solubility.

Table 3.4 XRD results of the samples heat-treated at 950, 1100 and 1300 °C.

Sample	Equilibrium Phases at 950 and 1100 °C	at 1300 °C
LNM30-60	$\text{La}_4\text{Ni}_3\text{O}_{10}$ , (Ni,Mg)O	$\text{La}_2(\text{Ni,Mg})\text{O}_4$ , (Ni,Mg)O
LNM50-45	$\text{La}_4\text{Ni}_3\text{O}_{10}$ , (Ni,Mg)O	$\text{La}_2(\text{Ni,Mg})\text{O}_4$ , (Ni,Mg)O
LNM32-43	$\text{La}_2(\text{Ni,Mg})\text{O}_4$ , $\text{La}_4\text{Ni}_3\text{O}_{10}$ , (Ni,Mg)O	$\text{La}_2(\text{Ni,Mg})\text{O}_4$ , (Ni,Mg)O
LNM55-35	$\text{La}_2(\text{Ni,Mg})\text{O}_4$ , $\text{La}_4\text{Ni}_3\text{O}_{10}$ , (Ni,Mg)O	$\text{La}_2(\text{Ni,Mg})\text{O}_4$ , (Ni,Mg)O
LNM57-28	$\text{La}_2(\text{Ni,Mg})\text{O}_4$ , (Ni,Mg)O	$\text{La}_2(\text{Ni,Mg})\text{O}_4$ , (Ni,Mg)O
LNM67-23	$\text{La}_2\text{O}_3$ , $\text{La}_2(\text{Ni,Mg})\text{O}_4$ , (Ni,Mg)O	$\text{La}_2(\text{Ni,Mg})\text{O}_4$
LNM55-15	$\text{La}_2\text{O}_3$ , $\text{La}_2(\text{Ni,Mg})\text{O}_4$ , (Ni,Mg)O	$\text{La}_2\text{O}_3$ , $\text{La}_2(\text{Ni,Mg})\text{O}_4$ , (Ni,Mg)O

The samples were heat-treated at various temperatures from 850 to 1300 °C, and the XRD results are summarized in Table 3.4 for the 950, 1100 and 1300 °C samples. In general, the picture of phase equilibria at 950 °C is consistent with results in the literature [94Vas, 96Vas]. However, careful analysis of the results and combinations of the results obtained from the samples heat-treated at higher temperatures reveal that the proposed substitution in the first sublattice is definitely not possible. In Fig. 3.40, XRD patterns of the LMN67-23 sample are given, which reveal that at 1300 °C, the sample is phase-pure  $\text{La}_2\text{NiO}_4$  and that at 950 °C, it contains lanthanum oxide/hydroxide and very small peaks of (Mg,Ni)O solid solution in addition. In contrast, at 1100 °C, the sample spectra show an additional, very small  $\text{La}_2\text{O}_3$  peak, indicated by arrow in the figure. Evidently there is a clear temperature dependence of the MgO solubility in the  $\text{La}_2(\text{Ni}_{1-x}\text{Mg}_x)\text{O}_4$  solid solution. Since the secondary peaks in the sample heat-treated at 1100 °C are very small, the maximum MgO solubility can be taken as 10 mol% MgO and can be represented in the form of  $\text{La}_2(\text{Ni}_{0.7}\text{Mg}_{0.3})\text{O}_4$ .

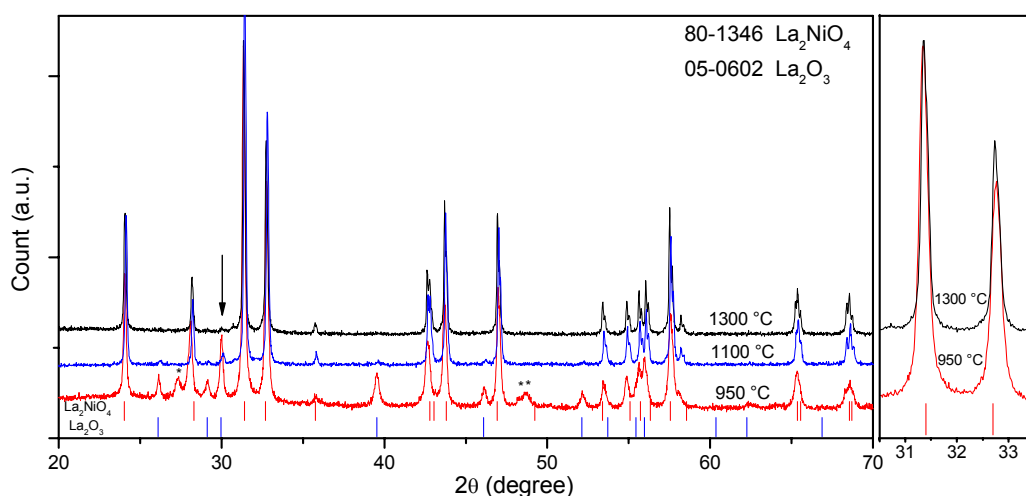


Fig. 3.40. XRD patterns of the LMN67-23 sample heat-treated at 950, 1100 and 1300 °C. Stars show  $\text{La}(\text{OH})_3$  peak positions, arrow shows the small  $\text{La}_2\text{O}_3$  peak found on the 1100 °C pattern. NiO peaks are not indicated since they are too small to detect.



Probably this solid solution could not be determined by Vashuk, *et al.* [94Vas, 96Vas], since all the compositions of the samples investigated were aligned along the direction where theoretically substitution should occur in the A-sublattice. Although the LMN67-23 sample investigated here contained 10 mol % MgO, almost no shift was observed in the  $\text{La}_2\text{NiO}_4$  peaks with respect to their positions in the pure material (Fig. 3.40). This is another indication of the substitution of  $\text{Ni}^{2+}$  ions by  $\text{Mg}^{2+}$  both have very similar ionic radii [69Sha]. If the substitution takes place in the  $\text{La}^{3+}$  site-sublattice, a more pronounced shift would be expected owing to the much smaller ionic radius. SEM-EDX analysis was performed on a LMN55-15 sample, in order to determine the MgO solubility limit in the  $\text{La}_2(\text{Ni}_{1-x}\text{Mg}_x)\text{O}_4$  solid solution. The associated SEM image and the XRD patterns are shown in Fig. 3.41 and Fig. 3.42, respectively.

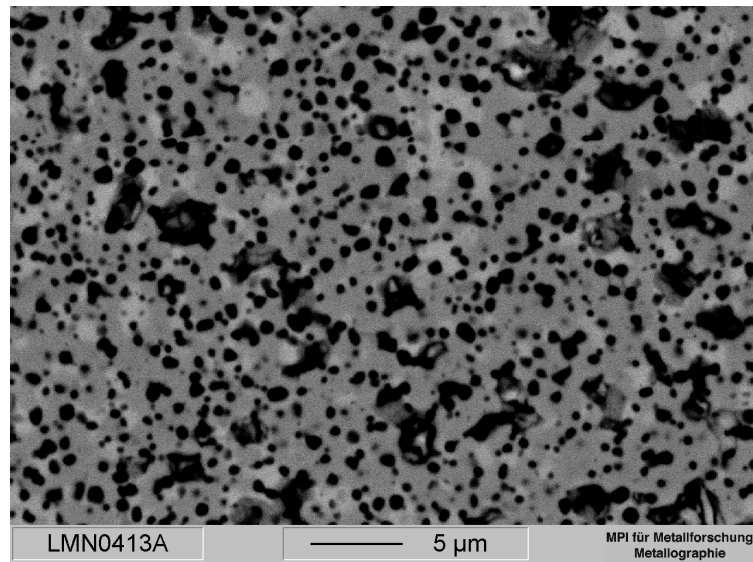


Fig. 3.41. SEM micrograph of the LMN55-15 sample heat-treated at 1300 °C. The bright areas are  $(\text{Ni,Mg})\text{O}$ , grey areas are  $\text{La}_2(\text{Ni,Mg})\text{O}_4$ , and the black spots are voids.

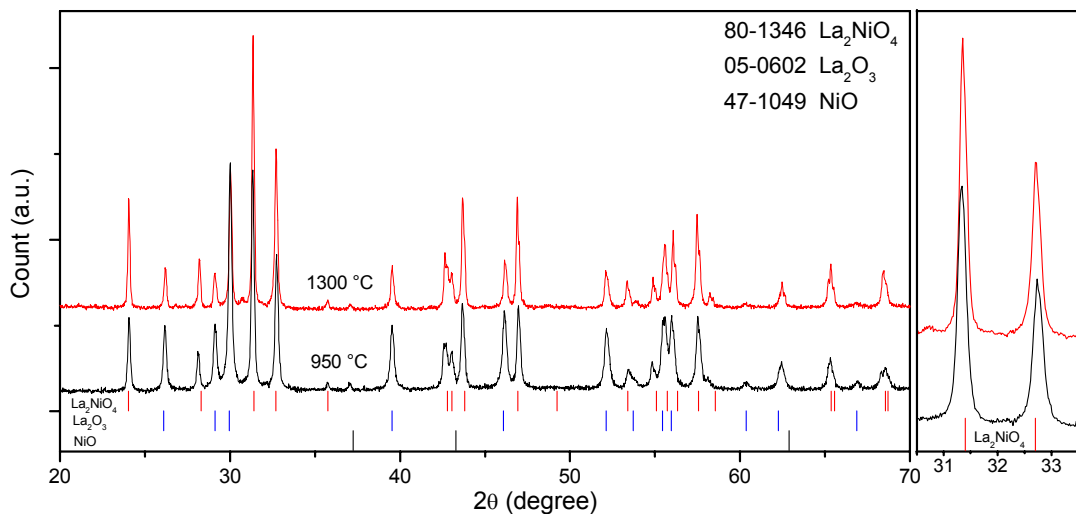


Fig. 3.42. XRD patterns of the LMN55-15 sample heat-treated at 950 and 1300 °C.

Similar problems were encountered during sample preparation, as in the La-Sr-Ni-O system. The sample reacted with moisture in the air; thus, the image quality is not very high. However, the EDX results were reproducible. According to the SEM-EDX analyses, the MgO content ( $16 \pm 1$  mol % MgO) in the  $\text{La}_2(\text{Ni}_{1-x}\text{Mg}_x)\text{O}_4$  solid solution at  $1300^\circ\text{C}$  was found to be almost equal to the NiO content ( $17 \pm 1$  mol % NiO and). The overall composition can be written as  $\text{La}_2(\text{Ni}_{0.5}\text{Mg}_{0.5})\text{O}_4$ . The composition of the (Mg,Ni)O solid solution of the three-phase field was also determined by using the EDX results of the same sample and was detected as  $20 \pm 1.2$  mol%. When applying Vegard's law to the XRD pattern of the (Mg,Ni)O solid solution (Fig. 3.42) having a lattice parameter of  $a = 4.204 \text{ \AA}$ , the NiO solubility was calculated as  $20.5 \pm 1.0$  mol %. This value is in excellent agreement with that derived from EDX analysis. Almost no shift was observed on the position of the peaks of the (Mg,Ni)O solid solution with changing temperature. The  $\text{La}_2\text{O}_3$  corner of the three-phase field was accepted directly from the quasi-binaries, which also did not show a temperature dependence. The results obtained from XRD and SEM-EDX studies were sufficient to construct the  $1300^\circ\text{C}$  isothermal section of the  $\text{La}_2\text{O}_3$ -MgO-NiO quasi-ternary system, which is given in Fig. 3.43.

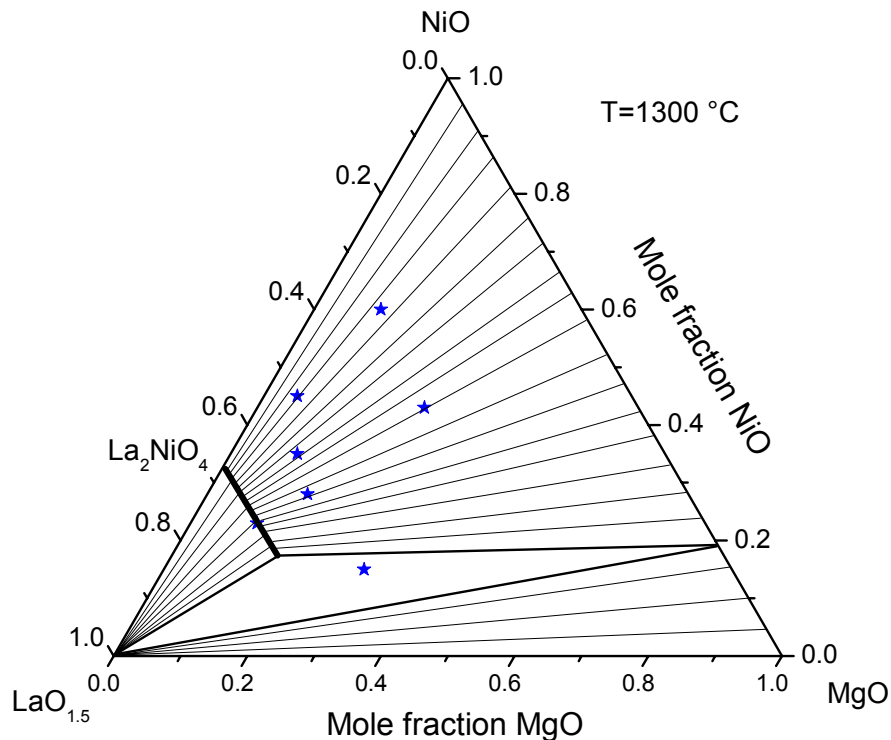


Fig. 3.43. Experimentally constructed  $1300^\circ\text{C}$  isothermal section of the phase diagram for the  $\text{LaO}_{1.5}$ -MgO-NiO system in air. The stars represent the samples compositions that were prepared and evaluated.

The phase equilibria at lower temperatures were investigated on the samples heat-treated at 950 and 1100 °C. The LMN30-60 and LMN50-45 samples were prepared to investigate the MgO solubility in the LaNiO<sub>3</sub> and La<sub>3</sub>Ni<sub>2</sub>O<sub>7</sub> compounds. As determined in previous sections of this dissertation, the LaNiO<sub>3</sub> compound decomposed in air above 980 °C to form the other RP-phases, NiO and O<sub>2</sub>. For that reason the LMN30-60 sample was heat-treated at 850 °C. The XRD patterns obtained at 850 and 950 °C are given in Fig. 3.44. The sample heat-treated at 850 °C shows only patterns of (Ni,Mg)O and LaNiO<sub>3</sub> shifted to lower angles. However, after the heat-treatment at 950 °C, the broad LaNiO<sub>3</sub> peaks were replaced by the relatively sharp La<sub>4</sub>Ni<sub>3</sub>O<sub>10</sub> peaks. Also the NiO peaks sharpened.

An additional sample that was heat-treated in pure oxygen atmosphere at 950°C yielded the same XRD patterns. After the heat-treatment at 950 °C, no shift was observed with respect to the original positions of the La<sub>4</sub>Ni<sub>3</sub>O<sub>10</sub> peaks. Obviously, the LaNiO<sub>3</sub> phase existed at low temperatures but decomposed with increasing temperature to La<sub>4</sub>Ni<sub>3</sub>O<sub>10</sub> phase. Also the La<sub>3</sub>Ni<sub>2</sub>O<sub>7</sub> phase did not appear in the higher-order system. None of the samples heat-treated at the low or high temperatures revealed any indication of the existence of this phase. This is consistent with the results of Vashuk, *et al.* [94Vas], in which evidence was not found for MgO solubility in the La<sub>4</sub>Ni<sub>3</sub>O<sub>10</sub> phase. However, the dissolution of very small amounts of MgO, may be below the detection limits of the XRD and may increase the stability of the La<sub>4</sub>Ni<sub>3</sub>O<sub>10</sub> phase in the higher-order system. This may explain the absence of the La<sub>3</sub>Ni<sub>2</sub>O<sub>7</sub> phase, which exists in the La-Ni-O system.

XRD patterns are shown in Fig. 3.45 for the LMN55-35 sample heat-treated at 1100 and 1300°. The sample heat-treated at 1100 °C (also at 950 °C) was located in the three-phase field, which consists of La<sub>2</sub>NiO<sub>4</sub>, La<sub>4</sub>Ni<sub>3</sub>O<sub>10</sub> and (Ni,Mg)O. As known from the La-Ni-O subsystem, the La<sub>4</sub>Ni<sub>3</sub>O<sub>10</sub> phase decomposes at high temperatures, and at 1300°C, the stable phase is La<sub>2</sub>NiO<sub>4</sub>, as demonstrated in the XRD spectra. The EDX analysis was not performed on the low-temperature heat-treated samples, because the average grain size of the samples was less than 1 μm which is the instrumental limit for the analysis. Therefore, the MgO solubility could not be determined by EDX. Also XRD is not a suitable technique to detect the solubility limit (if any) in this particular case. The substitution of Ni<sup>2+</sup> by the comparably sized Mg<sup>2+</sup> does not change the lattice parameters substantially. However, a small MgO solid solubility in La<sub>4</sub>Ni<sub>3</sub>O<sub>10</sub> is expected, although the homogeneity range cannot lie above 10 mol% MgO, because the LMN55-35 sample is in the three-phase field, and the amounts of the other phases are high. Consequently, the MgO solubility in the La<sub>4</sub>Ni<sub>3</sub>O<sub>10</sub> phase is very low or

even negligible. Therefore in the present work, it is taken as a stoichiometric compound for the thermodynamic modeling. The lattice parameter of the (Mg,Ni)O solid solution was measured in order to determine the third corner of the three-phase field. The lattice parameter was found to be  $a = 4.1927 \text{ \AA}$ , which corresponds to a MgO content of  $51 \pm 2 \text{ mol\%}$ .

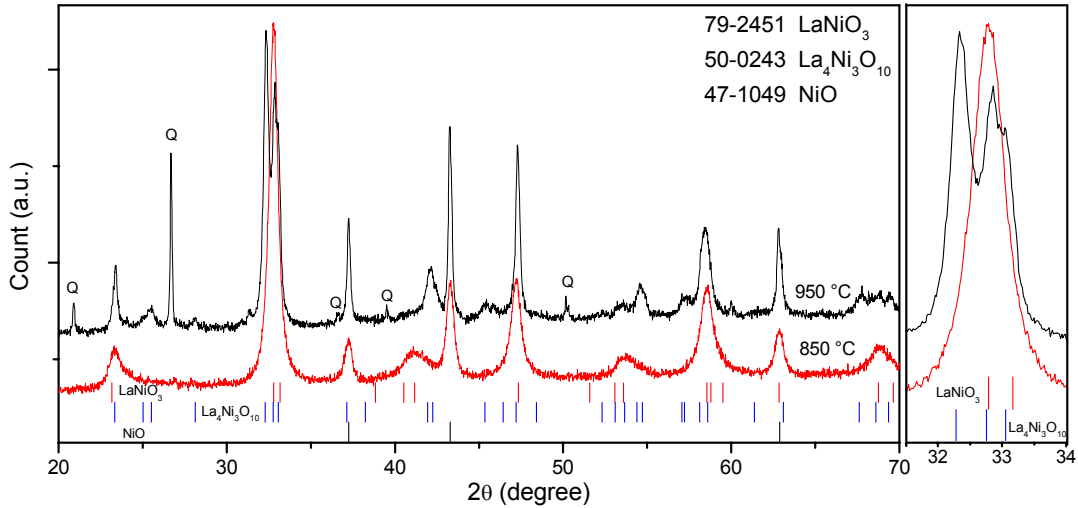


Fig. 3.44. XRD patterns of the LMN30-60 sample heat-treated at 850 and 950 °C. Quartz (Q) was used as a standard.

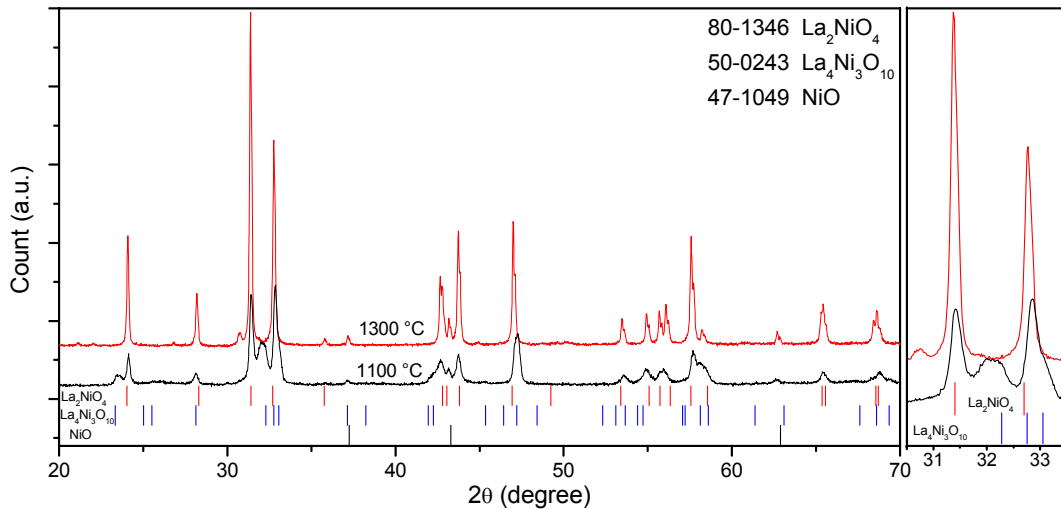


Fig. 3.45. XRD patterns of the LMN55-35 sample heat-treated at 1100 and 1300 °C.

Thermodynamic modeling of the system was performed by using only the experimentally determined phase equilibria, since measured thermodynamic data was not available for any component of the quaternary system. The parameters obtained for the  $\text{La}_2(\text{Ni,Mg})\text{O}_4$  solid solution are given in the Appendix, and the calculated 1300 and 1100 °C isothermal sections for the  $\text{LaO}_{1.5}\text{-MgO-NiO}$  system are shown in Fig. 3.46. A temperature term was introduced to reproduce the homogeneity range of the  $\text{La}_2(\text{Ni,Mg})\text{O}_4$  solid solution. The results are in

excellent agreement with the experimental one. Also the composition of the (Ni,Mg)O solid solution was well reproduced.

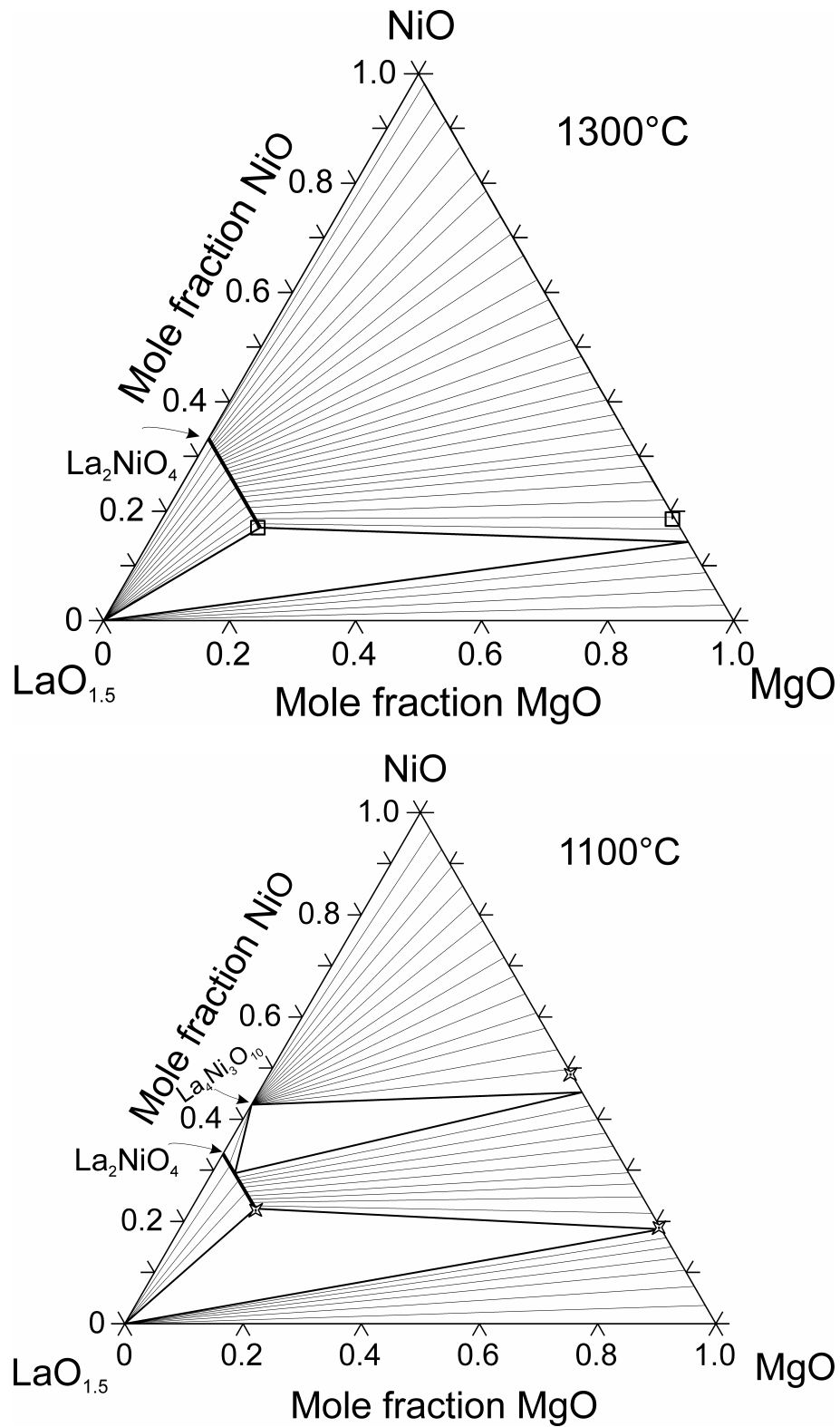


Fig. 3.46. The calculated 1300 and 1100 °C isothermal sections of the phase diagrams for the  $\text{LaO}_{1.5}$ - $\text{MgO}$ - $\text{NiO}$ , in air. The symbols show the experimentally determined boundaries.

### 3.3.8. The Sr-Ga-Ni-O Subsystem

No experimental data are available in the literature for this system. Therefore, the SrO-Ga<sub>2</sub>O<sub>3</sub>-NiO phase diagram was extrapolated from the constituent subsystems. The calculated 1200 °C isothermal section is given in Fig. 3.47. The results are similar to those for the SrO-Ga<sub>2</sub>O<sub>3</sub>-MgO system. SrGa<sub>2</sub>O<sub>4</sub> forms a three-phase field together with the NiGa<sub>2</sub>O<sub>4</sub> spinel and the NiO phases. The Ga-richer Sr gallates are in equilibrium with the spinel phase, whereas the Sr-richer ones are in equilibrium with NiO.

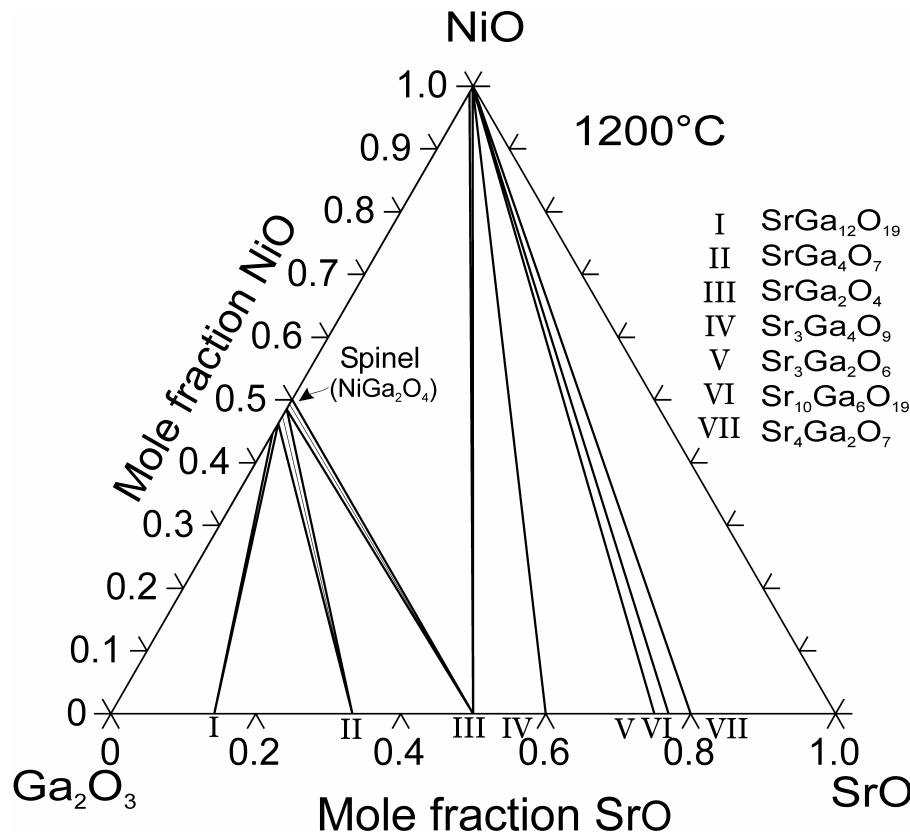


Fig. 3.47. The calculated 1200 °C isothermal section of the Ga<sub>2</sub>O<sub>3</sub>-SrO-NiO quasi-ternary system.

### 3.3.9. The Sr-Mg-Ni-O Subsystem

Similarly, experimental data are not available in the literature for the Sr-Mg-Ni-O system. Therefore the system was extrapolated from the constituent quasi-binaries. The calculated 1300 °C isothermal section is given in Fig. 3.48. It consists of a two-phase equilibria between SrO and the (Ni,Mg)O solid solution.

### 3.3.10. The Ga-Mg-Ni-O Subsystem

The formation of a complete solid solution was reported between  $\text{MgGa}_2\text{O}_4$  and  $\text{NiGa}_2\text{O}_4$  [85Ote]. Information in the literature related to the system is limited to the cation distribution in the  $\text{Mg}_x\text{Ni}_{1-x}\text{Ga}_2\text{O}_4$  spinel. A self-consistent set of Gibbs energy functions describing the oxide part of the system, which contains two solid solution phases of halite- and spinel-type has been published [05Zin1]. The calculated 1300 °C isothermal section of the  $\text{Ga}_2\text{O}_3$ -MgO-NiO quasi-ternary system is given in Fig. 3.49.

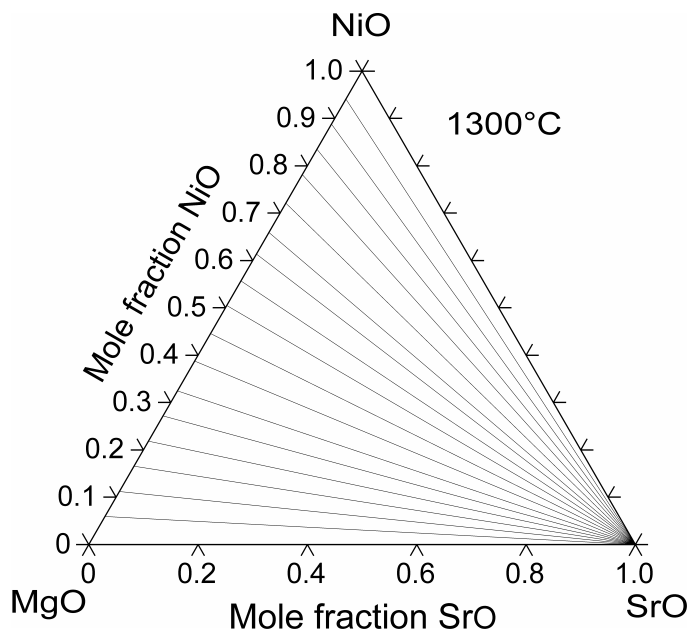


Fig. 3.48. The calculated 1300 °C isothermal section of the SrO-MgO-NiO quasi-ternary system.

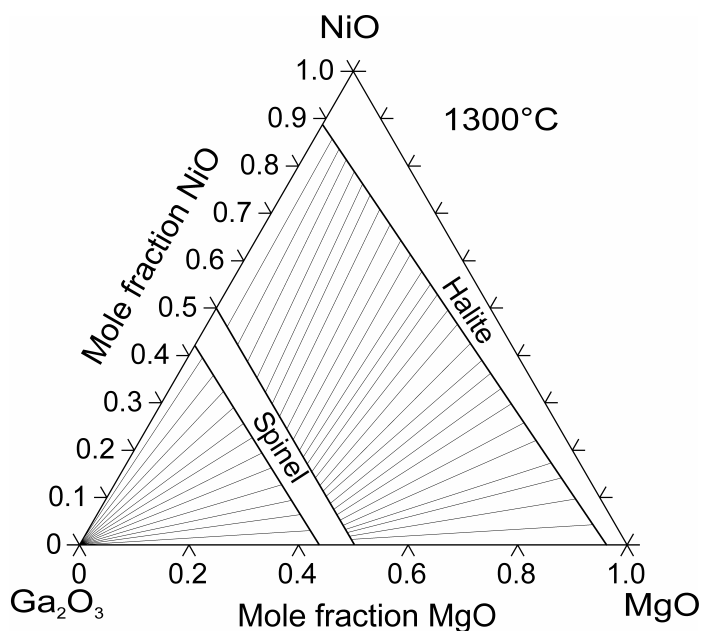


Fig. 3.49. The calculated 1300 °C isothermal section of the  $\text{Ga}_2\text{O}_3$ -MgO-NiO quasiternary system [05Zin1].

### 3.3.11. The La-Sr-Ga-Ni-O subsystem

In the literature, phase equilibria data are not available on the La-Sr-Ga-Ni-O system. Only two solid-solution phases have been reported,  $\text{La}_{0.9}\text{Sr}_{0.1}\text{Ga}_{0.5}\text{Ni}_{0.5}\text{O}_3$  (LSGN) [99Lon, 00Lec] and  $\text{LaSrGa}_{1-x}\text{Ni}_x\text{O}_4$  [95Rei]. The LSGN phase has been proposed for an IT-SOFC cathode material [00Lec]. In Fig. 3.50, the isothermal sections of the quasi-ternary subsystems have been combined. This kind of drawing represents the unfolded outer surface of the pyramid-shaped isobarothermal section of the quasi-quaternary  $\text{LaO}_{1.5}\text{-SrO-GaO}_{1.5}\text{-NiO}$  system, obtained by extrapolating from the data of the sub-systems. By using such a diagram, one could predict the reactivity and compatibility of  $\text{La}_2\text{NiO}_4$ ,  $(\text{La,Sr})_2\text{NiO}_4$  (LSN), or  $\text{La}_{0.9}\text{Sr}_{0.1}\text{Ga}_{0.5}\text{Ni}_{0.5}\text{O}_3$  (LSGN) with undoped  $\text{LaGaO}_3$ . As was shown previously,  $\text{La}_2\text{NiO}_4$  and undoped  $\text{LaGaO}_3$  are not chemically compatible. For the unknown system formed by  $(\text{La,Sr})_2\text{NiO}_4$  (LSN) and  $\text{LaGaO}_3$ , tie-lines inside the pyramid should be known, to represent internal the four-phase equilibria. According to the  $\text{LaO}_{1.5}\text{-GaO}_{1.5}\text{-SrO}$  section, five different three-phase fields exist on the line from the  $\text{LaGaO}_3$  compound towards the  $\text{LaO}_{1.5}\text{-SrO}$  quasibinary section, so the LSGN and  $\text{LaGaO}_3$ , phases are not expected to be chemically compatible. It should be also pointed out that the melilite-type  $\text{La}_{1-x}\text{Sr}_{1+x}\text{Ga}_3\text{O}_{7+\delta}$  phase is very stable, so it could be expected to extend into the higher-order system in the presence of NiO.

In order to support the prediction, a sample has been prepared, containing 50mol%  $\text{LaGaO}_3$  and 50mol%  $\text{LaSrNiO}_4$ . A mechanical mixture of the powders was ground in the mortar using ethanol. The prepared pellets were then heat-treated at  $1300^\circ\text{C}$  for 12h. The sample was characterized by XRD, and the patterns obtained are given in Fig. 3.51. In Fig. 3.51a a reaction between the components has clearly occurred. The characteristic peaks of  $\text{LaGaO}_3$  disappeared completely, and the peaks of LSN changed their position. The arrow in the figure indicates the characteristic peak of the melilite-type  $\text{La}_{1-x}\text{Sr}_{1+x}\text{Ga}_3\text{O}_{7+\delta}$  phase. In Fig. 3.51b the post heat-treatment pattern is given separately for detailed investigations. The pattern was fully indexed by using card files of the melilite-type  $\text{La}_{1-x}\text{Sr}_{1+x}\text{Ga}_3\text{O}_{7+\delta}$ ,  $\text{LaGaSrO}_4$  and NiO. It was not possible to estimate the NiO solubility in the first two phases, although the Ni substitution on Ga sites could be expected, as reported for  $\text{LaSrGa}_{1-x}\text{Ni}_x\text{O}_4$  [95Rei].

Reactivity between the other alternative cathode materials,  $\text{La}_{0.9}\text{Sr}_{0.1}\text{Ga}_{0.5}\text{Ni}_{0.5}\text{O}_3$  (LSGN) [99Lon, 00Lec] and undoped  $\text{LaGaO}_3$  cannot be seen directly from the diagram, since the equilibria extend through the pyramid. However, LSGN is a solid solution of  $\text{LaGaO}_3$ , A-site



substituted by Sr and B-site by NiO. According to the diagram, there is small SrO solubility in the A-sublattice and very large NiO solubility in the second sublattice of the  $\text{LaGaO}_3$  compound, and both components, LSGN and undoped  $\text{LaGaO}_3$ , are located in the same single phase field. Therefore, due to the composition gradient between the components, a reaction causing cation diffusion was inevitable.

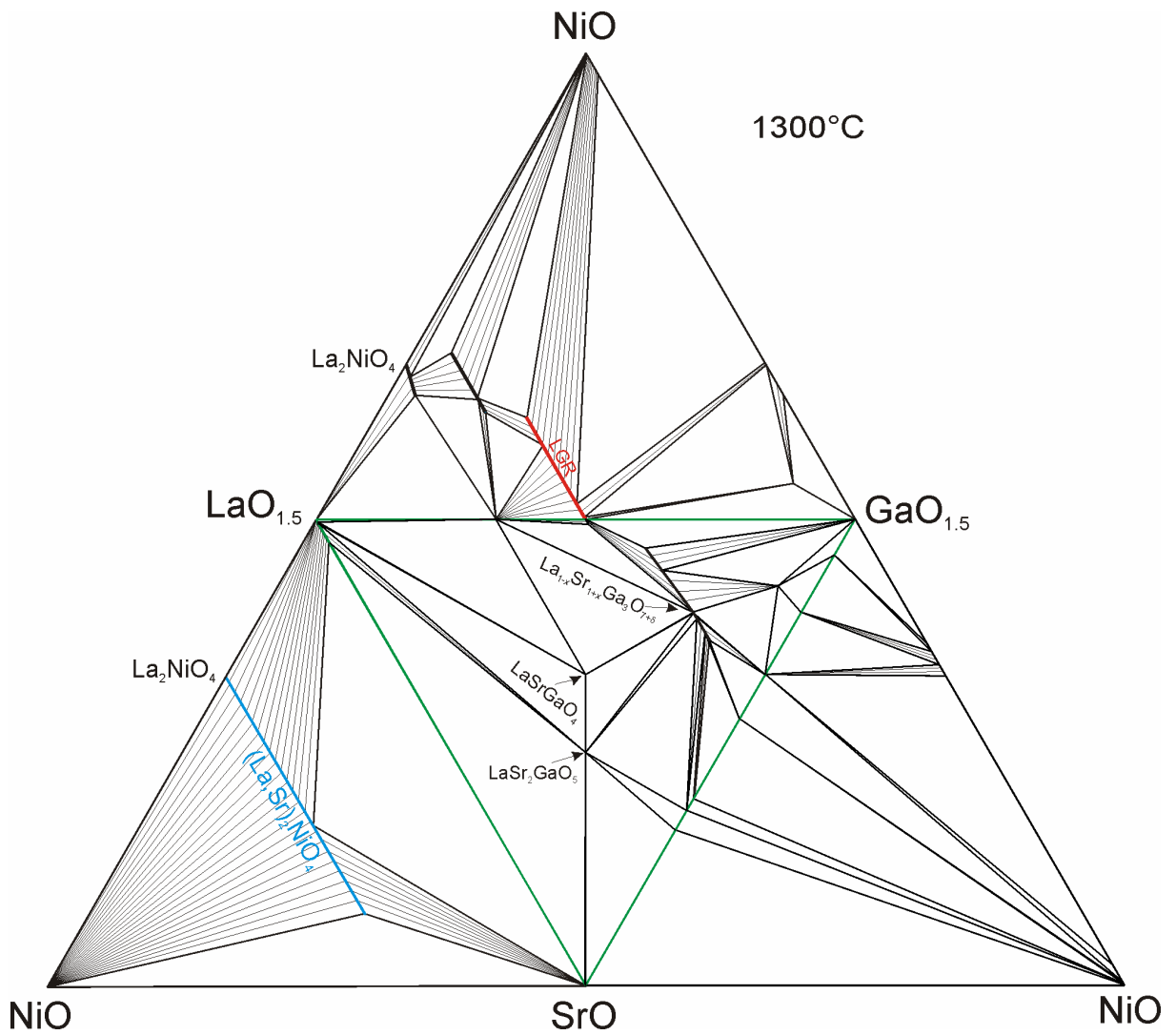


Fig. 3.50. The outer surface of the isobarothermal section of  $\text{LaO}_{1.5}\text{-SrO-GaO}_{1.5}\text{-NiO}$  phase diagram at  $1300^\circ\text{C}$  in air.

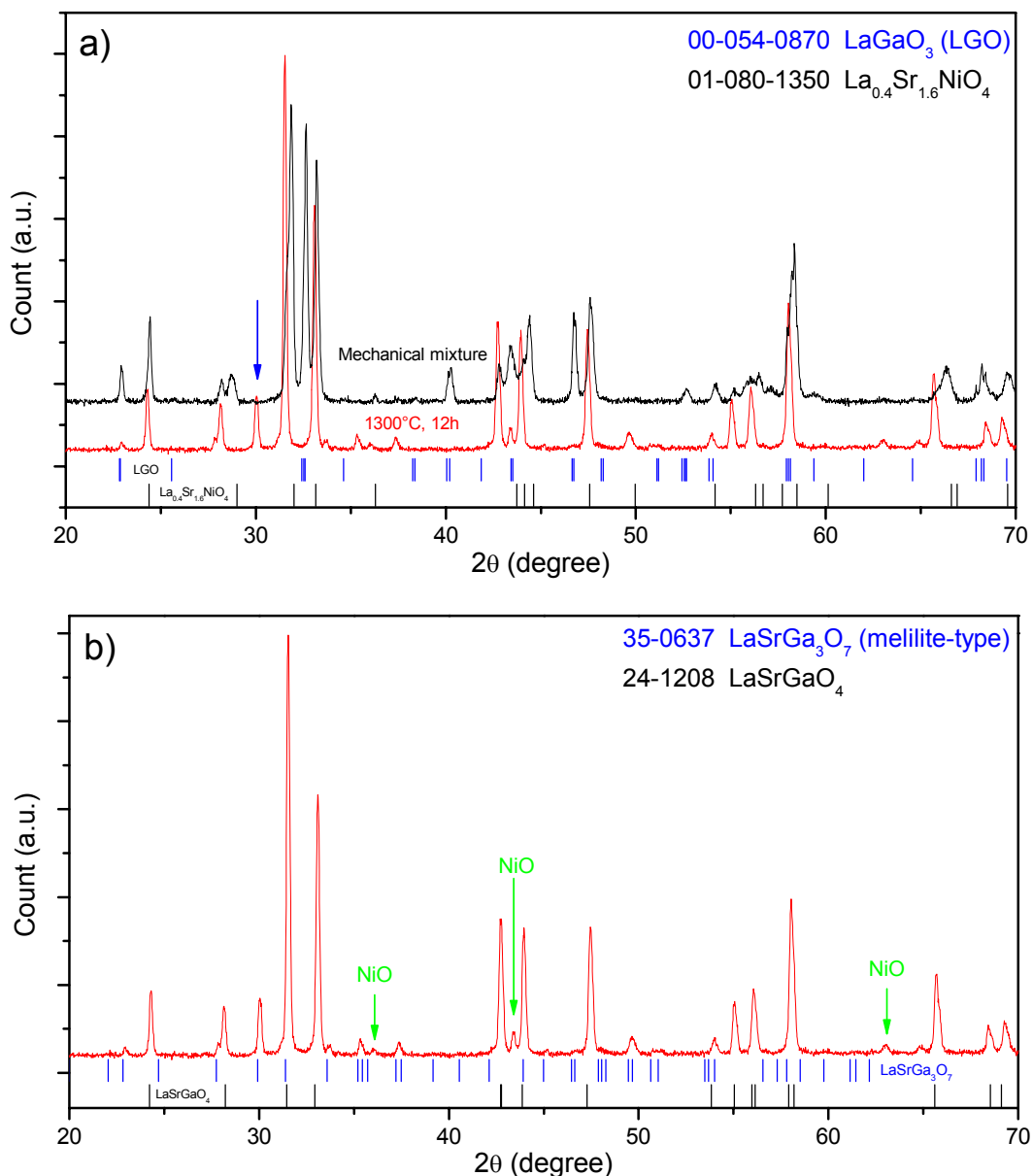


Fig. 3.51. XRD patterns of the LaGaO<sub>3</sub> (LGO) and LaSrNiO<sub>4</sub> (LSN), comparison of the pattern measured before and after heat-treatment at 1300°C for 12h (a); only the post heat-treatment pattern is shown for detailed characterization (b).

### 3.3.12. The La-Ga-Mg-Ni-O Subsystem

Literature data are not available for the phase equilibria in the La-Ga-Mg-Ni-O system. Only the existence of a LaGa<sub>0.65</sub>Mg<sub>0.15</sub>Ni<sub>0.2</sub>O<sub>3</sub> solid solution was reported [03Sha, 03Yar]. The combined isothermal sections of the subsystems are given in Fig. 3.52, in the form of the outer surface of the isobarothermal section of the LaO<sub>1.5</sub>-GaO<sub>1.5</sub>-MgO-NiO system. The undoped cathode-electrolyte reactivity has already been discussed above, but the LaO<sub>1.5</sub>-GaO<sub>1.5</sub>-MgO-NiO phase equilibria are important in order to determine the MgO and NiO

solubilities in the B-sublattice of  $\text{LaGaO}_3$ , which can give useful information for the anode-electrolyte interaction.

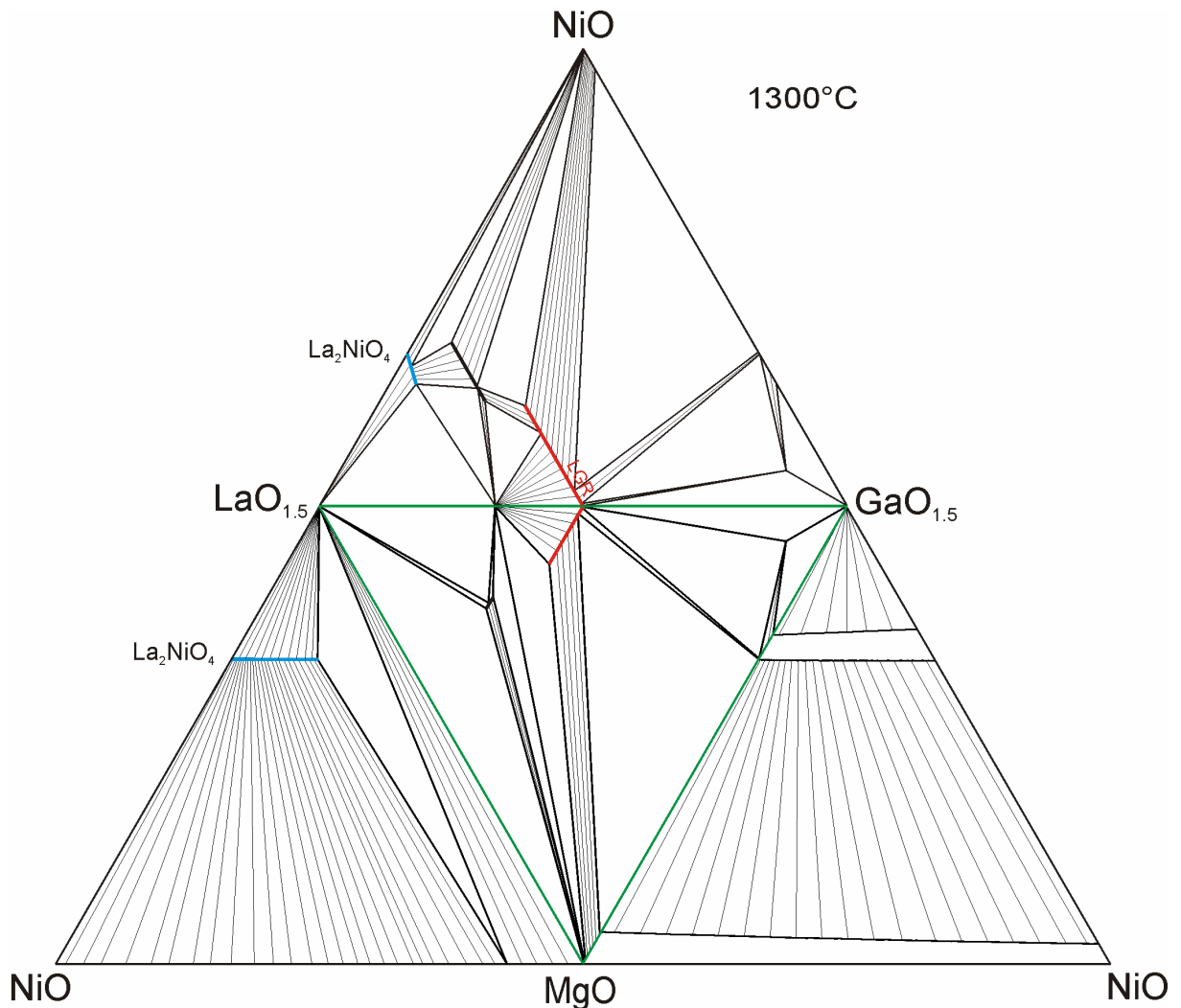


Fig. 3.52. The outer surface of the isobarothermal section of the  $\text{LaO}_{1.5}\text{-GaO}_{1.5}\text{-MgO-NiO}$  phase diagram at  $1300^\circ\text{C}$  in air.

However, additional experiments are necessary to determine quasi-quaternary phase equilibria. In order to determine the combined solubility of the Mg and Ni cations on the B-sublattice of  $\text{LaGaO}_3$ , ten samples were selected with the goal of comparing the type of cation-cation interaction. Three types of interactions are possible between cations of different valence charge: neutral, attractive, or repulsive. In an attractive interaction, the combined cation solubility in the  $\text{La}(\text{Ga,Mg,Ni})\text{O}_3$  solid solution is higher than that in  $\text{La}(\text{Ga,Mg})\text{O}_3$  and  $\text{La}(\text{Ga,Ni})\text{O}_3$ .

The compositions of the ten samples are represented on the isopleth shown in Fig. 3.53. This isopleth is related to the quasi-quaternary system shown in Fig. 3.52, where the  $\text{LaGaO}_3$  corner corresponds to the  $\text{LaGaO}_3$  composition on the  $\text{LaO}_{1.5}\text{-GaO}_{1.5}$  quasi-binary. The solid

solutions formed by  $\text{LaGaO}_3$  and  $\text{NiO}$  and by  $\text{LaGaO}_3$  and  $\text{MgO}$ , indicated by the red lines in Fig. 3.52, define the edges of the isopleth. Sample #1 was chosen to verify that Ni and Mg cations were incorporated into a single phase  $\text{LaGaO}_3$  lattice. Sample #2 and #8 were chosen to probe the solubility limit of the homogeneity range of the  $\text{La}(\text{Ga},\text{Mg},\text{Ni})\text{O}_3$  solid solution. If the samples were multi-phase, then they indicated that the boundary of homogeneity range lay between the pure  $\text{LaGaO}_3$  phase and the composition of interest. The relative intensity of the secondary phase peaks would indicate how close the composition of interest lay to the boundary. The remaining 7 compositions were chosen with the same strategy in mind. In the end, the boundary curvature of the homogeneity range could be estimated.

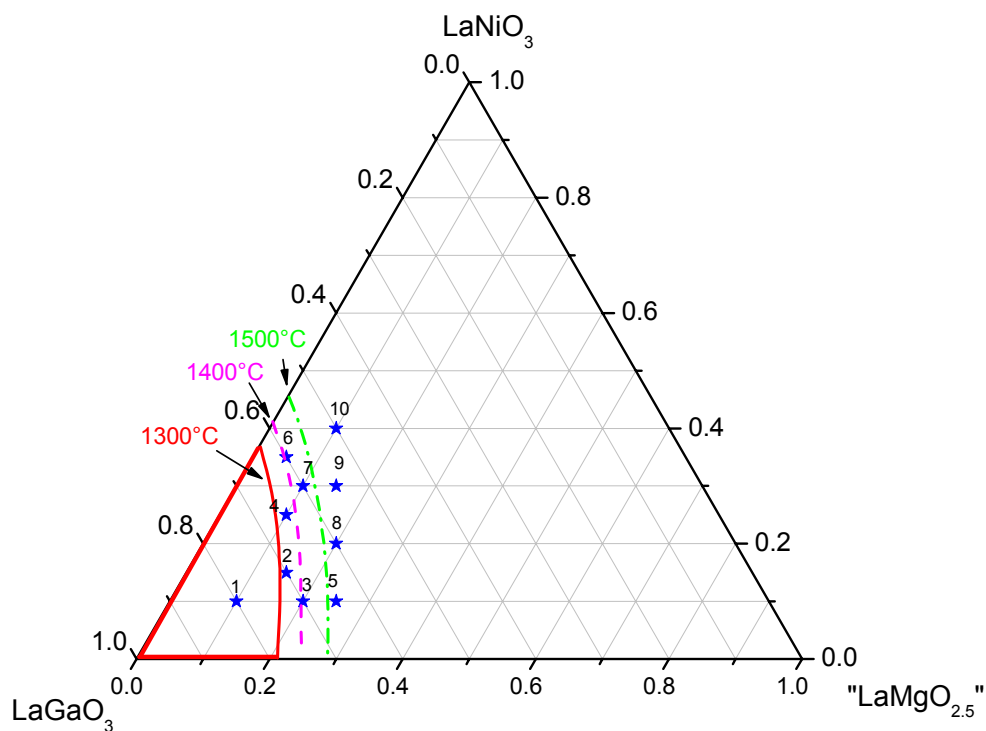


Fig. 3.53. The homogeneity range of the  $\text{La}(\text{Ga},\text{Mg},\text{Ni})\text{O}_3$  solid solution at various temperatures. The stars show the sample compositions investigated in this work.

Three sets of samples were prepared from the ten compositions chosen. One set was heat-treated at 1300 °C, one set at 1400 °C and one set at 1500 °C. The samples were characterized by XRD, and the results are summarized in Fig. 3.54. The patterns indexed to that of rhombohedral (LGR) and orthorhombic (LGO)  $\text{LaGaO}_3$ . The weak appearance of a peak at  $\sim 32^\circ 2\text{-theta}$  suggested that a secondary phase had formed in sample #2 at 1300 °C. In sample #3, the intensity of the weak peak had increased, indicating that more second phase had formed at 1300 °C. From the direction of curvature and the radius of curvature of the boundary, one could conclude that there is a slightly attractive interaction of  $\text{MgO}$  and  $\text{NiO}$ ,

and therefore an enhancement of the combined solubility in the  $\text{La}(\text{Ga},\text{Ni},\text{Mg})\text{O}_3$  solid solution.

In addition, the diffraction pattern from sample #4 at  $1300^\circ\text{C}$  showed a consistent splitting of the  $\text{LaGaO}_3$  peaks. In the inset figure, this splitting is pronounced for the peak at  $\sim 32.5^\circ$  2-theta suggests a structural phase transition from orthorhombic (LGO) to rhombohedral (LGR)  $\text{LaGaO}_3$ . It should be also pointed out that samples on the MgO-rich side always take the LGO structure, whereas on the NiO side the LGR phase is stable which is consistent with the previous findings.

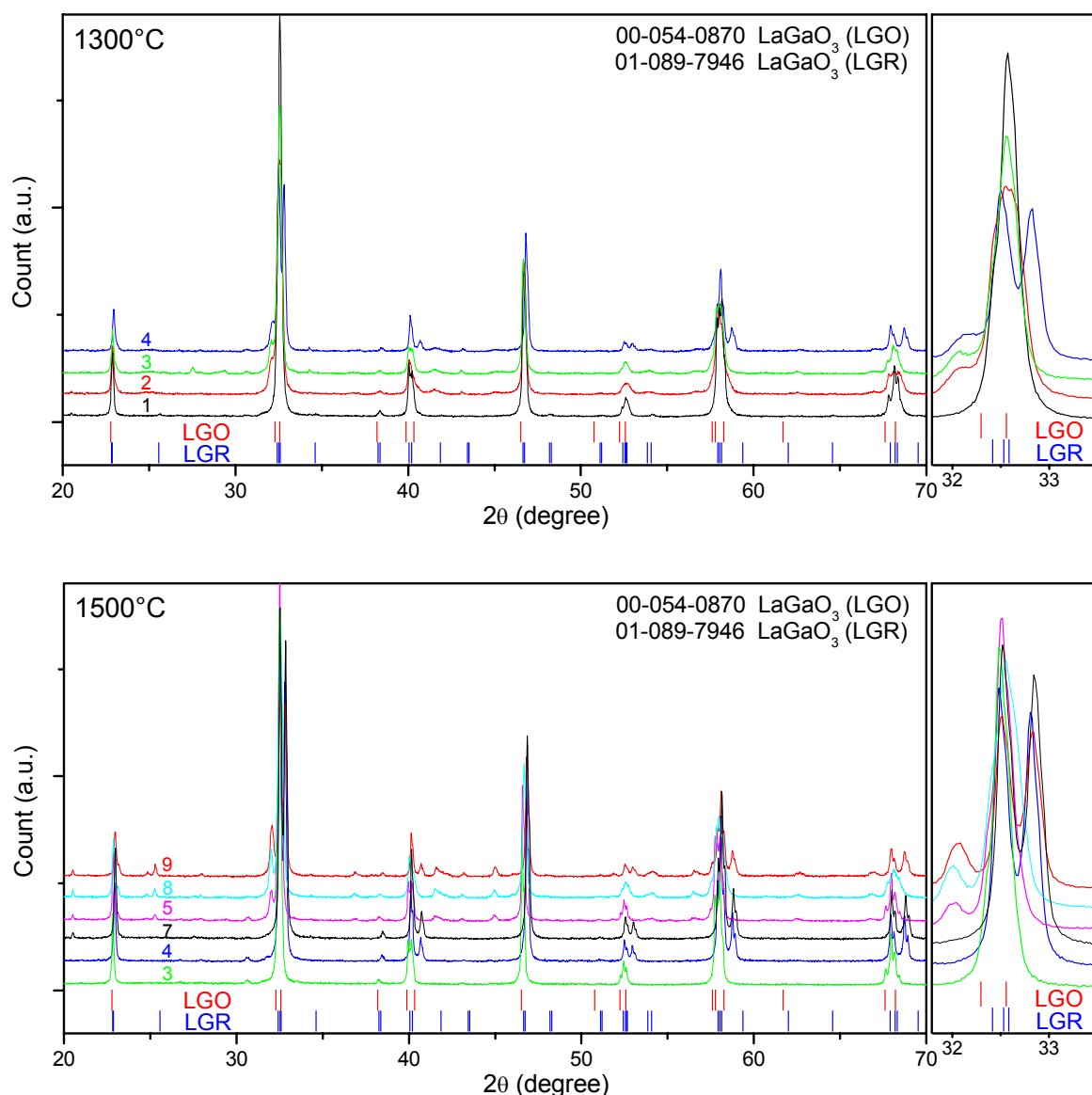


Fig. 3.54. XRD patterns of the samples heat-treated at  $1300$  and  $1500^\circ\text{C}$ . Numbers correspond to the samples in Fig. 3.53.

### 3.3.13. The La-Sr-Ga-Mg-Ni-O System

To predict the compatibility/reactivity under the fabrication and operation conditions of the LSGM based IT-SOFC systems, the results obtained in the subsystems were used, but have not been represented graphically. It is still possible to interpret the interactions between the electrodes and the LSGM electrolyte. The interaction between the undoped  $\text{La}_2\text{NiO}_4$  compound and the undoped  $\text{LaGaO}_3$  have already been discussed, and it is clear that they react. In addition, it has been found that various amounts of  $\text{SrO}$ ,  $\text{MgO}$ ,  $\text{Ga}_2\text{O}_3$  could be dissolved in  $\text{La}_2\text{NiO}_4$  to form a solid solution. Consequently,  $\text{La}_2\text{NiO}_4$  cannot be used as any component of LSGM based systems, not only due to its reactivity with LSGM, but also due to the solid solubility of the other cations. Recently, the  $(\text{La}_{0.9}\text{Sr}_{0.1})(\text{Ga}_{0.8}\text{Mg}_{0.2})\text{O}_3$  and the  $\text{La}_2\text{NiO}_4$  electrolyte-cathode system were investigated using electrochemical techniques, isotopic exchange/secondary ion mass spectrometry (SIMS), and XRD. The chemical activity of these materials have been noted [05Mun, 06Amo]. Although the exact reaction products were not discussed, a change was reported in the electrode performance [05Mun].

Experimental data is also not available on the interaction between LSGM and LSN cathodes. As it has been discussed and experimentally confirmed in this work, LSN and  $\text{LaGaO}_3$  (undoped) couples are also chemically active, reacting to form melilite-type  $\text{La}_{1-x}\text{Sr}_{1+x}\text{Ga}_3\text{O}_{7+\delta}$ ,  $\text{LaGaSrO}_4$  and  $\text{NiO}$ . In order to study the influence of  $\text{SrO}$ ,  $\text{MgO}$  and  $\text{NiO}$ , a sample containing 50 mol%  $(\text{La}_{0.8}\text{Sr}_{0.2})(\text{Ga}_{0.85}\text{Mg}_{0.15})\text{O}_3$  and 50 mol%  $\text{LaSrNiO}_4$  as a mechanical mixture was prepared and heat-treated at  $1300^\circ\text{C}$  for 12h. The sample was characterized by XRD, Fig. 3.55a shows a comparison of the XRD spectra for the mechanical mixture and the heat-treated sample. As in the undoped  $\text{LaGaO}_3$  (LGO)-LSN combination, LSGM and LSN, reacted, revealing the characteristic reflections of the melilite-type  $\text{La}_{1-x}\text{Sr}_{1+x}\text{Ga}_3\text{O}_{7+\delta}$  phase. For comparison, the pattern of the heat-treated sample is shown in Fig. 3.55b along with that of the  $\text{LaGaO}_3$  (LGO)-LSN system. Both patterns match perfectly, showing the same equilibria. Consequently, the LSN cathode is chemically incompatible with LSGM electrolytes.

The cathode alternative  $\text{La}_{0.9}\text{Sr}_{0.1}\text{Ga}_{0.5}\text{Ni}_{0.5}\text{O}_3$  (LSGN) [99Lon, 00Lec] and LSGM would be the best combination of the three systems investigated. As mentioned above, both materials have the same structure, but they are located at different ends of the LSGM solid solution. Although both LSGN and LSGM are fully doped, cation diffusion would still be expected in this case. As explained for the La-Ga-Mg-Ni-O system, if  $\text{MgO}$  and  $\text{NiO}$  were dissolved together in  $\text{LaGaO}_3$  the combined solubility would be enhanced. Some  $\text{NiO}$  diffusion from the

LSGN cathode to the LSGM electrolyte could occur by the replacement of MgO. Therefore, a change in the electrochemical performance of the system could be expected. However, it is not expected that the reaction would be as severe as in the case of  $\text{La}_2\text{NiO}_4$  and LSN. In the work of Lecarpentier and co-workers [00Lec], such a NiO diffusion through LSGM was observed, but it was reported that it is not significant and does not effect the performance of the system much.

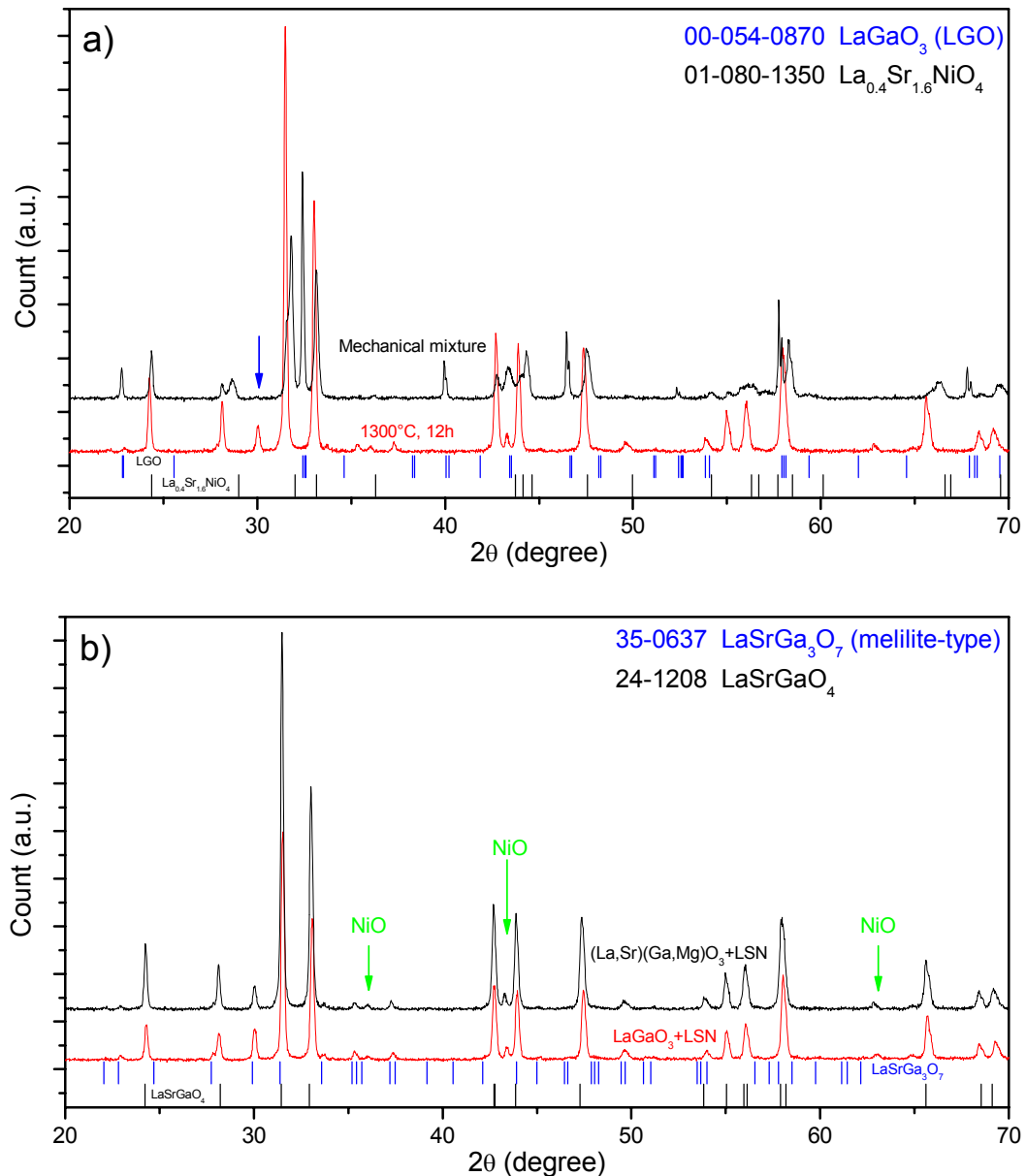


Fig. 3.55. XRD patterns of the  $(\text{La}_{0.8}\text{Sr}_{0.2})(\text{Ga}_{0.85}\text{Mg}_{0.15})\text{O}_3$  and  $\text{LaSrNiO}_4$  (LSN); comparison of the pattern obtained before and after heat-treatment at 1300°C for 12h (a), the patterns after the heat-treatment in comparison with pattern given in Fig. 3.51b which show undoped  $\text{LaGaO}_3$  (LGO) and LSN combination (b).

In all LSGM subsystems, the NiO reactivity was observed to occur by substituting of  $\text{Ga}^{3+}$  and/or  $\text{Mg}^{2+}$  ions in the second sublattice. It is also known that SrO substitution in the A-

sublattice had enhanced the solubility in the B-sublattice [01Maj1, 04Mat, Per]. Therefore, under the fabrication conditions, NiO dissolution is inevitable. In fact, the reactivity between these two components was also reported in the literature [99Hua, 01Zha, 06Dat, 06Rao]. In addition to the expected formation of solid solution [99Hua], the formation of the LaNiO<sub>3</sub> phase was reported [01Zha, 06Dat, 06Rao]. Obviously, the reported LaNiO<sub>3</sub> phase could not have been phase-pure, since it had decomposed into other lanthanum nickelates at 980°C, in air, as found in this work. In a recent study of Rao, *et al.* [06Rao], it has been found that the LaNiO<sub>3</sub>-type phase contains considerable amounts of other cations. This cannot be predicted from the obtained phase equilibria based on the subsystem but as it has been explained above, the formation of solid solution is obvious. Therefore, it can be concluded that NiO is chemically active with LSGM electrolytes, and it cannot be used as anode, because under standard fabrication conditions, it would react to form solid solution and/or new LaNiO<sub>3</sub>-type phase.

### **3.4. The Reactivity in IT-SOFC with CGO electrolyte**

Since Gd-doped ceria demonstrates the highest ionic conductivity among all the SOFC electrolytes shown in Fig. 1.2, it is therefore imperative to investigate the stability of the interface formed between this material and various common electrode materials. To this end, the following systems have been investigated.

#### **3.4.1. The Ce-Ni-O Subsystem**

Unlike the most systems of rare-earth elements with nickel and oxygen, ternary compounds do not form in the *Ce-Ni-O* system. Although Fratello and co-workers [96Fra] reported that the CeNiO<sub>3</sub> compound appeared around the melting point of NiO (1984 °C), the XRD analysis showed only peaks of NiO and CeO<sub>2</sub>. Although several investigations have confirmed that the solid solubility of NiO in CeO<sub>2</sub> and vice versa are negligible [93Ran, 98Hro, 00Mog], solubility limits as high as 33 mol % [92Pou, 00Pon, 99Lam] have been reported for NiO in CeO<sub>2</sub>. However, Ranløv and co-workers [93Ran] had shown that the solid solution Ce<sub>1-x</sub>Ni<sub>x</sub>O<sub>2</sub> mentioned by Pound [92Pou] became unstable at the temperature considered (1000 °C), and the corresponding ac impedance data and electrode tests reported by the same author [92Pou] should be interpreted in terms of a two-phase system. In other studies, where a noticeable solid solubility of NiO in CeO<sub>2</sub> had been reported [00Pon, 99Lam], samples were prepared by co-precipitation, impregnation, or sol-gel methods, followed by calcination at around 600 °C. In all these studies, no evidence has been found for



the existence of such extensive solid solutions at equilibrium conditions. Furthermore, due to the large difference in ionic radius between  $\text{Ni}^{2+}$  and  $\text{Ce}^{4+}$ , it seems unlikely that extended solid solutions would form with as much as 10 mol% NiO in  $\text{CeO}_2$  [93Ran]. Accordingly, the solid solubility of NiO in ceria lattice was described to be less than 1 mol % in a recent review on the physical, chemical and electrochemical behavior of ceria [00Mog].

Two samples with Ce:Ni ratios of 1:1 and 2:1 were prepared in order to investigate the existence of ternary compounds and mutual solid solubility of components, as well as the behavior of the system in a reducing atmosphere. The normalized XRD patterns are shown in Fig. 3.56 for the solid-state reaction products, which were heat-treated in air at 1200 °C for 120h. No shift was observed in the ceria and NiO peaks with respect to the original positions. Such a shift would have been an indication of some solid solubility. Moreover, no additional peaks were found that could have been associated with a ternary compound.

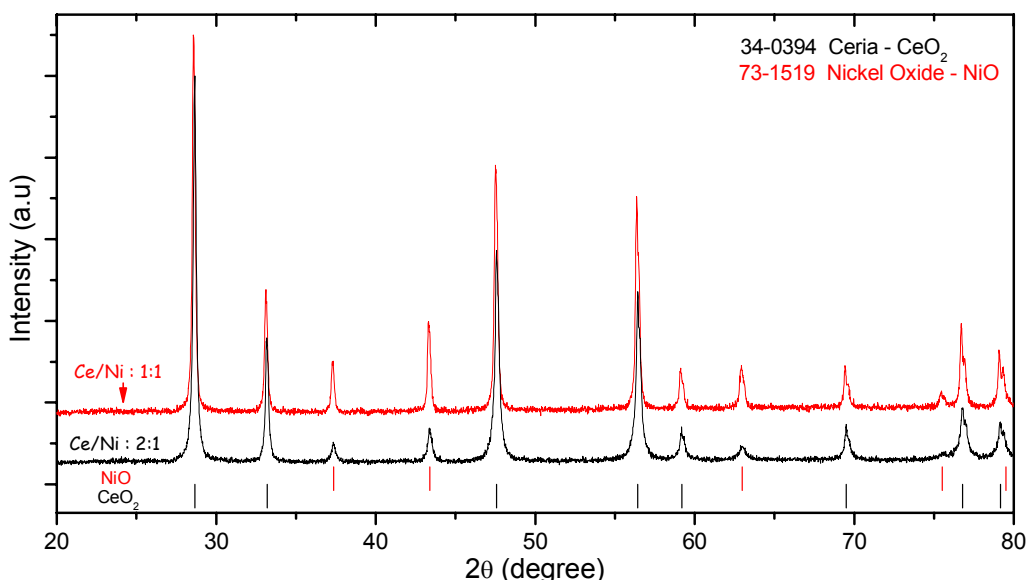


Fig. 3.56. XRD patterns of the solid-state reaction products of 1:1 and 2:1 ratio Ce:Ni samples annealed at 1200 °C in air. Vertical lines represent the original position of the peaks as given in the ICDD database [ICDD]

In addition, a 1:1 composition sample was heat-treated at 1600 °C for 10 h and quenched in air. The comparison of the XRD patterns before and after quenching is presented in Fig. 3.57. The aim of the quenching experiment was to obtain a projection of high temperature behavior of the components at room temperature. However, virtually identical XRD patterns were obtained from samples, which have been quenched or furnace cooled from 1600 °C. The results confirm earlier findings mentioned above [93Ran, 98Hro, 00Mog]. Therefore, the system was modeled thermodynamically using the experimental results obtained. Then a phase stability diagram was calculated (see Fig. 3.58), which served as the basis for designing

the reducing atmosphere experiments. Since there is no ternary compound and no detectable solubility of components, previously reported data on the Ce-O, Ce-Ni and Ni-O subsystems were used without additional parameters in the modeling. In the diagram, the dotted line delineates the boundary between metallic nickel and nickel oxide. The area surrounded by solid lines (in blue) shows the stability region of the intermediate cerium oxides. According to the calculated diagram, the experimental conditions were selected for the reducing atmosphere studies on samples having a Ce:Ni ratio of 1:1. These are shown on the diagram by circles. The experimental conditions shown in Fig. 3.58 were selected to represent the limits of the experimental setup, *i.e.*, the low-temperature and high-oxygen partial pressure combination and the high-temperature, low-oxygen partial pressure one.

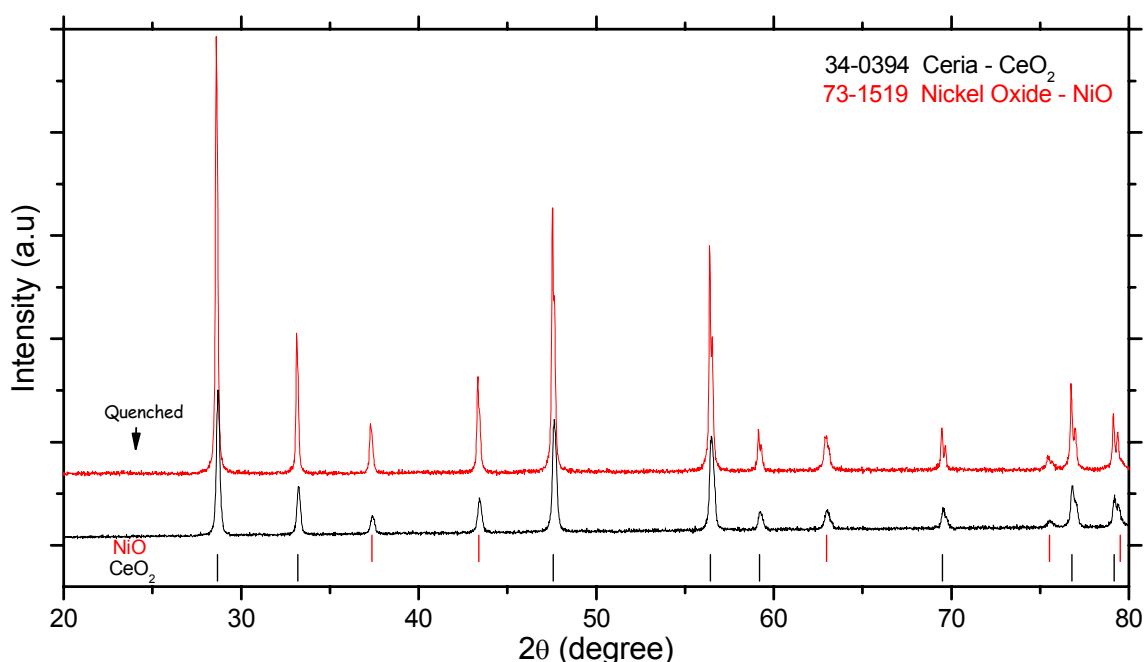


Fig. 3.57. XRD patterns of the solid-state reaction products of the 1:1 ratio of Ce:Ni sample, before and after quenching in air from a heat-treatment at 1600 °C for 10h. Vertical lines represent the original position of the peaks according to ICDD database [ICDD].

Fig. 3.59 shows the XRD patterns of samples before and after heat-treatments under a controlled oxygen partial pressure. Also shown are the furnace and thermostat temperatures, as well as the oxygen partial pressure that could be reached under these conditions (dash-dotted lines). Under the low oxygen partial pressure investigated, all NiO peaks had disappeared and metallic nickel peaks had increased in intensity, consistent with predictions from the calculated phase stability diagram in Fig. 3.58. In addition, neither a peak shift nor an unidentified peak had been observed. Thus, the XRD results are in good agreement with the calculated phase stability diagram (Fig. 3.58).

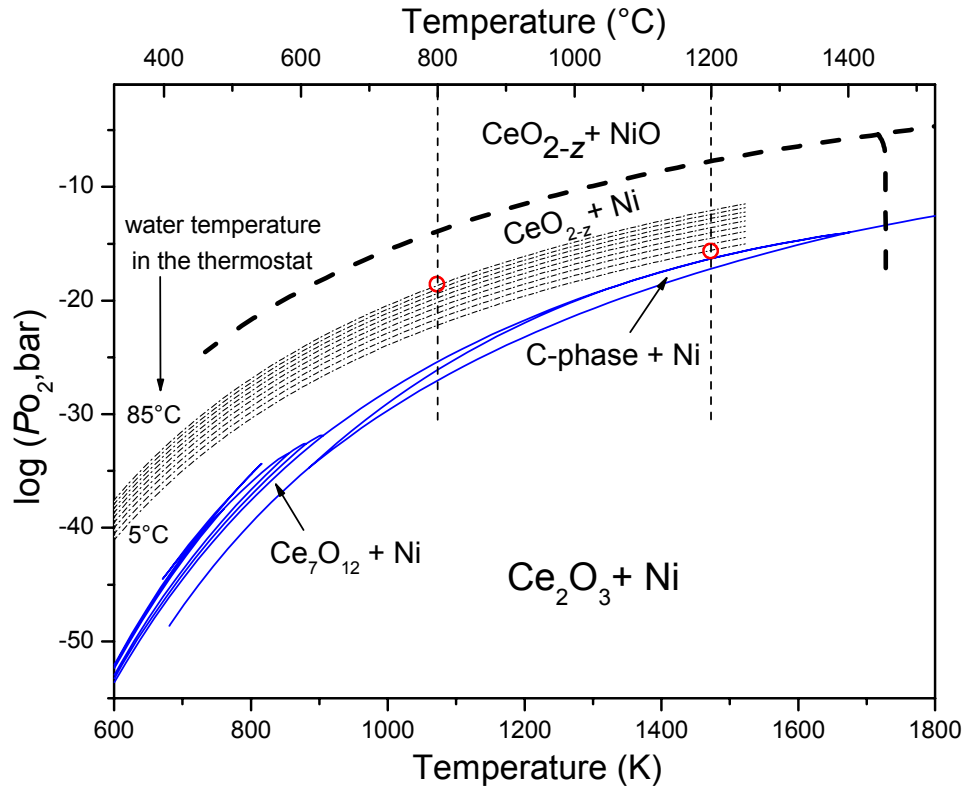


Fig. 3.58. Calculated phase stability diagrams for the Ce-Ni-O ternary system are shown, combined with the experimental parameters. The dash-dotted lines represent water temperature in the thermostat. The dashed lines show the stability region of the Ni-O system, while the solid lines (in blue) show the different phase fields in the Ce-O system. The circles represent the selected experimental conditions.

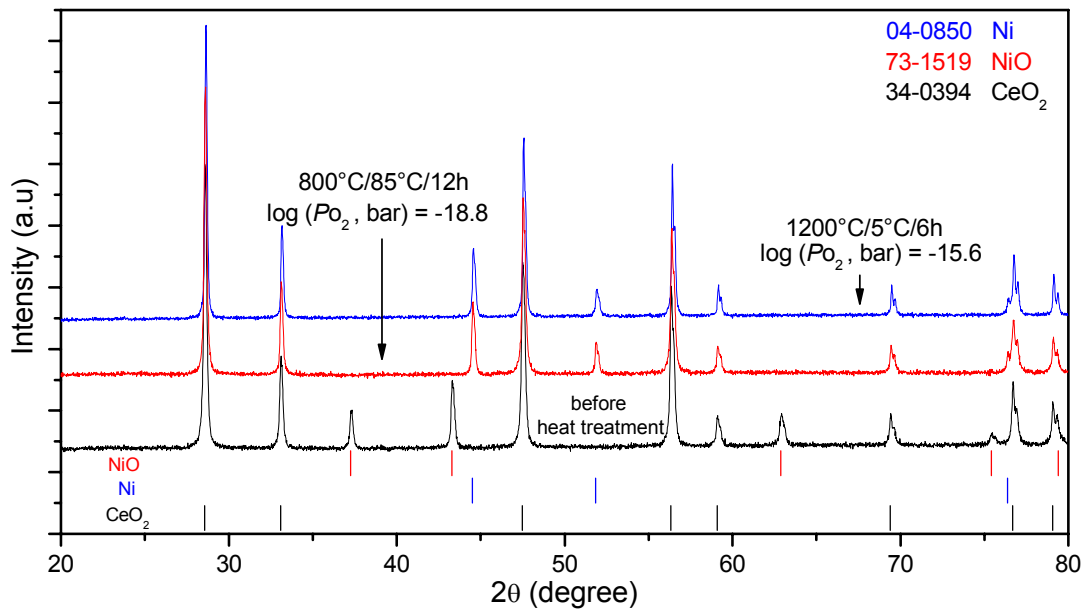


Fig. 3.59. XRD patterns of 1:1 ratio Ce:Ni sample before and after heat-treatment. Furnace and thermostat temperature, reaction duration and oxygen pressure are given on the patterns.

### 3.4.2. The Ce-Sr-O Subsystem

The sub-solidus phase equilibria in the CeO<sub>2</sub>-SrO quasi-binary section was first investigated by Mastromonaco and co-workers [69Mas], who reported the existence of two compounds, Sr<sub>2</sub>CeO<sub>4</sub> and SrCeO<sub>3</sub>. A temperature dependent SrO solubility in CeO<sub>2</sub> was also reported, whereas no detectable solid solubility of CeO<sub>2</sub> in SrO lattice was found [56Kel, 69Mas, 86Sor, 03Cha]. The Sr-Ce-O system was also investigated on the basis of chemical potential diagrams by Yokokawa and co-workers [90Yok]. It should be noted that the compound Sr<sub>2</sub>CeO<sub>4</sub> was omitted in the calculations, because the thermodynamic description of the compound was not known to date. In the recent calorimetric work of Basu, *et al* [04Bas], the enthalpy of formation of the Sr<sub>2</sub>CeO<sub>4</sub> compound was the only measured thermodynamic data on that particular compound. The available data for the SrCeO<sub>3</sub> compound consisted of the low temperature heat capacity (4-298K) [98Cor], the high temperature enthalpy increment [89Sah], and the DSC data [03Yam]. Even though, partial thermodynamic data are available for the compounds, a complete thermodynamic description of the system is still needed. Therefore, in this work, phase-pure ternary compounds were synthesized to measure the thermodynamic properties, and additional samples were prepared in order to investigate the phase equilibria of the system.

In Fig. 3.60 XRD powder patterns of Sr<sub>2</sub>CeO<sub>4</sub> and SrCeO<sub>3</sub> are compared with of ICDD database [ICDD]. The results reveal that the samples investigated are clearly of single phase. The samples were used for the thermodynamic characterization of the compounds. In order to determine the decomposition temperature for the SrCeO<sub>4</sub> compound an additional sample of the SrCeO<sub>3</sub>-Sr<sub>2</sub>CeO<sub>4</sub> two-phase field consisting of 60 mol% SrO (CS60) was prepared. TG/DTA was performed on both the Sr<sub>2</sub>CeO<sub>4</sub> and CS60 sample in order to the determine decomposition temperature of the Sr<sub>2</sub>CeO<sub>4</sub> compound.

Fig. 3.61 presents the TG/DTA curves measured from the phase-pure Sr<sub>2</sub>CeO<sub>4</sub> sample. Two endothermic peaks could be seen on the DTA plot. The peak appearing at around 766 °C corresponds to the decomposition of the carbonates, originating from the sample preparation. The small amount of weight loss (< 1 wt %) seen on the TG curve could be attributed to residual carbonate from the Sr carbonate pre-cursor. The second endothermic peak, which is determined to lie at 1453±3 °C, would correspond to the decomposition of the Sr<sub>2</sub>CeO<sub>4</sub> compound into SrCeO<sub>3</sub> and SrO. The decomposition temperature was reproduced with an accuracy of 3 K on the same sample, as well as on the CS60. The results are in good agreement with the data of Mastromonaco and co-workers [69Mas] (1430 °C). Only SrCeO<sub>3</sub>

and Sr-hydroxide (with various amounts of crystal water) could be observed after decomposition, and according to the XRD analysis, no indication could be found for the re-formation of the  $\text{Sr}_2\text{CeO}_4$  compound.

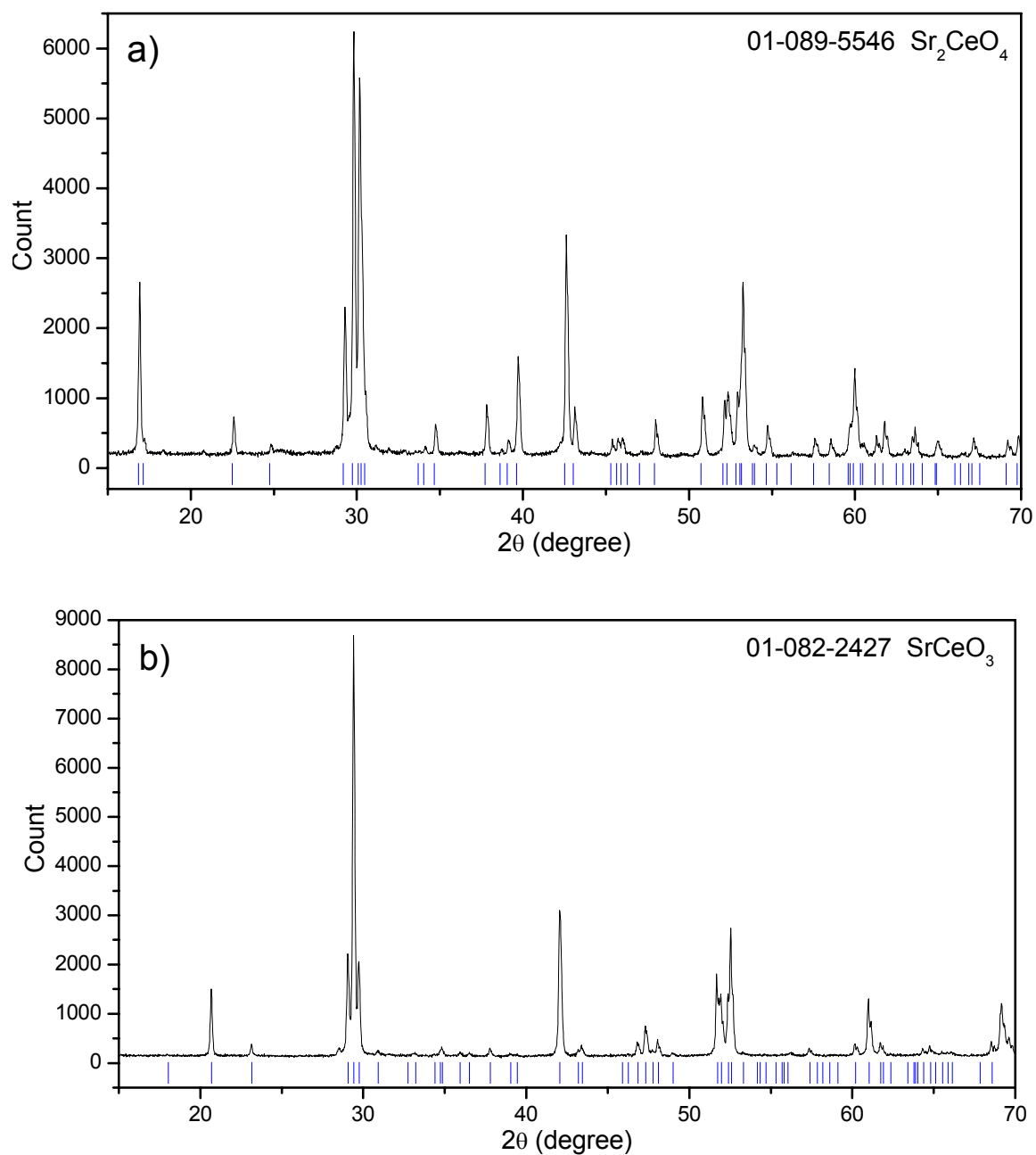


Fig. 3.60. XRD powder patterns of the  $\text{Sr}_2\text{CeO}_4$  (a) and  $\text{SrCeO}_3$  (b) compounds.

Fig. 3.62 presents the measured low-temperature heat capacity characterization of the  $\text{Sr}_2\text{CeO}_4$  compound. The data above 220 K exhibited a large scatter (see the inset figure). At higher temperatures, the scatter is not strongly pronounced, but it displays an unstable behavior with a higher slope. DSC analysis was performed for the 77-298K temperature range, but a peak indicative of a phase transition was not observed. When the room- and high-temperature  $C_p$  data were combined and compared with the theoretical Neumann-Kopp curve,

the room temperature data does not appear to fit the calculated curve. However, by adding 12 J/mol, the fit is much improved, as indicated by the dashed line. It should be also pointed out that the theoretical Neumann-Kopp curve coincides with the data at around 200-250 K. In the thermodynamic modeling, this situation was taken into account, and enabled an acceptable level of consistency for determining the heat capacity.

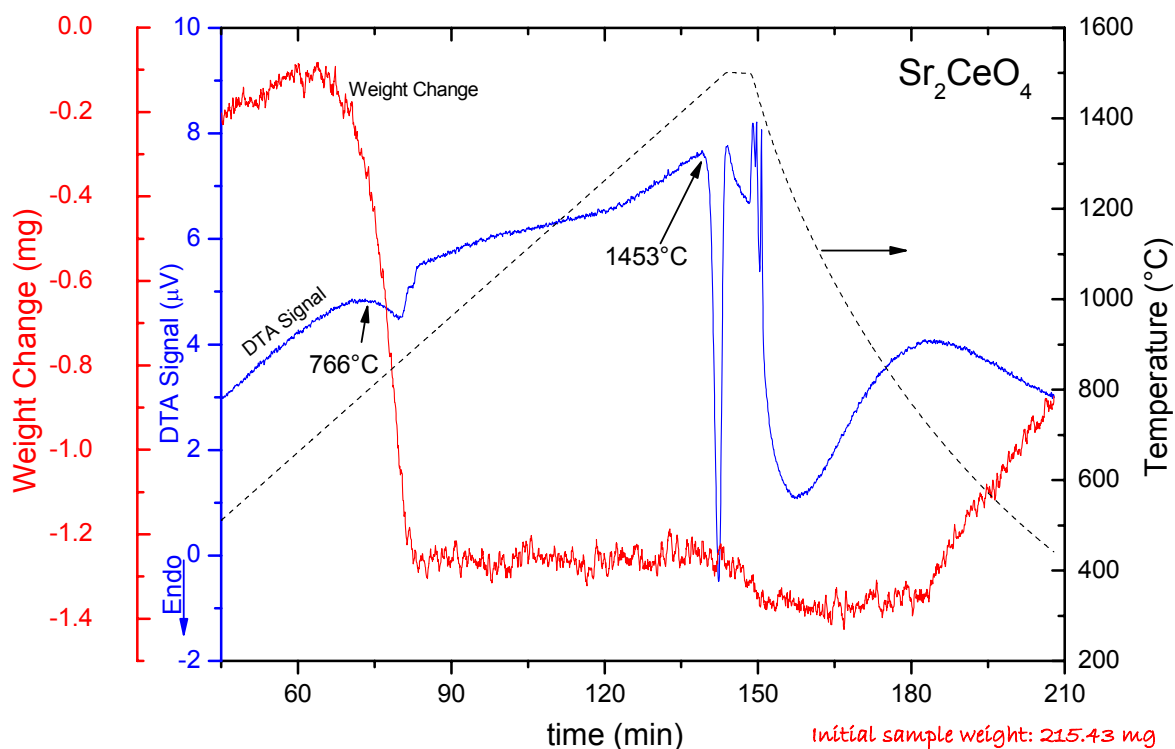


Fig. 3.61. TG and DTA curves recorded during heating and cooling the Sr<sub>2</sub>CeO<sub>4</sub> compound.

For the SrCeO<sub>3</sub> compound, the measured low temperature heat capacity is shown in Fig. 3.63. This diagram includes some literature data for the high temperature heat capacity, in addition to the theoretical Neumann-Kopp curve. Cordfunke, *et al* [98Cor] had combined the results of Saha, *et al* [89Sah] with their measured enthalpy increment data to generate the theoretical curve. Comparison with other existing data reveals a positive deviation using the data of Yokokawa, *et al* [90Yok], which is based on the work of Sorokina, *et al* [86Sor] and a negative deviation using those of Yamanaka, *et al* [03Yam]. In the present work, the high temperature heat capacity of the SrCeO<sub>3</sub> compound was measured by DSC and a reasonable agreement was established with the results of Cordfunke, *et al*. [98Cor], as also presented in Fig. 3.63.

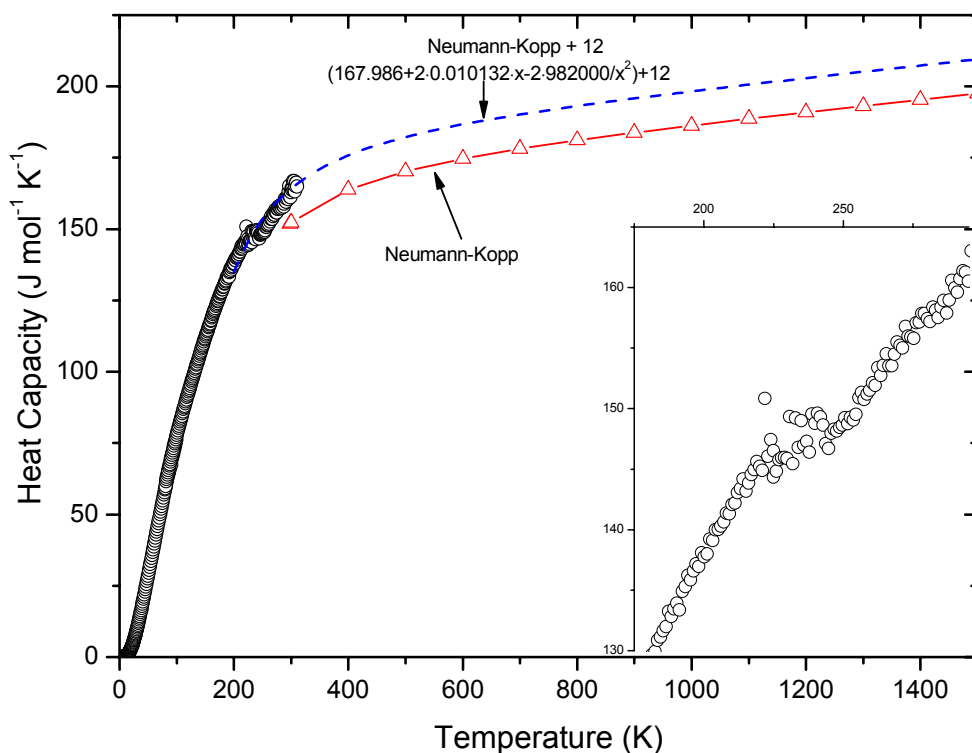


Fig. 3.62. The temperature-dependence of the molar heat capacity of  $\text{Sr}_2\text{CeO}_4$  is shown, where the open circles indicate the data measured for this work. The line with triangles shows the calculated (theoretical) Neumann-Kopp curve, while the dashed line indicates the calculated data systematically deviated to fit the room temperature data. Inset shows the variation of the measured heat capacity of the compound between 200 K and room temperature.

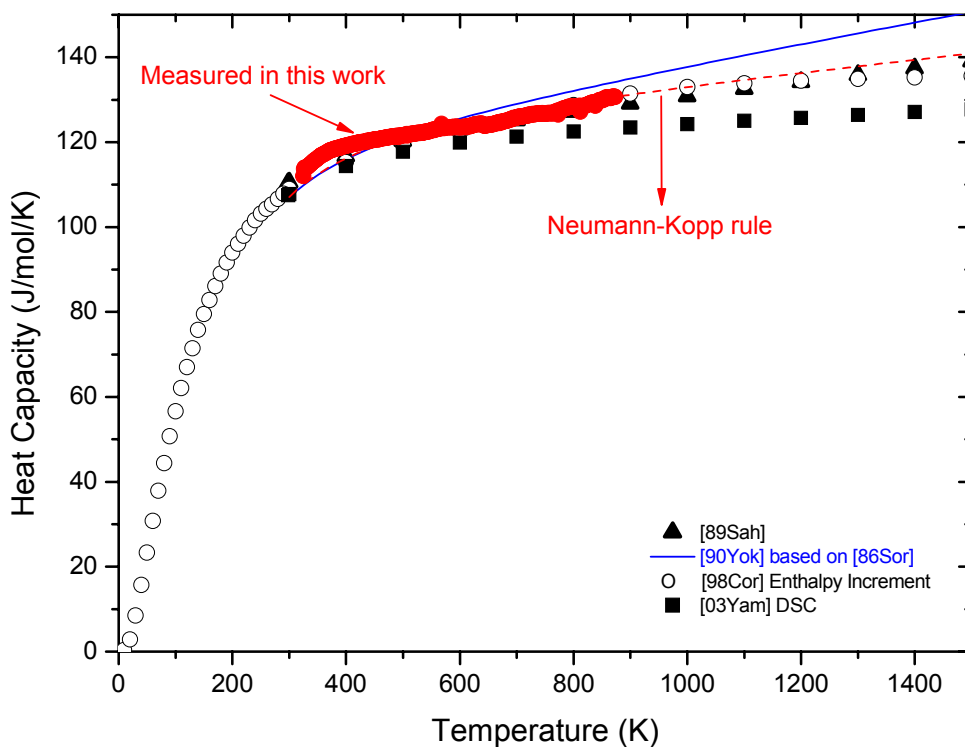


Fig. 3.63. The temperature dependence of the molar heat capacity of  $\text{SrCeO}_3$  is shown, using data measured by Cordfunke *et al.* [98Cor], other data from the literature, and combined with the heat capacity data above room temperature, measured in this present study.

SrO solubility in CeO<sub>2</sub> was investigated on a sample in the (Ce,Sr)O<sub>2-x</sub>-SrCeO<sub>3</sub> two-phase field by SEM-EDX analysis. The sample was heat-treated at 1400 °C, then quench-cooled in air. Fig. 3.64 shows the microstructural morphology as seen in the SEM. The solubility value (7.85±0.5 mol % SrO) determined from EDX analysis is in excellent agreement with the data of Mastromonaco and co-workers [69Mas]. For thermodynamic modeling of the (Ce,Sr)O<sub>2-x</sub> solid solution, both literature and the measured data were used.

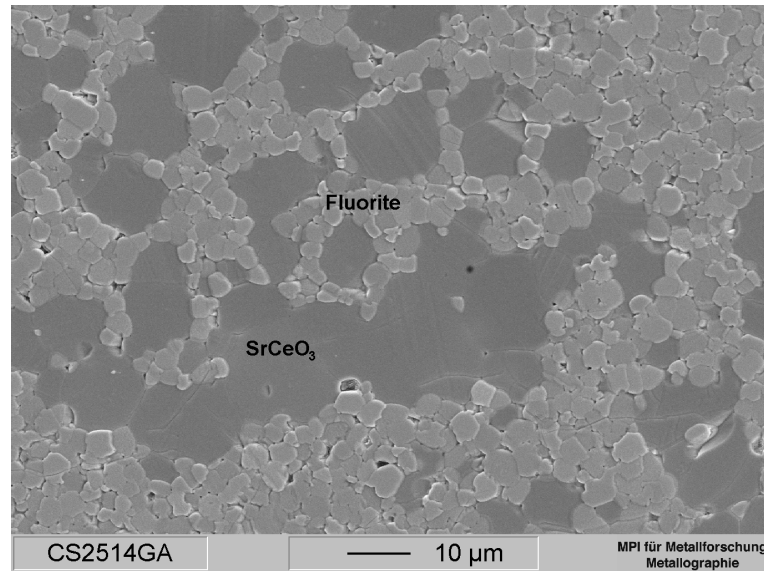
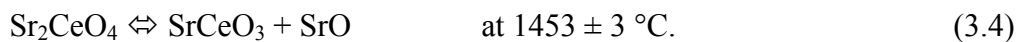


Fig. 3.64. SEM micrograph of the 25 mol% SrO-containing sample that was heat-treated at 1400 °C for 60 h and quench-cooled in air.

The description of both ternary compounds was obtained by simultaneously fitting the heat capacity data above 298 K and the standard entropy values, which were calculated by the numerical integration under the curve  $C_p/T$  vs.  $T$  within the temperature range of 0-298 K, according to the third law of thermodynamics. The heat capacities below 4 K were calculated using the  $T^3$ -approximation. The enthalpy of formation of SrCeO<sub>3</sub> [98Cor, 90Gou] and Sr<sub>2</sub>CeO<sub>4</sub> [04Bas] were taken from literature. In order to resolve the uncertainty in the high temperature heat capacity data of the Sr<sub>2</sub>CeO<sub>4</sub>, the decomposition reaction of the Sr<sub>2</sub>CeO<sub>4</sub> compound was used. The reaction is defined as follows:



In the first step of the optimization, the parameters of SrCeO<sub>3</sub> were determined, because those thermodynamic properties are well known. Then, the equilibrium at the decomposition temperature was applied, and finally, all parameters were optimized together. The optimization for the high temperature heat capacity of Sr<sub>2</sub>CeO<sub>4</sub> showed excellent agreement with the theoretical Neumann-Kopp curve. All phase equilibria and thermodynamics were reproduced very well.



The main discrepancy in the literature is in the liquidus part of the diagram. Preda, *et al.* [76Pre] reported that eutectic temperatures are at 1650 °C, for a composition of 70 mol% SrO and at 1760 °C for a composition of 28 mol% SrO. However, no liquid phase was detected at temperatures up to 1800 °C [81Lon]. Similar discrepancies were reported for the melting point of the SrCeO<sub>3</sub> compound. The value reported by Longo, *et al.*, at 1900 °C [81Lon] is substantially lower than obtained by Melekh, *et al.*, at 2223 °C [97Mel]. A large uncertainty was obtained, when using the liquidus data of Preda, *et al.* [76Pre] and data of Melekh, *et al.* [97Mel] together in the first step of the optimization. In the second step, the data of Preda, *et al.* were omitted and only the liquidus temperature determined by Melekh, *et al.* [97Mel] was taken into account. Using a regular interaction parameter, reasonable results have been obtained. The calculated CeO<sub>2</sub>-SrO quasi-binary section is given in Fig. 3.65, together with the experimental results and literature data. The obtained thermodynamic parameters of the ternary compounds in comparison with the literature data are presented in Table 3.5.

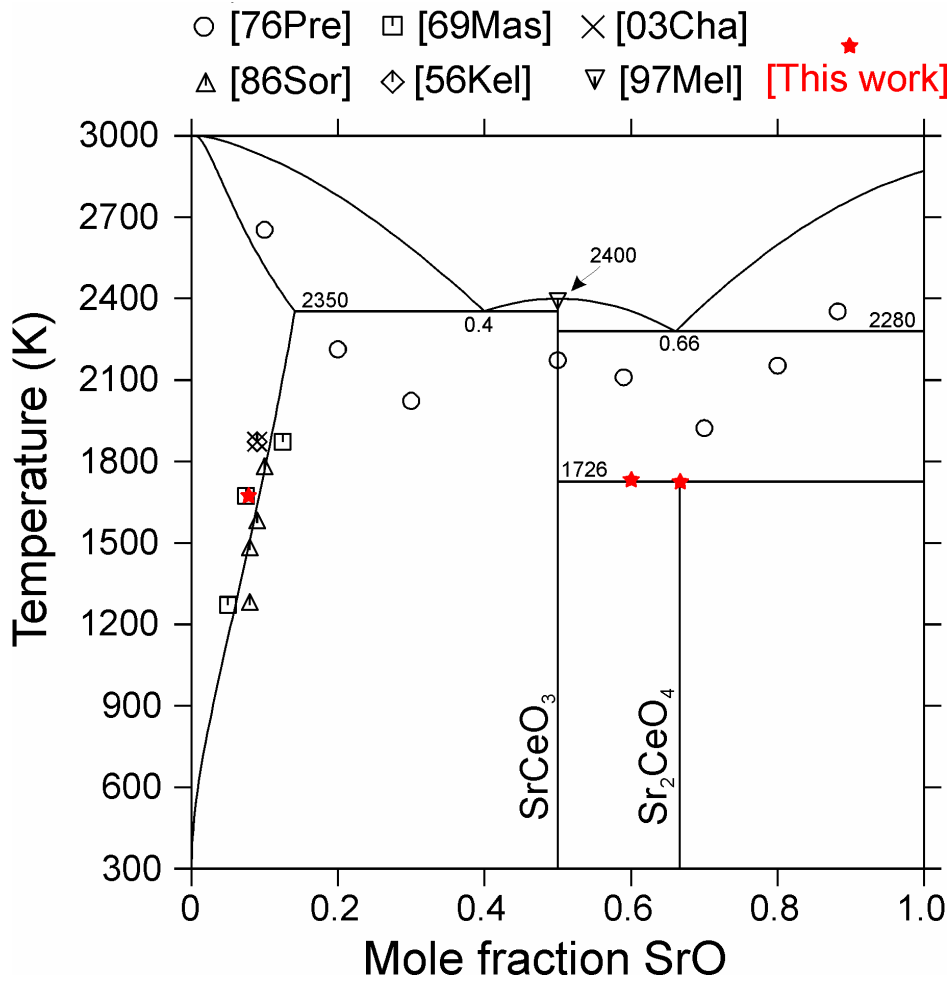


Fig. 3.65. The calculated CeO<sub>2</sub>-SrO phase diagram including literature data is presented with the experimental results of this work.

Table 3.5. The thermodynamic parameters obtained for the ternary compounds, compared with previously reported data.

Compound	$\Delta_f^\circ H_{298}$ (kJ·mol <sup>-1</sup> )	$^\circ S_{298}$ (J·mol <sup>-1</sup> ·K <sup>-1</sup> )	$C_p$ (J·mol <sup>-1</sup> ·K <sup>-1</sup> )	Reference
Sr <sub>2</sub> CeO <sub>4</sub>	- 2283.89 - 2777	182.1 ± 2.1	167.986 + 0.020264 $T$ - 1 964 000 $T^{-2}$	This work [04Bas]
SrCeO <sub>3</sub>	- 1687.08 -1687.9	131.19 125.6	120.426 + 0.014124 $T$ - 1584 000 $T^{-2}$ 114.63 + 0.02445 $T$ - 1345 000 $T^{-2}$	This work [86Sor]

The chemical potential diagrams of the Ce-Sr-O system at 700 and 1500 °C were calculated and are presented in Fig. 3.66. It can be seen from the diagrams that under SOFC operation conditions, the Sr<sub>2</sub>CeO<sub>4</sub> compound is not chemically compatible with cerium oxides, except the sesquioxide (Ce<sub>2</sub>O<sub>3</sub>) under highly reducing conditions. They react to form SrCeO<sub>3</sub>. Because the Sr<sub>2</sub>CeO<sub>4</sub> compound decomposes at 1453 °C into SrCeO<sub>3</sub> and SrO, the Sr<sub>2</sub>CeO<sub>4</sub> compound does not appear in the 1500 °C diagram (b), and new equilibria are established between SrO and SrCeO<sub>3</sub>. Hence, SrCeO<sub>3</sub> and SrO are compatible only above the decomposition temperature of Sr<sub>2</sub>CeO<sub>4</sub> compound. The SrO compound is compatible only with cerium sesquioxide under highly reducing conditions, and it reacts with all the other cerium oxides producing ternary compounds. The composition of these products would depend on the temperature and oxygen partial pressure of operation.

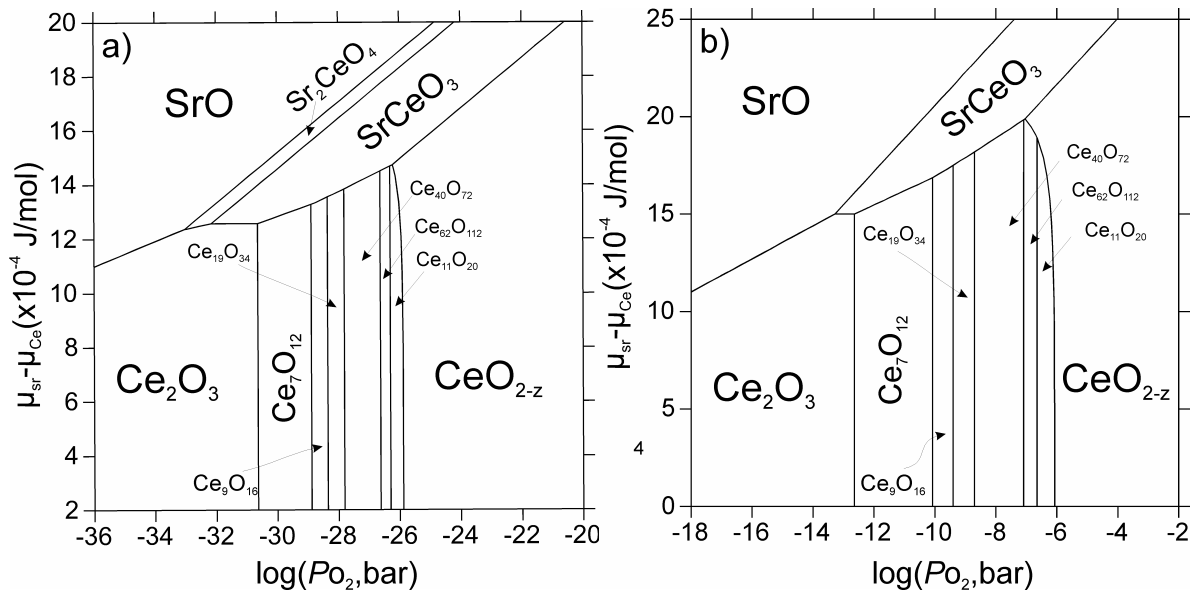


Fig. 3.66. Calculated phase stability diagrams of the Sr-Ce-O system at 700 °C (a) and at 1500 °C (b).

### 3.4.3. The Gd-Ni-O Subsystem

In the *Gd-Ni-O* system, the  $Gd_2O_3$ -NiO quasi-binary section was first experimentally investigated by Willer and Lehuede [70Wil]. It was reported that the system is of a simple eutectic type. Later the proposed diagram was confirmed by Dubois, *et al.* [86Dub] in their study of directionally solidified  $Gd_2O_3$ -NiO eutectics. It was shown in both studies that there was no detectable mutual solubility and that during crystal growth, B- $Gd_2O_3$  formed at low temperatures instead of C- $Gd_2O_3$ . It was also known that under normal conditions the  $K_2NiF_4$  structure would not be stable for small rare earth ions, such as  $Sm_2NiO_4$  and  $Gd_2NiO_4$  [93Che]. However, the existence of  $Gd_2NiO_4$  in the same quasi-binary section was reported by Vygovskii, *et al* [74Vyg]. To investigate this discrepancy, samples were prepared by a wet chemical method using co-precipitated hydroxides as starting materials. A short duration heat-treatment program was applied as follows: at 800 °C for 15 h, at 1000 °C for 6 h, and at 1200 °C for 3 hours. The crystal structure, magnetic properties and phase transition in the perovskite  $GdNiO_3$  compound were investigated in detail (*e.g.* [97Med]), but those results would not be considered in the present work, since  $GdNiO_3$  is a high pressure phase. No information has been found about its stabilization by another component in higher-order systems relevant to IT-SOFC technology.

In the present work, two samples were prepared at the gadolinia rich side of the  $Gd_2O_3$ -NiO quasi-binary diagram, with compositions of 25 mol % NiO (GN25) and 50 mol % NiO (GN50, *i.e.*, the “ $Gd_2NiO_4$ ” compound). Heat-treatments were performed at three different temperatures, 1000, 1250 and 1500 °C, each for 120h.

In Fig. 3.67, XRD patterns of the GN25 sample are given. The sample heat-treated at 1000 °C (Fig. 3.67-a) showed only the cubic gadolinia and nickel oxide peaks. There was no shift with respect to the original positions of the peaks, as expected from the literature [86Dub], and also no indication that a new phase had formed. With increasing temperature, at 1250 °C, a non-reversible cubic to monoclinic phase transition could be seen in Fig. 3.67b. Again, neither a peak shift with respect to the original positions of the phases, nor any indication of a new phase was observed.

Fig. 3.68 presents the XRD patterns of the GN50 sample heat-treated at 1250 and 1500 °C. As was the case for the GN25 sample, the monoclinic gadolinia (B-type) and nickel oxide peaks were determined in the GN50, and small cubic gadolinia peaks were determined on the 1250 °C pattern, which decreased with increasing temperature. The TG/DTA curve of the GN50 sample, calcined at 850 °C and heat-treated at 1000 °C, is shown in Fig. 3.69. During

the heating and cooling cycle, a negligible weight change was observed. Only when the operation mode changed from dynamic to isothermal could an abrupt change be observed on the graph, which is a common instrumental error. In the entire range of analysis up to the eutectic transition peak, a slowly varying DTA signal was observed, that could be associated with the cubic to monoclinic phase transition. The eutectic temperature was established to be 1575 °C by a very strong DTA peak, and it was reproduced with an accuracy of 5 K. The result was in close agreement with the value of 1536 °C, reported by Willer [70Wil]. Only B-Gd<sub>2</sub>O<sub>3</sub> and NiO peaks were observed by XRD analysis, without any additional peaks indicative of formation of a new phase.

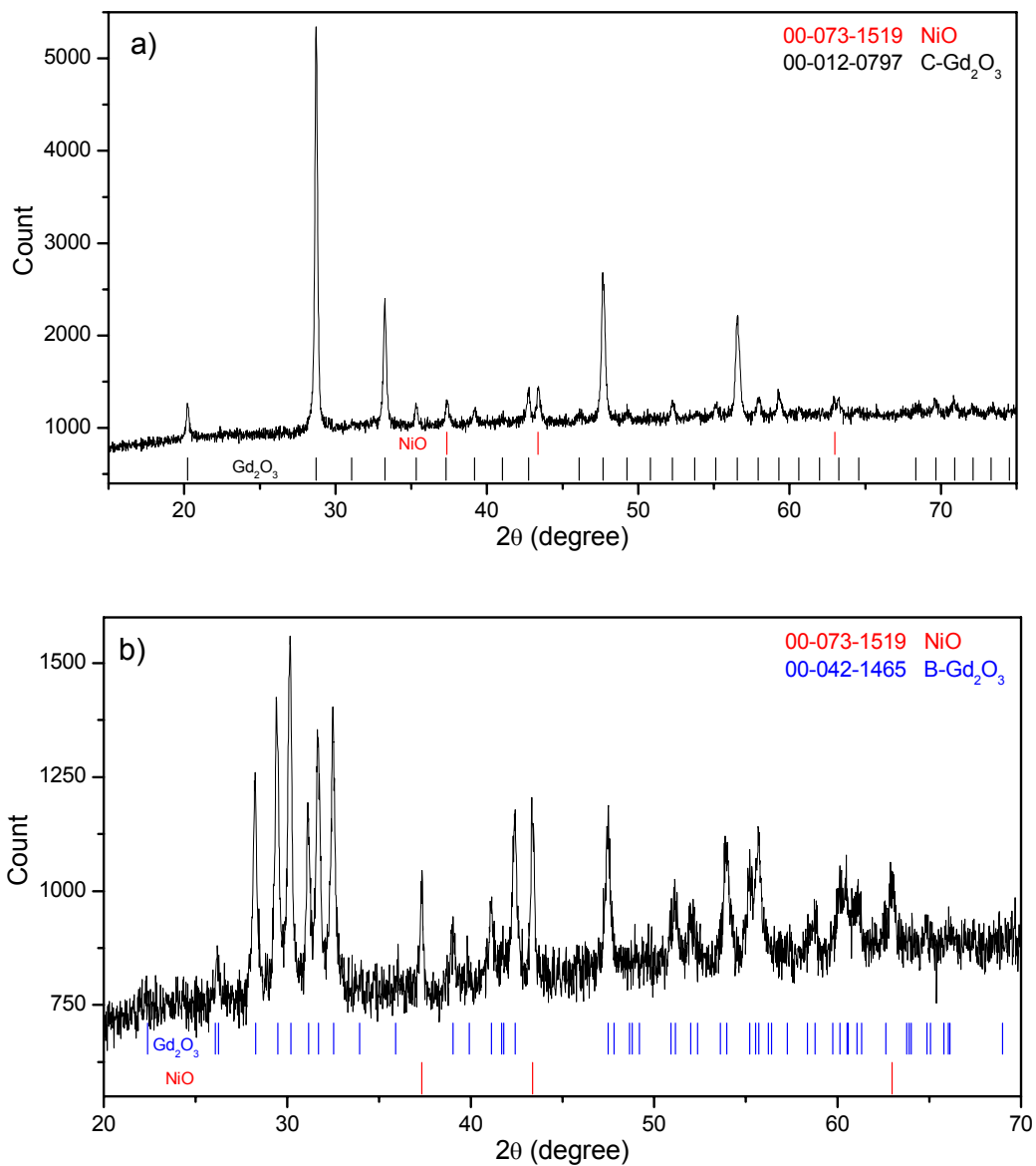


Fig. 3.67. XRD powder patterns of the sample containing 25 mol% NiO (GN25), heat-treated at 1000 °C (a) and 1250 °C (b) for 120 h.

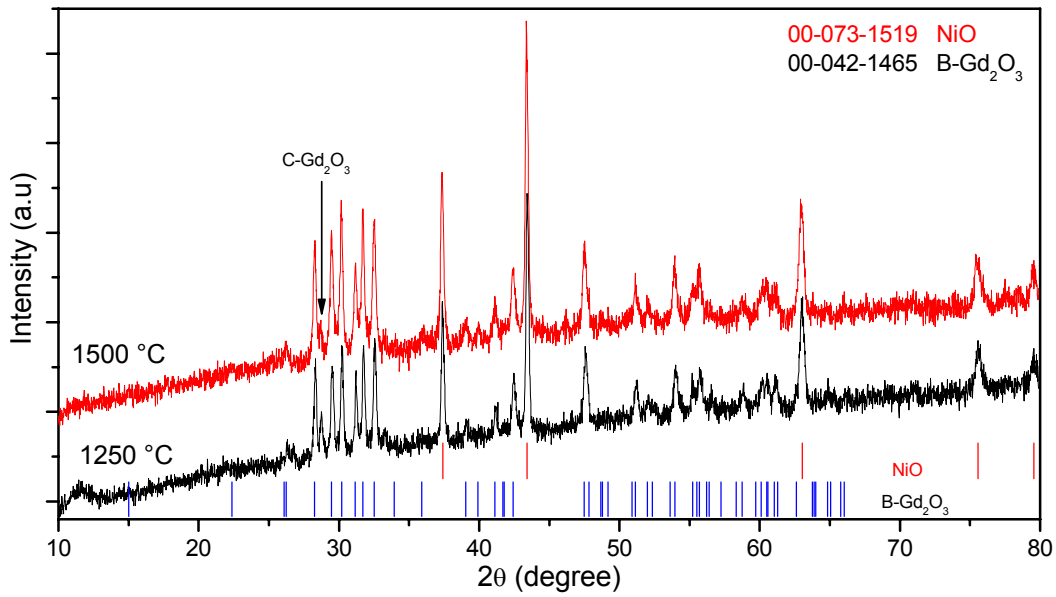


Fig. 3.68. XRD powder patterns of the sample containing 50 mol% NiO (GN50), heat-treated at 1250 °C and 1500 °C, for 120 h.

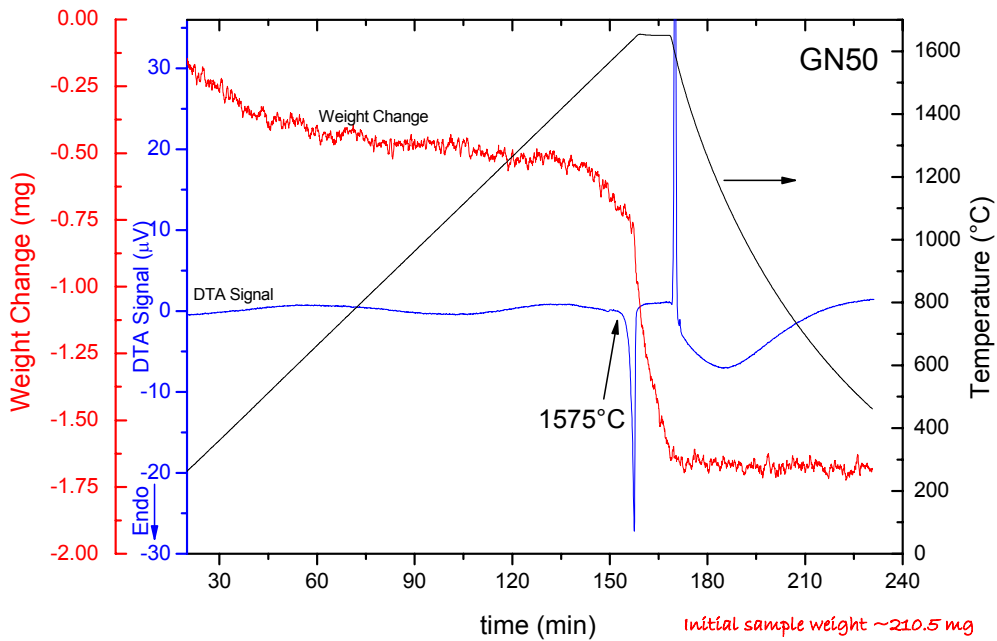


Fig. 3.69. TG and DTA curves recorded on heating and cooling the GN50 sample.

Since there is no mutual solubility between NiO and all modifications of gadolinia [70Wil] and no ternary compound, the system was modeled using the description of pure NiO and Gd<sub>2</sub>O<sub>3</sub>. For the liquid phase, the eutectic temperature determined in this work was used. The calculated Gd<sub>2</sub>O<sub>3</sub>-NiO quasi-binary phase diagram is presented in Fig. 3.70 with the literature data and experimental results obtained in this work marked by circle and star symbols.

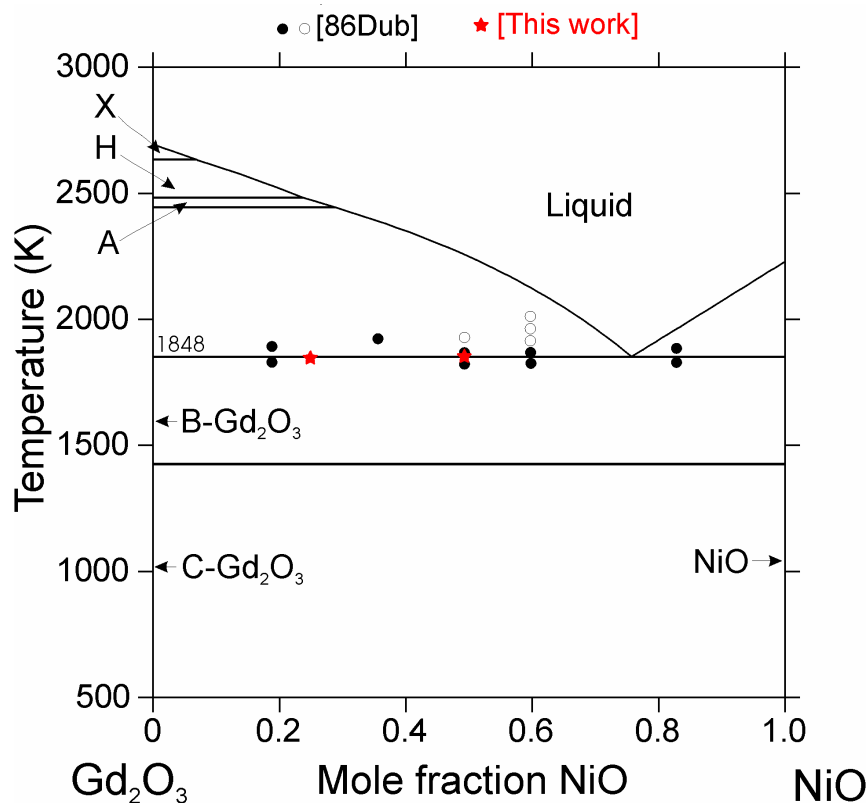


Fig. 3.70. The calculated Gd<sub>2</sub>O<sub>3</sub>-NiO quasi-binary phase diagram is being presented. Stars indicate the sample compositions used to determine the eutectic temperature experimentally in this work. Circles are the experimental results of Dubois and co-workers [86Dub]--open circles for the liquid phase, and closed circles for the two-phase fields.

The liquidus part of the diagram was modeled using a regular interaction parameter, and the eutectic temperature was reproduced well. However, good agreement could not be obtained on the eutectic composition. The application of a temperature-dependent term or subregular parameters did not improve the diagram. A more complicated model could be necessary to reproduce the composition but then this would generate more complications in the higher-order systems. Therefore, no further optimization was performed, and only the regular optimization parameters were applied. The obtained parameters are given in the Appendix.

In the metallic system, Gd and Ni were not mutually soluble [90Mas]. Thus, the data on the lower order subsystems were directly adapted, and phase stability diagrams of the Gd-Ni-O system were calculated at various temperatures, which are presented in Fig. 3.71. At low temperatures, both the cubic and the monoclinic modifications of gadolinia were in equilibrium with both Ni and NiO. With increasing temperature, the liquid phase began to appear, interrupting the direct contact between nickel oxide and gadolinia. Instead a new equilibrium was established between the liquid phase and separately, gadolinia and nickel oxide. On the diagram, gadolinia is simply written as Gd<sub>2</sub>O<sub>3</sub>, but it should be considered that

at 1152 °C the cubic to monoclinic transition takes place [06Zin1] and above this temperature monoclinic gadolinia is the stable phase and is below the cubic one.

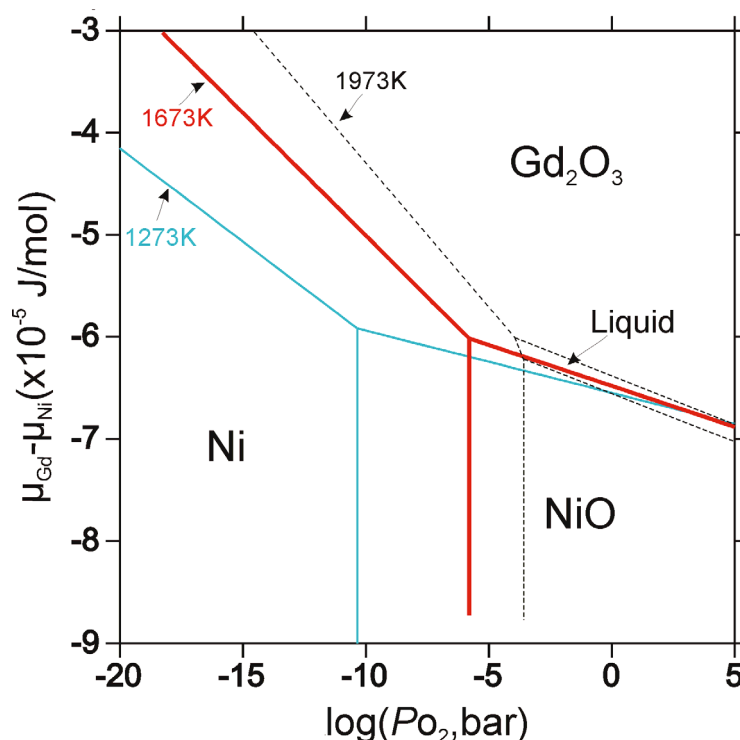


Fig. 3.71. The calculated phase stability diagram for the Gd-Ni-O system, at 1000, 1400 and 1700 °C.

### 3.4.4. The Gd-Sr-O Subsystem

In the *Gd-Sr-O* system the quasi-binary section Gd<sub>2</sub>O<sub>3</sub>-SrO was investigated by Kuschevskii, and co-workers [71Kus, 72Lop], by using XRD, DTA and petrographic analysis techniques. They had reported the existence of the compounds, Gd<sub>2</sub>SrO<sub>4</sub> and Gd<sub>4</sub>SrO<sub>7</sub>, which were stable above 1905 °C without homogeneity ranges. They had also determined a relatively high SrO solubility in Gd<sub>2</sub>O<sub>3</sub>, and a Gd<sub>2</sub>O<sub>3</sub> solubility in SrO of almost 10 mol%. Formation of the Gd<sub>2</sub>SrO<sub>4</sub> compound had been confirmed by several other groups [73Lop, 81Pep, 01Ant, 03Cha]. The melting point of this compound was reported as 2120 °C [71Kus, 73Lop]. The existence of Gd<sub>4</sub>SrO<sub>7</sub> was first reported by Barry and Roy [67Bar], in a study about the formation of compounds, when rare earth sesquioxides were in contact with alkaline earth oxides. The samples were prepared using the soft chemistry method, heat-treating at 1850 °C for 3 h and quenching into a jet of cold air, and characterized by X-ray powder diffraction. Sammels, *et al.* had reported the existence of another compound in the system, Gd<sub>2</sub>Sr<sub>2</sub>O<sub>5</sub>, which has a Brownmillerite structure [92Sam]. This phase was not observed in the work of Kuschevskii [71Kus] nor in any other study in the literature.

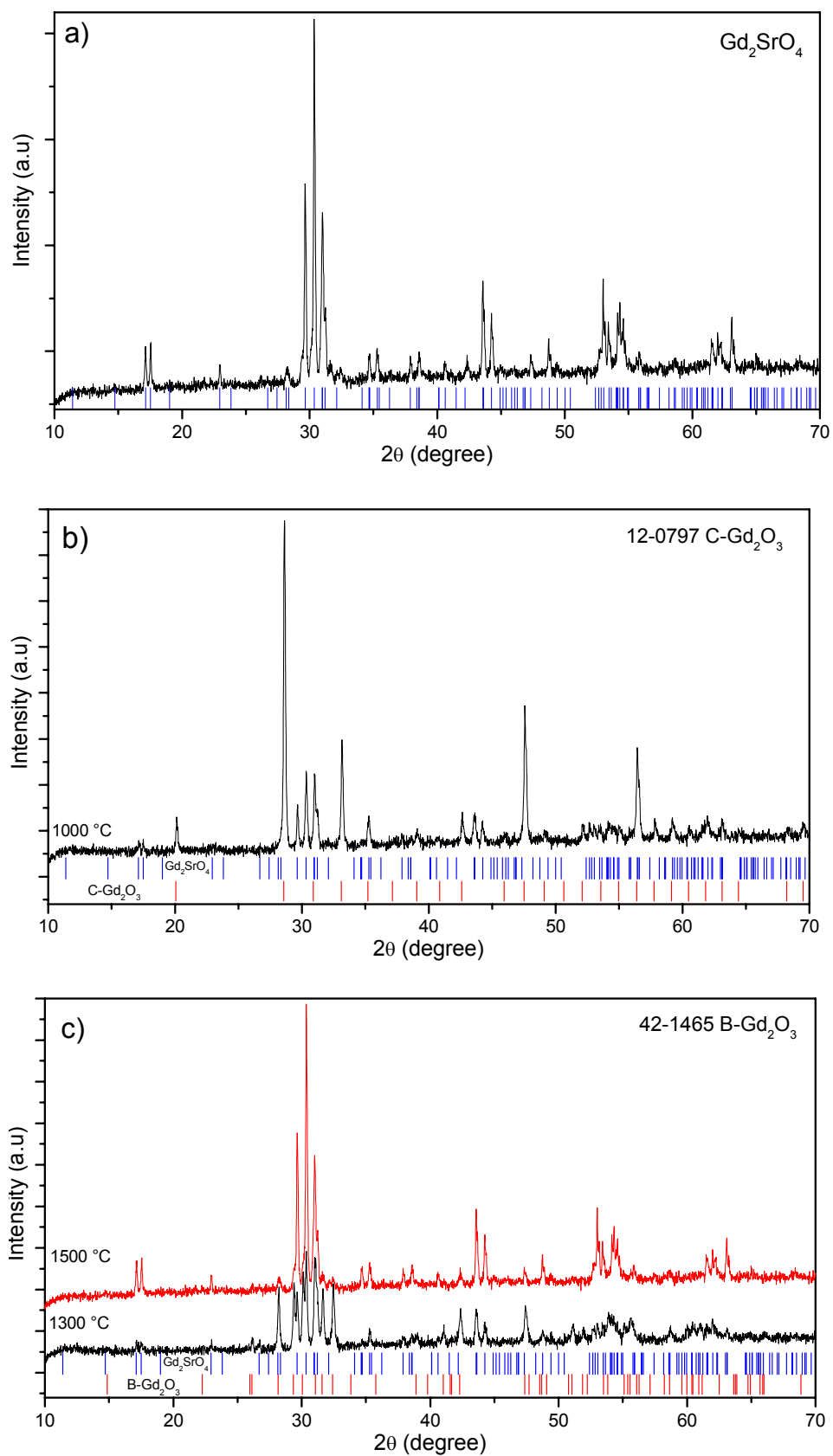


Fig. 3.72. XRD powder patterns of the samples,  $Gd_2SrO_4$  (a), GS25 heat-treated at  $1000^\circ C$  (b) and,  $1300^\circ C$  and  $1500^\circ C$  (c). Card file for the  $Gd_2SrO_4$  compound is generated in this work using the literature data [03Cha].



After heat treatment at 1300 °C for 120 h, the stoichiometric  $\text{Gd}_2\text{SrO}_4$  sample was characterized by XRD (see Fig. 3.72a). Comparison with the literature data [03Cha] revealed that the compound was phase-pure. Samples GS25 and GS67 were heat-treated at 1000, 1300 and 1500 °C, for 120 h. After heat-treatments, the samples were both furnace cooled and quenched in air. No significant effect of cooling rate was observed on the phase equilibria. The XRD pattern of the GS25 sample is given in Fig. 3.72b. As expected, at 1000 °C cubic-gadolinia was in equilibrium with the  $\text{Gd}_2\text{SrO}_4$  compound. There was almost no shift in the peaks of the gadolinia phase with respect to their original positions.

With increasing temperature, the non-reversible cubic to monoclinic phase transition began, and a new equilibrium was established between the monoclinic gadolinia (B- $\text{Gd}_2\text{O}_3$ ) and  $\text{Gd}_2\text{SrO}_4$  (Fig. 3.72c). The peak positions of both phases were aligned perfectly with their original (*i.e.*, phase pure) positions. SEM-EDX analysis was performed on the GS25 sample, which was heat-treated at 1500 °C and quenched in air, as shown in Fig. 3.73. According to the EDX analysis, both  $\text{Gd}_2\text{O}_3$  and  $\text{Gd}_2\text{SrO}_4$  did not deviate significantly from their stoichiometry. The Gd-rich side of the diagram was found to be in very good agreement with the experimental diagram of Kushchevskii [71Kus].

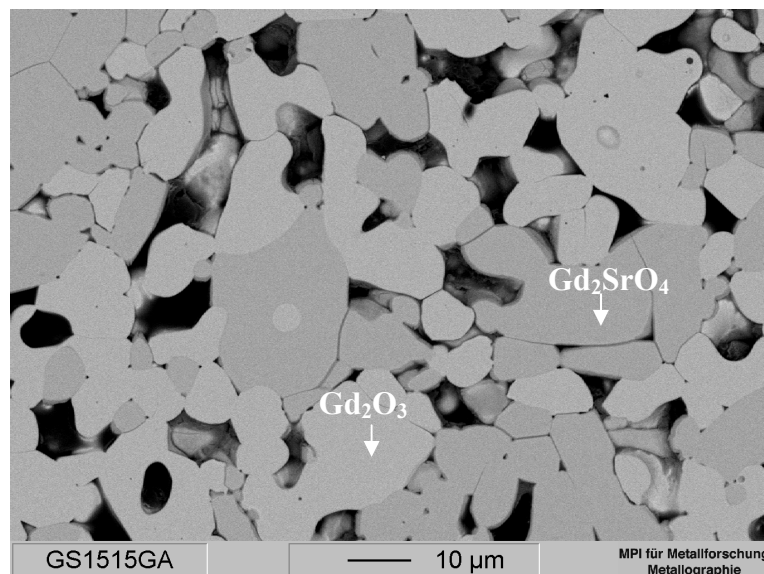


Fig. 3.73. SEM micrograph of 25 mol% SrO containing sample heat-treated at 1500 °C for 120 h and quenched in air.

The GS67 sample was heat-treated at 1300 °C for 120 h, and the measured XRD pattern is given in Fig. 3.74. Again, the  $\text{Gd}_2\text{SrO}_4$  peaks were aligned perfectly in their original positions without any apparent peak shift. SrO had transformed to a hydroxide, rendering it impossible to determine peak shift of the oxide, because the peak position of a hydroxide is directly related to its water content. Special care had been taken for the SEM sample preparation of

the SrO-rich side of the diagram. As with the other SEM micrographs imaged from SrO-containing samples, the image quality (Fig. 3.75) is not high, but the EDX results were highly reproducible. According to the EDX analyses, the  $\text{Gd}_2\text{SrO}_4$  phase remained stoichiometric. A small gadolinia solubility in SrO ( $1.9 \pm 0.4$  mol %) was detected, consistent with the observations of Kushchevskii [71Kus]. No indication for the existence of  $\text{Gd}_2\text{Sr}_2\text{O}_5$  [92Sam] was found, neither by XRD nor by SEM-EDX analyses. As demonstrated in Fig. 3.74, the XRD pattern matched well with the calculated  $\text{Gd}_2\text{SrO}_4$  and Sr-hydroxide patterns, and there was not an unidentified peak that could have belonged to  $\text{Gd}_2\text{Sr}_2\text{O}_5$ .

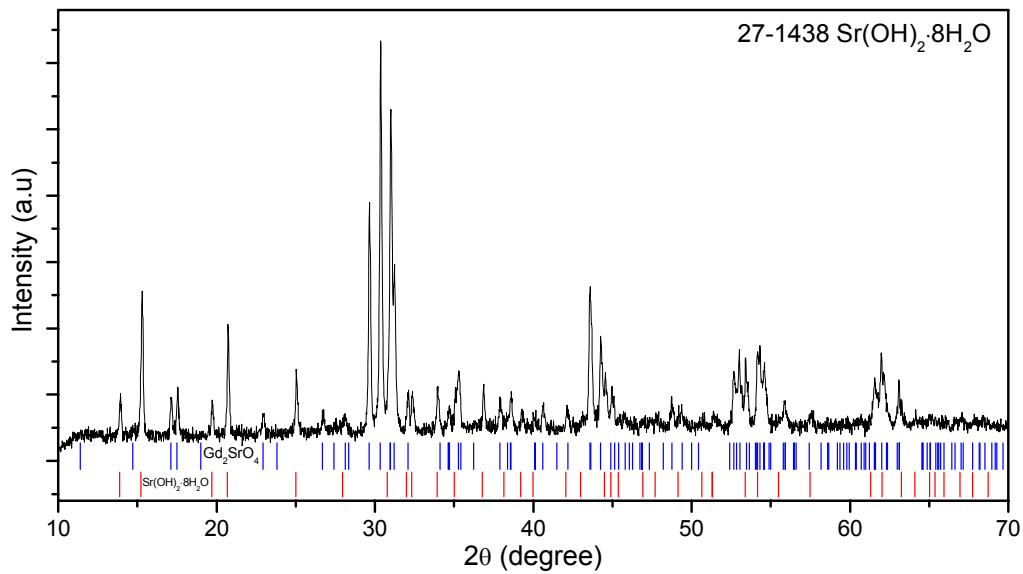


Fig. 3.74. XRD powder patterns of the GS67 samples heat-treated 1300 °C for 120 h.

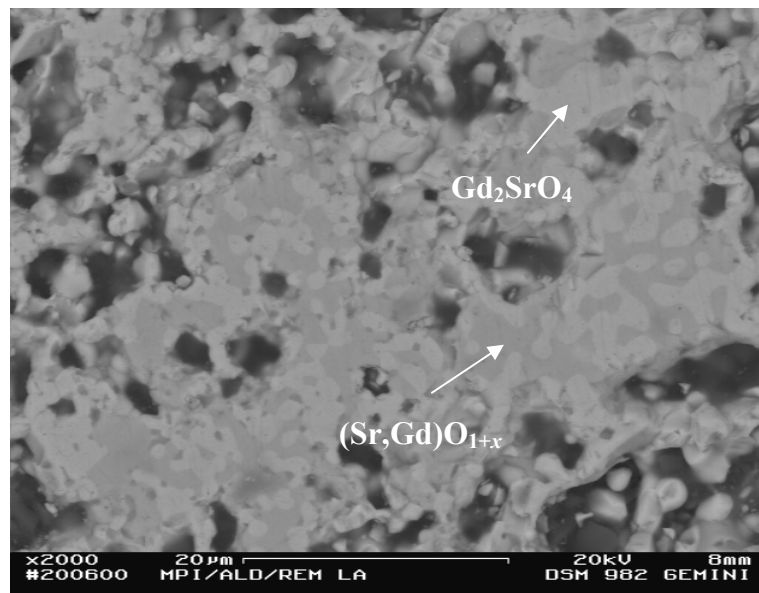


Fig. 3.75. SEM micrograph of 66.67 mol% SrO-containing sample heat-treated at 1300 °C for 120 h and quenched in air. Light grey areas are  $\text{Gd}_2\text{SrO}_4$ , and grey areas are  $(\text{Sr,Gd})\text{O}_{1+x}$ .

For thermodynamic modeling of the system, the phase equilibria obtained by Kushchevskii [71Kus] were used. Both  $\text{Sr}_4\text{Gd}_2\text{O}_7$  and  $\text{SrGd}_2\text{O}_4$  compounds were taken as stoichiometric. By using a limited number of parameters, the system was easily assessed. The SrO-rich side and the liquidus part of the diagram were in good agreement with the experimental diagram. Although the calculated melting points of the ternary compounds were very close to the experimental one, and the shape of the liquidus curve was in a reasonable agreement, a more complicated model would be necessary in order to improve the fit of the liquidus curve, which is out of scope of the thesis. The main difference between the experimental diagram [71Kus] and the calculated one could be found on the gadolinia-rich side. The stated high solubility of SrO in A-, H- and X-type  $\text{Gd}_2\text{O}_3$  could not be reproduced. A similar problem was also seen in the  $\text{La}_2\text{O}_3$ -SrO system [02Gru]. Although the ionic radius of  $\text{La}^{3+}$  is larger than that of  $\text{Gd}^{3+}$  [69Sha], the solubility of SrO in  $\text{Gd}_2\text{O}_3$  (all modifications) is higher than that of  $\text{La}_2\text{O}_3$ . It is possible that petrographic analysis was not sufficiently sensitive for analyzing the phase content. In addition, XRD might not have been sufficiently sensitive to locate the phase boundaries.

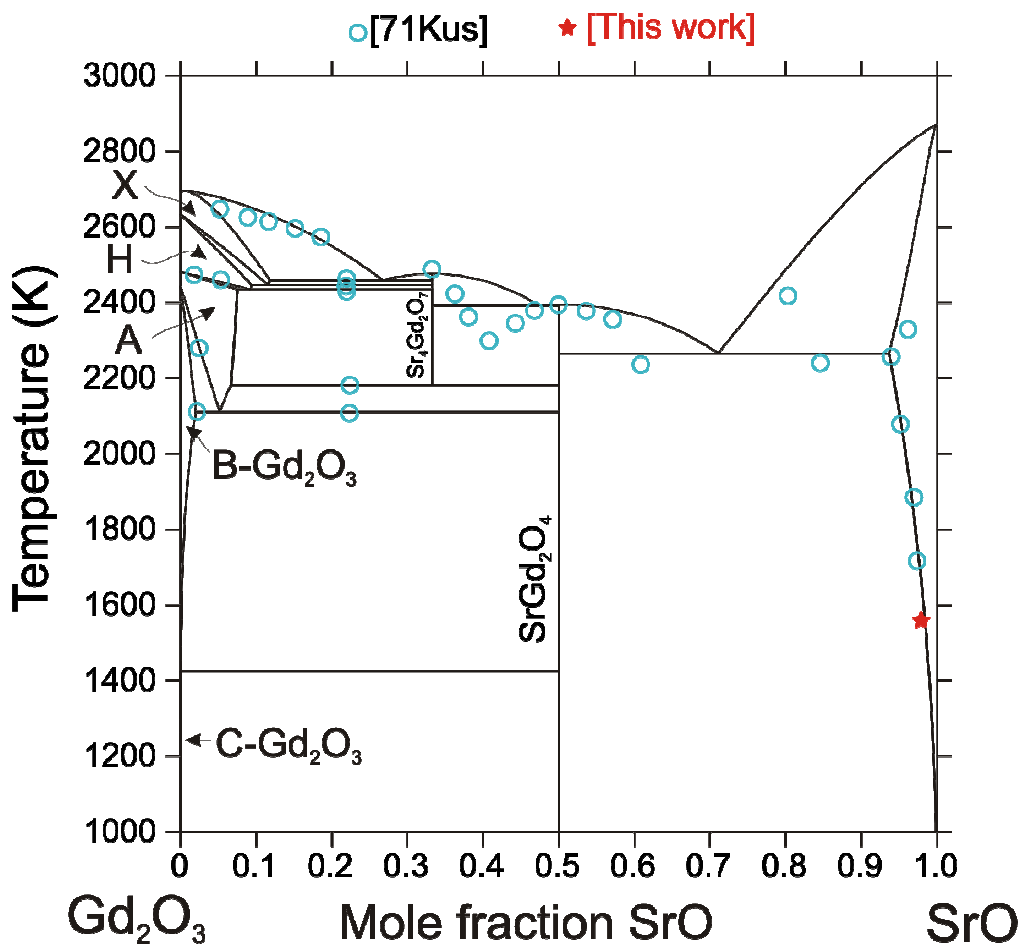


Fig. 3.76. The calculated  $\text{Gd}_2\text{O}_3$ -SrO quasi-binary phase diagram, containing literature data and experimental results from this work.

In the optimization procedure, first a metastable phase diagram (omitting the ternary phases) was calculated, and the homogeneity ranges of the A-, H-, X-phases in  $\text{La}_2\text{O}_3$  and  $\text{Gd}_2\text{O}_3$  were compared. Then, the system was re-optimized using all information including the ternary phases. The phase diagram constructed is shown in Fig. 3.76, coupled with the literature data and the experimental results from this work.

### 3.4.5. The Ce-Gd-Ni-O Subsystem

The chemical compatibility of the gadolinia-doped ceria (CGO) and Ni/NiO couple has been well-established [00Mog, 06Mor]. Therefore, relatively simple phase equilibria are expected for the  $\text{CeO}_2$ - $\text{GdO}_{1.5}$ -NiO quasi-ternary. The system was directly extrapolated from the subsystems defined in the previous sections. No additional interaction parameters were used. The calculated phase diagram is given in Fig. 3.77. To verify the predicted equilibria, three samples were prepared, CGN10-50, CGN33-33, and CGN60-20, having compositions as indicated in the Fig. 3.77. Heat-treatments were performed at 1300 and 1500 °C. After heat-treatment, the samples were either quenched or furnace cooled and characterized by XRD and SEM-EDX.

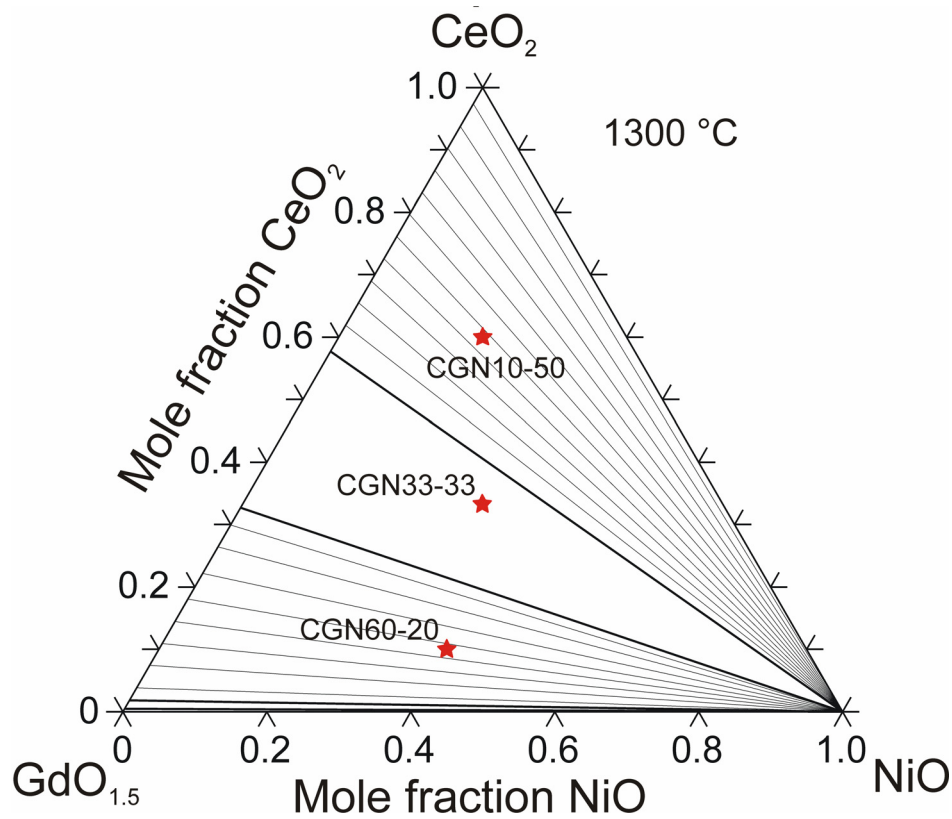


Fig. 3.77. Calculated 1300 °C isothermal section of the  $\text{CeO}_2$ - $\text{GdO}_{1.5}$ -NiO phase diagram. Stars show the experimental compositions investigated for validation of the predicted equilibria.

The XRD powder patterns of the samples heat-treated at 1500 °C are given in Fig. 3.78. Neither the heat-treatment temperature nor the cooling rate appeared to have an effect on the XRD patterns, *i.e.*, on phase equilibria. Therefore, only the patterns, which belong to the samples heat-treated at 1500°C, are provided for reference. According to the calculations, the CGN10-50 sample should be located in a two-phase field formed by (Ce,Gd)O<sub>2-x</sub> (fluorite structure) and nickel oxide in equilibrium. The corresponding XRD pattern is in very good agreement with the calculation. The other two samples, CGN33-33 and CGN60-20, showed additional peaks which belong to cubic gadolinia. Cubic gadolinia has almost the same peak positions as ceria with additional reflections. Therefore, it is not possible to distinguish between pure C-phase and F- and C-phase mixtures by using conventional XRD techniques, where the C-phase refers to the gadolinia-rich one, while the F-phase refers to the ceria-rich one. The NiO peaks were identical to the peak pattern of pure NiO for all the samples heat-treated at different temperatures and furnace cooled or quenched; clearly there was no detectable solubility of the other components, in agreement with the literature. For further characterization, SEM samples were prepared and analyzed.

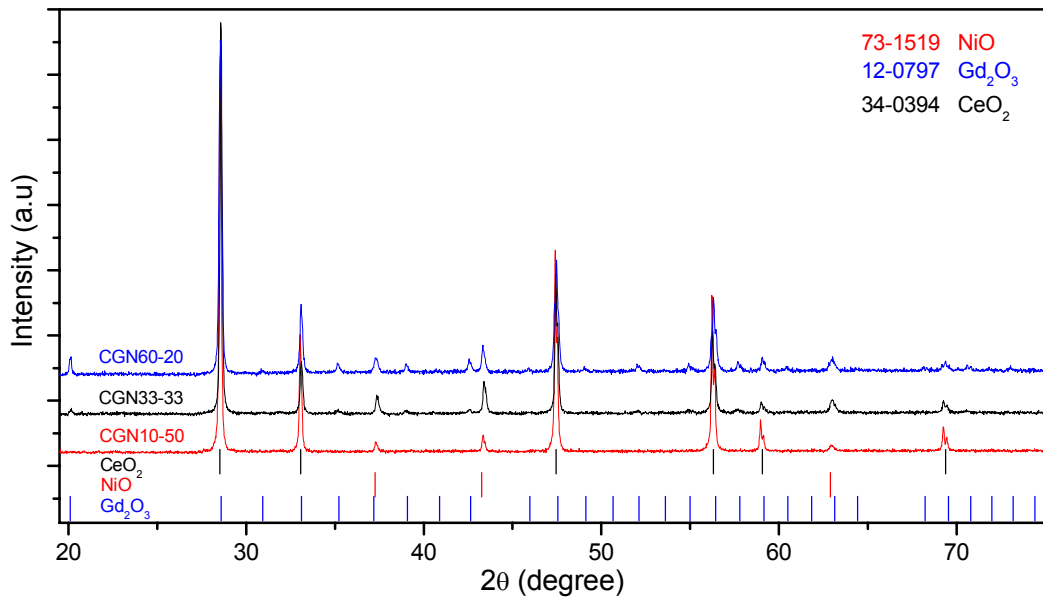


Fig. 3.78. XRD powder patterns of the samples heat-treated at 1500 °C for 120 h.

An SEM micrograph of CGN33-33 is shown in Fig. 3.79. In the figure, the dark grains are NiO, without detectable solubility of the other two components. The ceria-rich (F-type) and gadolinia rich-phases (C-type) could not be distinguished when imaged using the back-scattered electron mode, because both phases have the same constituent atoms, so the same atomic numbers would generate similar levels of relative contrast. Thermal etching also did

not reveal a difference between the two phases. Consequently, the extrapolation from the quasi-binary subsystem was used without applying any further interaction parameter.

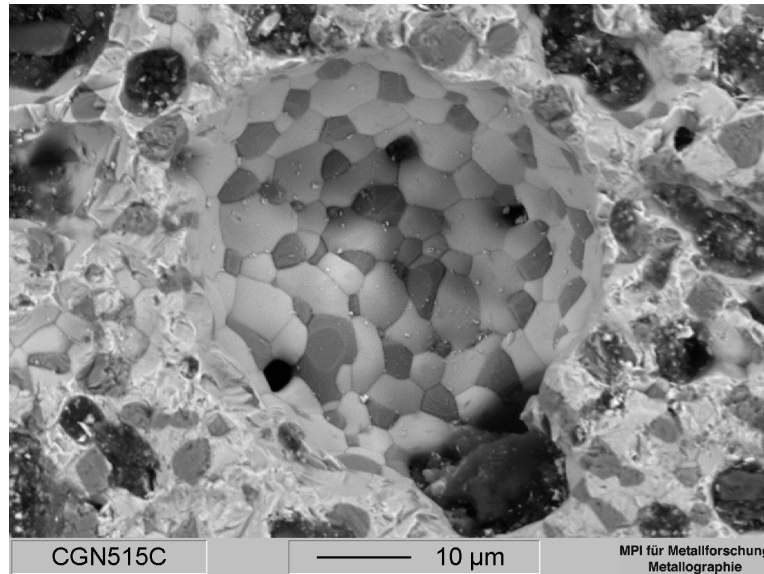


Fig. 3.79. An SEM micrograph of CGN33-33 sample heat-treated at 1500 °C for 120 h and thermally etched.

### 3.4.6. The Ce-Gd-Sr-O Subsystem

Even though the  $\text{SrCe}_{0.9}\text{Gd}_{0.1}\text{O}_3$  solid solution is technologically attractive as a proton conductor, no experimental or computational phase diagram or thermodynamic study is currently available in the literature about the Ce-Gd-Sr-O system, with the exception of the electrochemical performance data of this specific solid solution [01Lu, 05Kru]. Therefore, to investigate this system experimentally, 15 compositions were selected strategically for analysis, the minimum necessary to construct the phase equilibria diagram for this particular system. These compositions are indicated by stars on the experimentally derived phase diagrams in Fig. 3.80.

To determine the homogeneity range of the solid solutions, represented by the heavy black lines in Fig. 3.80, the compositions investigated were selected from 2- and 3-phase fields. For the  $\text{Sr}(\text{Ce},\text{Gd})\text{O}_3$  solid solution, CSG40-50, CSG30-50 were the compositions chosen. The extended solid solution of  $(\text{Gd},\text{Ce})_2(\text{Sr},\text{Ce})\text{O}_4$  was also investigated via samples CSG10-50, CSG20-50, CSG30-50, CSG10-40, CSG10-33, and CSG13-67. Next, to establish the 3-phase fields marked as “1” and “2”, samples CSG30-20, CSG37-33, CSG32-33, and CSG30-10 were chosen. Finally, based on prior knowledge of the  $\text{CeO}_2$ - $\text{GdO}_{1.5}$  and  $\text{CeO}_2$ - $\text{SrO}$  quasi-binaries and the samples in the SrO-poor regions of the system, the extension of the F-, C- and two-phase F+C fields into the ternary was investigated.

All 15 samples were prepared using the same Pechini-type method for the other samples in this study. Heat-treatments of the samples were performed at 1300 and 1500 °C. The XRD results are summarized in Table 3.6. Diffraction patterns indicated the phases present, while shifts in the peaks suggested solid solubility. In some cases, the degree of shift could be directly correlated with the degree of solubility, but lattice parameter anomalies were observed, where Vegard's law appeared to be violated and are described in detail below. For quantitative analysis, SEM-EDX was used to obtain phase compositions where possible. Based on these results, isothermal sections were constructed for phase equilibria in the CeO<sub>2</sub>-GdO<sub>1.5</sub>-SrO system at these temperatures and are presented in Fig. 3.80.

Table 3.6. Phase equilibria in the CeO<sub>2</sub>-GdO<sub>1.5</sub>-SrO system determined by XRD analysis at 1300 and 1500 °C.

Sample	Equilibrium Phases	
	1300 °C	1500 °C
CSG23-67	Sr <sub>2</sub> CeO <sub>4</sub> , Gd <sub>2</sub> SrO <sub>4</sub> *, SrO <sub>(SS)</sub> +OH	SrCeO <sub>3</sub> , Gd <sub>2</sub> SrO <sub>4</sub> , SrO <sub>(SS)</sub> +OH
CSG13-67	Sr <sub>2</sub> CeO <sub>4</sub> , Gd <sub>2</sub> SrO <sub>4</sub> *, SrO <sub>(SS)</sub> +OH	Gd <sub>2</sub> SrO <sub>4</sub> , SrO <sub>(SS)</sub> +OH
CSG40-50	SrCeO <sub>3</sub> , Gd <sub>2</sub> SrO <sub>4</sub> *	SrCeO <sub>3</sub> , Gd <sub>2</sub> SrO <sub>4</sub> **
CSG30-50	SrCeO <sub>3</sub> , Gd <sub>2</sub> SrO <sub>4</sub>	SrCeO <sub>3</sub> , Gd <sub>2</sub> SrO <sub>4</sub>
CSG20-50	SrCeO <sub>3</sub> , Gd <sub>2</sub> SrO <sub>4</sub>	SrCeO <sub>3</sub> , Gd <sub>2</sub> SrO <sub>4</sub>
CSG10-50	Gd <sub>2</sub> SrO <sub>4</sub> , SrO <sub>(SS)</sub> +OH	Gd <sub>2</sub> SrO <sub>4</sub> , SrO <sub>(SS)</sub> +OH
CSG10-40	Gd <sub>2</sub> SrO <sub>4</sub> , C	Gd <sub>2</sub> SrO <sub>4</sub> , C
CSG10-33	Gd <sub>2</sub> SrO <sub>4</sub> , C	Gd <sub>2</sub> SrO <sub>4</sub> , C
CSG60-20	SrCeO <sub>3</sub> , F	Sr(Ce,Gd)O <sub>3</sub> , F
CSG10-20	Gd <sub>2</sub> SrO <sub>4</sub> , C, B	Gd <sub>2</sub> SrO <sub>4</sub> , C, B
CSG30-10	Gd <sub>2</sub> SrO <sub>4</sub> **, C	Gd <sub>2</sub> SrO <sub>4</sub> *, C
CSG10-10	Gd <sub>2</sub> SrO <sub>4</sub> , C, B	Gd <sub>2</sub> SrO <sub>4</sub> , C, B
CSG37-33	SrCeO <sub>3</sub> , Gd <sub>2</sub> SrO <sub>4</sub> , F	SrCeO <sub>3</sub> , Gd <sub>2</sub> SrO <sub>4</sub> , F
CSG32-33	SrCeO <sub>3</sub> , Gd <sub>2</sub> SrO <sub>4</sub> , F	SrCeO <sub>3</sub> , Gd <sub>2</sub> SrO <sub>4</sub> , F
CSG30-20	Gd <sub>2</sub> SrO <sub>4</sub> , F	Gd <sub>2</sub> SrO <sub>4</sub> , F

\* : Small amount, \*\* : Very small amount, Gd<sub>2</sub>SrO<sub>4</sub>:(Gd,Sr)<sub>2</sub>(Sr,Ce)O<sub>4</sub> solid solution, SrCeO<sub>3</sub> : Sr(Ce,Gd)O<sub>3</sub> solid solution, Sr<sub>2</sub>CeO<sub>4</sub> : Sr<sub>2</sub>(Ce,Gd)O<sub>4</sub> solid solution, C : C-(Gd,Ce,Sr)<sub>2</sub>O<sub>3+x</sub>, B : B-(Gd,Ce,Sr)<sub>2</sub>O<sub>3+x</sub>, F : (Ce, Gd, Sr)O<sub>2-x</sub>

The main difference between the isothermal sections shown in Fig. 3.80 is the presence of a three-phase field labeled as “4” at 1300 °C that had disappeared and was replaced by a new equilibrium at 1500 °C, between a solid solution of SrO, Sr(Ce,Gd)O<sub>3</sub>, and (Gd,Sr)<sub>2</sub>(Sr,Ce)O<sub>4</sub>

(hereafter referred to as G2S). In addition, slight differences in the position of the all phase boundaries could be seen, due to the temperature dependence of solid solubility of the phases.

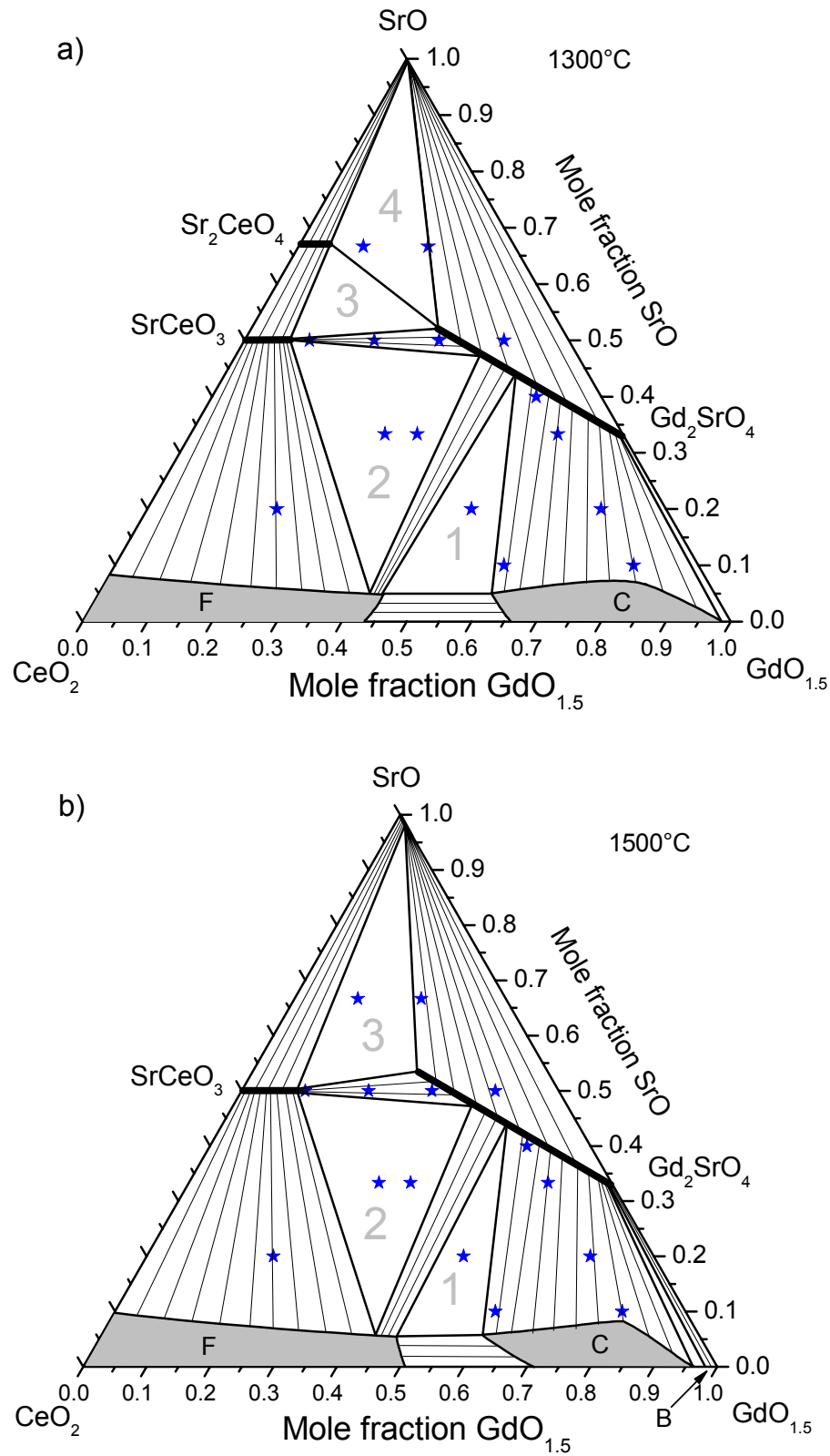


Fig. 3.80. Experimentally determined  $1300^\circ\text{C}$  (a) and  $1500^\circ\text{C}$  (b) isothermal sections of the  $\text{CeO}_2$ - $\text{SrO}$ - $\text{GdO}_{1.5}$  phase diagrams in air. Stars represent experimental compositions investigated in this work.



In the quasi-ternary system, no quaternary compound was found, but extended solid solutions of existing compounds were observed. Fig. 3.81 shows the XRD patterns of the CSG40-50 sample heat-treated at 1300 and 1500 °C. Expanding the pattern in the neighborhood of 30° 2 $\theta$  revealed that both samples contained small amounts of a secondary phase, which was the G2S solid solution. The peaks of SrCeO<sub>3</sub> shifted to higher angles, indicating lattice shrinkage due to substitution of the Ce<sup>4+</sup> ions by Gd<sup>3+</sup> ions, which have a smaller ionic radius [69Sha]. A similar shift could also be seen in the peak positions of Gd<sub>2</sub>SrO<sub>4</sub>, since it formed the G2S solid solution.

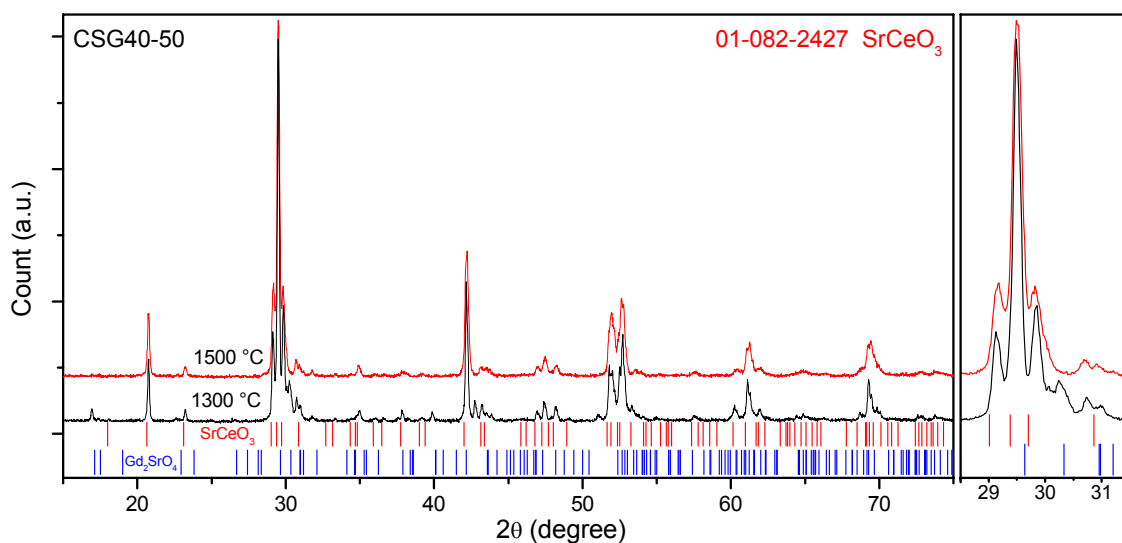


Fig. 3.81. XRD patterns of the CSG40-50 sample heat-treated at 1300 °C and 1500 °C. The card file used for Gd<sub>2</sub>SrO<sub>4</sub> in this study was based on data from the literature [03Cha].

Kruth, *et al.* [05Kru] had observed an anomaly in the variation of the unit cell parameters of SrCe<sub>1-x</sub>Gd<sub>x</sub>O<sub>3- $\delta$</sub>  with composition, reporting that the solid solution does not obey Vegard's law. For that reason, SEM-EDX analyses of the CSG30-50 sample were performed in order to quantify the solubility limit of gadolinia in SrCeO<sub>3</sub>. An SEM micrograph of the sample heat-treated at 1500 °C is shown in Fig. 3.82. The solubility limits of the SrCe<sub>1-x</sub>Gd<sub>x</sub>O<sub>3- $\delta$</sub>  solid solution at 1300 °C and 1500 °C were  $x = 0.12 \pm 0.01$  and  $x = 0.16 \pm 0.01$ , respectively. A slight temperature dependence of the homogeneity range was also identified. However, Kruth, *et al.* [05Kru] reported that in order to produce phase-pure SrCe<sub>0.9</sub>Gd<sub>0.1</sub>O<sub>3- $\delta$</sub>  heat-treatment should be performed above 1500 °C. Since in the present work the phase-pure SrCe<sub>0.88</sub>Gd<sub>0.12</sub>O<sub>3- $\delta$</sub>  was produced by soft chemistry processing at 1300 °C, this discrepancy could be attributed to the slower reactions kinetics of the mixed oxide route employed by Kruth, *et al.* [05Kru]. Therefore, in order to reach equilibria, longer annealing times and/or higher temperatures would be necessary if using the mixed oxide processing method.

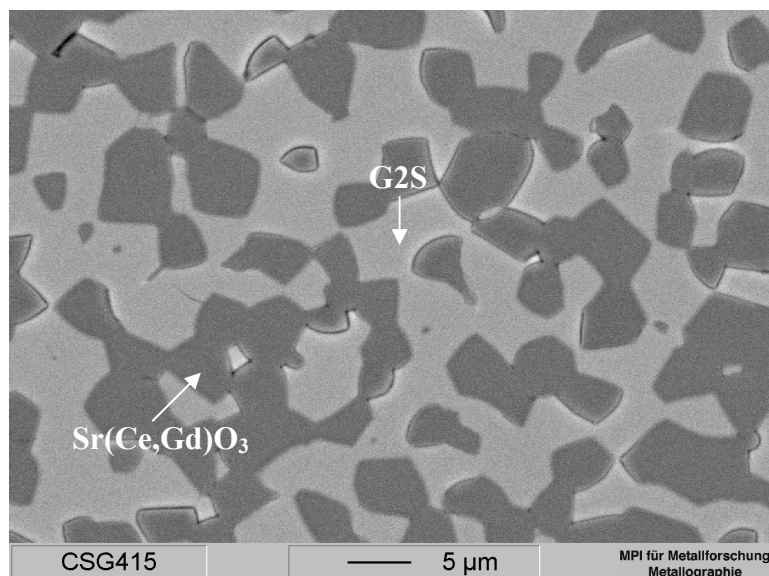


Fig. 3.82. An SEM micrograph of the CSG30-50 sample heat-treated at 1500 °C.

As in the case of  $\text{Sr}(\text{Ce}_{1-x}\text{Gd}_x)\text{O}_3$ , an anomalous lattice parameter change was expected for the  $\text{Sr}_2(\text{Ce,Gd})\text{O}_4$  solid solution with increasing content of  $\text{Gd}^{3+}$  ions, and that Vegard's law would not be obeyed. SEM-EDX characterization of the SrO-rich samples and the sample from the  $\text{Sr}(\text{Ce,Gd})\text{O}_3$ - $\text{Sr}_2(\text{Ce,Gd})\text{O}_4$ -G2S three-phase field was not performed, because it has been known from the quasi-binary  $\text{CeO}_2$ -SrO system that it would not be possible to distinguish between the  $\text{SrCeO}_3$  and  $\text{Sr}_2\text{CeO}_4$  phases and additionally sample preparation in the SrO-rich samples is always difficult because of the hygroscopic character of SrO. Therefore, the SrO corner of the diagram was directly connected to the broader of the homogeneity range of the  $\text{Sr}(\text{Ce,Gd})\text{O}_3$  solid solution with a straight line. The solubility limit of the  $\text{Sr}_2(\text{Ce,Gd})\text{O}_4$  at 1300 °C was calculated to be 5 mol %  $\text{GdO}_{1.5}$ , *i.e.* at  $\text{Sr}_2(\text{Ce}_{0.85}\text{Gd}_{0.15})\text{O}_4$ . The sample CSG23-67 contained 10 mol %  $\text{GdO}_{1.5}$  and it was in a three-phase field. Weak peaks of G2S were also observed, with a shift to lower angles, as well as strong ones of Sr-oxide/-hydroxide. Again, this corresponded to a smaller cell volume, owing to the substitution of  $\text{Ce}^{4+}$  ions by  $\text{Gd}^{3+}$  ions. Consequently, the solubility of  $\text{GdO}_{1.5}$  in  $\text{Sr}_2\text{CeO}_4$  was consistent with the estimated value. The  $\text{Sr}_2\text{CeO}_4$  peaks disappeared when the sample was heat-treated at 1500 °C, and a new equilibrium was established between  $\text{Sr}(\text{Ce,Gd})\text{O}_3$ , SrO and G2S.

For the extended G2S solid solution, Gd and Ce were observed to be soluble in  $\text{Gd}_2\text{SrO}_4$ , with ionic substitution occurring simultaneously in both sublattices. As it has been indicated above, the solid solution could be formally described as  $(\text{Gd,Sr})_2(\text{Sr,Ce})\text{O}_4$ .  $\text{Gd}_2\text{SrO}_4$  and  $\text{Sr}_2\text{CeO}_4$  have a very similar crystal structure; both are orthorhombic and have space group symmetry of  $Pbnm$  and  $Pbam$ , respectively. Fig. 3.84 shows XRD patterns of the samples with

compositions close to the solid solution. From the patterns, it is clear that there exists a solid solution over a broad range. In the expanded spectral regions (see the insets of Fig. 3.84), the CSG10-50 sample is compared with the other samples. The first inset on the left shows a comparison between CSG10-50 and the samples located in the G2S + Sr(Ce,Gd)O<sub>3</sub> two-phase field. A dramatic change in the diffraction pattern was observed; in addition to the peaks of Gd<sub>2</sub>SrO<sub>4</sub>, SrCeO<sub>3</sub>, peaks started to appear in both CSG20-50 and CSG30-50 samples, most noticeably in the ~29-30 and 42° 2θ range. The inset on the right shows a comparison between CSG10-50 and the samples located in the G2S + C-phase two-phase field. Although there was no C-phase peak in the CSG10-50 sample, peaks of the C-phase appeared in the CSG10-40 and CSG10-33 samples in addition to the Gd<sub>2</sub>SrO<sub>4</sub> peaks.

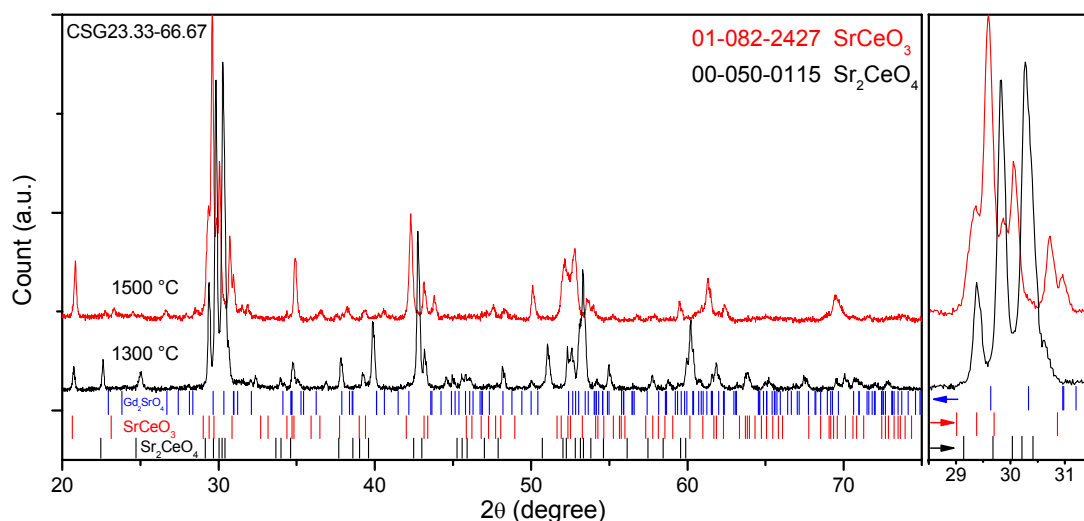


Fig. 3.83. The XRD patterns of the CSG23-67 sample heat-treated at 1300 °C and 1500 °C. Arrows show the direction of peak shift with respect to the original position [04ICDD]. The non-indexed peaks belong to those of Sr-oxide and -hydroxides. The card file for Gd<sub>2</sub>SrO<sub>4</sub> used in this study based on data from the literature [03Cha].

The homogeneity range of the G2S solid solution was determined using the CSG13-67 sample. A slight temperature-dependence was found for the solubility limit. With CSG13-67 samples heat-treated at 1300 °C, very small Sr<sub>2</sub>CeO<sub>4</sub> peaks were determined which disappeared when the sample was heat-treated at 1500 °C. The peak shifts of the G2S solid solution from samples heat-treated at 1300 and 1500 °C were very small indicating a slight temperature dependence. Therefore, the solubility limit was estimated slightly below and above the CSG23-67 sample for the 1300 °C and 1500 °C isothermal sections, respectively. The composition of the homogeneity range are 19 mol% CeO<sub>2</sub>, 52 mol% SrO, and 21 mol% CeO<sub>2</sub>, 54 mol% SrO, for 1300 °C and 1500 °C isothermal sections, respectively.

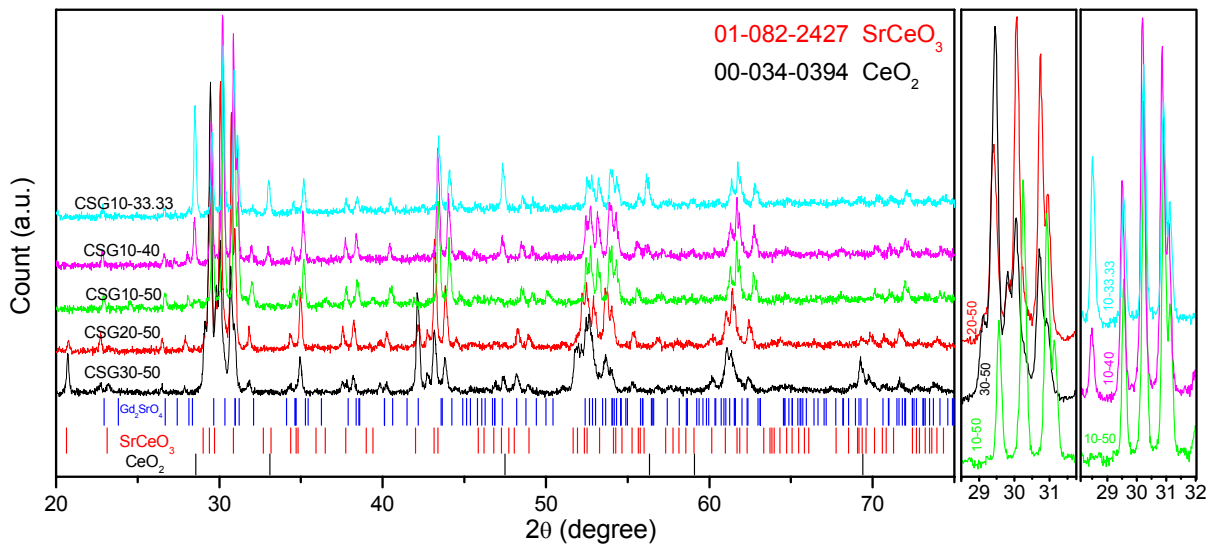


Fig. 3.84. XRD patterns of samples around the G2S solid solution. Samples were heat-treated at 1300 °C.

To determine the 3-phase fields labeled as “1” and “2” in Fig. 3.80, CSG30-20 and CSG37-33 were prepared and characterized. Fig. 3.85 shows the XRD patterns of the CSG30-20 and CSG37-33 samples. The equilibrium phases in the CSG37-33 sample are Sr(Ce,Gd)O<sub>3</sub>, G2S and F-phase, whereas the CSG30-20 sample corresponded to the equilibrium of G2S with C-phase or both C- and F-phases. As it is known from the discussion on the quasi-binary system CeO<sub>2</sub>-Gd<sub>2</sub>O<sub>3</sub> by XRD studies, it is not possible to differentiate between the single C-phase and C- and F- two-phase field. In addition, weak contrast during secondary electron imaging in the SEM did not enable distinguishing between the two, even qualitatively (see Fig. 3.86).

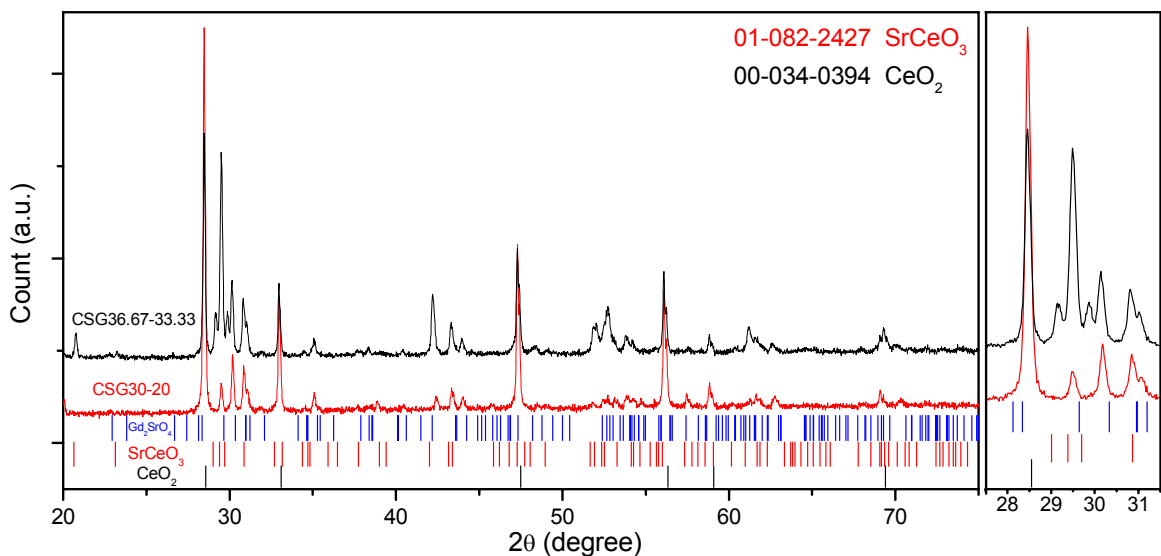


Fig. 3.85. XRD patterns of CSG30-20 and CSG37-33 samples, heat-treated at 1300 °C.

The extension of the C- and F-phase of the CeO<sub>2</sub>-Gd<sub>2</sub>O<sub>3</sub> quasi-binary section into the ternary diagram was also investigated by SEM-EDX analysis. In Fig. 3.87, micrographs of CSG10-20

(a) and CSG60-20 (b) are presented. The SrO solubility of the F-phase decreased only slightly with increasing gadolinia content *i.e.* the Gd ions did not affect the solubility of Sr ions in the  $\text{CeO}_2$  solid solution. The discussion on the  $\text{Gd}_2\text{O}_3$ -SrO quasi-binary section pointed out that there was almost no SrO solubility in gadolinia, neither in the C- nor in the B- $\text{Gd}_2\text{O}_3$  phases. However, the XRD analysis revealed shifts of the peaks of both C- and B- $\text{Gd}_2\text{O}_3$  toward lower angles, and SEM-EDX analyses also revealed considerable solubility of Ce and Sr ions. Evidently, in the presence of Ce ions, Sr ions could incorporate into the cubic gadolinia lattice. Monoclinic B-type gadolinia peaks were also determined in the CSG10-10 sample. The SEM-EDX results of CGS10-10, CSG10-20, CSG10-33 and CSG30-10 were used to estimate the extension of the C-phase at ternary composition. Based on the measurements, the maximum SrO content that could be incorporated into the C-phase was  $\sim 10$  mol%, which would be about the same as the value for the F-phase

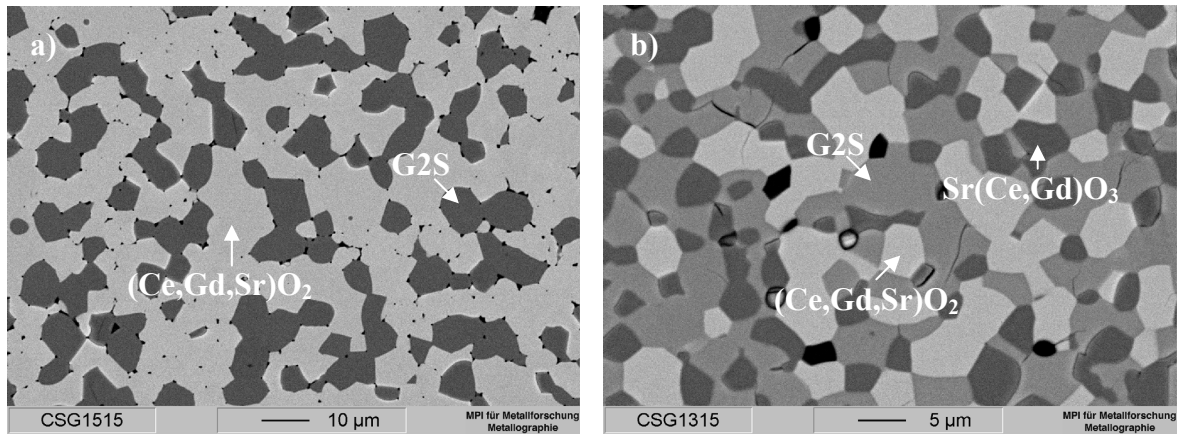


Fig. 3.86. SEM micrograph of the CSG30-20 (a) and CSG37-33 (b) samples, heat-treated at 1500 °C.

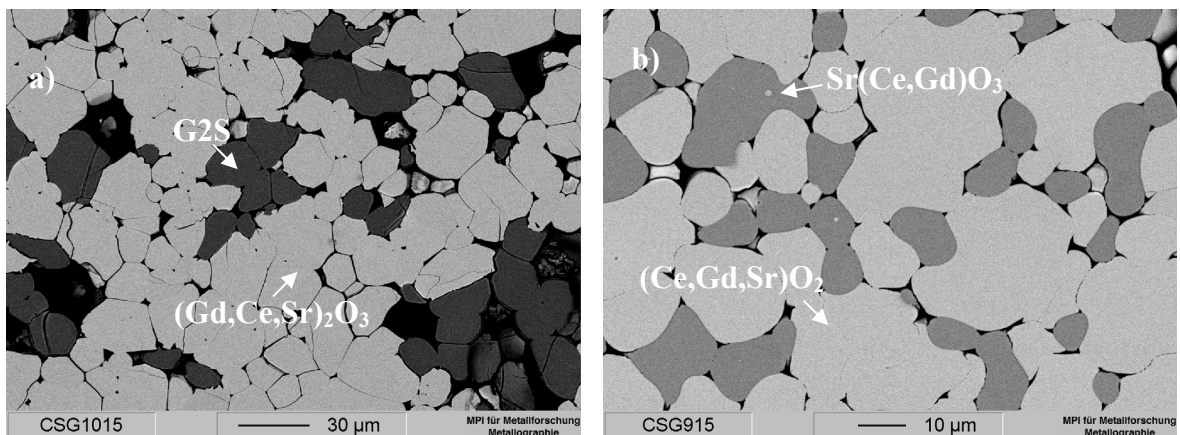


Fig. 3.87. SEM micrograph of the CSG10-20 (a) and CSG60-20 (b) samples, heat-treated at 1500 °C.

### 3.4.7. The Ce-Sr-Ni-O subsystem

For the Ce-Sr-Ni-O system, no experimental or computational phase studies are available in the literature. The only reported data related to the system were the structural and electrical properties of the  $\text{Ce}_{2-x}\text{Sr}_x\text{NiO}_{4-\delta}$  solid solution (C2N), which crystallized in the tetragonal  $\text{K}_2\text{NiF}_4$  [95Jam1, 02Mak]. The homogeneity range of the solid solution was not known but samples with two different compositions had been reported, for  $x = 1.7$  [02Mak] and 1.75 [95Jam1]. The value of  $x$  was controlled by the oxidation state of Ni, and for  $x = 1.75$  the composition of the solid solution could be written as  $\text{CeSr}_7\text{Ni}_4\text{O}_{11}$ , where Ni would be fully in the 3+ state [95Jam1]. In that same study, a sample having  $x = 1.67$  was prepared and heat-treated at 1100 °C.  $\text{Sr}_2\text{CeO}_4$  was also identified as a secondary phase.

To experimentally derive the phase equilibria in the  $\text{CeO}_2$ -SrO-NiO quasi-ternary system, nine different compositions were strategically chosen. The first composition investigated was CSN10-57, the  $\text{Ce}_{0.3}\text{Sr}_{1.7}\text{NiO}_{4-\delta}$  solid solution, the similar composition as the investigated by Makhanach *et al.* [02Mak]. Next, the limits of the homogeneity range for the solid solution, C2N, were evaluated by measuring the composition of the C2N in samples using SEM-EDX, CSN15-52 (for the ceria-rich end) and CSN05-62 (for the SrO-rich end) using XRD results (estimated). Finally the fields of 3-phases in equilibrium were determined. The samples were all prepared using the modified Pechini soft chemistry as described above. Heat treatments were performed at 1300 and 1400 °C on all sample compositions in air. However, formation of the liquid phase was observed on the most of samples. Thus, only the 1300 °C isothermal section was investigated. XRD patterns were used to identify the phases in equilibrium, while relative peak shifts were evaluated to determine if any solubility had occurred. XRD analysis data are summarized in Table 3.7, listing the phases present. For quantitative analysis of phase composition and check for changes in stoichiometry, EDX was performed at the SEM. Finally, using all of experimental data, the  $\text{CeO}_2$ -SrO-NiO quasi-ternary phase equilibria diagram at 1300 °C was constructed and presented in Fig. 3.88.

The diagram is a rather simple one and is dominated by the  $\text{Ce}_{2-x}\text{Sr}_x\text{NiO}_{4-\delta}$  solid solution. The XRD powder pattern of the CSN10-57 sample (where  $x = 1.7$ ) showing only peaks of the  $(\text{Ce,Sr})_2\text{NiO}_{4-\delta}$  structure and the internal quartz standard, is given in Fig. 3.89. The XRD pattern of the CSN10-57 sample was compared with the card file based on the work of James and Attfield [95Jam]. A slight shift with respect to the positions of the reference pattern was determined. When heat-treated at 1400 °C, the formation of a liquid phase was observed.

Table 3.7. Phase equilibria in the CeO<sub>2</sub>-SrO-NiO quasi-ternary system at 1300 °C, according to the XRD.

Sample	Equilibrium Phases
CSN10-70	SrO, Sr <sub>2</sub> CeO <sub>4</sub> , (Ce,Sr) <sub>2</sub> NiO <sub>4-x</sub>
CSN23-67	SrO, Sr <sub>2</sub> CeO <sub>4</sub> , (Ce,Sr) <sub>2</sub> NiO <sub>4-x</sub>
CSN05-62	SrO, NiO, (Ce,Sr) <sub>2</sub> NiO <sub>4-x</sub>
CSN10-57	(Ce,Sr) <sub>2</sub> NiO <sub>4-x</sub>
CSN15-52	Sr <sub>2</sub> CeO <sub>4</sub> , NiO, (Ce,Sr) <sub>2</sub> NiO <sub>4-x</sub>
CSN40-50	Sr <sub>2</sub> CeO <sub>4</sub> , SrCeO <sub>3</sub> , NiO
CSN30-37	Sr <sub>2</sub> CeO <sub>4</sub> , SrCeO <sub>3</sub> , NiO
CSN50-40	SrCeO <sub>3</sub> , NiO, (Ce,Sr)O <sub>2-x</sub>
CSN57-10	SrCeO <sub>3</sub> , NiO, (Ce,Sr)O <sub>2-x</sub>

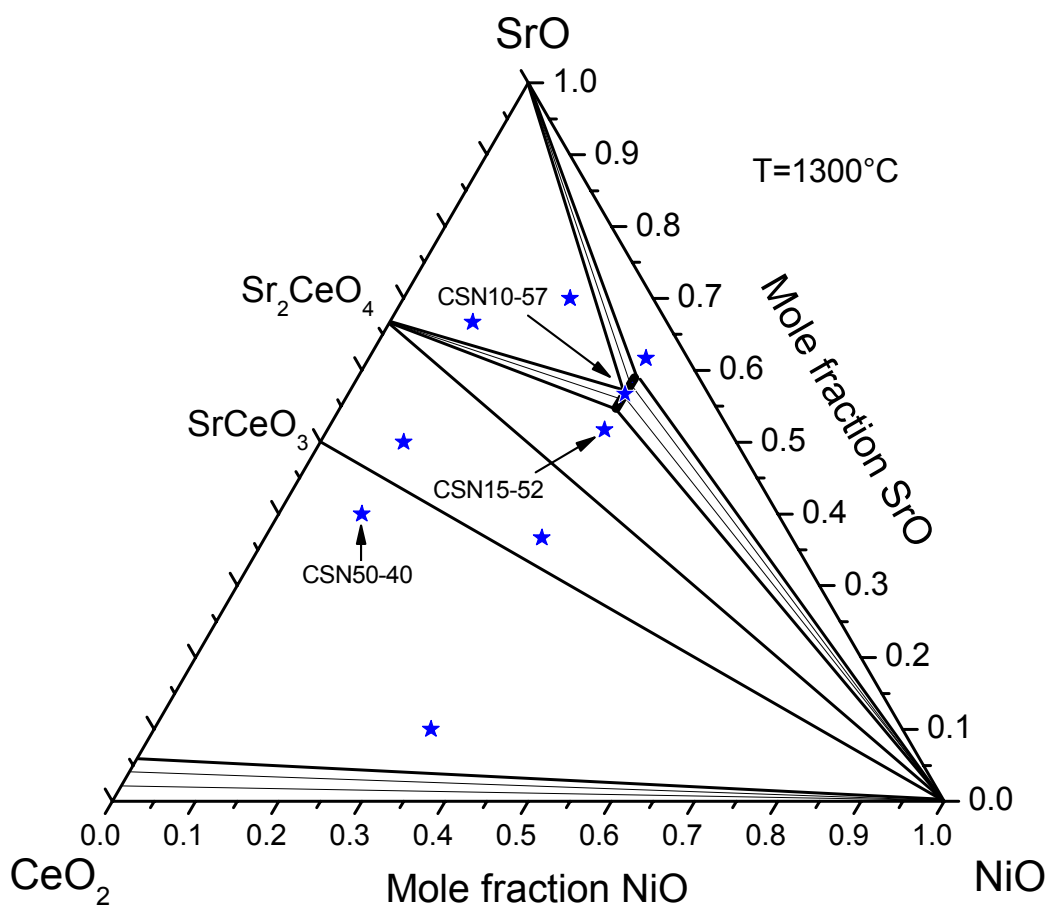


Fig. 3.88. The experimentally determined 1300 °C isothermal (in air) section of the CeO<sub>2</sub>-SrO-NiO phase diagram. Stars represent the selected sample compositions.

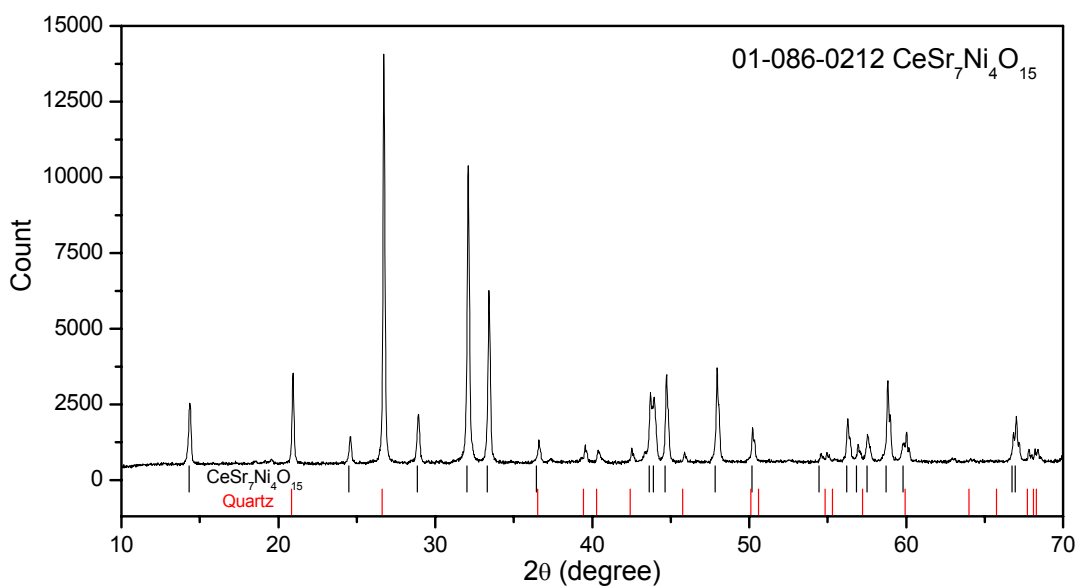


Fig. 3.89. XRD powder pattern of the CSN10-57 sample, quartz is used as an internal standard.

In order to determine the melting point, TG/DTA analyses were performed (Fig. 3.90). DTA revealed a sudden onset of melting at 1362 °C. XRD analysis performed after the DTA showed identical peak positions, indicating that the solid solution had molten congruently.

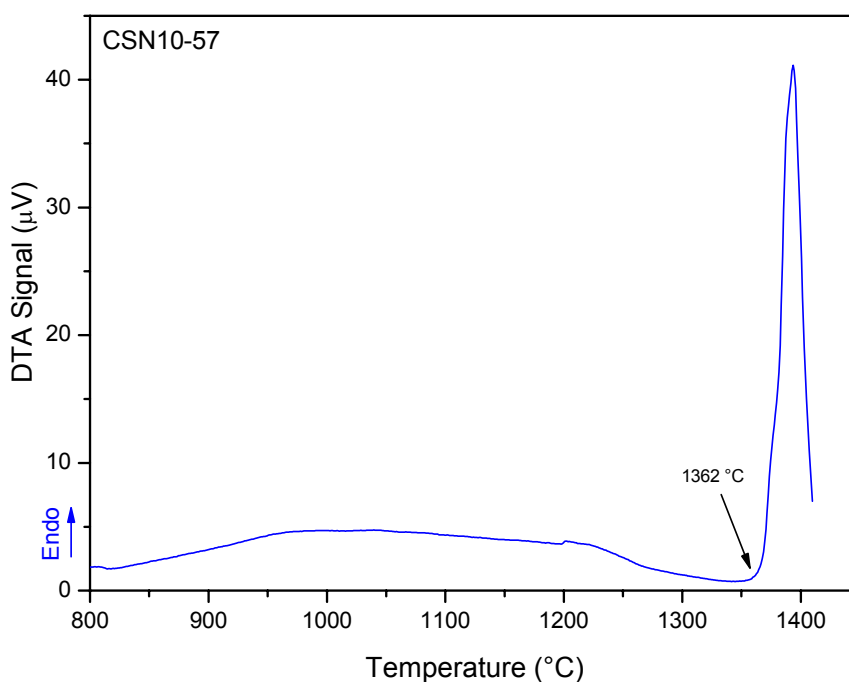


Fig. 3.90. DTA curve of the CSN10-57 sample showing strong melting peak of the solid solution.

The solubility limit of the ceria-rich side of the homogeneity range of the compound was investigated by SEM-EDX analysis of the CSN15-52 sample (Fig. 3.91). The existence of three phases can be clearly seen. According to the EDX analysis, NiO and Sr<sub>2</sub>CeO<sub>4</sub> were



determined without any solubility of the other both components. This result was confirmed by XRD analyses showing only peaks in the phase-pure positions. The composition of the  $K_2NiF_4$ -type solid solution was determined to be as Ce/Sr ratio of 1/5, which can be represented by the formula of  $CeSr_5Ni_3O_y$ . Although the existence of the composition  $LnSr_5Ni_3O_{11}$  (where Ln = lanthanides) for some lanthanides had been known [93Jam, 95Jam2], James and Attfield reported that the solid solution does not exist in the Ce-Sr-Ni-O system for the same composition,  $CeSr_5Ni_3O_{11}$  [95Jam1]. However, the sintering temperature that was used, 1100 °C, which was too low to obtain a phase-pure solid solution.

To determine the composition at the SrO-rich end of the C2N solid solution, CSN05-62 was characterized. Because of the hygroscopic nature of SrO, an SEM sample could not be prepared in the SrO-rich side of the diagram. Instead, the XRD pattern was examined. The diffraction pattern showed peaks of almost identical position with the solid solution peaks as the  $CeSr_7Ni_4O_{15}$  card file, in addition to the peaks of NiO and Sr-oxide/hydroxide. Consequently, the solid solution was defined between the  $CeSr_7Ni_4O_{15}$  and  $CeSr_5Ni_3O_{11}$  compositions.

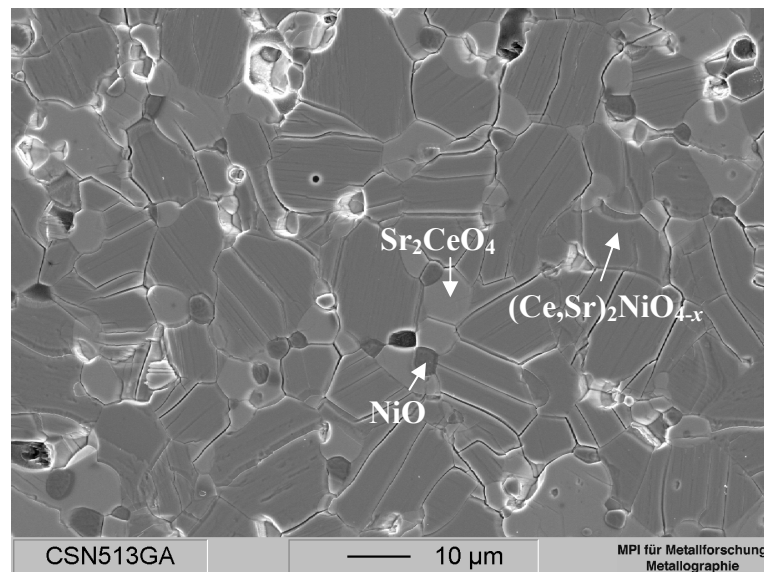


Fig. 3.91. An SEM micrograph of CSN15-52 sample heat-treated at 1300 °C for 120 h.

The CSN50-40 sample was characterized to investigate the equilibrium phases and their nature, in the  $SrCeO_3$ ,  $(Ce,Sr)O_2$  and NiO three-phase field. Fig. 3.92 shows a SEM micrograph of the microstructure morphology. EDX analysis showed that the NiO and  $SrCeO_3$  phases were stoichiometric, without solubility of the other components. The solubility of SrO in ceria was found to be  $6 \pm 0.8$  mol %, which is in good agreement with the quasi-binary data.

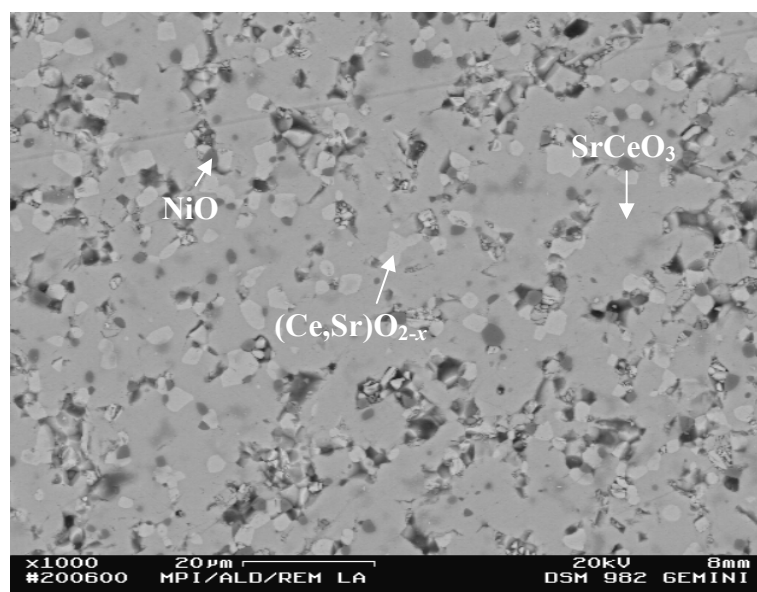


Fig. 3.92. An SEM micrograph of CSN50-40 sample heat-treated at 1300 °C for 120 h.

The samples CSN30-37 and CSN40-50 were used to characterize the three-phase field of NiO, SrCeO<sub>3</sub> and Sr<sub>2</sub>CeO<sub>4</sub>. EDX analysis of the CSN30-37 sample showed that NiO is stoichiometric, without solubility of the other components. The XRD pattern of the CSN30-37 sample is given in Fig. 3.93. Careful analysis of this XRD pattern shows that the peaks of both SrCeO<sub>3</sub> and Sr<sub>2</sub>CeO<sub>4</sub> are in their original positions revealing no detectable solubility of NiO.

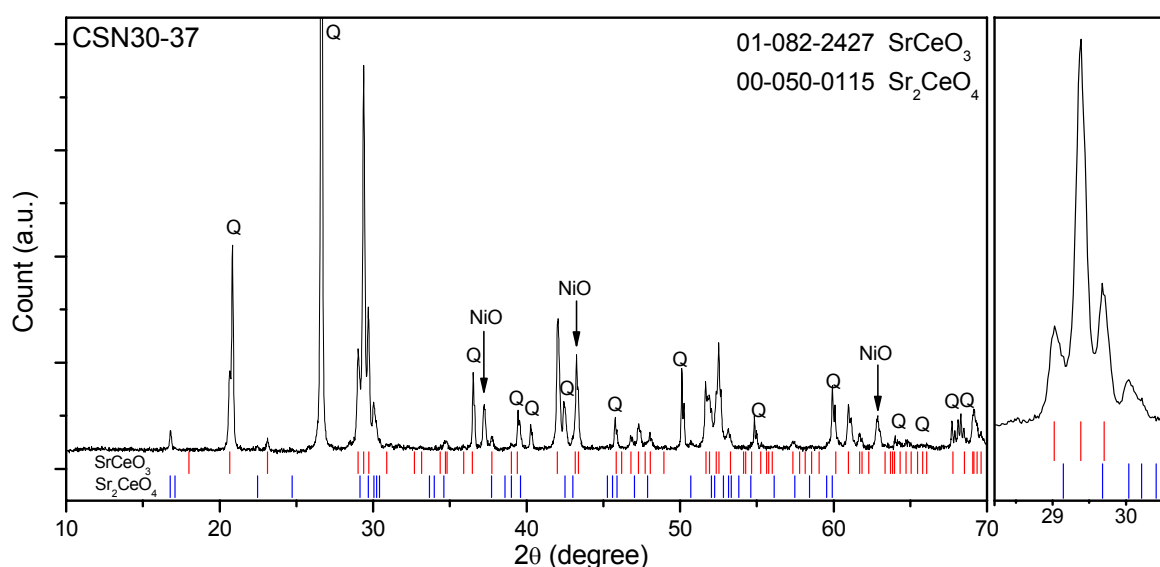


Fig. 3.93. XRD pattern of the CSN30-37 sample, heat-treated at 1300 °C. Quartz (Q) was used as a standard.

### 3.4.8. The Gd-Sr-Ni-O Subsystem

No phase equilibria data are available in the literature for the Gd-Sr-Ni-O subsystem. The only information available is from the stoichiometric solid solution of  $\text{GdSrNiO}_4$  that was prepared by Chen, *et al.* for studying the structural, electrical and magnetic properties [93Che]. Later James and Attfield [96Jam] had investigated two additional compositions from the  $\text{Gd}_{2-x}\text{Sr}_x\text{NiO}_4$  solid solution with  $x = 1.33$  and  $1.67$ .

As with the preceding subsystems, the objective in the present study was to derive experimentally an isothermal phase equilibria diagram. To this end, 16 strategically chosen sample compositions were prepared and analyzed. To investigate the homogeneity range of the previously reported  $\text{Gd}_{2-x}\text{Sr}_x\text{NiO}_4$  solid solution, a set of samples was prepared along the homogeneity range of this solid solution by changing the SrO concentration from 10 to 56.67 mol% ( $x$  in the range of 0.3 to 1.7): GSN57-10, GSN47-20, GSN37-30, GSN27-40, GSN17-50, GSN10-57. It had also been reported to in the literature that other lanthanide compounds possessing the  $\text{K}_2\text{NiF}_4$ -type undergo a structural transition, which motivated the study of the same samples to determine if  $\text{Gd}_{2-x}\text{Sr}_x\text{NiO}_4$  also displayed such a phase transition. To establish the 3-phase equilibrium fields, GSN20-60 and GSN40-50 were studied for field #1; GSN27-40 was used to confirm the GSN solid solution composition anchoring one of the three phases in field #1. GSN70-20 confirmed the 3 phases in equilibrium in phase field #2. For field #3, GSN57-10 and GSN40-10 were investigated. The equilibrium phases in field #4 were established by GSN10-46, GSN10-57, and GSN17-50. Finally, to prove that  $\text{Sr}_2\text{GdO}_4$  did not dissolve other components at 1300 °C and 1400 °C, GSN57-33 was analyzed.

All samples were heat-treated at 1300 and 1400 °C. The XRD results are compiled in Table 3.8. EDX on the SEM was also performed for quantitative analysis, as in the other subsystems. All results were used to construct the equilibrium phase diagram at 1300 °C shown in Fig. 3.94.

In the samples located close to the SrO-NiO quasi-binary section, liquid phase formation was observed after heat-treatment at 1400 °C. However, despite formation of the liquid phase, no difference was found between the XRD patterns of the samples heat-treated at 1300 and 1400 °C, *i.e.*, all phases in the system had molten congruently. The experimentally estimated isothermal section at 1300 °C is shown in Fig. 3.94. For the construction of the diagram, the liquid phase was not considered and the liquidus surface of the diagram was not investigated since it is out of the scope of the present work. However, the key conclusion stemming from this part of the study is that should the  $\text{Gd}_{2-x}\text{Sr}_x\text{NiO}_4$  solid solution can be used in an IT-SOFC

component, the cell fabrication/sintering temperatures must remain below 1400 °C, due to the formation of the liquid phase.

Table 3.8. Phase equilibria in the GdO<sub>1.5</sub>-SrO-NiO system at 1300 and 1400 °C according to XRD analyses.

Sample	Equilibrium Phases
GSN20-60	SrO <sub>(SS)</sub> + Sr-hydroxide, (Gd,Sr) <sub>2</sub> NiO <sub>4</sub> , Gd <sub>2</sub> SrO <sub>4</sub>
GSN40-50	SrO <sub>(SS)</sub> + Sr-hydroxide, (Gd,Sr) <sub>2</sub> NiO <sub>4</sub> , Gd <sub>2</sub> SrO <sub>4</sub>
GSN10-57	SrO <sub>(SS)</sub> + Sr-hydroxide, (Gd,Sr) <sub>2</sub> NiO <sub>4</sub> , NiO
GSN10-46	SrO <sub>(SS)</sub> + Sr-hydroxide, (Gd,Sr) <sub>2</sub> NiO <sub>4</sub> , NiO
GSN17-50	(Gd,Sr) <sub>2</sub> NiO <sub>4</sub> , SrO <sub>(SS)</sub> *+ Sr-hydroxide*, NiO*
GSN27-40	(Gd,Sr) <sub>2</sub> NiO <sub>4</sub>
GSN37-30	(Gd,Sr) <sub>2</sub> NiO <sub>4</sub>
GSN47-20	(Gd,Sr) <sub>2</sub> NiO <sub>4</sub> , NiO*, B-Gd <sub>2</sub> O <sub>3</sub> *
GSN57-10	(Gd,Sr) <sub>2</sub> NiO <sub>4</sub> , NiO, B-Gd <sub>2</sub> O <sub>3</sub>
GSN40-10	(Gd,Sr) <sub>2</sub> NiO <sub>4</sub> , NiO, B-Gd <sub>2</sub> O <sub>3</sub>
GSN57-33	(Gd,Sr) <sub>2</sub> NiO <sub>4</sub> , Gd <sub>2</sub> SrO <sub>4</sub>
GSN70-20	(Gd,Sr) <sub>2</sub> NiO <sub>4</sub> , B-Gd <sub>2</sub> O <sub>3</sub> , Gd <sub>2</sub> SrO <sub>4</sub>
GSN80-10	(Gd,Sr) <sub>2</sub> NiO <sub>4</sub> , B-Gd <sub>2</sub> O <sub>3</sub> , Gd <sub>2</sub> SrO <sub>4</sub>
GSN30-20	(Gd,Sr) <sub>2</sub> NiO <sub>4</sub> , NiO
GSN20-20	(Gd,Sr) <sub>2</sub> NiO <sub>4</sub> , NiO
GSN10-10	(Gd,Sr) <sub>2</sub> NiO <sub>4</sub> , NiO

\* in very small amount,

At the SrO-rich side of the diagram, as was the case for the Gd<sub>2</sub>O<sub>3</sub>-SrO quasi-binary system, relatively strong SrO peaks were observed, in addition to Sr-hydroxides. For the SrO peaks, a small shift to higher angles was observed with respect to the original phase-pure positions [ICDD], which could be attributed to shrinkage in the SrO lattice due to the incorporation of Gd and/or Ni, both of which have smaller ionic radius than Sr [69Sha]. The remaining SrO transformed to hydroxides containing either 2 or 8 moles of crystal water.

In Fig. 3.95, XRD patterns of the GSN20-60, GSN27-40 and GSN37-30 samples are being compared. The peak positions of the (Gd,Sr)<sub>2</sub>NiO<sub>4</sub> phase in both the GSN20-60 and the GSN27-40 sample are almost identical. Therefore, the corner of the three-phase field labeled “1” on the (Gd,Sr)<sub>2</sub>NiO<sub>4</sub> solid solution has simply been taken to be of the same composition as the GSN27-40 sample. The inset, *a*) in Fig. 3.95, shows peaks of Gd<sub>2</sub>SrO<sub>4</sub> which coincided with the phase-pure pattern, as indicated by the green lines. These peaks had also appeared in

the GSN40-50 sample, confirming no detectable solubility of the other components in  $\text{Gd}_2\text{SrO}_4$  (SrO-side). The third corner (SrO) of the three-phase field labeled “1” was taken directly from the SrO- $\text{Gd}_2\text{O}_3$  quasi-binary section that had revealed a small solubility of gadolinia in SrO. The XRD patterns measured from the GSN40-50 and GSN20-60 samples heat-treated at 1300 and 1400 °C were almost identical, except slight difference on the peaks of Sr-oxide/hydroxide. No liquid phase formation was observed in both samples heat-treated at 1400 °C.

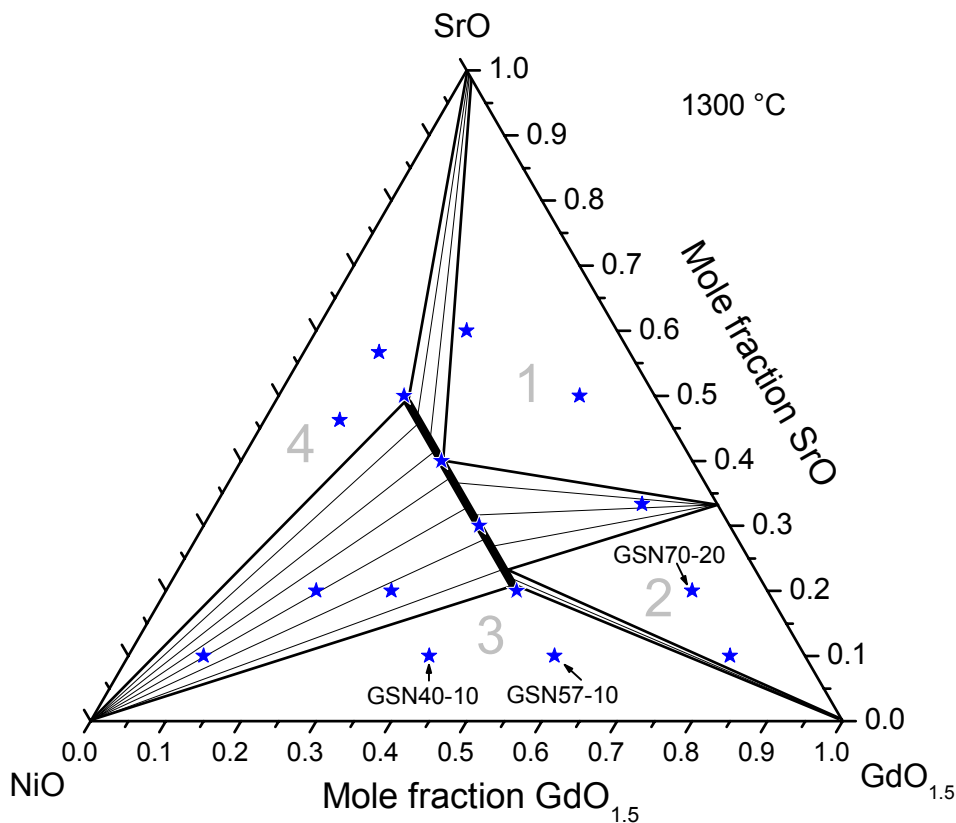


Fig. 3.94. The experimentally determined 1300 °C (in air) isothermal section of the  $\text{GdO}_{1.5}$ -SrO-NiO phase diagram. The numbers in gray are used to refer to the three-phase fields in the text.

Fig. 3.96 shows a SEM micrograph of the microstructure morphology of GSN70-20 sample located in the three-phase field, labeled “2”. The co-existence of the three phases was confirmed by XRD. The composition of the  $(\text{Gd,Sr})_2\text{NiO}_4$  phase was analyzed by SEM-EDX to be at 23.5 mol% SrO with the reproducibility of  $\pm 0.5$  mol%, without considerable deviations from the Sr+Gd to Ni ratio of 1 to 2. The gadolinia component of this three-phase equilibrium was found to be pure. Within the limits of error, no solubility of the other components was detected. No measurable peak shift was determined on the XRD pattern of  $\text{Sr}_2\text{GdO}_4$  compound. In addition, SEM-EDX analysis showed no solubility of NiO, and no deviation from stoichiometry. The GSN57-33 sample, which was located in the two-phase

field between the three-phase fields labeled “1” and “2”, was also used in order to confirm the absence of any solubility in the  $\text{Sr}_2\text{GdO}_4$  compound. The sample was heat-treated at 1300 and 1400 °C. In both cases, the XRD peaks of the  $\text{Sr}_2\text{GdO}_4$  had almost coincided perfectly with the phase-pure pattern, while SEM-EDX results again showed no detectable solubility of NiO or deviation from the stoichiometry. Thus, for the construction of the diagram, both  $\text{Sr}_2\text{GdO}_4$  and  $\text{GdO}_{1.5}$  were taken as stoichiometric compounds. The GSN70-20 sample heat-treated at 1400 °C gave perfectly matching XRD patterns to the one gained at 1300 °C confirming a phase equilibrium independent of temperature (in this temperature interval).

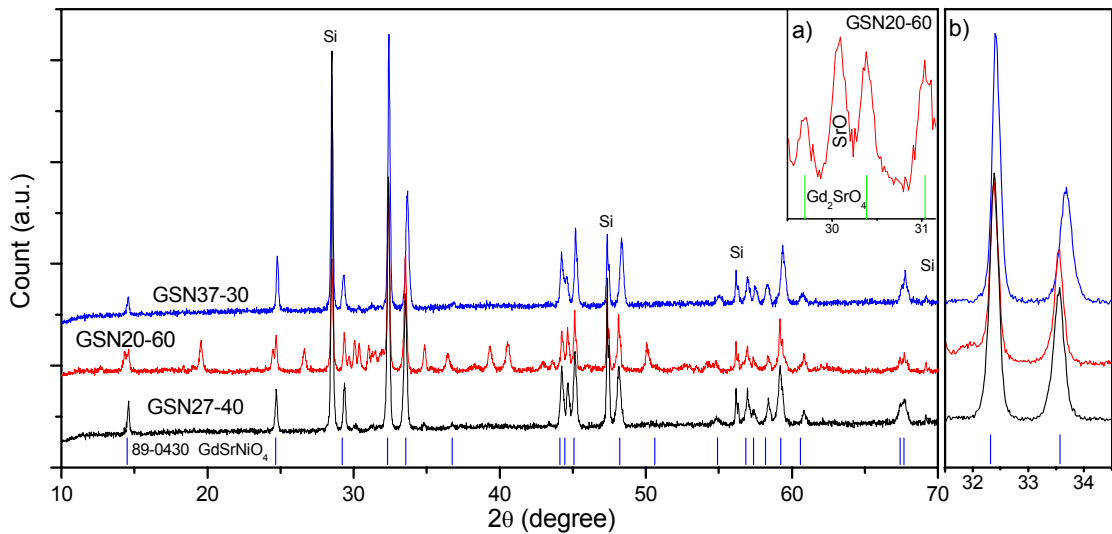


Fig. 3.95. XRD spectra of the samples in the SrO-rich part of the diagram showing almost the same peak positions (zoomed in inset *b*) of the GSN20-60 and GSN27-40 samples. Inset *a* shows the peak positions of  $\text{Gd}_2\text{SrO}_4$  phase in the GSN20-60 sample.  $(\text{Gd,Sr})_2\text{NiO}_4$  solid solution peaks were indexed using  $\text{GdSrNiO}_4$  pattern [ICDD]. The non-indexed peaks are  $\text{Gd}_2\text{SrO}_4$  and Sr-oxide/hydroxides. All the samples were heat-treated at 1300 °C.

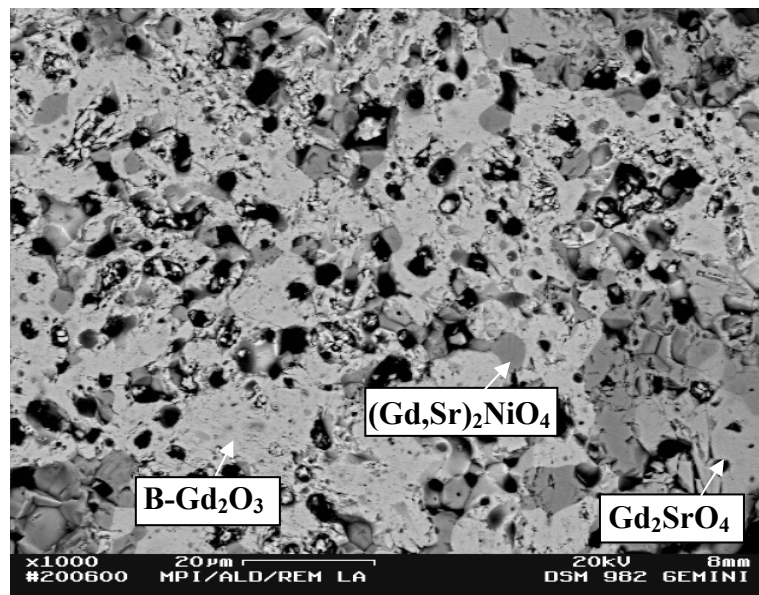


Fig. 3.96. SEM micrograph of GSN70-20 sample heat-treated at 1300 °C for 120 h.

SEM micrographs of samples, which are located in the three-phase field, labeled “3”, are given in Fig. 3.97a and b. The GSN57-10 sample was heat-treated at 1300 °C and the GSN40-10 sample at 1400 °C. No liquid phase formation was observed at these temperatures. The chemical compositions of both GSN40-10 and GSN57-10 samples are very close to each other and XRD analysis of the samples show identical peak positions.  $\text{GdO}_{1.5}$  and NiO were found to be almost pure without considerable solubility of the other two components. The SrO content of the  $(\text{Gd,Sr})_2\text{NiO}_4$  solid solution at the corner of the three-phase field is determined to be  $19.5 \pm 0.5$  mol%. According to the composition determined it can be expected that the GSN47-20 sample is located within the  $(\text{Gd,Sr})_2\text{NiO}_4$  homogeneity range. However, XRD analysis of the GSN47-20 sample heat-treated at 1300 °C, showed small peaks of secondary phases (Fig. 3.98). The heat-treatment was repeated, and an additional treatment was performed at 1400 °C, but in both cases, almost identical XRD patterns were obtained. Such small amounts of secondary phases and very similar SEM-EDX results indicate that the phase boundary is very close to the GSN47-20 sample. Considering the experimental error, the homogeneity range of the  $(\text{Gd,Sr})_2\text{NiO}_4$  solid solution on the gadolinia rich side was taken as slightly higher than the Sr-content in the GSN47-20 sample ( $x \sim 0.6$ ).

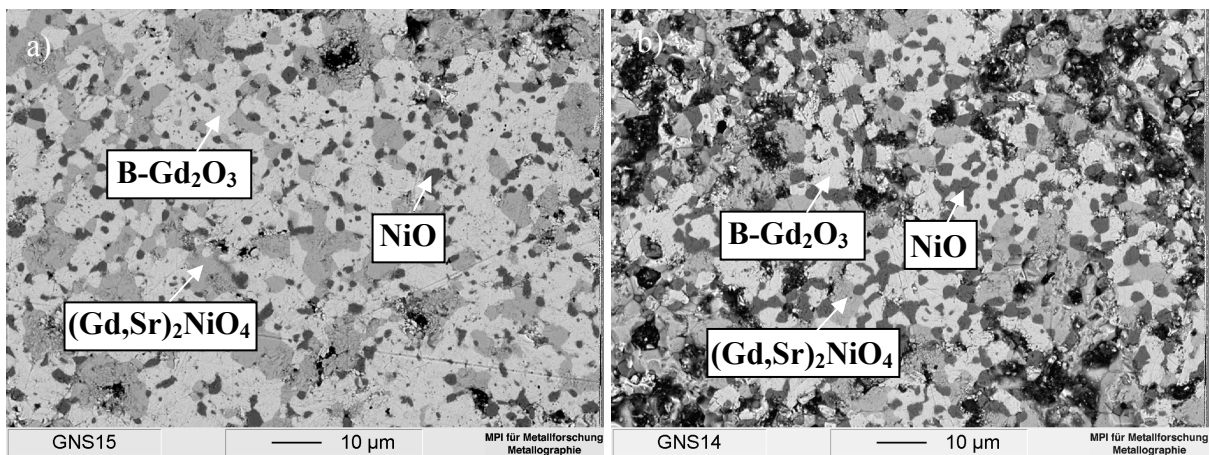


Fig. 3.97. An SEM micrograph of GSN57-10 (a) sample heat-treated at 1300 °C, and GSN40-10 (b) samples heat-treated at 1400 °C, both for 120 h.

Fig. 3.98 shows a comparison of XRD patterns of the samples of the various compositions of  $(\text{Gd,Sr})_2\text{NiO}_4$  solid solution heat-treated at 1300 °C. A shift of the peak positions with changing SrO content can clearly be seen. Just as in the gadolinia rich-side, the sample GSN17-50 prepared at the SrO-rich side was almost on the limit of the homogeneity range, because it contained a very small amount of secondary phases. After repeating consecutive heat-treatments, no differences were found. Samples in the three-phase field, labeled “4”, (GSN10-57 and GSN10-46) have the same solid solution peak positions and very close to

those of GSN17-50. The secondary peaks of the GSN17-50 sample disappeared after heat-treatment at 1400 °C, but the sample was completely molten. For the construction of the phase diagram, the corner on the solid solution of the three-phase field was taken as the composition of the GSN17-50 sample (slightly less  $\text{GdO}_{1.5}$ ), since the amount of the secondary phases is very small. The other corners were accepted from the SrO-NiO quasi binary section.

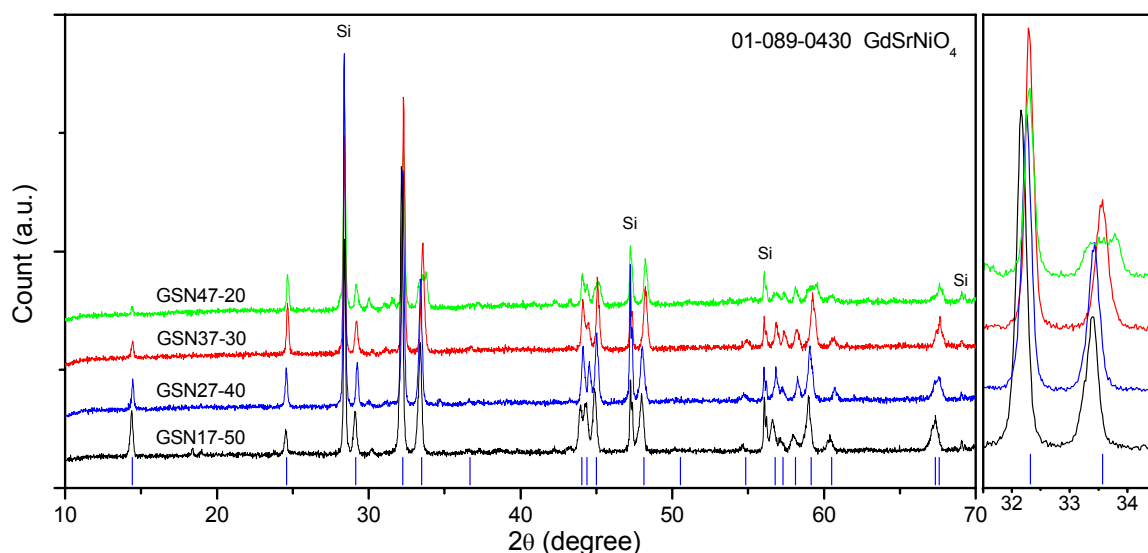


Fig. 3.98. XRD powder patterns of the samples along the  $\text{Gd}_{2-x}\text{Sr}_x\text{NiO}_4$  solid solution. The samples were heat-treated at 1300 °C for 120 h. Si was used as an internal standard.

The oxygen content was measured for the samples along the  $\text{Gd}_{2-x}\text{Sr}_x\text{NiO}_4$  solid solution, and the results are given in Table 3.9, together with the lattice parameters and cell volume data. It can be seen that the solid solution always has the same oxygen content as in the case of  $(\text{La,Sr})_2\text{NiO}_4$ . The average valence state of Ni increases with increasing SrO content and reaches 3.5+ for  $x = 1.5$ . This confirms the presence of  $\text{Ni}^{4+}$  ions, which were also implied in the  $(\text{La,Sr})_2\text{NiO}_4$  solid solution. In the literature, almost stoichiometric  $\text{Gd}_2\text{SrNiO}_{3.96\pm 0.003}$  was reported by Chen et al. [93Che], whereas James and Attfield reported a  $\text{Gd}_{0.33}\text{Sr}_{1.67}\text{NiO}_{3.71}$  solid solution.

The composition dependent lattice parameters of  $\text{Gd}_{2-x}\text{Sr}_x\text{NiO}_4$  are plotted in Fig. 3.99a. As it can be seen in the Fig. 3.98, with increasing SrO content peak positions shift to lower angles indicating expansion of the lattice. The measured lattice parameters were in good agreement with the literature data. No direct relation has been found between the lattice parameters and the SrO content. With increasing SrO content, the  $a$  increases, whereas  $c$  decreases. However, above  $x = 1.33$ ,  $c$  increases, while  $a$  does not change. In Fig. 3.99b data on volume change with increasing SrO content is summarized from this experimental work and from the



literature . Up to  $x = 1.5$  the change is linear whereas above this SrO content no volume change is seen at all. As it was already mentioned, the lattice parameters of the  $\text{Gd}_{2-x}\text{Sr}_x\text{NiO}_4$  solid solution of the three phase field (sample GSN10-57, where  $x = 1.7$ ) is very close to those in the sample GSN17-50 (see also Fig. 3.99a). Therefore, it can be concluded that the homogeneity range of the  $\text{Gd}_{2-x}\text{Sr}_x\text{NiO}_4$  solid solution on the SrO rich side reach up to  $x = 1.5$  where the average valence state of Ni is 3.5+. The data reported by James and Attfield [96Jam] were not taken into account because the solid solution is highly sub-stoichiometric, with respect to the oxygen content.

Table 3.9. Oxygen stoichiometry and lattice parameters of samples along the  $\text{Gd}_{2-x}\text{Sr}_x\text{NiO}_y$  solid solution.

Sample	$\langle x \rangle$	O (wt.%)	$\langle y \rangle$	AVS <sup>a</sup>	$a$ (Å)	$c$ (Å)	Vol. (Å <sup>3</sup> )
GSN47-20	0.6	16.16 ± 0.1	3.99 ± 0.03	2.6+	- <sup>b</sup>	- <sup>b</sup>	- <sup>b</sup>
GSN37-30	0.9	16.94 ± 0.1	3.96 ± 0.03	2.9+	3.7670	12.2210	173.422
GSN20-20 <sup>c</sup>	1	-	-	3.0+	3.7719	12.2010	173.586
GSN27-40	1.2	18.17 ± 0.1	4.02 ± 0.03	3.2+	3.7812	12.2007	174.439
GSN17-50	1.5	19.24 ± 0.1	4.02 ± 0.03	3.5+	3.7875	12.2620	175.901
GSN10-57 <sup>d</sup>	1.7	-	-	-	3.7875	12.2670	175.975

<sup>a</sup> Average Valence State of Ni

<sup>b</sup> *Bmab* structure,  $a = 5.2906$  Å,  $b = 5.3764$  Å,  $c = 12.2069$  Å,  $V = 347.226$  Å<sup>3</sup>

<sup>c</sup> Sample in the two-phase field. <sup>d</sup> Sample in the three-phase field.

The orthorhombic (S.G. *Bmab*) distortion of the  $\text{K}_2\text{NiF}_4$  (S.G. *I4/mmm*) structure is known for the  $\text{Ln}_{2-x}\text{Sr}_x\text{NiO}_4$  ( $\text{Ln} = \text{La}$  [90Tak],  $\text{Nd}$  [92Tak],  $\text{Pr}$  [93Che],  $\text{Sm}$  [93Che]). It manifests itself by splitting of some  $hk0$  reflections in the XRD pattern. Until now, such a structural change has not been reported for  $\text{Gd}_{2-x}\text{Sr}_x\text{NiO}_4$ . In Fig. 3.98, this peak splitting can be clearly seen at  $2\theta = 33^\circ$ . Lattice parameters of the new structure (S.G. *Bmab*) of the solid solution has been determined and given in Table 3.9. Comparing the XRD patterns of GNS70-20 (*Bmab*) and GNS30-20 (*I4/mmm*) it has been found that the phase transition starts at the composition very close to  $x = 0.75$ .

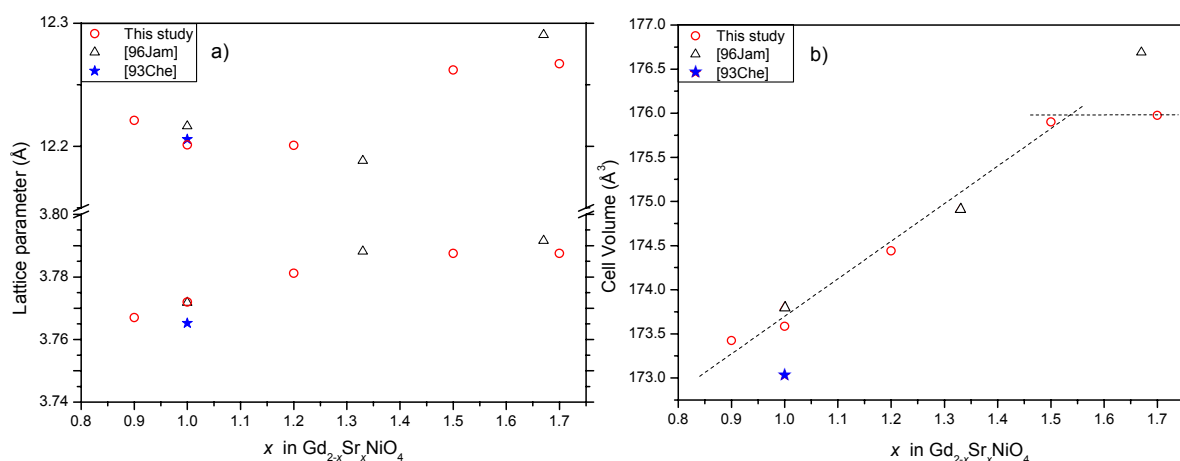


Fig. 3.99. The composition dependent lattice parameters (a) and cell volume (b) of the Gd<sub>2-x</sub>Sr<sub>x</sub>NiO<sub>4</sub> solid solution. The dashed line is linear fit of the experimental results obtained in this work, excluding sample where  $x = 1.7$ .

### 3.4.9. The Ce-Gd-Sr-Ni-O system

In Fig. 3.100, all the subsystems were combined to present the outer surface of the isobarothermal section of the CeO<sub>2</sub>-GdO<sub>1.5</sub>-SrO-NiO system at 1300 °C. The position of the commonly used Ce<sub>0.9</sub>Gd<sub>0.1</sub>O<sub>2-δ</sub> (CGO10) electrolyte is indicated on the figure by a star. The GdO<sub>1.5</sub>-SrO-NiO part of the diagram and partially the CeO<sub>2</sub>-SrO-NiO system are dominated, as previously described, by the K<sub>2</sub>NiF<sub>4</sub>-type solid solution and extends through the pyramid to form the extended (Ce,Gd,Sr)<sub>2</sub>NiO<sub>4±δ</sub> solid solution range. A sample containing a mechanical mixture of (Ce,Sr)<sub>2</sub>NiO<sub>4</sub> and (Gd,Sr)<sub>2</sub>NiO<sub>4</sub> solid solutions (in equal molar amount) was heat-treated at 1300°C, for 120h, and the resultant XRD patterns are given in Fig. 3.101. Both solid solutions have the same crystal structure and the same peak positions with a slight shift due to different lattice parameters. In the figure, only the most intense peaks are compared, since they have essentially the same XRD pattern, and before peaks of each solid solution could be identified heat treatment. After heat treatment, the splitting disappeared and the peaks merged, *i.e.*, indicating that a new solid solution, (Ce,Gd,Sr)<sub>2</sub>NiO<sub>4±δ</sub> has formed.

The compatibility/reactivity of the K<sub>2</sub>NiF<sub>4</sub>-type cathodes with CGO10 electrolyte could be predicted by using the isobarothermal phase equilibria diagram. From the CeO<sub>2</sub>-SrO-NiO part of the diagram, it could directly be used to predict that CGO10 would react with the (Ce,Sr)<sub>2</sub>NiO<sub>4</sub> solid solution to form Sr-Ce-O ternary compounds, because there is no direct contact between the (Ce,Sr)<sub>2</sub>NiO<sub>4</sub> solid solution and undoped CeO<sub>2</sub> and the same behavior

could be expected in a higher-order system. A sample has been prepared containing a mechanical mixture of 50 mol % CGO10 and 50 mol %  $\text{Gd}_{1.1}\text{Sr}_{0.9}\text{NiO}_4$  solid solution in order to confirm the predictions. The sample was heat-treated at  $1300^\circ\text{C}$  for 12h, and the XRD pattern measured is given in Fig. 3.102. The  $\text{Gd}_{1.1}\text{Sr}_{0.9}\text{NiO}_4$  solid solution peaks were compared with the  $\text{GdSrNiO}_4$  pattern, and the CGO10 phase with  $\text{CeO}_2$ . Both matched reasonably well with the phase-pure reference patterns. After the relatively short heat-treatment of 12h, as indicated in the diagram, they have started to react, and new phase equilibria were established between CGO10 and  $\text{SrCeO}_3$ . The intensity of the  $\text{GdSrNiO}_4$  peaks gradually decreased and  $\text{SrCeO}_3$  peaks appeared. In addition,  $\text{NiO}$  peaks were observed, as expected, since there is no  $\text{NiO}$  solubility in both  $\text{SrCeO}_3$  and ceria.

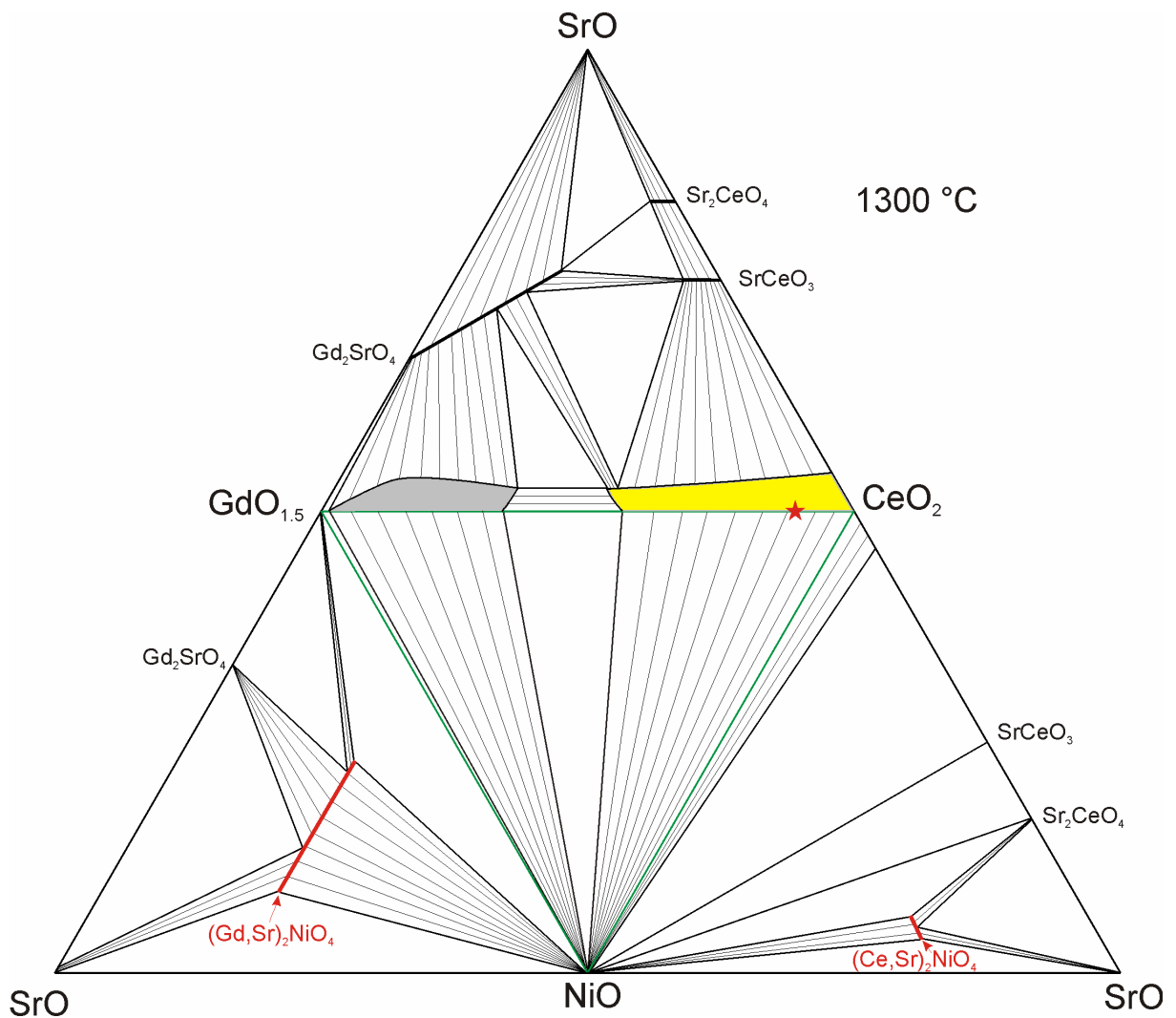


Fig. 3.100. The outer surface of the isobarothermal section of the  $\text{CeO}_2\text{-GdO}_{1.5}\text{-SrO-NiO}$  phase diagram at  $1300^\circ\text{C}$  in air. The star shows the composition CGO10 of the  $\text{Ce}_{0.9}\text{Gd}_{0.1}\text{O}_{2-\delta}$ .

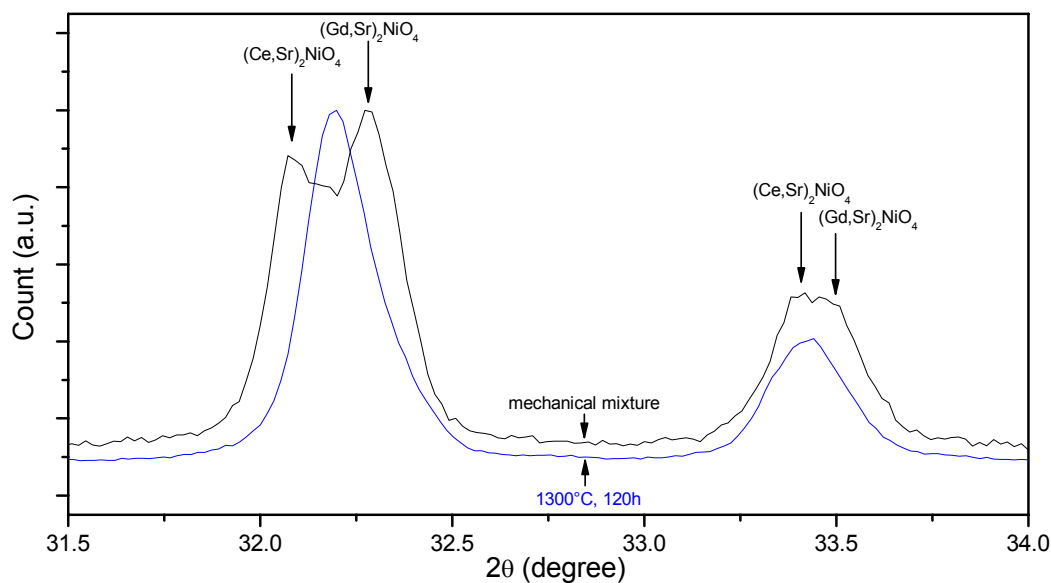


Fig. 3.101. Normalized XRD patterns of the mechanical mixture of  $(\text{Ce,Sr})_2\text{NiO}_4$  and  $(\text{Gd,Sr})_2\text{NiO}_4$  before and after the heat-treatment at  $1300^\circ\text{C}$  for 120h in air.

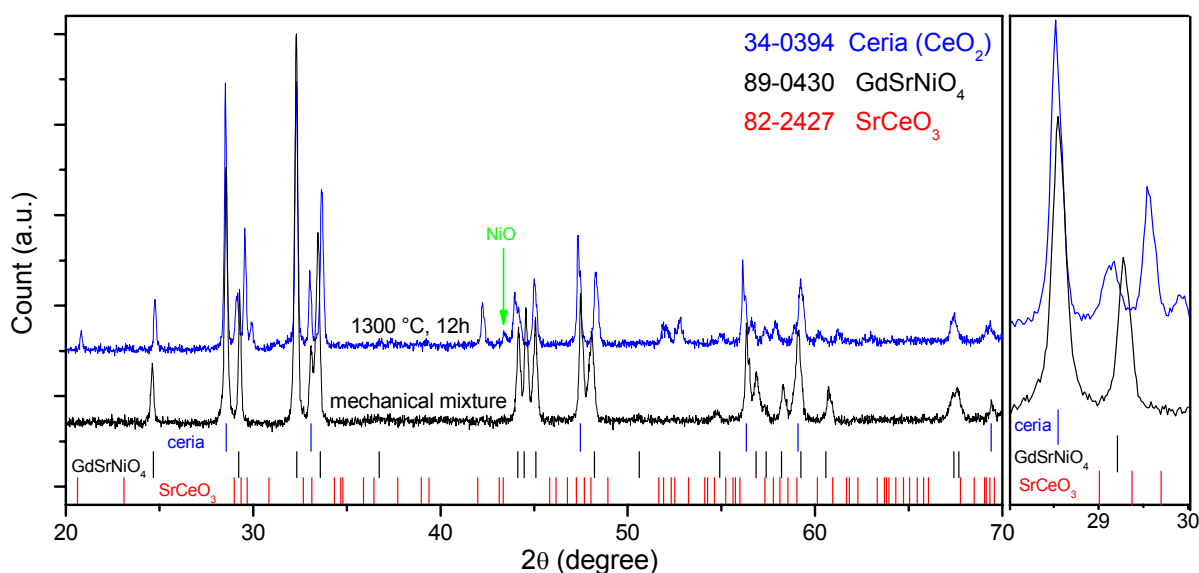


Fig. 3.102. XRD patterns of the mechanical mixture  $\text{CeO}_{0.9}\text{Gd}_{0.1}\text{O}_{2-\delta} + \text{Gd}_{1.1}\text{Sr}_{0.9}\text{NiO}_4$ , and the same sample after heat-treatment at  $1300^\circ\text{C}$ , 12h, in air.

In summary, it can be concluded that, any quasi-ternary and quasi-quaternary composition of  $(\text{Ce,Gd,Sr})_2\text{NiO}_4$ ,  $\text{K}_2\text{NiF}_4$ -type cathodes, are not chemically compatible with CGO10-type electrolytes, whereas NiO is unequivocally chemically compatible with this type of electrolytes.

### 3.4.10. The Ce-Gd-La-Ni-O system

Experiments were designed in order to check the reactivity/compatibility of  $\text{La}_2\text{NiO}_4$  cathodes with CGO10-type electrolytes. Direct mechanical mixing of the compounds and also the

Pechini-type soft chemical method (PSC) were used for the sample preparation. For both material combinations, 50 mol % + 50 mol % of the components were used, and the samples were characterized by XRD. The results are given in Fig. 3.103 and Fig. 3.104. After the heat-treatments, significant changes were detected in both cases in the diffraction patterns with respect to the phase-pure positions of the peaks. The sample prepared by the mixed oxide route and heat-treated at 1100°C consisted of primarily La<sub>2</sub>NiO<sub>4</sub> and CeO<sub>2</sub> phases, with the exception of some additional, very small peaks. With increasing temperature, a significant change can be seen on the CeO<sub>2</sub> peak positions. Normally, the most intense peak of CeO<sub>2</sub> appears around 28.55°. However, after the heat-treatment, another fluorite phase formed and its most intense peak appeared around 27.9°. A similar roughly 0.6° shift could be seen with all the other peaks. In summary, the sample prepared by PSC and heat-treated at 1300°C was composed predominantly of the new fluorite phase, while the other sample prepared by mixed oxide route contained ceria as well as the new fluorite phase, because La<sub>2</sub>NiO<sub>4</sub> reacted with the CGO-type electrolytes. It should also be pointed out that the samples heat-treated at 1300°C also contained NiO peaks. Fig. 3.104 shows the XRD pattern of the sample prepared by PSC and heat-treated at 1100°C, which contains in addition to La<sub>2</sub>NiO<sub>4</sub> and the fluorite phases, the La<sub>3</sub>Ni<sub>2</sub>O<sub>7</sub> peaks. Therefore, for 1100°C, the following reaction mechanism is proposed (oxygen balance was not taken into account):



At higher temperatures, the La<sub>3</sub>Ni<sub>2</sub>O<sub>7</sub> phase was not stable, and decomposed according to



It is expected that the lattice parameter of (Ce,Gd,La<sub>x</sub>)O<sub>2-δ</sub>, which has a fluorite structure, would be larger than that of ceria, since ionic radius of La<sup>3+</sup> is bigger than both of Ce<sup>4+</sup> and Gd<sup>3+</sup>. Therefore, the observed fluorite peaks belong to the solid solution. This model explains the formation of NiO peaks found only after the heat-treatment at 1300°C but not at 1100°C. Therefore, it could be concluded that La-nickelate type cathodes are also not compatible with CGO-type electrolytes. They react to form a solid solution unlike with Gd-containing cathodes, where new phases are forming.

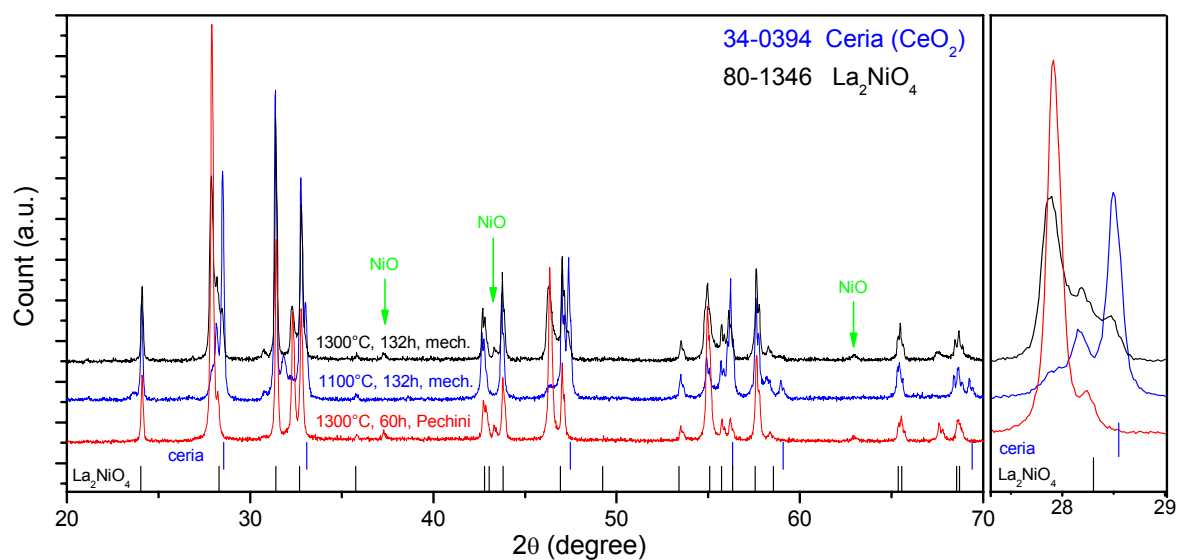


Fig. 3.103. XRD patterns of the mechanical mixture of CGO10 and  $\text{La}_2\text{NiO}_4$  heat-treated at various temperatures in air.

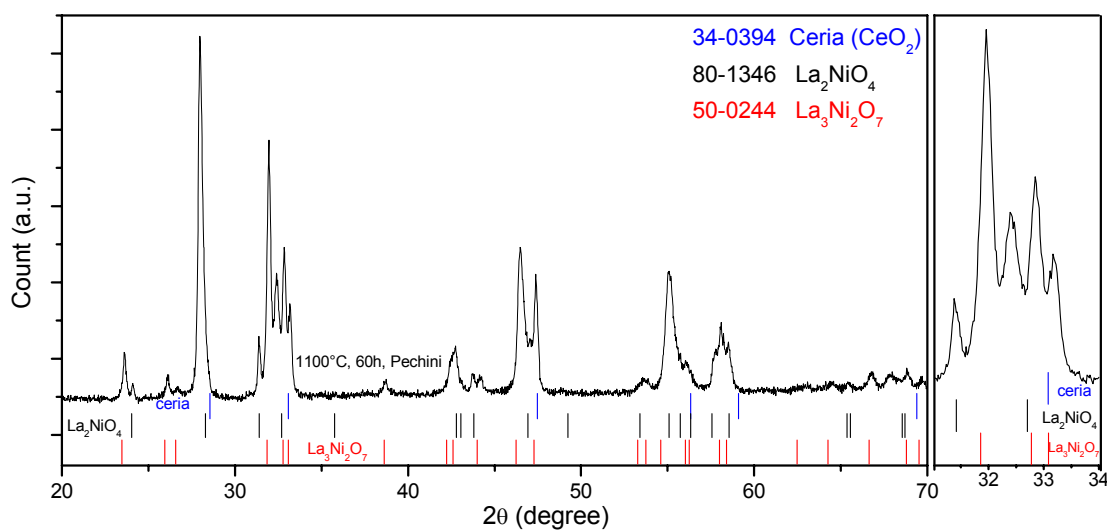


Fig. 3.104. XRD pattern of a sample composed of CGO10 and  $\text{La}_2\text{NiO}_4$ , prepared by soft chemical methods and heat-treated at 1100°C, for 60h, in air.

# *Chapter 4*

## **Summary and Outlook**

This work has reviewed and analyzed the equilibrium stability of systems of electrolyte and electrode material systems by experimental and computational phase studies. For each system considered, a brief literature review was presented on existing knowledge of the relevant diagrams of phase equilibria. Then to experimentally and computationally evaluate each system, a minimum number of specific compositions were chosen strategically, based on knowledge of the crystal structure, constituent ion properties, and constituent phase thermodynamics.

Using equilibration with the gas phase, adiabatic calorimetry and differential scanning calorimetry the thermodynamics of the  $\text{La}_3\text{Ni}_2\text{O}_7$ ,  $\text{La}_4\text{Ni}_3\text{O}_{10}$  and  $\text{LaNiO}_3$  ternary compounds in the La-Ni-O system were determined experimentally for the first time.

The La-Sr-Ni-O system was investigated experimentally along the  $\text{LaO}_{1.5}$ -SrO-NiO quasi-ternary section and modeled thermodynamically. The incorporation of SrO increased the stability of the  $(\text{La,Sr})_2\text{NiO}_4$  phase, which was found to exist at very low oxygen partial pressures. According to the calculations, it could even be considered as potential anode material, since it is redox-stable and has high electronic conductivity.

The sub-solidus phase equilibria of the quaternary La-Ga-Ni-O system were investigated experimentally along the  $\text{La}_2\text{O}_3$ - $\text{Ga}_2\text{O}_3$ -NiO quasi-ternary section. For the compounds,  $\text{La}(\text{Ga,Ni})\text{O}_3$ ,  $\text{La}_2(\text{Ni,Ga})\text{O}_4$ , and  $\text{La}_4(\text{Ni,Ga})_3\text{O}_{10}$ , extended solid solutions were found. The compound  $\text{LaNiGa}_{11}\text{O}_{19}$  with the magnetoplumbite-type structure has been observed for the first time. The system was modeled thermodynamically based on the experimental results. Chemical potential diagrams were calculated for the first time, from which proper fabrication and operation conditions of IT-SOFC systems could be derived.

The La-Mg-Ni-O system was investigated experimentally and computationally along the  $\text{La}_2\text{O}_3$ -MgO-NiO quasi-ternary section. A solid solution of  $\text{La}_2(\text{Ni,Mg})\text{O}_4$  was established, and its temperature dependent homogeneity range was measured.

Based on the experimental and literature data of the subsystems, the phase equilibria in the quasi-quaternary systems,  $\text{LaO}_{1.5}$ -SrO- $\text{GaO}_{1.5}$ -NiO and  $\text{LaO}_{1.5}$ - $\text{GaO}_{1.5}$ -MgO-NiO, were discussed, and the reactivity/compatibility of  $\text{La}_2\text{NiO}_4$ ,  $(\text{La,Sr})_2\text{NiO}_4$  and  $(\text{La,Sr})(\text{Ga,Ni})\text{O}_3$

cathodes with an undoped LaGaO<sub>3</sub> electrolyte was investigated experimentally. Finally, the phase equilibria data accumulated from the subsystems were applied to evaluate the reactivity between LSGM and relevant cathode materials, and as well as between LSGM and NiO-containing anode materials.

The Ce-Ni-O system was investigated experimentally under a highly reducing atmosphere in order to simulate the operation conditions of anode materials. The system was also modeled thermodynamically. Since no reaction would occur between CeO<sub>2</sub> and NiO under the standard fabrication and operating conditions of IT-SOFC systems, the technologically portent conclusion could be drawn from this analysis: the combination of CeO<sub>2</sub> and NiO would be well suited for an electrolyte-electrode system.

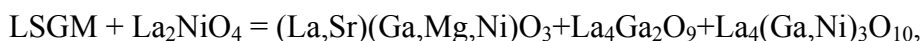
The Sr-Ce-O system was experimentally investigated along the quasi-binary section, SrO-CeO<sub>2</sub>. The thermodynamic properties of SrCeO<sub>3</sub> and Sr<sub>2</sub>CeO<sub>4</sub> compounds were measured and inconsistencies in the literature have been resolved. The complete system was modeled thermodynamically and chemical potential diagrams were calculated.

The Gd-Ni-O system was investigated experimentally along the quasi-binary Gd<sub>2</sub>O<sub>3</sub>-NiO. Literature inconsistencies were resolved, and the system was modeled thermodynamically. Similarly, the Gd-Sr-O system was investigated along the Gd<sub>2</sub>O<sub>3</sub>-SrO quasi-binary system experimentally and computationally.

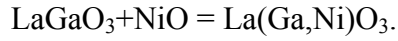
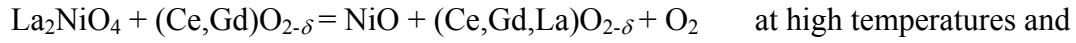
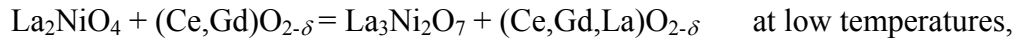
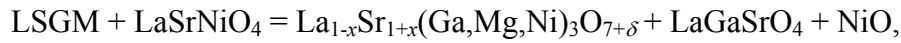
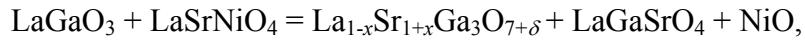
In the Ce-Gd-Ni-O system along the CeO<sub>2</sub>-GdO<sub>1.5</sub>-NiO quasi-ternary section, no chemical interaction was found between the (Ce,Gd)O<sub>2</sub> solid solution and NiO.

The quasi-ternary system CeO<sub>2</sub>-GdO<sub>1.5</sub>-SrO was investigated experimentally for the first time. Extended solid solutions of Sr<sub>2</sub>(Ce,Gd)O<sub>4</sub>, Sr(Ce,Gd)O<sub>3</sub> and (Gd,Sr)<sub>2</sub>(Sr,Ce)O<sub>4</sub> were found. Similarly, the phase diagrams of CeO<sub>2</sub>-SrO-NiO and GdO<sub>1.5</sub>-SrO-NiO were constructed for the first time. The homogeneity range of the Gd<sub>2-x</sub>Sr<sub>x</sub>NiO<sub>4</sub> solid solution was determined and a composition dependent phase transition was found.

Selected subsystems were combined in order to predict the reactivity between IT-SOFC components under cell fabrication conditions. It has been found that La- and Gd-containing K<sub>2</sub>NiF<sub>4</sub>-type cathodes would not be compatible chemically with CGO electrolytes since they react to form new compounds or solid solutions. Some important reaction mechanisms determined in the present work are:





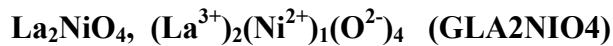


The experimentally and computationally determined phase equilibria diagrams are sufficient to predict the interaction between the relevant SOFC components. However, in order to formulate the conditions more precisely, additional thermodynamic work is necessary. For a comprehensive modeling of the thermodynamics of higher-order systems, the defect chemistry of the solid solutions must also be known.

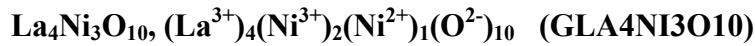
# Appendix

## The thermodynamic parameters obtained in the present work

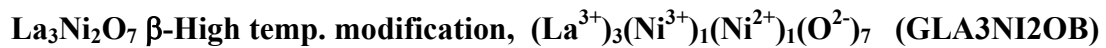
### *Stoichiometric compounds*



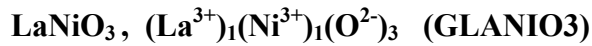
$$^{\circ}G = -2095505.05 + 1035.851 \cdot T - 178.04 \cdot T \cdot \ln(T) - 7.089 \cdot 10^{-3} \cdot T^2 + 1214190.0 \cdot T^{-1}$$



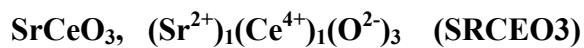
$$^{\circ}G = -4599428.42 + 2368.154 \cdot T - 405.247 \cdot T \cdot \ln(T) - 3.260 \cdot 10^{-2} \cdot T^2 + 2130000 \cdot T^{-1}$$



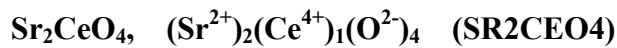
$$^{\circ}G = -3357179.32 + 1778.316 \cdot T - 301.86 \cdot T \cdot \ln(T) - 1.712 \cdot 10^{-2} \cdot T^2 + 1580000 \cdot T^{-1}$$



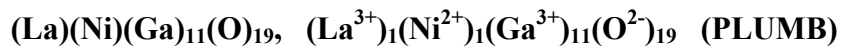
$$^{\circ}G = -1248964.33 + 696.185 \cdot T - 118.12 \cdot T \cdot \ln(T) - 0.0096 \cdot T^2 + 648000 \cdot T^{-1}$$



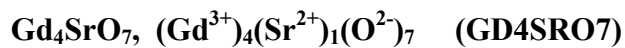
$$^{\circ}G = -1728929.5 + 688.491 \cdot T - 120.426 \cdot T \cdot \ln(T) - 0.007062 \cdot T^2 + 792000 \cdot T^{-1}$$



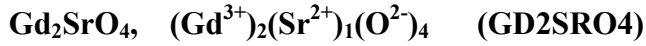
$$^{\circ}G = 2 \cdot \text{GSROSOL} + \text{GCEO2} - 9201.9095 - 12.5927 \cdot T$$



$$^{\circ}G = 0.5 \cdot \text{GLA2O3A} + \text{GNIO} + 5.5 \cdot \text{GGA2O3} - 155000$$



$$^{\circ}G = 2 \cdot \text{GGD2O3C} + \text{GSROSOL} + 82630 - 67.473 \cdot T$$



$${}^{\circ}G = \text{GGD2O3C} + \text{GSROSOL} - 90312 + 13.49 \cdot T$$

***Solution phases***



$${}^{\circ}G_{\text{La}^{3+};\text{Ni}^{2+};\text{O}^{2-}}^{\text{LSN}} = \text{GLA2NIO4}$$

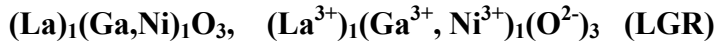
$${}^{\circ}G_{\text{La}^{3+};\text{Ni}^{3+};\text{O}^{2-}}^{\text{LSN}} = 0.5 \cdot \text{GLA2NIO4} + 0.5 \cdot \text{GLA2O3A} + 0.5 \cdot \text{GNIO} + 11.526 \cdot T - 12000$$

$${}^{\circ}G_{\text{La}^{3+};\text{Ni}^{4+};\text{O}^{2-}}^{\text{LSN}} = \text{GLA2NIO4} + 2200$$

$${}^{\circ}G_{\text{Sr}^{2+};\text{Ni}^{2+};\text{O}^{2-}}^{\text{LSN}} = 2 \cdot \text{GSROSOL} + \text{GNIO} + \text{GHSEROO}$$

$${}^{\circ}G_{\text{Sr}^{2+};\text{Ni}^{3+};\text{O}^{2-}}^{\text{LSN}} = 2 \cdot \text{GSROSOL} + 1.5 \cdot \text{GNIO} + 0.5 \cdot \text{GLA2O3A} + \text{GHSEROO} - 0.5 \cdot \text{GLA2NIO4} \\ + 11.526 \cdot T - 12000$$

$${}^{\circ}G_{\text{Sr}^{2+};\text{Ni}^{4+};\text{O}^{2-}}^{\text{LSN}} = 2 \cdot \text{GSROSOL} + \text{GNIO} + \text{GHSEROO} + 2200$$

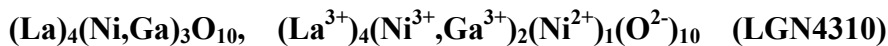


$${}^{\circ}G_{\text{La}^{3+};\text{Ga}^{3+};\text{O}^{2-}}^{\text{LGR}} = \text{GLGR}^*$$

$${}^{\circ}G_{\text{La}^{3+};\text{Ni}^{3+};\text{O}^{2-}}^{\text{LGR}} = \text{GLANIO3}$$

$${}^0L_{\text{La}^{3+};\text{Ga}^{3+};\text{Ni}^{3+};\text{O}^{2-}}^{\text{LGR}} = -12000$$

$$* \text{GLGR} = -1531220 + 637.1524 \cdot T - 109.72865 \cdot T \cdot \ln(T) - 0.0139853 \cdot T^2 + 476600 \cdot T^{-1} \quad [06Zin3]$$



$${}^{\circ}G_{\text{La}^{3+};\text{Ni}^{3+};\text{Ni}^{2+};\text{O}^{2-}}^{\text{LGN4310}} = \text{GLA4NI3O10}$$

$${}^{\circ}G_{\text{La}^{3+};\text{Ga}^{3+};\text{Ni}^{2+};\text{O}^{2-}}^{\text{LGN4310}} = \text{GGA2O3} + \text{GNIO} + 2 \cdot \text{GLA2O3A} - 176000$$

$${}^0L_{\text{La}^{3+};\text{Ga}^{3+};\text{Ni}^{3+};\text{Ni}^{2+};\text{O}^{2-}}^{\text{LGN4310}} = -42500$$

**(La)<sub>2</sub>(Ni,Ga)O<sub>4</sub>, (La<sup>3+</sup>)<sub>2</sub>(Ni<sup>2+</sup>,Ga<sup>3+</sup>,Va)<sub>1</sub>(O<sup>2-</sup>)<sub>4</sub> (LGN214)**

$${}^{\circ}G_{La^{3+},Ni^{2+},O^{2-}}^{LGN214} = GLA2NIO4$$

$${}^{\circ}G_{La^{3+},Ga^{3+},O^{2-}}^{LGN214} = GLA2O3A + 0.5 \cdot GGA2O3 - 0.5 \cdot GHSEROO + 21000$$

$${}^{\circ}G_{La^{3+},Va,O^{2-}}^{LGN214} = +GLA2O3A + GHSEROO + 21000$$

$${}^0L_{La^{3+},Ni^{2+},Ga^{3+},O^{2-}}^{LGN214} = -150000$$

**(La)<sub>2</sub>(Ni,Mg)O<sub>4</sub>, (La<sup>3+</sup>)<sub>2</sub>(Ni<sup>2+</sup>,Mg<sup>2+</sup>)<sub>1</sub>(O<sup>2-</sup>)<sub>4</sub> (LGM214)**

$${}^{\circ}G_{La^{3+},Ni^{2+},O^{2-}}^{LGM214} = GLA2NIO4$$

$${}^{\circ}G_{La^{3+},Mg^{2+},O^{2-}}^{LGM214} = GLA2O3A + GMGOSOL + 32600 - 16.1 \cdot T$$

$${}^0L_{La^{3+},Ni^{2+},Mg^{2+},O^{2-}}^{LGM214} = 0$$

**Liquid, (Sr<sup>2+</sup>, Gd<sup>3+</sup>,Ni<sup>2+</sup>,Ce<sup>4+</sup>) (O<sup>2-</sup>) (Liq)**

$${}^{\circ}G_{Sr^{2+},O^{2-}}^{Liq} = 2 \cdot GSROLIQ$$

$${}^{\circ}G_{Ce^{4+},O^{2-}}^{Liq} = 2 \cdot GCEO2LQ$$

$${}^{\circ}G_{Ni^{2+},O^{2-}}^{Liq} = 2 \cdot GNIOLIQ$$

$${}^{\circ}G_{Gd^{3+},O^{2-}}^{Liq} = +124733 - 47.759 \cdot T + GGD2O3B$$

$${}^0L_{Sr^{2+},Ce^{4+},O^{2-}}^{Liq} = -182634.72$$

$${}^0L_{Gd^{3+},Ni^{2+},O^{2-}}^{Liq} = -20000$$

$${}^0L_{Gd^{3+},Sr^{2+},O^{2-}}^{Liq} = -123280$$

$${}^1L_{Gd^{3+},Sr^{2+},O^{2-}}^{Liq} = -8800$$

**(Sr,Gd)O, (Sr<sup>2+</sup>,Gd<sup>3+</sup>,Va)<sub>1</sub>(O<sup>2-</sup>)<sub>1</sub> (Halite)**

$${}^{\circ}G_{Sr^{2+},O^{2-}}^{Halite} = \text{GSROSOL}$$

$${}^{\circ}G_{Gd^{3+},O^{2-}}^{Halite} = 0.5 \cdot \text{GGD2O3C} + 48600$$

$${}^{\circ}G_{Va,O^{2-}}^{Halite} = 0$$

$${}^0L_{Gd^{3+},Sr^{2+},O^{2-}}^{Halite} = -12000$$

**C-(Gd,Sr)<sub>2</sub>O<sub>3</sub>, (Gd<sup>3+</sup>,Sr<sup>2+</sup>)<sub>2</sub>(O<sup>2-</sup>,Va)<sub>3</sub> (M2O3C)**

$${}^{\circ}G_{Gd^{3+},O^{2-}}^{M2O3C} = \text{GGD2O3C}$$

$${}^{\circ}G_{Gd^{3+},Va}^{M2O3C} = \text{GGD2O3C} - 3 \cdot \text{GHSEROO}$$

$${}^{\circ}G_{Sr^{2+},O^{2-}}^{M2O3C} = \text{SRB\_ALPC} + \text{GHSEROO} - 0.3333 \cdot \text{RE\_ALPHA} + 15.87691 \cdot T$$

$${}^{\circ}G_{Sr^{2+},Va}^{M2O3C} = \text{SRB\_ALPC} - 2 \cdot \text{GHSEROO} + 0.6667 \cdot \text{RE\_ALPHA} + 15.87691 \cdot T$$

$${}^0L_{Gd^{3+},Sr^{2+},O^{2-}}^{M2O3C} = +198000 - 60.9 \cdot T$$

$${}^0L_{Gd^{3+},Sr^{2+},Va}^{M2O3C} = +198000 - 60.9 \cdot T$$

**B-(Gd,Sr)<sub>2</sub>O<sub>3</sub>, (Gd<sup>3+</sup>,Sr<sup>2+</sup>)<sub>2</sub>(O<sup>2-</sup>,Va)<sub>3</sub> (M2O3B)**

$${}^{\circ}G_{Gd^{3+},O^{2-}}^{M2O3B} = \text{GGD2O3B}$$

$${}^{\circ}G_{Gd^{3+},Va}^{M2O3B} = \text{GGD2O3B} - 3 \cdot \text{GHSEROO}$$

$${}^{\circ}G_{Sr^{2+},O^{2-}}^{M2O3B} = \text{SRB\_ALPB} + \text{GHSEROO} - 0.3333 \cdot \text{RE\_ALPHA} + 15.87691 \cdot T$$

$${}^{\circ}G_{Sr^{2+},Va}^{M2O3B} = \text{SRB\_ALPB} - 2 \cdot \text{GHSEROO} + 0.6667 \cdot \text{RE\_ALPHA} + 15.87691 \cdot T$$

$${}^0L_{Gd^{3+},Sr^{2+},O^{2-}}^{M2O3B} = +198860 - 60.9 \cdot T$$

$${}^0L_{Gd^{3+},Sr^{2+},Va}^{M2O3B} = +198860 - 60.9 \cdot T$$

**A-(Gd,Sr)<sub>2</sub>O<sub>3</sub>, (Gd<sup>3+</sup>,Sr<sup>2+</sup>)<sub>2</sub>(O<sup>2-</sup>,Va)<sub>3</sub> (M2O3A)**

$${}^{\circ}G_{Gd^{3+},O^{2-}}^{M2O3A} = GGD2O3A$$

$${}^{\circ}G_{Gd^{3+},Va}^{M2O3A} = GGD2O3A -3 \cdot GHSEROO$$

$${}^{\circ}G_{Sr^{2+},O^{2-}}^{M2O3A} = SR\_ALPHA+GHSEROO-0.3333 \cdot RE\_ALPHA+15.87691 \cdot T$$

$${}^{\circ}G_{Sr^{2+},Va}^{M2O3A} = SR\_ALPHA-2 \cdot GHSEROO+0.6667 \cdot RE\_ALPHA+15.87691 \cdot T$$

$${}^0L_{Gd^{3+},Sr^{2+},O^{2-}}^{M2O3A} = +164600 -60.9 \cdot T$$

$${}^0L_{Gd^{3+},Sr^{2+},Va}^{M2O3A} = +164600 -60.9 \cdot T$$

**H-(Gd,Sr)<sub>2</sub>O<sub>3</sub>, (Gd<sup>3+</sup>,Sr<sup>2+</sup>)<sub>2</sub>(O<sup>2-</sup>,Va)<sub>3</sub> (M2O3H)**

$${}^{\circ}G_{Gd^{3+},O^{2-}}^{M2O3H} = GGD2O3H$$

$${}^{\circ}G_{Gd^{3+},Va}^{M2O3H} = GGD2O3H -3 \cdot GHSEROO$$

$${}^{\circ}G_{Sr^{2+},O^{2-}}^{M2O3H} = SRH\_ALPH+GHSEROO-0.3333 \cdot RE\_ALPHA+15.87691 \cdot T$$

$${}^{\circ}G_{Sr^{2+},Va}^{M2O3H} = SRH\_ALPH-2 \cdot GHSEROO+0.6667 \cdot RE\_ALPHA+15.87691 \cdot T$$

$${}^0L_{Gd^{3+},Sr^{2+},O^{2-}}^{M2O3H} = +134000 -60.9 \cdot T$$

$${}^0L_{Gd^{3+},Sr^{2+},Va}^{M2O3H} = +134000 -60.9 \cdot T$$

**X-(Gd,Sr)<sub>2</sub>O<sub>3</sub>, (Gd<sup>3+</sup>,Sr<sup>2+</sup>)<sub>2</sub>(O<sup>2-</sup>,Va)<sub>3</sub> (M2O3X)**

$${}^{\circ}G_{Gd^{3+},O^{2-}}^{M2O3X} = GGD2O3X$$

$${}^{\circ}G_{Gd^{3+},Va}^{M2O3X} = GGD2O3X -3 \cdot GHSEROO$$

$${}^{\circ}G_{Sr^{2+},O^{2-}}^{M2O3X} = SRX\_ALPH+GHSEROO-0.3333 \cdot RE\_ALPHA+15.87691 \cdot T$$

$${}^{\circ}G_{Sr^{2+},Va}^{M2O3X} = SRX\_ALPH-2 \cdot GHSEROO+0.6667 \cdot RE\_ALPHA+15.87691 \cdot T$$

$${}^0L_{Gd^{3+},Sr^{2+},O^{2-}}^{M2O3X} = +118600 -60.9 \cdot T$$

$${}^0L_{Gd^{3+},Sr^{2+},Va}^{M2O3X} = +118600 -60.9 \cdot T$$

RE\_ALPHA = 0

SRB\_ALPC = 45000

SRB\_ALPB = 40000

SR\_ALPA = 25000

SRH\_ALPH = 40000

SRX\_ALPH = 40000

# References

- [Pech] M.P. Pechini, "Method of preparing lead and alkaline earth titanates and niobates and coating method using the same to form a capacitor" US Patent No. 3,330,697.
- [Per] M. Zinkevich, personal communication, 2006.
- [SGTE] The SGTE unary database, version 4.4, SGTE (Scientific Group Thermodata Europe), Grenoble, France, 2001.
- [ICDD] ICDD, International Centre for Diffraction Data, 12 Campus Boulevard, Newtown Square, PA, USA, 2005, <http://www.icdd.com/>.
- [32War] H.V. Wartenberg, E. Prophet, *Z. Anorg. Chem.*, 208: 369-379, 1932.
- [37War] H. von Wartenberg, K. Eckhardt, *Z. anorg. allgem. Chemie*, 232: 179-187, 1937.
- [59Sha] M.W. Shafer and R. Roy, *J. Am. Ceram. Soc.*, 42: 563-570 (1959),
- [60Bra1] G. Brauer, K.A. Gingerich, U. Holtschmidt, *J. Inorg. Nucl. Chem.* 16: 77-86, 1960.
- [60Bra2] G. Brauer, K.A. Gingerich, *J. Inorg. Nucl. Chem.*, 16: 87-99, 1960.
- [61Sch] S.J. Schneider, R.S. Roth, J.L. Waring, *Journal of Research of the National Bureau of Standards-A*, 65: 345-374, 1961.
- [64Bev] D.J.M. Bevan, J. Kordis, *J. Inorg. Nucl. Chem.*, 26: 1509-1523, 1964.
- [64Tre] S.G. Tresvyatskii, L.M. Lopato, *Izdatelstvo Akademii Nauk SSSR*, 155-158, 1964.
- [65Foe] M. Foex, *Bull. Soc. Franc. Miner. Crystallogr.*, 88: 521-&, 1965.
- [66Foe] M. Foex, J.P. Traverse, *Rev. Int. Hautes Temper. Et Refract.*, 3: 429-453, 1966.
- [67Bar] T.L. Barry, R. Roy, *Journal of Inorganic & Nuclear Chemistry*, 29: 1243-48, 1967.
- [69Bat] P. Batti, G. Slocari, *Annali di Chimica*, 59: 155-161, 1969.
- [69Lop] L.M. Lopato, *Russ. J. Inorg. Chem.*, 14: 449-&, 1969.
- [69Kat] G. Katz, S. Kachi, R. Roy, *Jpn. J. Appl. Phys.*, 8: 429-435, 1969.
- [69Sha] R.D. Shannon, C.T. Prewitt, *Acta Cryst.*, B25: 925-946, 1969.
- [69Que] F. Queyroux, *Revue Internationale Des Hautes Temperatures Et Des Refractaires*, 6: 111-&, 1969.
- [70Kau] L. Kaufman, H. Bernstein, *Computer Calculation of Phase Diagrams*, Academic Press, New York, 1970.
- [70Rud] V.S. Rudenko, A.G. Boganov, *Izvestiya Akademii Nauk SSSR*, 6: 2158-2165, 1970.
- [70Wil] B. Willer, P. Lehuede, *Revue De Chimie Minerale*, 7: 989-&, 1970.
- [71Bou] C. Boulesteix, P. Caro, M. Gasgnier et al., *Colloques internationaux C.N.R.S.*, 205: 361-367, 1971.
- [71Kus] A.E. Kustschewskij, "Interaction of Sm, Gd, Dy, Yb and Y oxides with SrO" PhD thesis, Inst. Probl. Materialoved., Kiev, 1971.



- [71Tre] S.G. Treswjatskij; L.M. Lopato, A.W. Schewtschenko, A.E. Kustschewskij, *Colloques internationaux C.N.R.S.*, 205 : 247-253, 1971.
- [72Lop] L.M. Lopato, A.V. Shevchenko, A.E. Kushchevskii, *Inst. Probl. Materialoved., Kiev, USSR. Poroshkovaya Metallurgiya (Kiev)*, 12: 88-92, 1972.
- [72Sco] B.A. Scott, K.H. Nichols, R.M. Potemski, J.M. Woodall, *Appl. Phys. Lett.*, 21: 121-122, 1972.
- [73Lop] L.M. Lopato, A.E. Kushchevskii, *Inst. Probl. Materialoved., Kiev Ukrainskii Khimicheskii Zhurnal (Russian Edition)*, 39: 7-9, 1973.
- [75Gai] P.L. Gai, C.N.R. Rao, *Z. Naturfors. Sect. A - J. Phys. Sci.*, 30: 1092-1093, 1975.
- [75Oba] H. Obayashi, T. Kudo, *Jap. J. Appl. Phys.*, 14: 330-335, 1975.
- [75Pan] R.J. Panlener, R.N. Blumenthal, J.E. Garnier, *J. Phys. Chem. Solids*, 36: 1213-1222, 1975.
- [75Ray] S.P. Ray, A.S. Nowick, D.E. Cox, *J. Solid State Chem.* 15: 344-351, 1975.
- [76Kob] Kobzareva VP, Kovba LM, Lopato LM, Lykova LN, Shevchenko AV, *Zhurnal Neorganicheskoi Khimii*, 21: 1651-1654, 1976.
- [76Lop] L.M. Lopato, *Ceramurgia International*, 2: 18-32, 1976.
- [77Gop] J. Gopalakrishnan, G. Colsmann, B. Reuter, *Journal of Solid State Chemistry*, 22: 145-149, 1977.
- [78Vyg] I.I. Vygovskii, M.V. Kniga, T.I. Metelitsa, *Izvestiya Akademii Nauk SSSR, Neorganicheskie Materialy*, 10: 78-80, 1974.
- [79Nak] T. Nakamura, G. Petzow, L.J. Gauckler, *Mater. Res. Bull.*, 14: 649-659, 1979.
- [80Dub] V.A. Dubok, A.A. Vecher, V.V. Lashneva, A.G. Voropaev, *Izvestiya Akademii Nauk SSSR, Neorganicheskie Materialy*, 16: 1797-1799, 1980.
- [81Pep] J.G. Pepin, *Journal of Applied Crystallography*, 14: 70-71, 1981.
- [84Ric] M. Ricken, J. Nölting, I. Riess, *J. Solid State Chem.* 54: 89-99, 1984.
- [86Ram] R.A.M. Ram, L. Ganapathi, P. Ganguly, C.N.R. Rao, *J. Solid State Chem.*, 63: 139-147, 1986.
- [85Miz] M. Mizuno, T. Yamada, T. Ohtake, *J. Ceram. Soc. Jpn.*, 93: 295-300, 1985.
- [85Ote] C. Otero Arean, M.C. Trobajo-Fernandez, *Phys. Status Solidi-A*, 92: 443-447, 1985.
- [86Dub] B. Dubois, G. Dhalenne, F. Dyvoire, A. Revcolevschi, *J. Am. Ceram. Soc.*, 69: C-6-C8, 1986.
- [86Hil] M. Hillert, B. Jansson, *J. Am. Ceram. Soc.*, 69: 732-734, 1986.
- [86Lin] T.B. Lindemer, *Calphad*, 10: 129-136, 1986.
- [87Gme] E. Gmelin, *Thermochimica Acta*, 110: 183-208, 1987.
- [88Nit] T. Nitadori, M. Muramatsu, M. Misono, *Bulletin of the Chemical Society of Japan*, 6: 3831-3837, 1988.
- [88Pet] A. N. Petrov, V. A. Cherepanov, A. Zuyev, V. M. Zhukovsky, *J. Solid State Chem.*, 77: 1-14, 1988.
- [88Rie] I. Riess, R. Koerner, M. Ricken, J. Noelting, *Solid State Ionics*, 28: 539-541, 1988.

- [89Kor] R. Korner, M. Ricken, J. Noltig, I. Riess, *J. Solid State Chem.*, 78: 136-147, 1989.
- [89Moo] P.B. Moore, P.K. Sengupta, Y. Lepage, *Am. Mineralogist*, 74: 1186-1194, 1989.
- [90Bry] H.M. O'Bryan, P.K. Gallagher, G.W. Berkstresser, C.D. Brandle, *J. Mater. Res.*, 5: 183-189, 1990.
- [90Kit] K. Kitayama, *J. Solid State Chem.*, 87: 165-172, 1990.
- [90Mas] T.B. Massalski (Ed.), *Binary Alloy Phase Diagrams*, Second Edition, ASM International, Materials Park, Ohio, 1990.
- [90Sre] K. Sreedhar, C.N.R. Rao, *Materials Research Bulletin*, 25: 1235-1242, 1990.
- [90Tak] Y. Takeda, R. Kanno, M. Sakano, O. Yamamoto, M. Takano, Y. Bando, H. Akinaga, K. Takita, J.B. Goodenough, *Materials Research Bulletin*, 25: 293-306, 1990.
- [90Tay] J.R. Taylor, A.T. Dinsdale, *Z. Metallkd.*, 81: 354-366, 1990.
- [90Tak2] J. Takahashi, T. Toyoda, T. Ito, M. Takatsu, *J. Mater. Sci.*, 25: 1557-1562, 1990.
- [91Cav] R.J. Cava, B. Batlogg, T.T. Palstra, J.J. Krajewski, W.F. Peck, A.P. Ramirez, L.W. Rupp, *Physical Review B*, 43: 1229-1232 Part B, 1991.
- [91Lav] O.A. Lavrova, V.A. Somenkov, A.K. Tkalich, S. S. Shul'shtein, *Superconductivity: Physics, Chemistry, Technology (USA)*, 4: 1743-1745, 1991.
- [91Din] A.T. Dinsdale, *Calphad*, 15: 317-425, 1991.
- [91Kat] M. Kato,; Y. Maeno,; T. Fujita, *Journal of the Physical Society of Japan*, 60: 1994-2001, 1991.
- [91Tka] A.K. Tkalich, V.P. Glazkov, V.A. Somenkov, S.S. Shil'shtein, A.E. Kar'kim, A.V. Mirmel'shtein, *Superconductivity: Physics, Chemistry, Technology (USA)*, 4: 2280-2286, 1991.
- [91Yok] H. Yokokawa, N. Sakai, T. Kawada and M. Dokiya, *J. Electrochem. Soc.*, 138: 2719-2727, 1991.
- [92Fur] Y. Furukawa, S. Wada, *Journal of The Physical Society of Japan*, 61: 1182-1185, 1992.
- [92Ota] S.B. Ota, E. Gmelin, *Measurement Science & Technology*, 3: 1047-1049, 1992.
- [92Pou] B. G. Pound, *Solid State Ionics*, 52: 183-188, 1992.
- [92Sam] A.F. Sammells, R.L. Cook, J.H. White, J.J. Osborne, R.C. MacDuff, *Solid State Ionics*, 52: 111-23, 1992.
- [92Tak] Y. Takeda, M. Nishijima, N. Imanishi, R. Kanno, O. Yamamoto, *Journal of Solid State Chemistry*, 96: 72-83, 1992.
- [93Che] S.C. Chen, K.V. Ramanujachary, M. Greenblatt, *Journal of Solid State Chemistry*, 105: 444-457, 1993.
- [93Dic] J. Dicarolo, A. Mehta, D. Banschick, A. Navrotsky, *Journal of Solid State Chemistry*, 103: 186-192, 1993.
- [93Gra] X. Granados, J. Fontcuberta, M. Vallet-Regí, M. J. Sayagué and J. M. González-Calbet, *Journal of Solid State Chemistry*, 102: 455-464, 1993.
- [93Jam] M. James, J.P. Attfield, *J. Solid State Chem.*, 105, 287-293, 1993.

- [93Hal] B. Hallstedt, *Calphad*, 17: 281-286, 1993.
- [93Hof] H.E. Hofer, W. F. Kock, *J. Electrochem. Soc.*, 140: 2889-2894, 1993.
- [93Ran] J. Ranlov, F. W. Poulsen, M. Mogensen., *Solid State Ionics*, 61: 277-279, 1993.
- [93Ric] D.E. Rice, D.J. Buttrey, *J. Solid State Chem.*, 105: 197-210, 1993.
- [93Say] M.J. Sayagues, M. Valletregi, A. Caneiro, J.M. Gonzalezcalbet, *Solid State Ionics*, 66: 21-26, 1993.
- [94Kem] van der Kemp, W.J.M., Blok, J.G., van der Linde P.R., Oonk, H.A.J., Schuijff, A., Verdonk, M.L., *Calphad*, 18: 255-267, 1994.
- [94Vas] V.V. Vashuk, O.P. Olshevskaya, S.A. Prodan, Y.G. Zonov, S.P. Tolochko, *Inorganic mat.*, 30: 901-904, 1994.
- [94Zha] Z. Zhang, M. Greenblatt, J.B. Goodenough, *Journal of Solid State Chemistry*, 108: 402-409, 1994.
- [95Jam1] M. James, J.P. Attfield, *Chem. Mater.*, 7: 2338-2341, 1995.
- [95Jam2] M. James, J.P. Attfield, J. Rodriguez-Carvajal, *Chem. Mater.*, 7: 1448-1452, 1995.
- [95Kow] M. Kowalski, P.J. Spencer, *Calphad*, 19: 229-243, 1995.
- [95Rei] D. Reinen, U. Kesper, D. Belder, *Journal of Solid State Chemistry*, 116: 355-363, 1995.
- [95Ste] B.C.H. Steele, *Solid State Ionics*, 75: 157-165, 1995.
- [95Yam] H. Yamane, K. Ogawara, M. Omori, T. Hirai, *J. Am. Ceram. Soc.*, 78: 2385-2390, 1995.
- [95Tan] S. Taniguchi, T. Nishikawa, Y. Yasui, Y. Kobayashi, J. Takeda, S.I. Shamoto, M. Sato, *J. Phys. Soc. Jap.*, 64 : 1644-1650, 1995.
- [95Zha] Z. Zhang, M. Greenblatt, *J. Solid State Chem.*, 117: 236-246, 1995.
- [96Fra] V.J. Fratello, G.W. Berkstresser, C.D. Brandle, A.J. VenGraitis, *J. Crystal Growth*, 166: 878-882, 1996.
- [96Jam] M. James, J.P. Attfield, *Journal of Materials Chemistry*, 6: 57-62, 1996.
- [96Kob] Y. Kobayashi, S. Taniguchi, M. Kasai, M. Sato, T. Nishioka, M. Kontani, *J. Phys. Soc. Jap.*, 65: 3978-3982, 1996.
- [96Ram] A.P. Ramirez, P.L. Gammel, S.W. Cheong, D.J. Bishop, P. Chandra, *Physical Review Letters*, 76: 447-450, 1996.
- [96Ris] D. Risold, B. Hallstedt, L.J. Gauckler, *Calphad*, 20: 353-361, 1996.
- [96Vas] V.V. Vashuk, O.P. Olshevskaya, S.P. Prodan, *Inorganic mat.*, 32: 436-9, 1996.
- [97Car] M.D. Carvalho, F.M.A. Costa, I.D.S. Pereira, A. Wattiaux, J.M. Bassat, J.C. Grenier, M. Pouchard, *Journal of Materials Chemistry*, 7: 2107-2111, 1997.
- [97Gre] M. Greenblatt, Z. Zhang, M.H. Whangbo, *Synth. Met.*, 85: 1451-1452, 1997.
- [97Kyo] T. Kyomen, H. Tamura, M. Oguni, M. Itoh, K. Kitayama, *J. Phys. Condes. Matter*, 9: 1841-1850, 1997.
- [97Sas] H. Sasaki, H. Harashina, S. Taniguchi, M. Kasai, Y. Kobayashi, M. Sato, T. Kobayashi, T. Ikeda, M. Takata, M. Sakata, , *J. Phys. Soc. Jap.*, 66: 1693-1697, 1997.

- [97Med] M.L. Medarde, *Journal of Physics-Condensed Matter*, 9: 1679-1707, 1997.
- [98Cor] E.H.P. Cordfunke, A.S. Booij, M.E. Huntelaar, *Journal of Chemical Thermodynamics*, 30: 437-447, 1998.
- [98Hea] P.J. Heaney, A. Mehta, G. Sarosi, V.E. Lamberti, A. Navrotsky, *Physical Review B*, 57: 10370-10378, 1998.
- [98Hil] M. Hillert, *Phase equilibria, phase diagrams and phase transformations, their thermodynamic basis*, Cambridge university press, Cambridge, pp: 407-409, 1998.
- [98Hua] K.Q. Huang, R.S. Tichy, J.B. Goodenough, *Journal of the American Ceramic Society*, 81: 2565-2575, 1998.
- [98Hui] J.P.P. Huijsmans, F.P.F. van Berkel, G.M. Christie, *Journal of Power Sources*, 71: 107-110, 1998.
- [98Hro] M. Hrovat, J. Holc, S. Bernik, D. Makovec, *Mater. Res. Bull.*, 33: 1175-1183, 1998.
- [98Mat] N.I. Matskevich, F.A. Kuznetsov, D. Feil, K.J. Range, *Thermochimica Acta*, 319: 1-5, 1998.
- [98Sau] N. Saunders and A.P. Miodownik, *CALPHAD Calculation of Phase Diagrams*, Pergamon Materials Series, New York, 1998.
- [98Vas] V.V. Vashook, S.P. Tolochko, L. Yushkevich, L.V. Makhnach, I.F. Kononyuk, H. Altenburg, J. Hauck, H. Ullmann, *Solid State Ionics*, 110: 245-253, 1998.
- [98Yam] H. Yamane, M. Shimada, B.A. Hunter, *J. Solid State Chem.*, 141: 466-474, 1998.
- [99Alo] J.A. Alonso, M.J. Martinez-Lope, M.T. Casais, J.L. Martinez, G. Demazeau, A. Largeteau, J.L. Garcia-Munoz, A. Munoz, M.T. Fernandez-Diaz, *Chemistry of Materials*, 11: 2463-2469, 1999.
- [99Ara] Y. Arachi, H. Sakai, O. Yamamoto, Y. Takeda, and N. Imanishi, *Solid State Ionics*, 121: 133-139, 1999.
- [99Hua] P.N. Huang, A. Horky, A. Petric, *Journal of the American Ceramic Society*, 82: 2402-2406, 1999.
- [99Hro] M. Hrovat, S. Bernik, J. Holc, Z. Samardzija, *J. Mater. Res.*, 14: 2351-2354, 1999.
- [99Lam] C. Lamonier, A. Ponchel, A. D'Huysser, L. Jalowiecki-Duhamel. *Catalysis Today*, 50: 247-259, 1999.
- [99Lon] N.J. Long, F. Lecarpentier, H.L. Tuller, *Journal of Electroceramics*, 3: 399-407, 1999.
- [99Kha] V. V. Kharton, A. P. Viskup, E. N. Naumovich and F. M. B. Marques, *J. Mater. Chem.*, 9: 2623-2629, 1999.
- [99Mat] A. Manthiram, J.P. Tang, V. Manivannan, *Journal of Solid State Chemistry*, 148: 499-507, 1999.
- [99Mil] J.E. Millburn, M.A. Green, D.A. Neumann, M.J. Rosseinsky, *Journal of Solid State Chemistry*, 145: 401-420, 1999.
- [99Vas] V. V. Vashook, I. I. Yushkevich, L. V. Kokhanovsky, L. V. Makhnach, S. P. Tolochko, I. F. Kononyuk, H. Ullmann and H. Altenburg, *Solid State Ionics*, 119: 23-30, 1999.
- [00Lec] F. Lecarpentier, H.L. Tuller, N. Long, *Journal of Electroceramics*, 5: 225-229, 2000.

- [00Lin] C.D. Ling, D.N. Argyriou, G.Q. Wu, J.J. Neumeier, *J. Solid State Chem.*, 152: 517-525, 2000.
- [00Mog] M. Mogensen, N.M. Sammes, G.A. Tompsett., *Solid State Ionics*, 129: 63-94, 2000.
- [00Pon] A. Ponchel, A. D'Huysser, C. Lamonier, L. Jalowiecki-Duhamel, *Phys. Chem. Chem. Phys.*, 2 : 303-312, 2000.
- [00Ski] S. J. Skinner and J. A. Kilner, *Solid State Ionics*, 135: 709-712, 2000.
- [00Sin] S.C. Singhal, *Solid State Ionics* 135: 305-313, 2000.
- [00Tan] J.P. Tang, R.I. Dass, A. Manthiram, *Materials Research Bulletin*, 35: 411-424, 2000.
- [00Tas] AC Tas, Majewski, Aldinger, *Journal of the American Ceramic Society*, 83: 2954-2960, 2000
- [00Vas] V.V. Vashook, N. Trofimenko, H. Ullmann and L. Makhnach, *Solid State Ionics*, 131, 329-336, 2000.
- [00Wan] S.R. Wang, T. Kobayashi, M. Dokiya, T. Hashimoto, *Journal of the Electrochemical Society*, 147: 3606-3609, 2000.
- [01Ant] A.S. Antony, K.S. Nagaraja, G.L.N. Reddy, O.M. Sreedharan, *Materials Letters*, 51: 414-419, 2001.
- [01CRC] CRC Handbook of Chemistry and Physics, CRC Press 2001, pp. 6-10.
- [01Gru] A.N. Grundy, B. Hallstedt, L.J. Gauckler, *J. Phase Equilib.*, 22: 105-113, 2001.
- [01Hil] M. Hillert, *Journal of Alloys and Compounds*, 320: 161-176, 2001.
- [01Hui] J.P.P. Huijismans, *Current Opinion in Solid State & Materials Science*, 5: 317-323, 2001.
- [01Ken] B.J. Kennedy, T. Vogt, C.D. Martin, J.B. Parise, J.A. Hriljac, *Journal of Physics-Condensed Matter*, 13: L925-L930, 2001.
- [01Ler] M. Lerch, H. Boysen, T. Hansen, *J. Phys. Chem. Solids*, 62: 445-455, 2001.
- [01Lu] Lu Z, Liu J, Huang XQ, Liu ZG, Liu W, He TM, Su WH, *Chemical Journal of Chinese Universities*, 22: 630-633, 2001.
- [01Ive] E. Ivers-Tiffée, A. Weber, D. Herbstritt, *Journal of the European Ceramic Society* 21: 1805-1811, 2001.
- [01Jur] J. R. Jurado, *J. Mater. Sci.*, 36: 1133-1139, 2001.
- [01Maj1] P. Majewski, M. Rozumek, H. Schluckwerder, F. Aldinger, *J. Am. Ceram. Soc.*, 84: 1093-1096, 2001.
- [01Maj2] P. Majewski, M. Rozumek, F. Aldinger, *J. Alloys Compd.*, 329: 253-258, 2001.
- [01Ste] B.C.H. Steele, A. Heinzl, *Nature*, 414 (6861): 345-352, 2001
- [01Ste] B.C.H. Steele, *J. Mater. Sci.*, 36: 1053-1068, 2001.
- [01Vor] V.I. Voronin, I.F. Berger, V.A. Cherepanov, L.Y. Gavrilova, A.N. Petrov, A.I. Ancharov, B.P. Tolochko, S.G. Nikitenko, *Nuclear Instruments & Methods in Physics Research - A* 470: 202-209, 2001.
- [01Wu] G. Wu, J.J. Neumeier, M.F. Hundley, *Phys. Rev. B*, 63: 245120/1-5, 2001.

- [01Zha] X. Zhang, S. Ohara, H. Okawa, R. Maric, T. Fukui, *Solid State Ionics*, 139: 145-152, 2001.
- [02And] J.O. Andersson, T. Helander, L. Höglund, P. Shi, B. Sundman, *Calphad*, 26: 273-312, 2002.
- [02Ban] D.O. Bannikov, V.A. Cherepanov, *Z. anorg. allg. Chem.*, 628: 2180, 2002.
- [02Gru] A.N. Grundy, B. Hallstedt, L.J. Gauckler, *Acta Materialia*, 50: 2209-2222, 2002.
- [02Mak] L.V. Makhnach, S.P. Tolochko, V.V. Vashuk, O.V. Strukova, O.P. Ol'shevskaya, Y.G. Zonov, *Inorganic Materials*, 38: 1258-1263, 2002.
- [02Maj] P. Majewski, Rozumek, Tas, Aldinger, *J. Electroceramics*, 8: 65-73, 2002.
- [03Bra] N.P. Brandon, S. Skinner, B.C.H. Steele, *Annual Review of Materials Research* 33: 183-213, 2003.
- [03Cha] Chaker H, Kabadou A, Toumi M, Ben Hassen R, *Powder Diffraction*, 18: 288-292, 2003.
- [03Rez] L.A. Reznitskii, S.E. Filippova, *Russian Journal of Inorganic Chemistry*, 48: 1671-1673, 2003.
- [03Ski] S. Skinner, *Solid State Sciences*, 5: 419-423, 2003.
- [03Sha] A.L. Shaula, A.P. Viskup, V.V. Kharton, D.I. Logvinovich, E.N. Naumovich, J.R. Frade, F.M.B. Marques, *Materials Research Bulletin*, 38: 353-362, 2003.
- [03Yar] A.A. Yaremchenko, A.L. Shaula, D.I. Logvinovich, V.V. Kharton, A.V. Kovalevsky, E.N. Naumovich, J.R. Frade, F.M.B. Marques, *Materials Chemistry and Physics*, 82: 684-690, 2003.
- [04Bas] M.A. Basu, R.V. Wandekar, S.R. Bharadwaj, D. Das, *Journal of Thermal Analysis and Calorimetry*, 78: 715-722, 2004.
- [04Bob] M.A. Bobina, N.A. Yakovleva, L.Y. Gavrilova, V.A. Cherepanov, *Russian Journal of Physical Chemistry*, 78: 1340-1343, 2004.
- [04DoE] Fuel Cell Handbook, 7<sup>th</sup> Edition, EG&G Technical Services, US. Department of Energy, Office of Fossil Energy, 2004.
- [04Geu] S. Geupel, M. Zinkevich, F. Aldinger, "Thermodynamic modeling of the La<sub>2</sub>O<sub>3</sub>-Ga<sub>2</sub>O<sub>3</sub>-MgO system", 6<sup>th</sup> European SOFC- Forum, 28 June-2 July 2004, Lucerne, Switzerland, pp. 1123-1132.
- [04Gro] V. Grover, A.K. Tyagi, *Materials Research Bulletin*, 39: 859-866, 2004.
- [04Kha] V.V. Kharton, F.M.B. Marques, A. Atkinson, *Solid State Ionics*, 174: 135-149, 2004.
- [04Mat] A. Matraszek, L. Singheiser, D. Kobertz, K. Hilpert, M. Miller, O. Schulz, M. Martin, *Solid State Ionics*, 166: 343-350, 2004.
- [04Pal] M. Palumbo, G. Borzone, S. Delsante, N. Parodi, G. Cacciamani, R. Ferro, L. Battezzati and M. Baricco, *Intermetallics*, 12: 1367-1372, 2004.
- [04Vel] N. Velinov, N. Brashkova, V. Kuzhukharov, "Synthesis and Functional Properties of La<sub>2</sub>NiO<sub>4</sub> as Cathode Material for SOFCs" 6<sup>th</sup> European SOFC- Forum, 28 June-2 July 2004, Lucerne, Switzerland, pp. 1322-1329.
- [04Zin1] M. Zinkevich, F. Aldinger, *J. Am. Ceram. Soc.*, 87: 683-691, 2004.

- [04Zin2] M. Zinkevich, F.M. Morales, H. Nitsche, M. Ahrens, M. Rühle, F. Aldinger, *Z. Metallkd.*, 95: 756-762, 2004.
- [04Zin3] M. Zinkevich, F. Aldinger, *J. Alloys and Comp.*, 375: 147-161, 2004.
- [04Zin4] M. Zinkevich, S. Geupel, H. Nitsche, M. Ahrens, F. Aldinger, *Journal of Phase Equilibria and Diffusion*, 25: 437-447, 2004.
- [04Zin5] M. Zinkevich, S. Geupel, N.Solak, F. Aldinger, "Phase Diagrams and Thermodynamics of Materials for Intermediate-Temperature Solid Oxide Fuel Cells", 6<sup>th</sup> European SOFC- Forum, 28 June-2 July 2004, Lucerne, Switzerland, pp. 1476-1485.
- [05Che] J. Cheng, A. Navrotsky, X.D. Zhou, H.U. Anderson, *J. Mater. Res.*, 20: 191-200, 2005.
- [05He] T.M. He, P.F. Guan, L.G. Cong, Y. Ji, H. Sun, J.X. Wang, J. Liu, *Journal of Alloys and Compounds*, 393: 292-298, 2005.
- [05Kru] A. Kruth, G.C. Mather, J.R. Jurado, J.T.S. Irvine, *Solid State Ionics*, 176: 703-712, 2005.
- [05Mog] L. Moggi, F. Prado, H. Ascolani, M. Abbate, M.S. Moreno, A. Manthiram, A. Caneiro, *J. Solid State Chem.*, 178: 1559-1568, 2005.
- [05Mun] C.N. Munnings, S.J. Skinner, G. Amow, P.S. Whitfield, I.J. Davidson, *Journal of Fuel Cell Science and Technology*, 2: 34-37, 2005.
- [05Zin1] M. Zinkevich, S. Geupel, F. Aldinger, *Journal of Alloys and Compounds*, 393: 154-166, 2005.
- [05Zin2] M. Zinkevich, *Journal of Solid State Chemistry* 178: 2818-2824, 2005.
- [06Agu1] A. Aguadero, J. A. Alonso, M. J. Martínez-Lope, M. T. Fernández-Díaz, M. J. Escudero, L. Daza, *J. Mater. Chem.*, 16: 3402-3408, 2006.
- [06Agu2] A. Aguadero, M.J. Escudero, M. Perez, J.A. Alonso, V. Pomjakushin, L. Daza, *Dalton Transactions*, 36: 4377-4383, 2006.
- [06Amo1] G. Amow, S.J. Skinner, *Journal of Solid State Electrochemistry*, 10: 538-546, 2006.
- [06Amo2] G. Amow, I.J. Davidson, S.J. Skinner, *Solid State Ionics*, 77: 1205-1210, 2006.
- [06Ban1] D.O. Bannikov, A.P. Safronov, V.A. Cherepanov, *Thermochimica Acta*, 451: 22-26, 2006.
- [06Ban2] D.O. Bannikov, V.A. Cherepanov, *J. Solid State Chem.*, 179: 2721-2727, 2006.
- [06Che] W.Q. Chen, A. Navrotsky, *Journal of Materials Research*, 21: 3242-3251, 2006.
- [06Dat] P. Datta, P. Majewski, F. Aldinger, *Mater. Chem. Phys.* (2006), (in press) doi:10.1016/j.matchemphys.2006.11.011
- [06Dra] M.A. Dragan, "Defect chemistry, transport properties and thermodynamic stability of acceptor doped and undoped layered La<sub>2</sub>NiO<sub>4</sub>", PhD Thesis, RWTH Aachen, Germany, 2006.
- [06Mor] M. Mori, E. Suda; B. Pacaud, K. Murai, T. Moriga, *Journal of Power Sources*, 157: 688-694, 2006.
- [06Rao] M.V. Rao, S. Sturm, F. Phillipp, M. Zinkevich, *International Journal of Materials Research*, 97: 789-793, 2006.

- [06Sol] N. Solak, M. Zinkevich, F. Aldinger, *Fuel Cells*, 6: 87-92, 2006.
- [06Zin1] M. Zinkevich, *Prog. Mater. Sci.* doi:10.1016/j.pmatsci.2006.09.002 (*in press*), 2006
- [06Zin2] M. Zinkevich, D. Djurovic, F. Aldinger, *Solid State Ionics* 177: 989-1001, 2006.
- [06Zin3] M. Zinkevich, S. Geupel, F. Aldinger, A. Durygin, S.K. Saxena, M. Yang, Z.K. Liu, *Journal of Physics and Chemistry of Solids*, 67: 1901-1907, 2006.
- [07Sol] N. Solak, M. Zinkevich, J. Golczewski, F. Aldinger, H. Nitsche, M. Ahrens, R. Dinnebier, "La<sub>3</sub>Ni<sub>2</sub>O<sub>7</sub> ceramics: material with unusually low thermal conductivity", *Adv. Mater.* (2007), *in preparation*.



# Curriculum Vitae (Lebenslauf)

Name: Nuri Solak  
Gender: Male  
Date of Birth: 26.10.1977  
Place of Birth: Gürün, Turkey  
Nationality: Republic of Turkey

## Education:

**2003-now:** PhD student, Max-Planck Institute for Metals Research,  
Supervisor: Prof. Dr. Fritz Aldinger  
Group Leader: Dr. Matvei Zinkevich  
Thesis: Interface Stability in the Intermediate Temperature Solid Oxide  
Fuel Cells.

**1999-2002:** M.Eng., Metallurgical and Materials Engineering,  
Istanbul Technical University, Institute of Science and Technology.  
Supervisor: Prof. Dr. Süheyla Aydın  
Co-Supervisor: Prof. Dr. Mustafa Ürgen  
Thesis: Oxidation Behavior of Nitride Based Hard Ceramic Thin Film  
Coatings.

**1995-1999:** B.Eng., Metallurgical Eng., Istanbul Technical University

## Work Experience:

**2000-.**: Research Assistant, Istanbul Technical University  
Dept. of Metallurgical and Materials Engineering.